THERMAL MANAGEMENT and CONTROL
of
SPACE SATELLITE SYSTEMS and SUBSYSTEMS
in ORBIT

by

Peter Arnold van Wyk

Thesis presented in partial fulfillment of the requirement for the degree of Master of Science in Engineering at the University of Stellenbosch.

Thesis Supervisor: RT Dobson

November 2002

DEPARTMENT of MECHANICAL ENGINEERING

UNIVERSITY of STELLENBOSCH

Stellenbosch University http://scholar.sun.ac.za

Declaration

I, Peter Arnold van Wyk, the undersigned, hereby declare that the work contained in this thesis is my own original work and has not previously, in its entirety or in part, been submitted at any university for a degree.

Signature of candidate

18 November 2002

Stellenbosch University http://scholar.sun.ac.za

Summary

The focus of this thesis is on South Africa's first micro space satellite SUNSAT, and the thermal modelling thereof. Background theory with relevance to thermal management and control of satellite systems and subsystems is presented. The mission profile and subsystem makeup of SUNSAT is also briefly discussed, with emphasis placed on the physical structure, possible orbit paths, internal heat generation, and the environmental heating. The environmental heating on the satellite surfaces from the direct and reflected earth solar radiation, as well as the earth emitted infrared radiation, is determined from the developed computer program ORBIT-FLUX. This program was used in tandem with numerical programs (developed in house), as well as an outsourced program TAS (Thermal Analysis Systems) to model SUNSAT for two possible orbit paths. The resistance-capacitance formulation method was used to develop the numerical programs, which served initially to establish the validity of TAS.

The first approximated thermal model of SUNSAT's batteries was the 7 lumped-mass model that focused on the batteries since their overheating is the suspected reason for SUNSAT'S failure to complete its mission. A numerical program as well as a similar TAS model was developed, and the results showed correlation to within 3°C. A lumped-mass model of SUNSAT was also developed, both numerically and using TAS. The models were tested and the results showed that the temperatures of the models were sensitive to changes in internal heating as well as varying emissivity and absorptivity. The numerical and TAS lumped-mass model results did not correlate well, possibly due to the higher number of control volumes used in the TAS lumped-mass model. The TAS SUNSAT 2 model was developed as advancement on the lumped-mass model. The higher number of control volumes and the effect of adding solar panels gave a more realistic model of SUNSAT. The results did not show good correlation with actual SUNSAT temperature data possibly due to the fact that the solar panels were not mounted on the model body as they were on SUNSAT; but the TAS SUNSAT 2 model did set the platform for the more advanced TAS SUNSAT 3 model. This thermal model included the effects of the solar panel mountings, and had a higher number of control volumes, which gave a better physical representation of the SUNSAT subsystems. The model was tested for possible orbit paths of SUNSAT. The results showed excellent correlation to actual SUNSAT data. For the comparison of the TAS SUNSAT 3 model results with data from SUNSAT for July 1999 showed that the SUNSAT battery temperature was modelled to within 8°C. And for June 2000, this same comparison was to within 1°C.

Stellenbosch University http://scholar.sun.ac.za

A thermal management and control case study was done on a simple system (which included a cubic box and an internal solid block with heat generation) to illustrate the effects of using various passive and active thermal control hardware to regulate temperatures. The results showed that internal surfaces painted black provide for maximum heat sharing, and lowest block temperatures. The block temperatures were found to be very sensitive to changes in the cube external optical surface properties. A slight increase in emissivity lowered the block temperature, while a slight increase in absorptivity increased the block temperature. Heat pipes were also found to lower the temperatures of the block and immediate subsystems by providing a path of low thermal resistance to the flow of heat from the block directly to the radiator. The effect of thermal insulation was also investigated. For the two materials (rubber and plastic) that were tested, it was noticed that although insulation material does give more thermal control and predictability over a subsystem by thermally isolating it from its environment, it can cause a subsystem that has heat generation to become too hot.

Recommendations were made relating to future micro satellite thermal management and control with regard to; thermal modelling techniques, acquisition of tried software, positioning of temperature sensors for optimisation of thermal data, and the verification of optical surface properties by physical measurement.

Stellenbosch University http://scholar.sun.ac.za

Opsomming

Hierdie tesis fokus op Suid-Afrika se eerste mikro ruimte satelliet, SUNSAT, en die termiese ontwikkeling daarvan. Agtergrond teorie met betrekking tot die termiese bestuur en kontrole van die satelliet-sisteme en subsisteme word aangebied. Die missie-profiel en die samestelling van die subsisteme word ook kortliks bespreek met die klem op die fisiese strukture, moontlike wentelbane, interne hitte-opwekking, en die omgewingsverhitting. Die omgewingsverhitting op die oppervlaktes van die satelliet, veroorsaak deur direkte en weerkaatste aard/son bestraling, sowel as deur infrarooi bestraling afkomstig van die aarde, word bepaal deur die ontwikkelde rekenaarprogram ORBIT-FLUX. Hierdie program word gebruik in tandem met numeriese programme (intern ontwikkel), so wel as 'n uitgekontrakteerde program TAS (Termiese Analiese Sisteme) om SUNSAT vir twee moontlike wentelbane te modelleer. Die weerstands-kapasitansie formuleringsmetode is gebruik om die numeriese programme te ontwikkel. Hierdie programme is oorspronklik gebruik om die validiteit van TAS vas te stel.

Die eerste benaderde termiese model van SUNSAT se batterye was die 7 gekonsentreerde-massa model wat gefokus het op die batterye aangesien daar vermoed is dat oorverhitting van die batterye die rede is waarom SUNSAT nie sy missie voltooi het nie. 'n Numeriese program so wel as 'n gelyksoortige TAS model is ontwikkel en die resultate korreleer tot binne 3°C.'n Gekonsentreerde-massa model van SUNSAT is ook ontwikkel, numeries en met gebruik van TAS. Die modelle is getoets en die resultate toon dat die temperature van die modelle gevoelig is vir veranderinge in interne hitte sowel as vir wissellende uitstralingsvermoë en absorpsievermoë. Die numeriese- en die TAS gekonsentreerde-massa model resultate het nie goed met mekaar korrelleer nie, moontlik weens die hoë aantal kontrole volumes wat in die TAS gekonsentreerde-massa model gebruik is. Die TAS SUNSAT 2 model is 'n verdere ontwikkeling van die gekonsentreerde-massa model. Die hoër aantal kontrole volumes en die byvoeging van solarpanele het tot gevolg gehad dat hierdie 'n meer realistiese model van SUNSAT is. Die resultate het nie goed gekorrelleer met die temperatuurdata van die werklike SUNSAT nie, moontlik weens die feit dat die solarpanele nie op die bakwerk monteer is, soos in die geval van SUNSAT nie. Nietemin het het die TAS SUNSAT 2 model gelei tot die meer gevorderde TAS SUNSAT 3 model. Hierdie termiese model het die solarpaneel montuur ingesluit en het 'n hoër aantal kontrole volumes gehad, wat 'n beter fisiese weergawe van die SUNSAT subsisteme tot gevolg gehad het. Die model is getoets vir moontlike wentelbane van SUNSAT. Die resultate het 'n hoë korrellasie getoon met die data van die werklike SUNSAT. 'n Vergelyking van die TAS SUNSAT 3 model resultate met data van SUNSAT vir Julie 1999 wys

Stellenbosch University http://scholar.sun.ac.za

dat die SUNSAT battery temperatuur dieselfde is tot binne 8°C. Vergelyk met die resultate vir Junie 2000 was dit binne 1°C.

'n Termiese bestuurs- en kontrolestudie is gedoen op 'n eenvoudige sisteem (insluitende 'n kubieke boks en 'n interne soliede blok met hitte opwekking) om die uitwerking van die gebruik van passiewe en aktiewe termiese kontrole hardeware wat temperature reguleer, te illustreer. Die resultate toon dat interne oppervlaktes wat swart geverf is, lei tot die maksimum hitte-deling, en die laagste bloktemperature. Daar is gevind dat bloktemperature baie gevoelig is vir veranderinge in die eienskappe van die kubus se eksterne optiese oppervlaktes. 'n Effense vermedering van uitstralingsvermoë verlaag die bloktemperatuur, terwyl 'n effense vermedering van absorpsievermoë die bloktemperatuur verhoog. Daar is ook gevind dat hittepype die temperatuur van die blok en onmiddelike subsisteme verlaag deur om 'n pad van lae termiese weerstand teen die vloei van hitte vanaf die blok, direk na die verkoeler te verskaf. Die uitwerking van termiese isolasie is ook ondersoek. In die geval van die twee materiale (rubber en plastiek) wat getoets is, is daar opgemerk dat, alhoewel isolasie materiaal meer termiese beheer oor die subsisteem en voorspelbaarheid tot gevolg gehad het deurdat die subsisteem termies van die omgewing isoleer is, kan dit veroorsaak dat die subsisteem te warm word.

Aanbevelings is gemaak met betrekking tot toekomstige mikro satelliet bestuur en kontrole en wel in verband met die volgende: termiese modelleringstegnieke, die aanskaffing van getoetste sagteware, die plasing van temperatuut sensors vir die beste termiese data, en die verifikasie van die eienskappe van optiese oppervlaktes deur fisiese meting.

Stellenbosch University http://scholar.sun.ac.za

Dedication

This thesis is dedicated to my loving family who never stopped encouraging and supporting me in my aspirations to do something great with my life. To each and every one of them, thank-you.

A special dedication goes to Mr and Mrs Stewart without whose support I may never have reached my goals. Your kindness and generosity have, and will continue to, serve as an example for my family, my friends, and myself. Thank-you.

Stellenbosch University http://scholar.sun.ac.za

Acknowledgments

I would like to take this opportunity to acknowledge the fact that I would not have been able to succeed at this thesis if it were not for the blessings and guidance from the greatest teacher of them all, God.

To Mr Dobson ("Sir"), I want to say thank-you for your enthusiastic and dedicated support throughout this thesis. Your insight and knowledge have been invaluable to this project as well as to my future.

I would also like to take this opportunity to thank the SUNSpace Company, and the NRF for their financial support.

Stellenbosch University http://scholar.sun.ac.za

Contents

Stellenbosch University http://scholar.sun.ac.za

Stellenbosch University http://scholar.sun.ac.za

Stellenbosch University http://scholar.sun.ac.za

Nomenclature

a	universal variable
A	area [m^2]
A	position variable
Alt	altitude [km]
b	universal variable
B	position in space
c	specific heat [J/kgK]
C	thermal capacitance [J/K]
E	emissive power [W/m^2]
f	fraction (0 to 1)
F	view factor
g	length [m]
G	irradiance
h	heat transfer coefficient [W/m^2K]
h	length [m]
J	radiosity [W/m^2]
I	intensity [W/m^2]
k	thermal conductivity [W/mK]
L	length [m]
m	mass [kg]
m	variable
n	variable
$\dot{Q}$	heat transfer rate [W]
$\dot{Q}'''$	volumetric heat generation [W/m^3]
r	radius[m]
R	thermal resistance of conductivity [W/K]
R	thermal resistance of radiation [m^{-2}]
R	radius [km]
S	length [m]
t	time [s]
T	temperature [K]
T	length [m]
U	internal energy [J]

Stellenbosch University http://scholar.sun.ac.za

V	volume [m^3]
W	length [m]
x	length [m]

Greek Symbols

ρ	density [kg/m^3]
α	hemispherical averaged thermal absorptivity
ε	hemispherical averaged thermal emissivity
σ	Stefan-Boltzmann constant [5.6697×10^{-8} W/m^2K^4]
θ	angle [°]
τ	transmittance
η	extension factor
δ	thickness [m]
Ω	Right ascension of the ascending node at the vernal equinox [°]

Subscripts

1,2…	control volume variables
a	positional variable
b	blackbody
b	positional variable
bat	battery
bp	bottom-plate
bt	bottom-tray
cf	carbon fiber material
cs	cross sectional (area)
ds	direct solar radiation
int	internal
e	environment
eq	equivalent
E	directions East
earth	the earth
ee	earth emitted radiation

Stellenbosch University http://scholar.sun.ac.za

eq	equivalent
er	earth reflected solar radiation (albedo)
ext	external
GaAs	gallium arsenide solar cells
glass	glass material
i, ii,..	position
IR	infrared
kap	Kapton material
m	variable
mb	middle-body
model	model of SUNSAT
n	variable
N	direction North
RTV	RTV glue material
s	surface (area)
S	direction South
sat	satellite
sp	solar panel, satellite panel
space	space as a vacuum
ss	satellite surface
tp	top-plate
trays	aluminum trays of SUNSAT
ub	upper-body
W	direction West

Stellenbosch University http://scholar.sun.ac.za

Abbreviations and Acronyms

ADCS	Attitude Determination and Control Subsystem
Ag	Silver
Al	Aluminum
AO	Atomic Oxygen
BOL	Beginning Of Life
CPL	Capillary Pumped Loop
DET	Direct Energy Transfer
EOL	End Of Life
EPS	Electrical Power System
ESL	Electronic Systems Laboratory
FEP	Fluorinated Ethylene Propylene
FMH	Free Molecular Heating
GaAs	Gallium Arsenide
IR	Infrared
LDEF	Long Duration Exposure Facility
LEO	Low Earth Orbit
InP	Indium Phosphide
MLI	Multi Layer Insulation
NASA	National Aeronautical Space Administration
OBC	On Board Computer
OSR	Optical Solar Reflectors
PAS	Projected surface Area in the direction of the Sun
PPT	Peak Power Tracking
RAM	Random Access Memory
RF	Radio Frequency
RH	Relative Humidity
Si	Silicon
TAS	Thermal Analysis Systems
TCMD	Telemetry Command
TCS	Thermal Control System
TTC	Telemetry Tracking and Command
TLM	Telemetry
SA	Solar Array

Stellenbosch University http://scholar.sun.ac.za

SR	Shunt Regulator
SUNSAT	Stellenbosch University Satellite
VCHP	Variable Conductance Heat Pipe

Stellenbosch University http://scholar.sun.ac.za

List of Tables

Stellenbosch University http://scholar.sun.ac.za

Stellenbosch University http://scholar.sun.ac.za

Stellenbosch University http://scholar.sun.ac.za

List of Figures

Stellenbosch University http://scholar.sun.ac.za

Stellenbosch University http://scholar.sun.ac.za

Stellenbosch University http://scholar.sun.ac.za

Stellenbosch University http://scholar.sun.ac.za

Stellenbosch University http://scholar.sun.ac.za

Stellenbosch University http://scholar.sun.ac.za

Stellenbosch University http://scholar.sun.ac.za

2 BACKGROUND INFORMATION

This chapter provides general information relating to thermal management and control from a systems perspective, heat transfer, satellite systems and subsystems, the space environment; and does not necessarily apply to SUNSAT. The detail level of the information is sufficient to provide for a basic understanding, and preview into the remaining chapters of this thesis.

2.1 Literature Study of Micro Space Satellite Thermal Management Control Mechanisms

The literature study is focused at establishing the role of thermal management and control in micro space satellite systems by looking at the mechanisms behind the philosophy and theory that support satellite thermal design as a whole. This includes the role of thermal control, heat transfer theory, and information relating to the environment that supports the satellite through most of its life: space.

2.1.1 The Role of Thermal Management and Control in Micro Space Satellites

"Satellites perform better and last longer when their components remain within certain temperature limits, usually but not always, near the level at which they were assembled. Satellite thermal control deals with the theory and practice by which these temperatures are produced, and the function of the thermal engineer is to determine the influencing factors and manage them within the constraints of the satellite as one system," (Karam, 1998). The task and purpose of the TCS is to control the temperature of individual satellite components so that proper operation is maintained throughout the mission. These temperatures need to be maintained for nominal operation (or even survivability) of those components. Thermal control must begin with establishing the temperature specifications of the satellite components under which they are intended to exist and perform for the various stages of the satellite's life.

Some components have very narrow operational temperature ranges such as the batteries, which need to be maintained between 0 °C and 20 °C in a satellite that at some locations has a temperature variation of between -100 °C and +100 °C due to the space environment (Karam, 1998). Table 2.1 gives temperature limits for certain satellite components.

Stellenbosch University http://scholar.sun.ac.za

Solar cells usually operate over a wide temperature range; however, it is desirable to operate them as low as possible in the range, because the lower the operating temperature, the higher the solar cell efficiency (Larson, 1992). Temperature range specification serves to protect the subsystems from thermal damage, but does not guarantee optimal performance of the subsystem. Each subsystem has some optimal operating temperature (Karam, 1998).

Table 2.1 Temperature limits for certain satellite components (Karam, 1998)

COMPONENT	CRITICAL TEMPERATURE/ S
Batteries (NiCd)	0 to 20°C
Power regulating unit	0 to 40°C
Attitude control wheel	-5 to 45 °C
Attitude control electronics	0 to 40°C
Earth sensors (mounts)	-5 to 50°C
Solar array	-100 to 85°C
Inactive structure	-100 to 100°C

Thermal control must also attempt to smooth out the temperature variations and gradients that can occur on the satellite in order to prevent thermal fatigue and strain on delicate wires and solder joints, promoting early failures. Payloads such as cameras and telescopes are affected in performance by temperature gradients. For example, the temperature gradient of a camera support structure may not be more than 0.5 °C (Larson, 1992) in order to minimize differential thermal expansion, which distorts the satellite structure and adversely affects the directional accuracy of the imager.

2.1.1.1 Thermal management from a systems perspective

The thermal control of a satellite whilst in orbit is the prime objective of any thermal control system, but an adequate thermal design must meet the specifications for all the expected environments and operating conditions. These environments include; the earth ground environment, the launch module environment, the transfer to final orbit environment, and the final operating environment. Each environment places its own specific constraints on the design of the TCS. The variable environmental factors to name a few include: solar heating, infrared radiation, humidity, dust, free-molecular heating (FMH) and uv-radiation. This short list illustrates the diversity of the environmental factors that can influence the operating temperatures of the satellite. Every factor needs to be considered in the design of the TCS and a mission plan for each environment set out.

Stellenbosch University http://scholar.sun.ac.za

From the thermal analysis and control standpoint, the missions can be divided into four discrete phases, each with their own unique environments. These phases are given in table 2.2 below.

Table 2.2 Satellite environments (Piscane, 1994)

Phase	Time	Environment
Ground operations	Months up to launch	Laboratory, 20 °C, 40 RH, shipping
Launch	30 min	Sun, earth, albedo, fairing radiation, and aerodynamic heating
Transfer orbit	Hours to days	Sun, earth, albedo, and arbitrary attitude
Final orbit	Years	Sun, earth, and albedo, changing operating modes and attitudes

For the ground operations where the satellite is un-powered, ambient temperature and humidity limits are specified to keep all components within non-operating temperature limits and to prevent moisture condensation. In this case, the environment can be controlled and no detailed TCS needs to be integrated into the satellite design. During the launch phase, the satellite environment becomes more severe. The satellite is located in the launch module where it is susceptible to fairing radiation and FMH. The fairing temperatures can become as high as 370 °C (Piscane, 1994). The satellite environment can still be controlled for this case. Typically, conditioned air would be blown through the launch module to ensure the satellite subsystems do not overheat.

The transfer of the satellite into its final orbit and position is critical. If the satellite is disorientated it may be that there are surfaces getting heated by the solar radiation that are not designed for it. Or a surface may be facing space and getting too cold, which may effect the lifetime of certain components. It is during this phase that the satellite's attitude must be stabilized, antennas deployed, and bus and payload powered up as quickly as possible (Piscane, 1994).

The final operating environment is by far the most demanding on the satellite and TCS with respect to heat loads. These heat loads include direct solar radiation, earth reflected solar radiation (albedo), and the earth emitted infrared radiation.

Stellenbosch University http://scholar.sun.ac.za

The variation in temperatures experienced by components and subsystems in the final orbit, is due to the variable thermal environment that a satellite experiences throughout the life of the mission. To name a few of the changes that occur during the mission: changes in attitude, altitude, power dissipation, direction and distance of sun, changes in surface properties, and operating modes contribute to the variable thermal environment.

2.1.1.2 Thermal control considerations

An interaction exists between the thermal control subsystem and the other satellite subsystems such as the power, structures, attitude, communications and command subsystems. Once in operation, the excess heat generated within these subsystems needs to be removed either to another subsystem that requires heating or as waste heat to space. The heat that is rejected to space is done so by external radiating surfaces of the satellite (radiators). These radiators are covered with thermal coatings that have a specific solar absorptivity and reflectivity, and infrared emissivity. All solar and infrared radiation that arrives at the satellite external surfaces from the environment is either reflected or absorbed (assuming opaque surfaces). The radiators are constantly radiating heat to space, which can be approximated as a vacuum at 0 K or –273 °C (Piscane, 1994). The rate of heat removal is dependant on the temperature, the area and the thermal surface properties of the radiator.

"Cold-spots" (low temperatures relative to subsystem limits) often occur in satellites at locations where there is little internal heat generation and a very low heat transfer rate to a specific location. "Hot-spots" (high temperatures relative to subsystem limits) on the other hand are exactly the opposite of cold-spots. These thermal conditions are not desirable in equipment that is susceptible to temperature gradients or operating temperatures different from the design temperatures. For this reason, the TCS needs to manage the "flow" of heat through satellite, between subsystems, and to/from space.

Figure 2.1 shows the flow chart of the interaction between the TCS sub-functions. Heat is collected from the environment and also rejected by the radiators to the environment. Heat inside the satellite, is transported as necessary to subsystems, to be stored in heat sinks or to be rejected. The TCS also provides subsystems with heat as required. Many factors drive the design and development of a satellite TCS. Figure 2.2 illustrates several possible inputs and outputs for a particular TCS. The inputs are the TCS design drivers in that they provide the information about the satellite and the mission, which is then used to establish the requirements of the TCS.

Stellenbosch University http://scholar.sun.ac.za

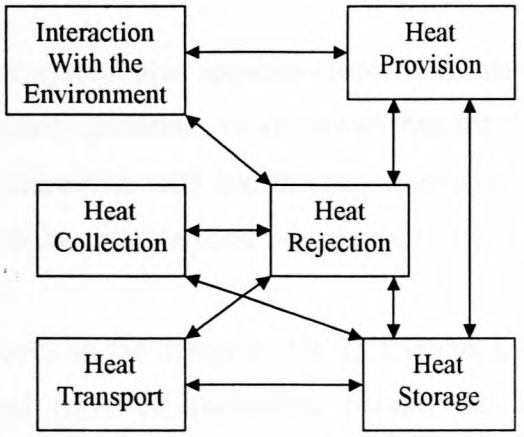

Figure 2.1 Interaction between the TCS sub-functions

Attitude control is considered as one point of interaction on the TCS because of its primary influence in determining the position of the orbit and thus the external heat loads on the satellite and the radiator orientation for heat removal. Structural design needs close coordination with the thermal design since the structure is the basic heat transfer path for conducting waste electrical energy to the radiators. From a heat transfer perspective, a structure of low thermal conductive resistance allows for heat to be rapidly transported by the structure to the radiators and into space. This reduces any chance of undesirable thermal gradients in the satellite. For this reason, a structure of high thermal conductivity such as aluminum is often used.

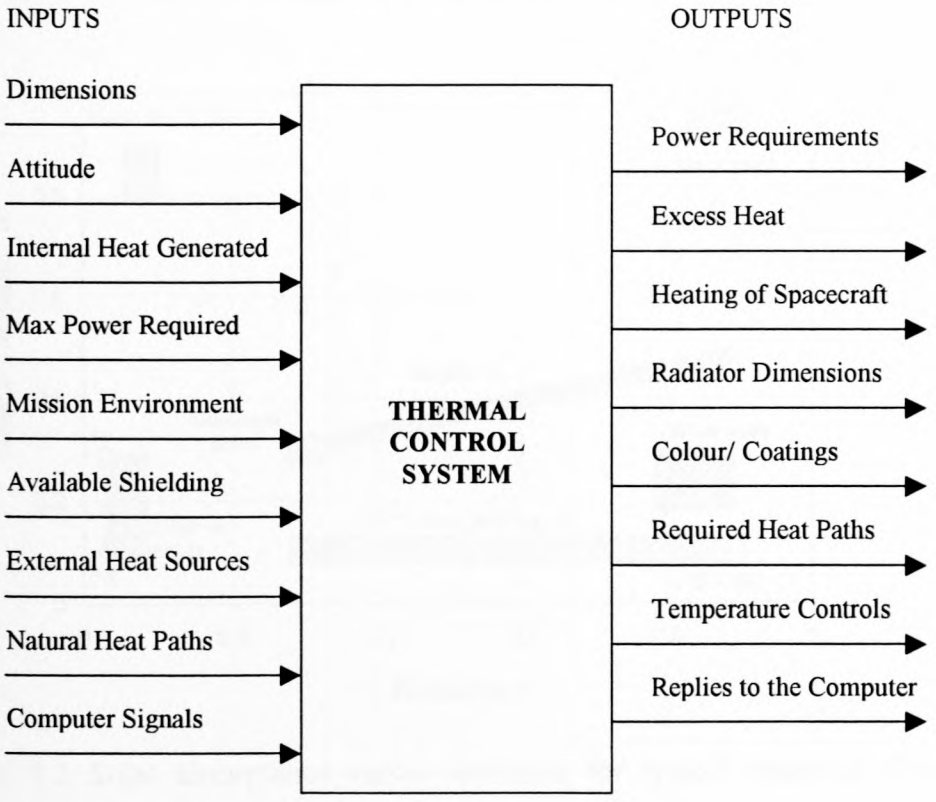

Figure 2.2 Thermal control system interface (tsgc.utexas.edu, 1995)

Stellenbosch University http://scholar.sun.ac.za

The power system also requires close coordination with the thermal control system. The power system usually generates more power than can be used. The power subsystem typically has the greatest interaction with the thermal control subsystem because the majority of the dissipated heat within the satellite must be radiated to space.

The difficulty in the design of the TCS is that it is dependant on assumptions that cannot be 100 % verified (i.e., environmental parameters, spacecraft physical parameters, workmanship tolerances) and is therefore prone to a certain measure of design uncertainty (Chalmers, 1988).

2.1.1.3 Thermal Control Mechanisms

Satellite thermal control mechanisms are classified as either *passive* or *active*. A passive thermal control system on a satellite in orbit relies on controlling the conductive and radiative heat paths, and has no moving parts, fluids, or electrical power input. Passive thermal control subsystems include for example: sun shields, radiating fins, thermal surface finishes, heat sinks, and multi layer insulation (MLI). Figure 2.3 shows a few thermal surface finishes and there respective optical properties. In deciding on the best thermal surface finish involves not only selecting the finish based on the optical properties, but also their stability, mechanical properties, out-gassing characteristics, cost, mass, electrical properties, and ease of handling (Piscane, 1994).

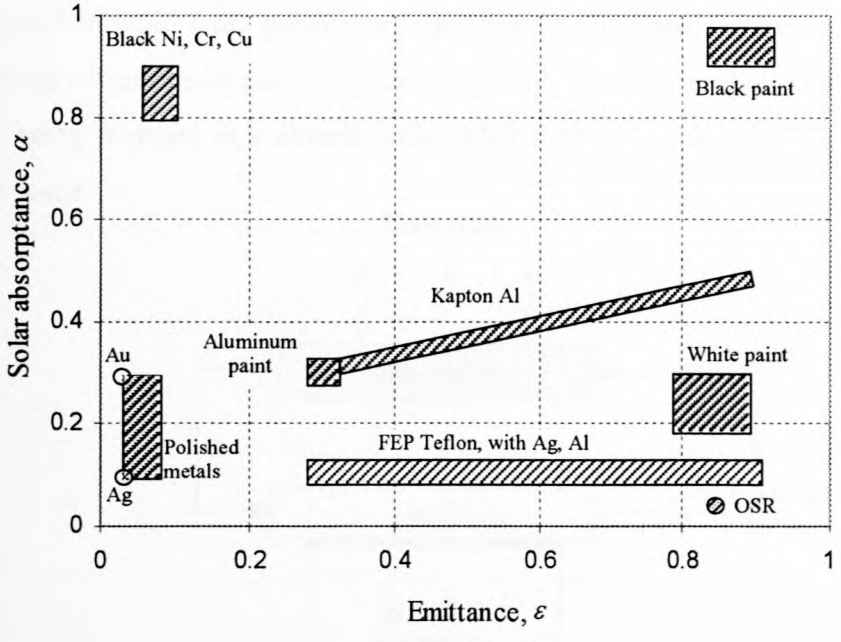

Figure 2.3 Solar absorptance versus emittance for typical materials (Piscane, 1994) (Note: Fluorinated ethylene propylene (FEP), and optical solar reflectors (OSR))

Stellenbosch University http://scholar.sun.ac.za

A passive system illustration is shown in figure 2.4 below. Heat is taken away from the electric equipment by conducting it to a "cold plate" at a low temperature. This low temperature is induced by the fact that the cold plate is coupled to the radiator, which radiates the heat into deep space.

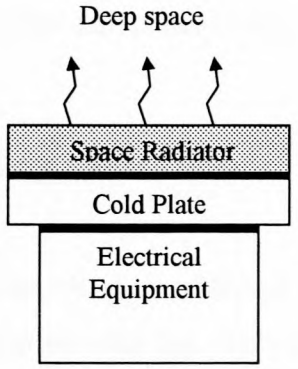

Figure 2.4 Passive thermal control

An active thermal control system is used in addition to the passive system when a passive system is not adequate. This is usually due to variations in the environment and component heat-generation rates, along with degradations of surface finishes over time, that can drive the temperature variations in a passive design to ranges larger than some components can withstand. Because of this, electrical heaters and thermostats are sometimes required to protect components under cold-case environmental conditions or to make up for heat that is not dissipated when an electronic box is turned off. Pumped-loop systems might also be used to counter the effects of increased internal heat generation, and this is illustrated in figure 2.5. In comparison to the previously mentioned case of passive control, the heat is removed from the "cold plate" by a fluid being pumped in a closed cycle rather than by conduction. This heat in turn is radiated to deep space.

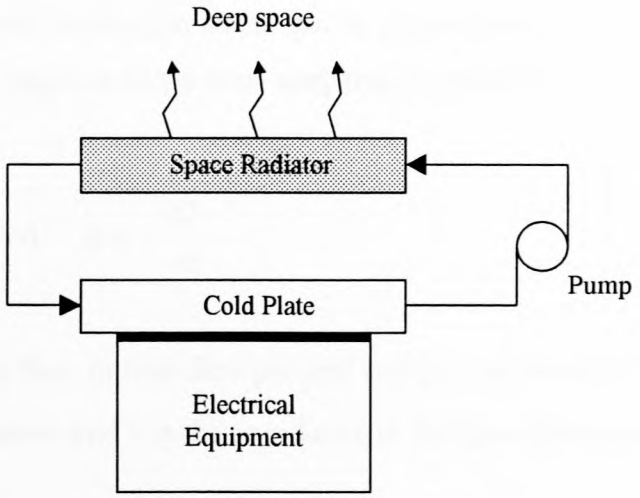

Figure 2.5 Active thermal control

Stellenbosch University http://scholar.sun.ac.za

Radiators that can extend to vary the surface area facing deep space are used to control the rate at which heat is removed from the satellite system. The larger the surface area of the radiator, the higher is the heat removal rate. Heat pipes are also extensively used in satellites to provide a super-conducting path for heat to the radiators. Other common active devices include: thermoelectric coolers and phase change materials.

2.1.2 Heat Transfer Mechanisms

In thermodynamics, heat is defined as energy transfer due to temperature gradients or differences. Consistent with this viewpoint, thermodynamics recognizes only two modes of heat transfer: conduction and radiation (Mills, 1995). For example, heat transfer through an aluminum tray on a satellite is by conduction, whereas heat transfer from the sun to the satellite surface is by thermal radiation. In air at normal pressure, conduction is by molecules that travel a very short distance (~ 0.65 μm) before colliding with another molecule and exchanging energy. Radiation is by photons, which travel almost unimpeded through the air from one surface to another. Strictly speaking, convection is the transport of energy by motion of a medium. It is common engineering practice to use the term convection more broadly and describe heat transfer from a surface to a moving fluid also as convection, or convective heat transfer, even though conduction and radiation play a dominant role close to the surface, where the fluid is stationary. In this sense, convection is regarded as a distinct mode of heat transfer (Mills, 1995).

2.1.2.1 Conduction

Fourier's law of heat conduction states that in a homogeneous substance, the local heat flux is proportional to the negative of the local temperature gradient

$$\frac{\dot{Q}}{A} = \dot{q} \quad \text{and} \quad \dot{q} \propto -\frac{dT}{dx} \tag{2.1}$$

where $\dot{q}$ is the heat flux, or heat flow per unit area perpendicular to the flow direction [W/m^2], T is the local temperature and x is the coordinate in the flow direction. Introducing the constant of proportionality k,

Stellenbosch University http://scholar.sun.ac.za

$$\dot{q} = -k\frac{dT}{dx} \tag{2.2}$$

where k is the thermal conductivity of the substance and has the units [W/m^{2}K] (Mills, 1996). Introducing the cross-sectional area A into equation 2.2 and integrating (assuming k is not a function of x or T)

$$\dot{Q} = kA\left(\frac{T_1 - T_2}{L}\right) \tag{2.3}$$

Where, T_1 and T_2 are the surface temperatures kept at steady state temperature and L is the thickness of the material being analysed.

The analogy to an electric network in which temperature difference represents a potential difference and heat flow between two points in a material, an electric current gives rise to the quantity known as conduction thermal resistance R_{12}, which may be viewed as the inverse of conductance.

$$\dot{Q}_{12} = \frac{T_1 - T_2}{R_{12}} \tag{2.4}$$

where, $R_{12} = \dfrac{L}{kA}$.

The resistance model for conductive heat transfer is shown in the figure 2.6.

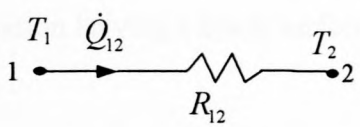

Figure 2.6 Thermal resistance model for conduction

If there is several materials sandwiched together, the rate of heat transfer by conduction through the materials can be computed similar to the way electric current flows through resistances connected in series:

$$\dot{Q} = \frac{T_1 - T_N}{\sum_{i=1}^{N-1} R_{i(i+1)}} \tag{2.5}$$

Stellenbosch University http://scholar.sun.ac.za

For the specific case of two materials sandwiched together, the contact surfaces between the two materials offer a resistance to conductive heat transfer. This is known as contact resistance and can be represented by an additional thermal resistor in equation 2.5. The quality of the contact made between two materials is strongly dependant on the roughness of the material surface and the contact pressure.

Since satellites are typically made up from an aluminum framework, any heat generated internally (e.g. batteries, amplifiers) or externally (irradiation) is transferred by conduction through the satellite frame. Also, conduction is the primary means of transferring heat from internal hot spots to the radiators on the outside of the satellite, which in turn radiates the heat to deep space, or to cold spots within the satellite.

2.1.2.2 Radiation

Radiation can be simply defined as the transmission of energy by way of electromagnetic waves. Radiation can be transmitted in a wide range of wavelengths, but thermal radiation effects are associated in the band of wavelengths from 0.1 to 100 μm. This range of thermal radiation is made up of ultraviolet radiation (range 0.1 – 0.4 μm), visible radiation (wavelength 0.4 - 0.7 μm), and infrared radiation (IR). (Mills, 1997.) The range 0.225 to 7 μm contains 99.78 % of the total solar output. Of the remainder, 0.03 % occurs below 0.225 μm and 0.19 % above 7 μm (Langton, 1969).

A black surface (or blackbody) is defined as a surface that absorbs all incident radiation, reflecting none. The radiation leaving a black surface is given by the Stefan-Boltzmann law as

$$E_b = \sigma T^4 \tag{2.6}$$

where E_b is the blackbody emissive power, T is the absolute temperature [K], and σ is the Stefan-Boltzmann constant $\approx 5.67 \times 10^{-8}$ W/m^{2}K^4 (Mills, 1995).

If a body is exposed to radiation, it will absorb some, reflect some, and transmit some of the radiation through the body. From this we deduce that

$$\alpha + \rho + \tau = 1 \tag{2.7}$$

Stellenbosch University http://scholar.sun.ac.za

Where α is the absorptivity (fraction of absorbed incident radiation), ρ is the reflectivity (fraction of reflected incident radiation) and τ is the transmittance (fraction of transmitted incident radiation).

Radiation emitted by a "real" body is less than that of a blackbody emitting at the same temperature. For this reason, black bodies are taken as a reference, and a quantity known as the emissivity of a surface is defined as the ratio of energy emitted by a real surface to that by a black body at the same temperature.

$$\varepsilon = \frac{E}{E_b} \tag{2.8}$$

For a gray surface, α and ε are constant, and equal and independent of temperature (Mills, 1995). These surface radiation properties depend on the nature of the surface. The chemical composition, physical structure, and roughness all influence these surface properties (Mills, 1995). They are also dependent on the directional properties and wavelength of the radiation. For many surfaces, the average absorptance to short-wavelength solar radiation is very different from its value for longer wavelengths. (This may be significant in space where both solar and infrared radiations respectively, are dominant.) The surface properties (α and ε) are typically averaged over all wavelengths and directions, to allow for a more usable form know as the *hemispherical emittance* or *hemispherical absorptance*. The typical variation of spectral absorptance (α_λ) with wavelength is shown for white paint in figure 2.7 below.

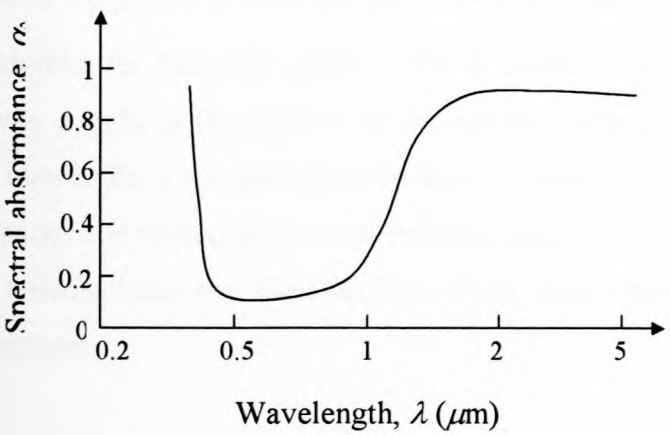

Figure 2.7 Spectral absorptance of white paint (Lyle, 1973)

The energy exchange between two isothermal surfaces, i and j, is described by the equation

$$\dot{Q}_{ij} = \varepsilon_i A_i F_{ij} \sigma \left(T_i^4 - T_j^4 \right) \tag{2.9}$$

Stellenbosch University http://scholar.sun.ac.za

Where F_{ij} is the shape factor or view factor from surface *i* to surface *j* and is only dependant on the geometry of the surfaces and the space between them. A_i is the surface area of surface *i*.

For satellite thermal control, thermal radiation is the only means of removing the excess heat generated internally from satellite subsystems. Excess heat is emitted from the satellite radiators as infrared radiation to the earth and to space. The rate at which the heat is removed from the radiators is dependant on the temperature, emittance and area of the radiator; as well as the temperature of the earth and space, and the view factor from the satellite radiators to earth and space. (Refer to appendix B for a detailed description of radiation in space.)

2.1.2.3 Convection

Convection is heat transfer from a surface to a fluid flowing over it either as a result of a pressure difference (forced convection) or due to variations in gravity and density (natural free convection) (Mills, 1995). Usually the total heat transfer from a surface is required and not the actual variation of the heat flux along the surface. It is thus convenient to define an average heat transfer coefficient $\bar{h}$ (W/m^{2}K) for an isothermal surface *i* of area *A* by the relation

$$\dot{q} = \frac{\dot{Q}}{A} = \bar{h}(T_i - T_\infty) \tag{2.10}$$

where $\dot{q}$ or $\dot{Q}$ is the heat convected over surface area A at temperature T_i, T_∞ is the fluid temperature far from the surface, and $\bar{h}$ is the convection coefficient, which is primarily the quantity sought in the physics of convection. Since space is essentially a vacuum, convection heat transfer does not take place on satellite surfaces during space operation. During the ground operations convection does occur between the satellite and the surrounding air. Also, convective heat transfer heats the outer surface of the launch module as the module ascends through the atmosphere.

2.1.3 The Space Environment

In near-earth space, the temperature of the residual atmosphere (the exosphere), is approximately 1000 K. However, the satellite will not attain thermal equilibrium with these molecules as the free mean path (i.e. the mean distance that the molecules travel between collisions) is much larger than the dimensions of the atmosphere (Underwood).

Stellenbosch University http://scholar.sun.ac.za

Because of the tenuous nature of the residual atmosphere, conduction and convection effectively do not take place, and so the primary form of heat transfer between the satellite and its environment is radiation. Overall satellite thermal control during operation in space is usually achieved by balancing the energy emitted by the satellite, with the internal heat dissipated by the electrical equipment and the energy absorbed from the environment. The environmental heating for LEO (Low Earth Orbiting) satellites is made up of three distinct heat loads. These include the direct solar radiation, reflected earth solar radiation (albedo) and the earth emitted radiation.

2.1.3.1 Environmental Heat Loads

Direct Solar Radiation

Of the phenomenally large quantity of energy leaving the sun's surface, a minute fraction reaches the outer atmosphere of the earth. The earth is at a distance of 1 astronomical unit, or 1.5 x 10^{11} m (Gilmore, 1994), from the sun. Solar radiation is a term used to describe visible and near-visible (ultraviolet, visible and near-infrared) radiation emitted from the sun. The sun can be considered as a blackbody emitting radiation at an average temperature of 5800 K (Mills, 1995). The spectral radiation received by the earth from the sun (solar spectral irradiance) is shown in figure 2.8.

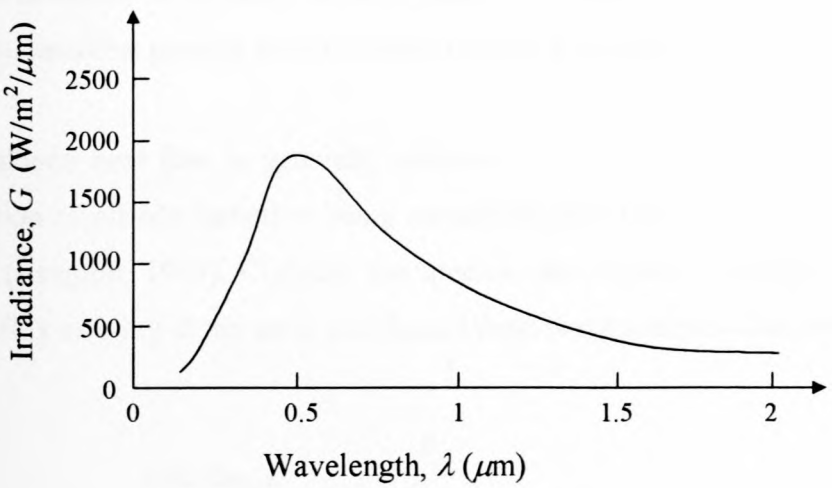

Figure 2.8 Solar spectral irradiance curve (Lyle, 1973)

Outside the earth's atmosphere, the solar flux has an average yearly intensity of approximately 1353 W/m^2 (Piscane, 1994).

Stellenbosch University http://scholar.sun.ac.za

This value varies inversely with the square of the distance from the sun. Because of the elliptical nature of the earth's orbit around the sun, the actual value of solar flux varies from 1300 W/m^2 at aphelion (furthest position from the sun) to 1400 W/m^2 at perihelion (closest position to the sun) (Piscane, 1994).

The heat load on the satellite surface generated from the solar irradiation, is given by the following equation:

$$\dot{Q}_{ds} = \alpha A \dot{q}_{ds} \tag{2.11}$$

where, α is the hemispherical solar absorptivity, A is the satellite surface area projected in the direction of the sun, and $\dot{q}_{ds}$ is the solar flux averaged as 1353 W/m^2.

Albedo Radiation

The *albedo* is defined as the fraction of direct solar radiation that is reflected from the ground, ground cover, and bodies of water on the surface of the earth and includes backscattering by the atmosphere. The albedo also varies over different areas of the earth. The variation of albedo with latitude is given in appendix J, table J8 (Gilmore, 1994). The albedo is often averaged across the globe as 0.36 for calculation purposes (Langton, 1969). (Table J2 gives a complete list of averaged albedo for various planets.) Although the albedo tends to increase for higher North and South latitudes, the amount of solar radiation received for these latitudes is very low. For his reason, satellites passing over the poles receive a low albedo heat flux (W/m^2).

The albedo heat flux is generally taken as varying with the cosine of the angle between the direction of albedo radiation being considered and the line joining the centres of the sun and earth (Langton, 1969). Consider the specific case shown in figure 2.9 below. A fraction of the solar flux arriving at the earth is reflected from two locations of equivalent area, A and B.

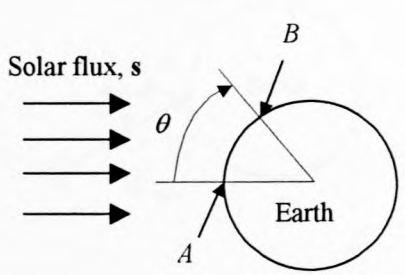

Figure 2.9 Albedo heat flux

Stellenbosch University http://scholar.sun.ac.za

Assuming that the average albedo is applicable to this case, then the solar flux arriving at each surface is thus reflected equally well. But the albedo heat flux at location B is lower than that at location A, which is at the sub-solar point on the earth and thus the highest possible albedo heat flux location. It follows that the albedo heat flux from location B in terms of that from location A is

$$\dot{q}_{er,B} = \dot{q}_{er,A} \cos\theta \tag{2.12}$$

where the albedo heat flux from location A is defined as

$$\dot{q}_{er,A} = a\dot{q}_{ds} \tag{2.13}$$

and a is the *albedo*.

The albedo flux is assumed to be diffuse; that is to say, solar radiation reflected by the earth and backscattering is done so in all directions and is based on Lambert's Cosine Law, which is the condition for diffuse radiation. The intensity of the albedo heat flux is determined as

$$I_{er} = \frac{\dot{q}_{er}}{\pi} \tag{2.14}$$

where I_{er} is the intensity and is defined as the heat flow from a surface per unit solid angle, per unit area projected normal to the direction (Mills, 1995). Consider figure 2.10 below. The surface dA_{sat} of a satellite, receives energy at a rate $d\dot{Q}_{er}$ that is reflected from an area dA_{earth} on the earth. The angle between the incoming solar radiation and the normal of the area dA_{earth} is given as α_1. The angle locating the satellite surface in space relative to the earth is given by the angle α_2. Angle α_3 locates the satellite surface normal relative to the satellite-earth chord of length L.

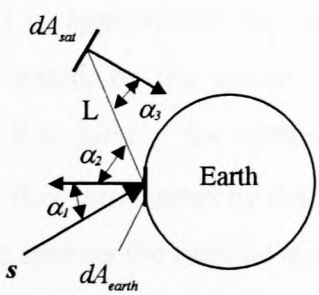

Figure 2.10 Schematic of satellite surface element in earth orbit

Stellenbosch University http://scholar.sun.ac.za

The rate of heat flow between dA_{earth} and dA_{sat} can be defined as

$$d\dot{Q}_{er} = I_{er} dA_{earth} \cos\alpha_2 d\omega_{earthsat} \tag{2.15}$$

where $d\omega_{earthsat}$ is the solid angle, which is determined for this particular case as

$$d\omega_{earthsat} = \frac{dA_{sat} \cos\alpha_3}{L^2} \tag{2.16}$$

From equations 2.11 and 2.12 the albedo heat flux from dA_{earth} is derived as

$$\dot{q}_{er} = a\dot{q}_{ds} \cos\alpha_1 \tag{2.17}$$

Substituting equation 2.17 into equation 2.14 results in

$$I_{er} = \frac{a\dot{q}_{ds} \cos\alpha_1}{\pi} \tag{2.18}$$

By substituting equations 2.16 and 2.18 into equation 2.15 and rearranging, the rate of heat flow from area on the earth dA_{earth} to the satellite area dA_{sat} is derived as

$$d\dot{Q}_{er} = \frac{a\dot{q}_{ds} \cos\alpha_1 \cos\alpha_2 \cos\alpha_3 dA_{earth} dA_{sat}}{\pi L^2} \tag{2.19}$$

Integrating equation 2.19 over the earth for a single satellite position will result in the total albedo heating on the satellite surface for that position. As the satellite moves in its orbit, so the total albedo heating varies. (The total albedo heat load would include the surface absorptivity of the satellite surface in equation 2.19.)

Common practice is to approximate the total albedo heating by taking the albedo heat flux to vary as previously stated, by the cosine of the angle between the direction of albedo being considered and the line joining the centre of the sun and earth (angle α_1 in figure 2.10). The fraction of this heat flux intercepted by the satellite surface is taken to be equivalent to the view factor of the earth as seen by the satellite surface (Piscane, 1994).

Consider the example of a spherical satellite in orbit. For this particular case, the average albedo, a, is equal to 0.3 and the solar constant is set equal to 1353 W/m^2. The angle between the earth-sun line and the earth-satellite line is θ.

Stellenbosch University http://scholar.sun.ac.za

The variation of the incident albedo heat flux on a unit cross-sectional area of the spherical satellite as a function of altitude above the earth surface is given in figure 2.11 below.

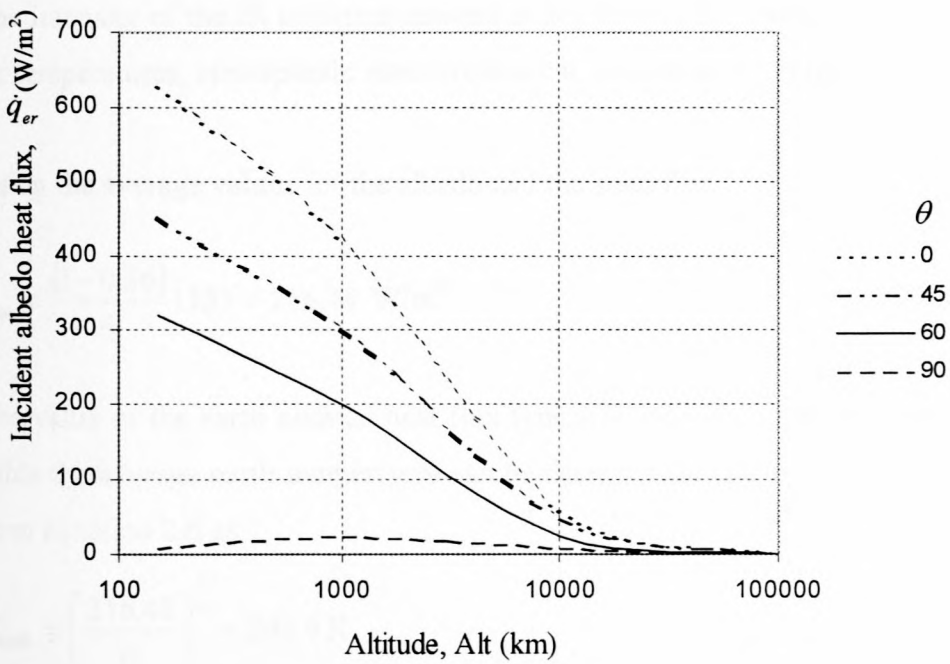

Figure 2.11 Incident albedo heat flux on a spherical satellite of unit cross-sectional area as a function of altitude (Lyle, 1973)

Earth Emitted Radiation

The earth achieves thermal equilibrium by balancing the energy received (absorbed) from the sun with the energy re-emitted as long-wavelength IR radiation. This balance is maintained fairly well on a global annual average (Gilmore, 1994). The balance between the incoming solar radiation and that emitted by the earth is

$$\dot{Q}_{ds} = \dot{Q}_{ee}$$

It follows after substitution

$$(1-a)A_{e,cs}\dot{q}_{ds} = A_{e,s}\dot{q}_{ee}$$

Substituting for the areas

$$(1-a)(\pi R_e^2)\dot{q}_{ds} = (4\pi R_e^2)\dot{q}_{ee}$$

Stellenbosch University http://scholar.sun.ac.za

After rearranging and solving

$$\dot{q}_{ee} = \frac{(1-a)}{4}\dot{q}_{ds} \tag{2.20}$$

The intensity of the IR radiation emitted at any time is dependant on factors such as surface and air temperatures, atmospheric moisture content, and cloud coverage (Gilmore, 1994).

Using the average values for the albedo and the solar flux

$$\dot{q}_{ee} = \frac{(1-0.36)}{4}1353 = 216.48 \text{ W/m}^2$$

The value of the earth emitted heat flux typically used is 216 W/m^2 (Piscane, 1994). From this value the average earth temperature can be determined (assuming that the earth is a black body) from equation 2.6 as

$$T_{earth} = \left(\frac{216.48}{\sigma}\right)^{\frac{1}{4}} = 248.6\,\text{K}$$

This correlates well with table J1 (Langton, 1969).

From the earth emitted heat flux of 216 W/m^2, the amount that reaches the satellite is dependent on the view factor of the earth as seen by the satellite. The earth emitted heat load on the satellite surface is in turn dependant on the surface properties of the satellite. The earth emitted heat load on a single satellite panel of area A_{sp} with a surface emissivity of ε_{sp} can be determined as

$$\dot{Q}_{sp} = \varepsilon_{sp} A_{sp} F_{sp,earth} \dot{q}_{ee} \tag{2.21}$$

where $F_{sp,earth}$ is the view factor.

Consider the example of a satellite panel of unit area and whose normal passes through the centre of the earth; and the surface is also assumed black. The altitude of the panel above the earth is varied, and the earth emitted heat load on the satellite panel is plotted in figure 2.12. (The view factor is determined from equation B26 in appendix B)

Stellenbosch University http://scholar.sun.ac.za

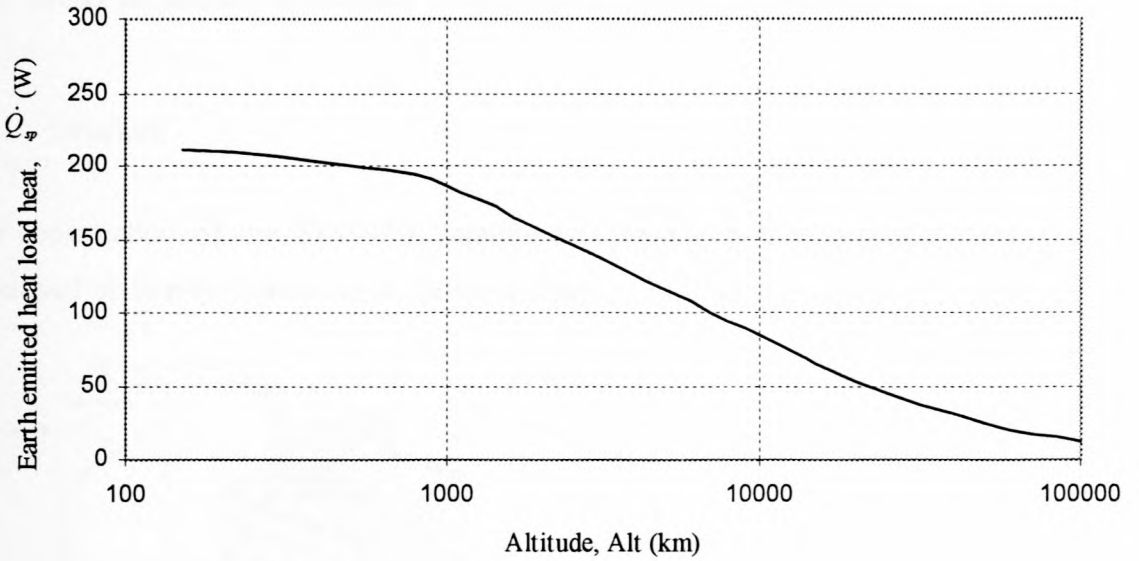

Figure 2.12 Earth emitted heat load on a satellite panel of unit area and whose normal passes through the centre of the earth

2.1.3.2 Satellite Heating in Space

The direct solar radiation is the highest heat load on the satellite surface and has the largest effect on satellite operating temperatures. The position of the satellite relative to the sun and the projected area of the satellite surface in the direction of the sun determine the heat load on the satellite.

The albedo heat load is significant when the satellite passes over the sunlit portion of the earth. The earth-facing surface of the satellite is most affected by the albedo heat load.

The earth-emitted radiation is taken to be constant throughout the satellite orbit around the earth. According to Gilmore (1994), the earth-facing surface of the satellite emits infrared radiation in the same wavelength range as it receives from the earth. This is commonly known as the back-load on a satellite. This may create a problem in selecting the appropriate thermal surface finish for a radiator, since a single thermal surface finish that allows for high emittance will also result in high absorption.

The role of the earth in some LEO satellites is to provide a cool down period for the satellite as it passes through the earth's shadow. The only environmental heating on the satellite during the earth eclipse is from the earth emitted heat flux.

Stellenbosch University http://scholar.sun.ac.za

2.2 Study of Satellite Operating Subsystems applicable to SUNSAT

2.2.1 Structure

The construction of the SUNSAT satellite was based on the popularized tray construction developed by Surrey University as shown in figure 2.13 (Schoonwinkel, 1997).

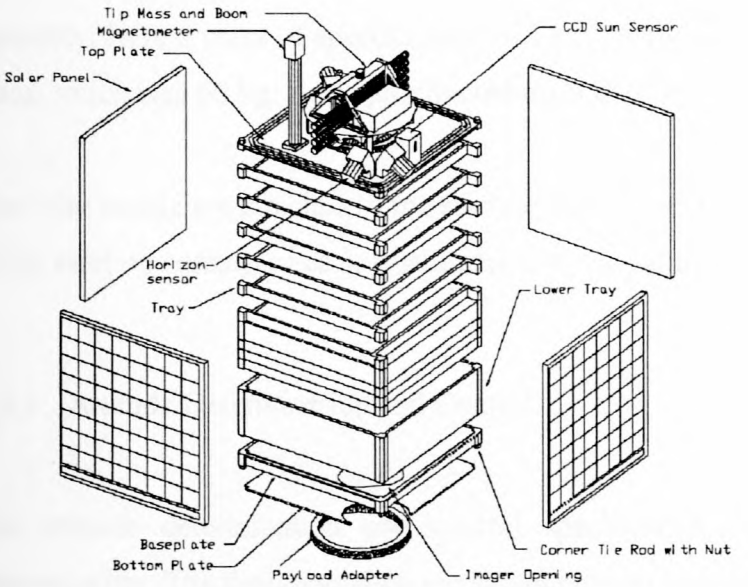

Figure 2.13 Exploded-view of SUNSAT (Schoonwinkel, 1997)

Each tray, as well as the top and base plates, have holes on their corners through which a tie rod passes. Nuts on the threaded ends of the tie rods are torqued to press the trays together. Each of the 11 trays houses particular electronic and mechanical components. A typical tray forms one subassembly and consists of 4 sides, 2 support beams and a printed circuit board. Further more, the imager, reaction wheels and batteries are also contained within the satellite without sacrificing the tray structure.

Aluminum alloy 7075-T6 was selected for all of the primary structural parts and most of the component structures. It has a good strength and stiffness-to-weight ratio. The high thermal conductivity of aluminum helps to reduce hot or cold spots within the satellite bus and payload equipment. Other benefits of an aluminum satellite structure include: moderate corrosion resistance, non-magnetic, readily available at reasonable costs, is easy to machine and is also not susceptible to cold welding when in contact in vacuum. (van der Westhuizen, 1995).

Stellenbosch University http://scholar.sun.ac.za

The aluminum trays were all surface treated with Alodine. Alodine is a gold-coloured chromate conversion coating. Alodine was used since it provided a protective coating for easy handling, provide a good base or primed surface for paints, and has the advantage of being electrical conductive (Strümpfer, 2002). (Refer to table J3 for optical surface properties of aluminum treated with Alodine)

The aluminum structure, consisting of the top plate, trays, base plate and payload adapter assembly, have a mass of approximately 15 kg. This is approximately 25% of the satellite's total mass, which was 60 kg. An approximated mass breakdown of SUNSAT is given in table J4.

The solar panels are attached to the satellite body at the tray corners. Four M4 bolts on each side of the satellite connected each solar panel to the satellite body (Blom, 2002).

2.2.2 Attitude Determination and Control

The attitude determination and control specifications on SUNSAT were stringent for a microsatellite. The design goal was to be able to point the pushbroom imager bore sight to within 1 km accuracy from an 800 km altitude, which amounts to a pitch and roll error of less than 1.2 m-radians (Mostert, 1997). Five types of attitude sensors were used. A 3-axis magnetometer was used to measure the strength and direction of the geomagnetic field. This low power (100 mW) device can be operated continuously to provide attitude accuracy to within 1 degree. Coarse attitude information is also derived to within 5 degrees from six cosine-law solar cells mounted on each facet of the satellite. Horizon sensors, a fine sun sensor and a star sensor served as the accurate attitude measuring devices. Attitude control was achieved through a passive gravity gradient boom and tip mass, combined with two redundant active actuation methods. The gravity gradient boom and tip mass stabilized the satellite nominally earth pointing, thus requiring minimum control energy. The satellite was also kept in a slow Z-spin during normal operation (not during imaging), for improved solar thermal distribution (Mostert, Schoonwinkel, 1997). Slow attitude motions and coarse pointing to within 1 degree is achieved through magnetorquers. Accurate pointing and stabilisation during imaging is provided by 4 servomotor driven reaction wheels. (Mostert, 1997.)

Stellenbosch University http://scholar.sun.ac.za

2.2.3 Communications

The SUNSAT communications payloads comprises of a high-speed data links and as well as Amateur Radio transmitters and receivers in the 145 and 435 MHz amateur radio bands. A separate S-band downlink conveyed image data at up to 60 Mbit/s to the 4.5 m diameter dish antenna at Stellenbosch and possibly at other locations. An L-band receiver on SUNSAT permitted up-linking of data at 2 Mbit/s, and could be coupled to the S-Band downlink for data gateway experiments. This means that large data files could be exchanged among remote locations on earth, which are not well served by other amateur communications systems. (Mostert, 1997.) For thermal reasons, the communications power amplifiers were located in the SUNSAT bottom-plate. The power amplifiers have approximately an 18 W power output. By placing the amplifiers in the bottom plate, the 18 W of heat can be removed from amplifiers by emitting it to space from the bottom surface of SUNSAT.

2.2.4 Command Data and Handling

Redundant computers of differing type provided SUNSAT with necessary flight control. General flight management tasks such as scheduling, imager control and communications management were performed by an Intel 386 processor, backed up by an Intel 80C188 processor. Both had access to all peripherals, but the 386 processor was the preferred flight controller. A T800 processor was dedicated to the fine attitude control system, but its tasks can be taken over by the 386 processor in case of failure. Seven additional embedded micro controllers provide further support for telemetry, telecommand, and power control and attitude control subsystems. A separate RAM disc of 64 Mega byte, which is accessible by both processors, was provided for storage of imager data or large files for store-and-forward applications. (Mostert, 1997.)

2.2.5 Power

The electrical power subsystem (EPS) provides, stores, distributes, and controls satellite electrical power as shown in figure 2.8 (Larson, 1992). To perform these functions, SUNSAT's power system consists of four photovoltaic gallium-arsenide (GaAs) solar panels, two nickel-cadmium (NiCd) batteries, several distributed regulators and shunt topology respectively (Mostert, 1997).

Stellenbosch University http://scholar.sun.ac.za

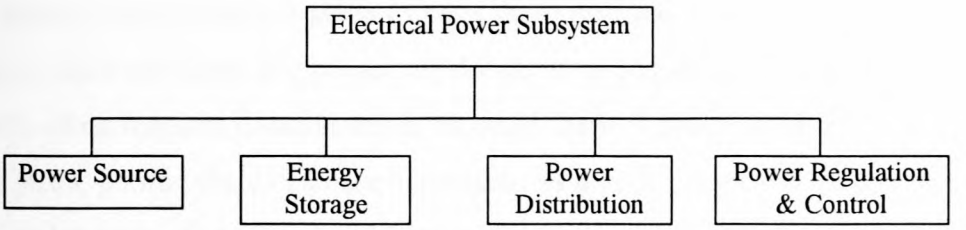

Figure 2.14 Electrical power subsystem functions

2.2.5.1 Solar Panels

Solar cells are used predominately for low-earth orbiting satellites. Photovoltaic cells are well documented and reliable, thus making them ideal candidates for low earth orbiting satellites.

All the key issues in selecting solar cells for a particular operation include factors such as: satellite configuration, required power level (peak and average), operating temperatures, shadowing, radiation environment, illumination or orientation, mission life, mass and area, cost, and risk.

The energy conversion efficiency of a solar cell is defined as the power output divided by the power input. The power input value for a planar solar panel, is the direct solar heat flux (1353 W/m^2). Thus, a solar panel with a BOL efficiency of 18% will provide 243.5 W/m^2. A comparison of performance of three different solar cells is given in table 2.3. It is noted that the difference reported on efficiencies between laboratory cells (theoretical) and production cells (achieved) is significant. Solar arrays using GaAs and indium phosphide (InP) resist radiation degradation better than silicon and provide a greater end of life (EOL) power for a given area (Larson, 1992).

Table 2.3 Performance comparison for photovoltaic cells (Larson, 1992)

	Silicon	**Gallium Arsenide**	**Indium Phosphide**
Planar cell theoretical efficiency	18%	23%	22%
Achieved efficiency	14%	18%	19%

The temperature of a typical flat solar panel receiving normal incident direct solar heat flux is about 67 °C in LEO. The reference temperature for silicon cells is 28 °C, with performance falling off 0.5 % per degree above 28 °C (Larson, 1992).

Stellenbosch University http://scholar.sun.ac.za

A photovoltaic system is sized to meet the power requirements at EOL, with the resulting solar array often oversized for power requirements at beginning of life (BOL). This excess power at BOL often requires considerations to avoid thermal problems. For a mission lasting longer than 10 years, photovoltaic cells are considered as a poor power source due to natural degradation in the solar array. The typical value of performance degradation measured as a reduction in power production for Silicon and GaAs solar cells is 3.75% and 2.75% per year, respectively (Larson, 1992).

Solar panel illumination intensity depends on orbital parameters such as the sun incidence angles, eclipse periods, solar distance, and the concentration of solar energy. For some satellites, tracking and pointing mechanisms on the solar array often adjust for these influences. In the case of SUNSAT, these solar panels are mounted on the side panels of the satellite and are subjected to a Z-axis (in the direction of the earth centre) spin orbit. For this reason, the efficiency of the solar cells in terms of time illuminated is less than that for controlled illumination. But the advantage of the Z-axis spin, is a reduced average solar panel temperature, which improves the performance of the solar cells and thus the power output.

The four gallium-arsenide solar panels used on SUNSAT are more costly than the heavier and slightly less efficient than silicon solar panels. Each of the solar panels has ten "strings" (row of solar cells) containing 19 solar cells per string. The solar panels each have the capacity to generate 30 W of power in full sunlight (Mostert, 1997).

2.2.5.2 Batteries (Energy Storage)

Energy storage is an integral element of the satellite's power subsystem. Any satellite that uses photovoltaic cells as a power source requires a system to store energy for peak power demands and during eclipse periods. A battery typically consists of individual cells connected in series. The number of cells required is determined by the bus-voltage.

In the case of SUNSAT, two NiCd battery packs consisting of 5 cells each were used to provide an unregulated bus voltage of 12 V to 14 V. The batteries have the capacity to provide 1Ah of power to the satellite subsystems. The two battery packs were used to provide the satellite with power during eclipse during which time the batteries are discharged. When the solar panels again receive direct solar radiation, the batteries are recharged.

Stellenbosch University http://scholar.sun.ac.za

These continued cycles of charge and discharge causes the batteries performance to deteriorate over time and is the limiting factor in the batteries lifetime. Based on this, it can be said that batteries are the single most limiting item on the lifetime of a LEO satellite (Larson, 1992). This fact is true provided the batteries operate within their design temperature range. As the temperature of these batteries rises above their range, their maximum useful life decreases significantly. Below this range, the electrolyte may freeze and damage the battery (Larson, 1992). As a general rule of thumb, batteries are coated with a high emitting surface so as to radiate the internal heat generated away as efficiently as possible and to reduce any hot spots (Larson, 1992), thus increasing the lifetime of the batteries and possibly the mission.

2.2.5.3 Power regulation

The electrical power generated by the solar array needs to be controlled to prevent battery overcharging and undesired spacecraft heating. To do this a power regulator is required. Power regulation divides into three main categories: controlling the solar array (SA), regulate bus voltage, and charging the battery. Two main types of regulators are used: the peak-power tracker (PPT) and the direct-energy-transfer (DET) subsystem. The PPT is a non-dissipative subsystem because it extracts the exact power a satellite requires up to the peak power. The DET subsystem is a dissipative subsystem because it dissipates power not used by the batteries. However, a DET subsystem can dissipate this power at the array or through external banks of shunt regulators (SR) to avoid internal power dissipation since this excess power would be converted to heat and is undesired internally. The two systems are shown schematically below. (Larson, 1992)

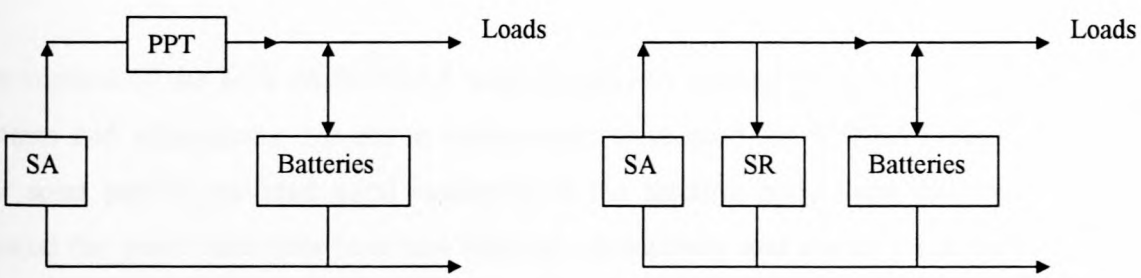

(a) Peak Power Tracking (PPT) systems (b) Direct Energy Transfer (DET) systems

Figure 2.15 Techniques for power regulation (Larson, 1992)

The solar panels are connected to the battery charge regulators and the batteries directly to the power bus on the satellite.

Stellenbosch University http://scholar.sun.ac.za

Distributed regulators ensure that the required voltages are supplied to each of the subsystems. In the event of failure of the battery charge regulator or the batteries, the solar panel output would be supplied directly to the power bus.

The peak power capability on SUNSAT was 90 W to be able to handle peak loads during imaging data transmissions. Depths of discharge of the batteries were limited to 20% to ensure a lifetime of 5 years (Mostert, 1997). A shunt topology was used to control battery charging on SUNSAT. The topology consisted of several shunt switches, between the solar cells and the batteries, one for every two strings. By closing one or more of these switches the charging current can be regulated. An 8031 micro controller controls the closing and opening of the switches. If the micro controller fails, the on-board computers of the satellite can also control the switches.

Voltage regulation is done by several distributed regulators. To avoid a single point of failure, each subsystem has its own power regulator. Thus, if one subsystem fails, its power can be cut off completely and the satellite could still function as far as power is concerned. (Mostert, 1997.)

2.2.6 Thermal Control

The thermal control subsystem (TCS) is an integral part of every satellite. Its purpose is to maintain all the components on a satellite within their respective temperature limits. Many factors influence the design and development of the TCS.

The mission of the TCS on SUNSAT was to passively control the temperature of the satellite's systems and subsystems. No active mechanisms were used for SUNSAT thermal control. The four solar panels provided good insulation to the satellite body from environmental heating, because the panel materials have low thermal conductivity and are only thermally connected to the body through several bolts. The critical surfaces of SUNSAT were the top-plate, which faced space, and bottom-plate, which faced the earth. Both of these surfaces served as radiators for waste internal heat. These surfaces were not well insulated from the satellite trays and thus were able to allow heat to flow from the body, through the trays and then to be radiated.

With the SUNSAT structure being essentially aluminum, heat was readily able to flow through the trays, but because of the contact resistances between the trays, not that well from tray to tray.

Stellenbosch University http://scholar.sun.ac.za

The least thermal resistive path between the trays and to the top or bottom plates is through the tray corner aluminum column. The trays are attached to one another at the corner columns using tie rods.

The selection of specific surface coatings to attain the desired thermal effects was essential to the operation of SUNSAT. The top-plate was coated with an aluminized Kapton layer. Specific attitude sensors on the top plate were covered with thermal blankets to protect them from direct solar radiation. All the aluminum surfaces of SUNSAT were treated with Alodine including the bottom-plate surface.

Stellenbosch University http://scholar.sun.ac.za

3 SUNSAT EXPERIMENTAL SET-UP and RESULTS

This chapter looks at the set-up and mission of SUNSAT, as well as the methods and results of the temperature data recorded during its orbit in space.

3.1 SUNSAT, South Africa's First Micro Space Satellite

SUNSAT is a micro space satellite that was developed by graduate students at Stellenbosch Univeristy and was launched in February 1999 on the Delta II rocket from Vandenberg Launch Centre in California. SUNSAT was designed to be approximately 60 kg in mass. It has a length and width of 45 cm, and a height of 49 cm (un-extended boom). SUNSAT was designed to serve as a technology demonstrator. The satellite has three main payloads, namely: a push broom type imager, packet communications systems and scientific experiments for NASA and the CSIR. Figure 3.1 below shows SUNSAT in its operational mode with fully extended gravity gradient boom. The launcher attachment ring is used to attach SUNSAT to the launch module for launch and final excursion into space. SUNSAT failed to complete its mission in early February 2001, due to suspected failure of the NiCd batteries; probably caused by overheating.

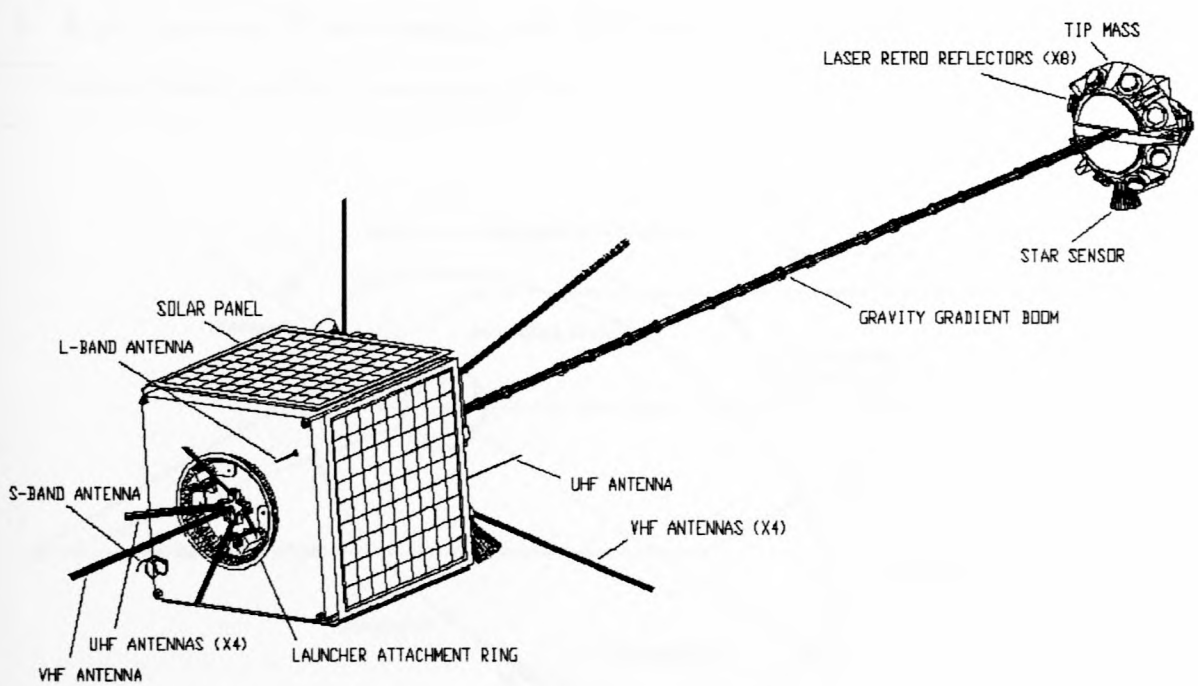

Figure 3.1 SUNSAT in its operational configuration (Mostert, 1997)

Stellenbosch University http://scholar.sun.ac.za

3.2 Operating Envelopes

The design lifetime of SUNSAT was 5 years with the dependency on the lifetime of the batteries. Since SUNSAT was the second satellite (and not the primary payload) on the launch module, it was placed into a non-ideal orbit path with a drift of approximately one hour in 70 days relative to the earth-sun vector. Its orbit was also chosen to suit the Danish Ørsted satellite. (Schoonwinkel, 1997.) The altitude of the satellite above the earth varied from approximately 600 to 800 km.

The seven orbit parameters that define the orbit of SUNSAT are listed in table 3.1 from 1 to 7 (Eglington, 1993). Figure 3.2 shows the typical orbit path, for which the major orbit parameters, ω, Ω and i are defined accordingly.

Table 3.1 SUNSAT orbit parameters

1. Orbit Eccentricity, e = 0.00134
2. Inclination, i = 98.7°
3. Semi-major axis, a = 7203 km
4. Argument of Perigee, ω = 110.95°
5. Orbit period, τ = 100.7 min
6. Right ascension of the ascending node at the vernal equinox, Ω = 225°
7. Rate of change of right ascension, $d\Omega/dt$ = 0.9856°

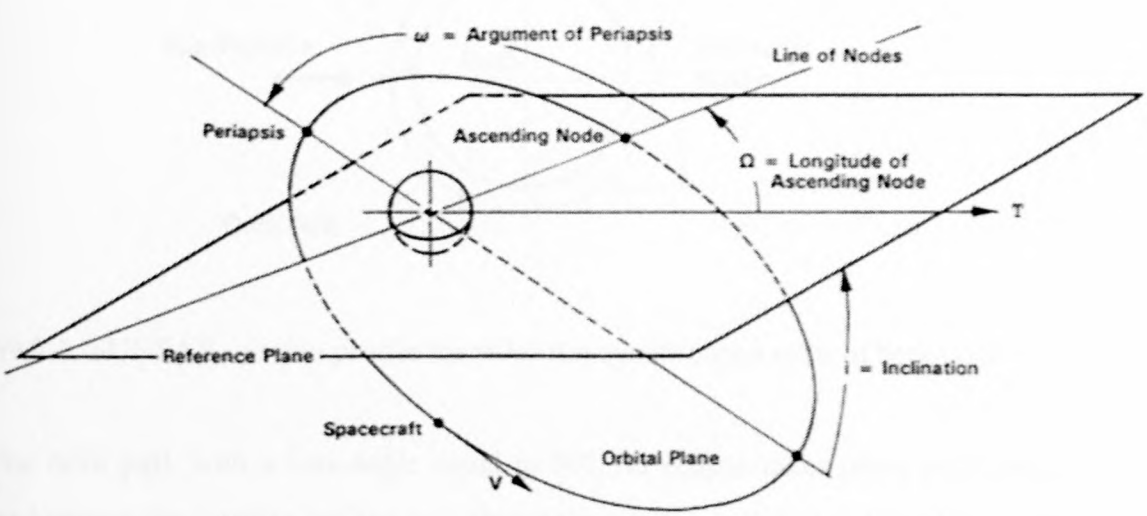

Figure 3.2 Classical orbital elements (Brown, 1992)

Stellenbosch University http://scholar.sun.ac.za

The intended mission profile of SUNSAT is estimated for the purposes of this project as a circular polar sun-synchronous orbit with an orbit beta-angle (β) equivalent to 0°. The β-angle angle is defined as the minimum angle between the plane of the orbit path and the sun vector and can vary from –90° to + 90° as illustrated in figure 3.3.

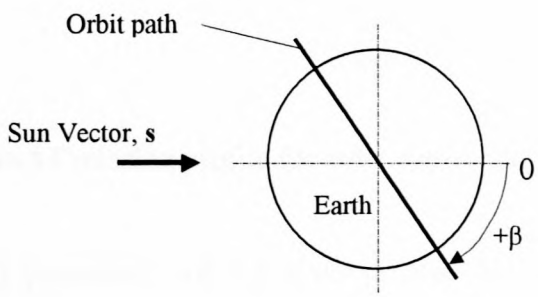

Figure 3.3 Orbit beta-angle schematic

Figure 3.4 shows the idealized polar sun-synchronous orbit path for a beta-angle equivalent to 0°. As viewed from the sun, such an orbit would appear edgewise. A satellite in such an orbit would pass over the sub-polar point on the earth (the point on the earth where the sun is directly overhead), but it would also have the longest eclipse time due to the shadowing by the full diameter of the earth.

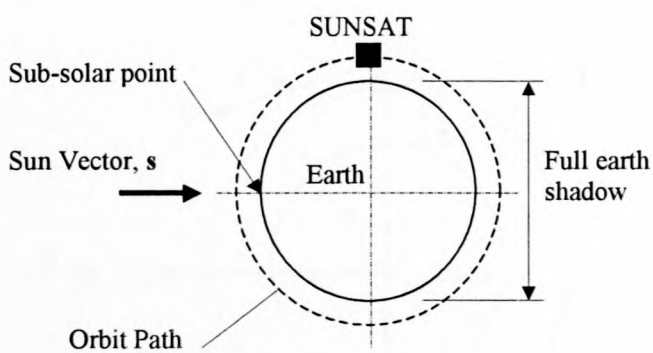

Figure 3.4 SUNSAT mission profile for polar sun-synchronous orbit of beta-angle equal to 0°

For the orbit path with a beta-angle equal to 90°, no eclipse takes place since the earth never comes between the satellite and the sun. Hence the satellite is in full sun conditions. This mission profile is shown in figure 3.5.

Stellenbosch University http://scholar.sun.ac.za

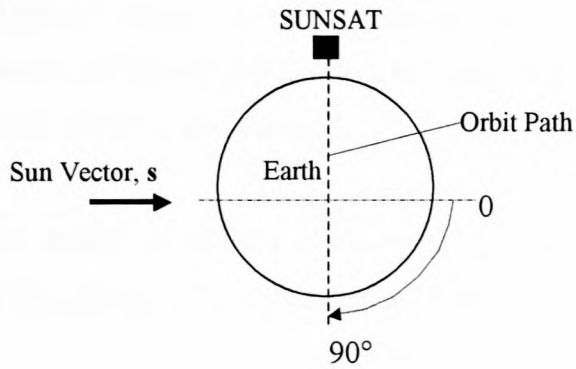

Figure 3.5 SUNSAT mission profile for polar sun-synchronous orbit of beta-angle equal to 90°

The geometrical parameters of the approximated SUNSAT polar sun-synchronous orbit are shown in figure 3.6. The angle θ is the angle of rotation of the satellite around the earth from the global z-axis. SUNSAT was subjected to a "spin" or rotation about its local Z-axis. The angle ϕ is the angle of rotation of the satellite around the local Z-axis that passes through the earth center. Approximately six rotations occurred during a single orbit around the earth under normal operation. This enabled the satellite to distribute the incoming solar heat loads evenly over the solar panels. The result of which is a reduction in temperature gradients across the satellite.

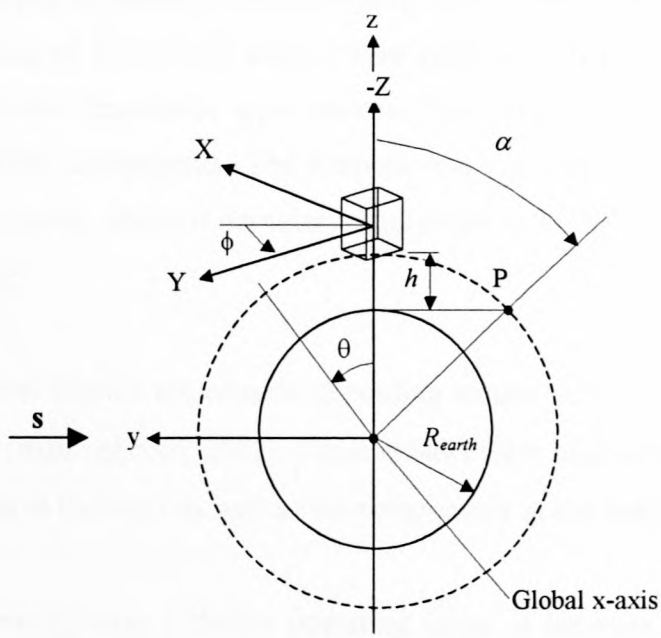

Figure 3.6 SUNSAT geometrical parameters

Position P indicates the point at which the shadow cast by the earth intersects the orbit path of the satellite. The angle α at which the shadow begins, is measured from the global z-axis. The earths average radius, R_{earth}, may be taken as 6371 km (Piscane, 1994).

Stellenbosch University http://scholar.sun.ac.za

The altitude of SUNSAT above the earth, h, is averaged at 700 km. This value of altitude actually varies between 600 km and 800 km. The position of the satellite is defined relative to the position of the sun vector, **s**, and the earth.

Due to the passive nature of SUNSAT's thermal control, it relied heavily on cooling its subsystems during the eclipse period that lasted ± 35 min of the total orbit time of ± 100 min.

Piscane (1994) assumes that the albedo heat flux (refer to section 2.1.3) varies with the cosine of the angle θ. That is to say, the albedo heat flux is zero for $\theta = 0°$, increases to a maximum for $\theta = 90°$, and then decreases back to zero as θ tends to 180° (Piscane, 1994). The albedo heat flux received by SUNSAT is not exactly zero for $\theta = 0°$ and 180°, because the reflection is diffuse, but it is small and can thus be safely neglected (Lyle, 1973). Thus, it is to say that the effective heating of SUNSAT by the albedo heat flux occurs only when SUNSAT passes over the sunlit portion of the earth (half the earth on the sun vector side).

3.3 Temperature Measurements

There were two types of thermal sensors used to monitor the temperatures of specific SUNSAT components. A total of 35 thermal sensors were used on SUNSAT. The type of thermal sensors includes: LM335 and thermistor type sensors. The most attention was given to the critical subsystems and their components. The temperatures were monitored from a ground station at Stellenbosch University, where if necessary, alterations to SUNSAT's orientation around its own axis could be made.

The LM335 thermal sensors are capable of reading temperature in the range of -40°C to 100°C, accurately to 1°C (national.com, 2002). These sensors were used to monitor the thermal health of all the components in the trays as well as the components in the bottom plate.

The thermistor sensors have a design operating range of between – 30°C and 100°C, and an accuracy of 1% (alphasensors.com, 1998). The thermistor sensors were used predominately to monitor the temperatures of the solar panels and ADCS components on the top plate.

A complete listing in tabular form of the approximate location of the temperature sensors in SUNSAT is summarized in appendix J, table J6.

Stellenbosch University http://scholar.sun.ac.za

The database of all the results from the onset of SUNSAT in orbit is stored at the ESL (Electronic Systems Laboratory) and can be retrieved using the software "Telemetry Client". The channels that were used for each of the sensors are also given in table J6.

A problem associated with the analogue to digital conversion from the thermal sensors was that small changes in temperature could not be converted to digital data due to filtering limitations of the analogue signal. Only changes in temperature of approximately 0.5°C could be detected. Figure 3.7 below shows the detailed temperature response of the SUNSAT batteries for some random time step of 2000 s. What is noticeable is that the digital signal only responds if the temperature changes by 0.5°C.

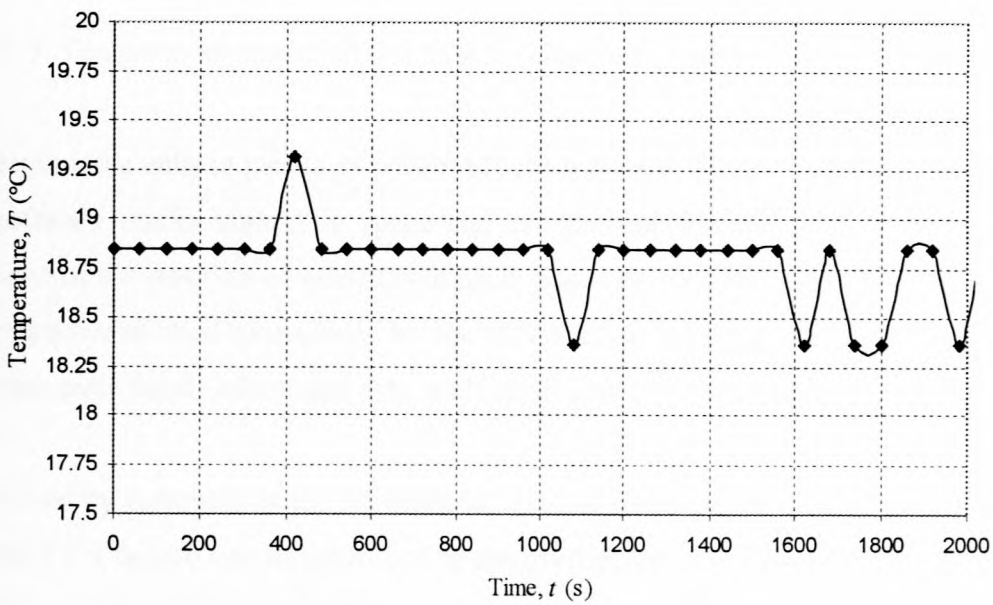

Figure 3.7 Temperature data of SUNSAT batteries from LM335 thermal sensor

A problem faced in interpreting the temperature data of the solar panels was that the solar panels operated between the temperature range of approximately -45 and 100°C, but the thermistor sensors could only read temperatures as low as -30°C. The result was that the sensors became saturated, and no temperature reading could be taken below -30°C. Figure 3.8 shows the detailed temperature response of the SUNSAT +Y solar panel and the limitation of these thermistors at low temperatures is evident. (Note: the high density of data at low temperatures.)

Stellenbosch University http://scholar.sun.ac.za

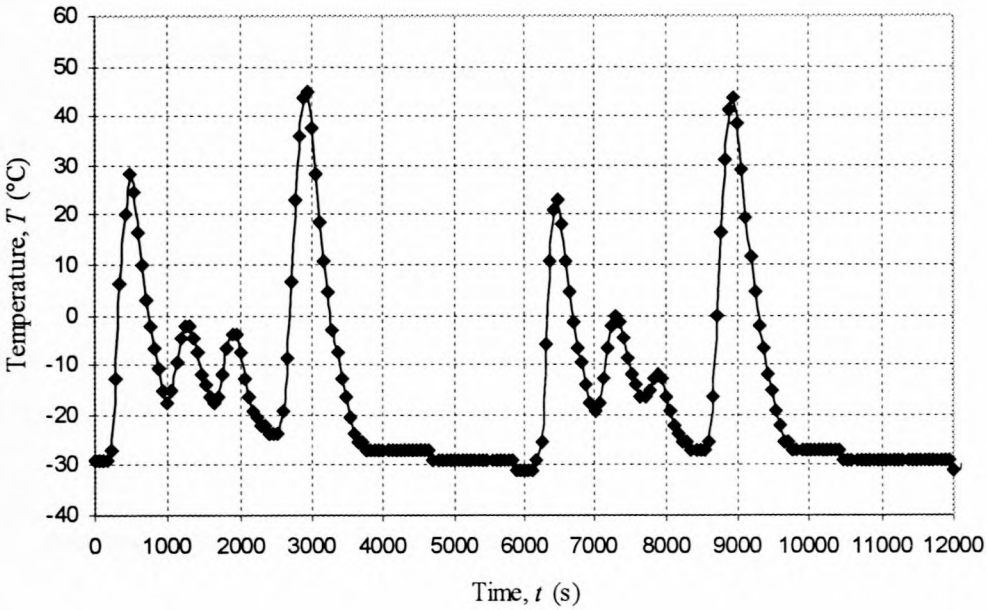

Figure 3.8 Temperature data of SUNSAT +Y solar panel from thermistor thermal sensor

To determine the eclipse period of SUNSAT, the software "Nova" was used (Retief, 2002). The Nova software tracks objects in space and can provide history data as well as make future predictions of the position of satellites in orbit; based on the orbit parameters given in table 3.1. This program was used extensively by the SUNSAT ground station to predict when SUNSAT would pass over South Africa and data could be downloaded and uploaded as required.

It is believed by members of the Stellenbosch ground station team (Retief, 2002), that the reason for SUNSAT's failure can be attributed to the overheating, overcharging and ultimate failure of the NiCd batteries. This belief is supported by the gradual change in the orbit of SUNSAT, from full eclipse to full sun conditions (according to the Nova software), and the resulting gradual increase in the temperature of the batteries.

Figure 3.9 shows the averaged monthly plot of eclipse time (maximum = ± 2160 s) from July 1999 to July 2000. (The periods of maximum sunlight occurred July/August 1999, and the actual end of full-eclipse occurred on the 10th of June 2000.) What is evident from the figure is the rapid decrease in eclipse time from December 1999 to July 2000. From July 2000 onwards (not shown), SUNSAT does drift back into eclipse. But by that time, it is believed that damage to the power supply subsystem was already a forgone conclusion. It was only in April 2000 that action was taken to try to alleviate the high temperatures of the batteries (which is evident in figure 3.10).

Stellenbosch University http://scholar.sun.ac.za

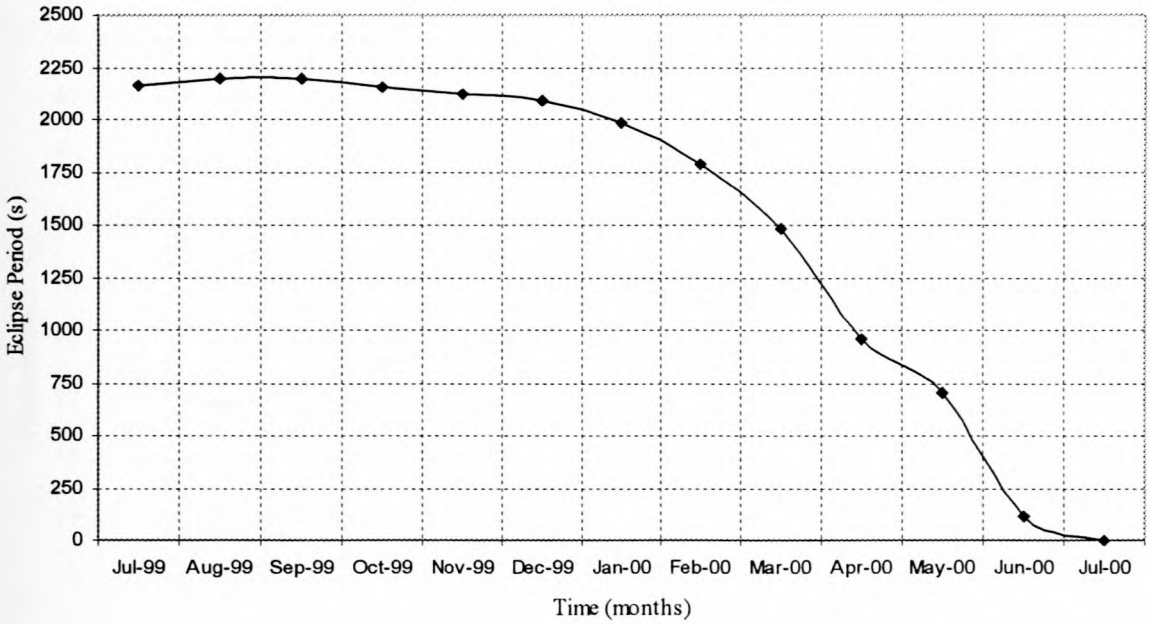

Figure 3.9 SUNSAT monthly averaged eclipse period from July 1999 to July 2000

The monthly average battery temperature from July 1999 to July 2000 is shown in figure 3.10. Keeping in mind that NiCd batteries are designed to operate between 0°C and 20°C, the increase in battery operating temperature up to ±40°C, had to have detrimental consequences on battery performance. During April/May 2000 the spin rate was increased and the satellite was re-orientated so that the bottom-plate faced space and received no solar radiation (Retief, 2002). This did allow for slight cooling, but not sufficient, and a further increase in battery temperature was inevitable.

The reduction in eclipse period does seem to be the logical reason for the overheating of the SUNSAT batteries based on the information presented in figures 3.9 and 3.10. However, overheating of the batteries could also be attributed to other factors. To name a few: an increase in the internal electrical resistance of the battery, a reduction in the thermal optical performance of surface coatings, failure to control the discharge depth of the batteries, failure to accurately regulate the charging of the batteries, increase in internal thermal contact resistances between trays, and degradation of solar panel thermal optical performance. (As unlikely as some of these possibilities may appear, in space nothing can be taken for granted.)

Stellenbosch University http://scholar.sun.ac.za

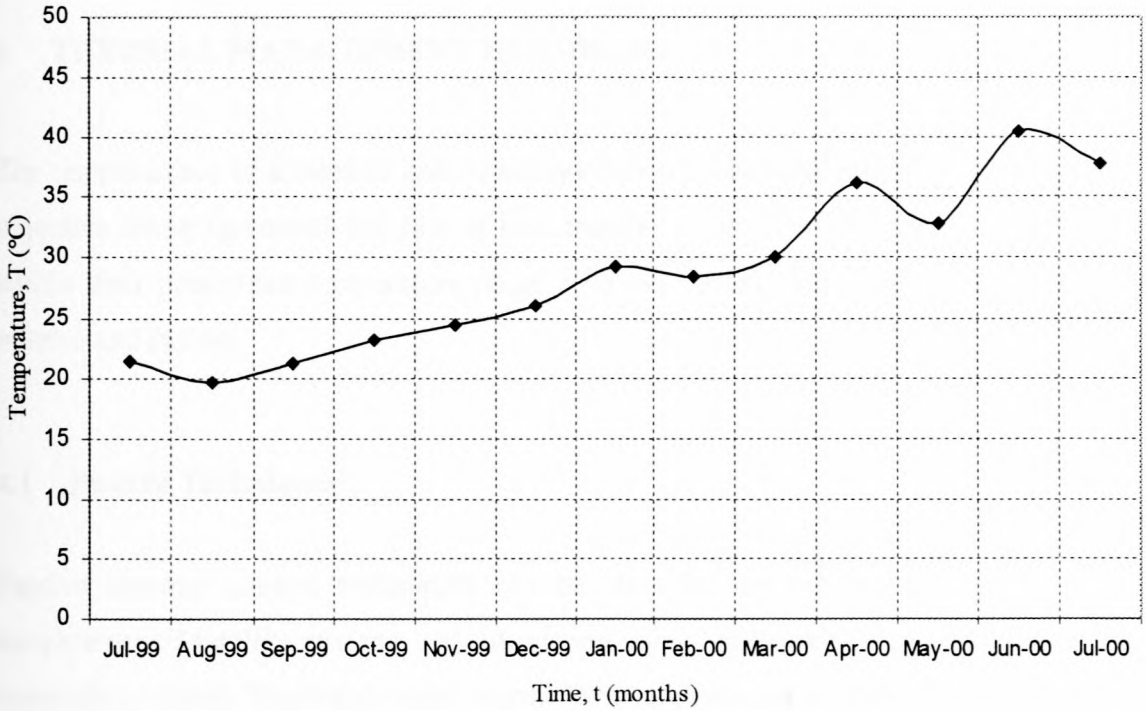

Figure 3.10 SUNSAT monthly averaged battery temperature from July 1999 to July 2000

The temperatures of relevant SUNSAT thermal sensors are presented in appendix I. Only selected number of temperature responses is shown for specific components or regions of SUNSAT. These regions also correspond to regions in the thermal models presented in chapter 6. Also note that not all the sensors worked, and hence no useful information was stored from many of the sensors. Two sets of data for different time periods in SUNSAT's life are presented. The first set is for the orbit condition when SUNSAT was approximately in a maximum eclipse period during July/August 1999. The second set of data is for the orbit condition of no eclipse, i.e., full sunlight in June 2000.

Stellenbosch University http://scholar.sun.ac.za

4 THERMAL MANAGEMENT HARDWARE

The temperatures of a satellite and its subsystems are managed either passively or actively. The objective being to control the rate of heat transfer so as to ensure that the subsystems operate within their prescribed temperature range. The two techniques used in thermal control include *passive* and *active*.

4.1 Passive Techniques

Passive thermal control techniques can be classified as the measures used to control the temperature of satellite systems and subsystems using hardware that has no moving components, materials or fluids. Passive thermal control hardware requires no electrical energy input. Passive techniques are the first consideration in satellite thermal design due to the reduced satellite mass, less strain on the power subsystem and lower rate of failure associated with them.

4.1.1 Thermal Surface Finishes

One of the most critical passive elements in any satellite TCS is the external radiating surface (radiators). The effective surface is one that offers a low absorptance and high reflectance of energy in the solar band, and a high infrared emittance at the appropriate radiator temperatures (Chalmers, 1988). Table J7 gives a list of properties of common surface finishes (Gilmore, 1994).

The external surface of a satellite couples the satellite to space. Because these surfaces are also exposed to external sources of energy such as solar radiation and earth emitted IR, their radiative properties must be selected to achieve an energy balance at the desired temperature between the satellite internal dissipation, $\dot{Q}_{\text{int}}$, external heat loads and radiation from the surface of the satellite to space, as illustrated in figure 4.1.

Stellenbosch University http://scholar.sun.ac.za

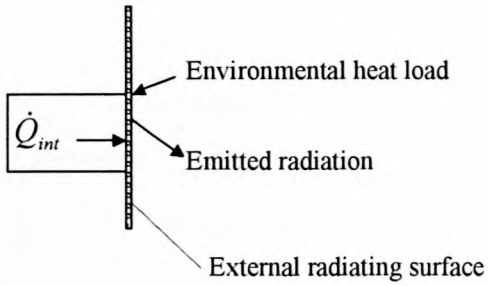

Figure 4.1 Satellite radiator energy balance

There are four basic types of thermal control surfaces that are used extensively on satellite surfaces.

1. Solar reflectors, which have a low solar absorptivity but high emissivity, are useful in a solar or albedo environment as they reflect much of the impinging energy while retaining the high emissivity needed for efficient rejection of satellite waste heat (Karam, 1998). Solar reflectors are characterised by very low α/ε ratios. The ideal spectral absorptance of solar reflectors is shown in figure 4.2a, along with the actual properties of a common solar reflector; white paint (Gilmore, 1994).

2. *Solar absorbers*, absorb solar energy while emitting only a small percentage of the infrared energy. Polished metal surfaces approximate solar absorbers (Gilmore, 1994). They have a high α/ε ratio and are very seldom used on satellite surfaces exposed to the sun because of the high and unpredictable temperatures associated with them (Karam, 1998). The ideal spectral absorptance characteristics of this thermal control surface are shown in figure 4.2b, along with the typical characteristics of polished aluminum alloy (Gilmore, 1994).

3. *Flat absorbers*, such as black paint, absorb throughout the spectral range, i.e., in both the solar and IR bandwidth. Black paint is used inside the satellite to improve heat sharing by radiation. Figure 4.2c (Gilmore, 1994) shows the ideal spectral absorptance property of flat absorbers, as well as the typical characteristics of black paint (Gilmore, 1994).

4. *Flat reflectors* reflect energy throughout the spectral range and would typically be used on satellite subsystems that are sensitive to radiation heat loads. Figure 4.2d shows the properties of such a control surface, as well as the characteristics of a good flat reflector such as aluminum paint (Gilmore, 1994)

Stellenbosch University http://scholar.sun.ac.za

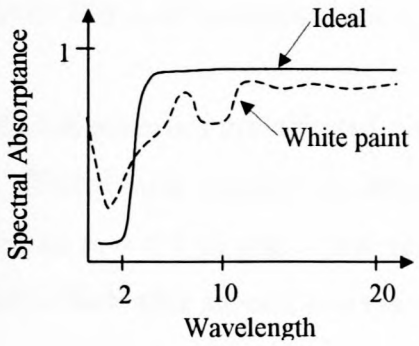

(a) Solar reflector

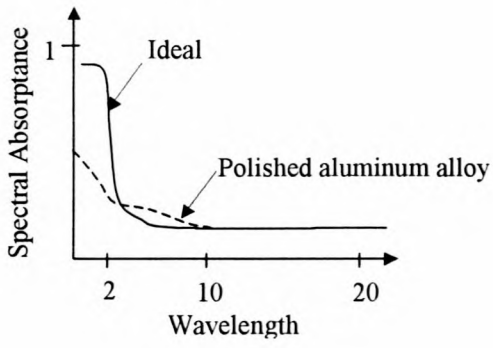

(b) Solar absorber

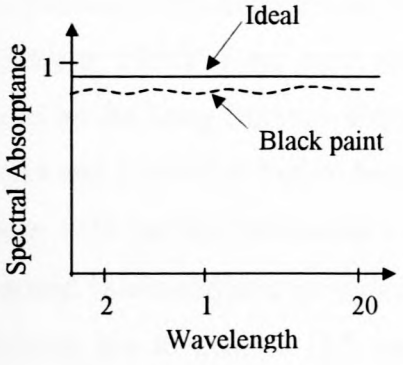

(c) Flat absorber

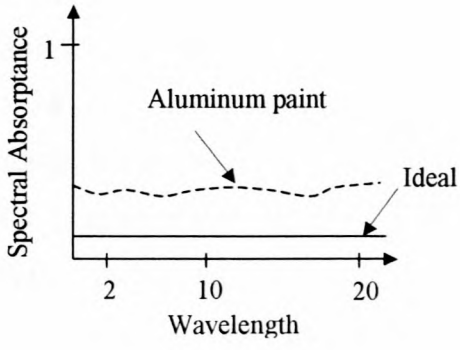

(d) Flat reflector

Figure 4.2 Ideal representation of four passive thermal control surfaces (Gilmore, 1994) (Wavelength in μm)

One of the problems associated with surface coatings, is the degradation of the surface optical properties once in space operation. These effects can seriously influence the thermal design, resulting in higher or lower temperatures than expected. The reasons for this gradual, but influential degradation of the optical properties, can be attributed to: contamination from spacecraft debris and volatiles, corruption from exposure to ultraviolet radiation and charged elementary particles (atomic oxygen). Contamination affects almost any surface finish, but it varies with temperature and proximity and shape factor to the contaminating source. (Karam, 1998.)

The result of these degradation processes is to increase the solar absorptivity with little or no effect on the IR emittance. For the satellite, this means an increase in the amount of solar radiation absorbed, the result of which is a higher average operating temperature.

Stellenbosch University http://scholar.sun.ac.za

Depending on how severe the degradation is, this can seriously reduce the design life of the satellite if it is not accounted for in the thermal design phases.

Different materials are affected differently by exposure to the space environment. White paints are effected most strongly by ultraviolet radiation and charged particles, and can degrade from $\alpha = 0.2$ to $\alpha = 0.7$ in just a few years. Kapton also shows substantial degradation and can turn almost black after several years in orbit (Gilmore, 1994).

The effects of the interaction of thermal surface finishes with atomic oxygen (AO) are significant in the presence of solar radiation on the surfaces leading in the direction of satellite motion (the *ram-direction*). This degradation effect is most pronounced at a satellite altitude from 200 to 500 km (Karam, 1998). Tests were done by NASA to investigate the long-term effects of AO on samples on the Long Duration Exposure Facility (LDEF), which remained in LEO for 69 months (5 years and 9 months) before being retrieved: Kapton samples from the LDEF revealed severe damage, with surface recessions exceeding 250 μm in 69 months of exposure. Silvered Teflon (silverized fluoroethylene propylene Teflon) with the Teflon facing out, also showed physical alterations, but its erosion (2.5 μm from 125 μm) did not appear as rapid as Kapton, and its optical properties seemed only slightly effected despite some deformation and change in colour. Mylar also showed similar susceptibility to AO as Kapton did. (Karam, 1998.)

For the case of SUNSAT, the top surface was coated with Kapton (solar reflector). This surface was not, under normal operation in the ram-direction, and thus can be assumed to be fairly unaffected by the degradation effects of atomic oxygen. The bottom aluminum plate of SUNSAT was surface treated with Alodine, which behaved as a flat reflector. The earth thermal radiation was a permanent heat load on the bottom surface under normal operation, and thus it was necessary for the passive thermal control. This was aimed at preventing overheating of the batteries that were situated in the bottom-plate.

4.1.2 Multi Layer Insulation (MLI)

Just as critical as the radiators are for heat rejection, the MLI is critical to reduce the heat transfer to/from surfaces, which experience large environmental heat load fluctuations. MLI is used to prevent the flow of heat, and in doing so, minimize the thermal interaction of a system with its environment.

Stellenbosch University http://scholar.sun.ac.za

The thermal design philosophy behind the SUNSAT satellite was to insulate the satellite from its surroundings using the four solar panels, while waste heat was radiated from the top and bottom surfaces. Although the use of MLI in SUNSAT's case was only limited to the blankets covering 75 % of the attitude sensors on the top-plate (Koekemoer, 2002), the principle behind the use of MLI is the same as for the four solar panels: reduce the thermal interaction of the satellite subsystems with the space environment.

MLI is composed of multiple layers of low-emittance films. Typically layers are formed from thin sheets of Kapton or Mylar (1/4 mil thick) with vacuum deposited aluminum finish on one side (Gilmore, 1994). Heat transfer through MLI is a combination of radiation, conduction, and under atmospheric conditions, convection (Gilmore, 1994). In vacuum conditions, there is no convection of air between layers, and hence no heat transfer by convection. Radiation heat transfer through the layers is dependant on the number of layers. The heat transfer rate through the layers can be approximated by a black body model (Mills, 1995) as

$$\dot{Q}_{MLI} = \left(\frac{1}{m+1}\right) A\left(\sigma T_1^4 - \sigma T_2^4\right) \tag{4.1}$$

where m is the number of layers, and T_1 and T_2 are the temperatures of the outer layers.

4.1.3 Honeycomb

Honeycomb material is used predominantly on satellites for providing structural stiffness to solar panels, while keeping the mass low. This lightweight material is typically constructed from aluminum sheets that are formed into hexagonal shaped cells as shown in figure 4.3. These hollow thin walled cells provide the solar panel with not only structural stiffness, but also a highly resistive path to heat transfer.

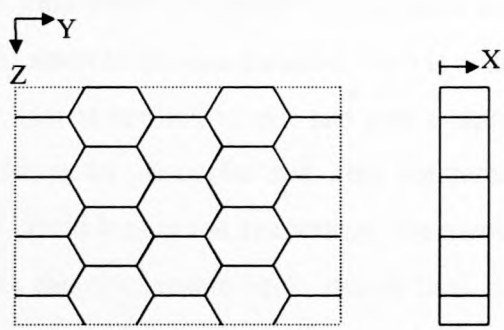

Figure 4.3 Honeycomb configuration

Stellenbosch University http://scholar.sun.ac.za

The dominant mode of heat transfer through the honeycomb is conduction. Appendix A gives a detailed comparison of the two modes of heat transfer, conduction and radiation, and also explains how to go about determining the effective thermal conductivity in the honeycomb for each of the three directions. The highest thermal conductivity occurs in the direction perpendicular to the honeycomb plate i.e., the X-direction. It was also shown in appendix A that the effect of radiation is small compared to conduction heat transfer for the particular honeycomb that was used on SUNSAT.

4.2 Active Techniques

Active thermal control techniques can be classified as the measures used to control the temperature of satellite systems and subsystems using hardware that requires either moving components, materials and/or fluids. Most active systems require electrical energy input, which often puts strain on the energy design and management. Active techniques are only considered if sufficient thermal control is not possible with passive techniques. Often a combination of the two is used to obtain the desired operating temperatures.

4.2.1 Heat Pipes

Heat pipes are able to transfer heat at a high rate and in doing so, improve the distribution of heat within a satellite and reduce undesirable hot and cold spots. The ability of heat pipes to work under zero gravity is what makes them attractive to satellite thermal control. Their light weight, flexibility, and reliable performance can prove critical to the proper operation of a satellite (Chalmers, 1988).

The basic heat pipe (refer to figure 4.4) consists of a tube in which an interior capillary wick (grooves, mesh, sintered porous material, etc.) is soaked with liquid and then sealed at saturation conditions. As heat is applied to one end (the evaporator), a differential pressure is created and the vapour is driven to the cooler end (the condenser), where it condenses back into the wick. But because of liquid loss at the evaporator, the meniscus there depresses, resulting in a capillary head that drives the condensate back, which then forces the process to repeat. (Karam, 1998.) There are various types of heat pipes and each has its own distinct characteristics and applications to satellite systems.

Stellenbosch University http://scholar.sun.ac.za

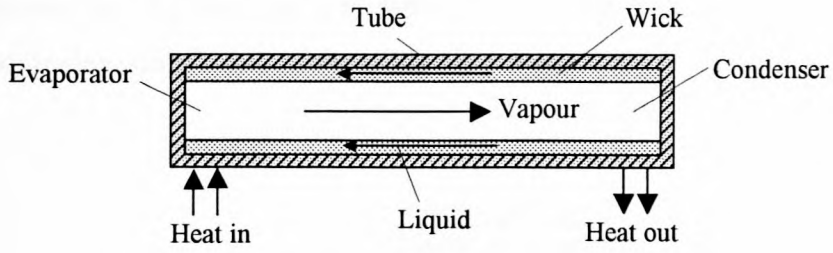

Figure 4.4 Basic heat pipe

The variable conductance heat pipe (VCHP) is used for applications where it is required to remove or add heat to a system at a constant rate. Often the rate at which heat is added at the evaporator may be either too high or too low, in which case a VCHP can be used to control the rate at which the heat is transferred by the heat pipe. The condenser end of the VCHP consists of a reservoir of non-condensable gas that moves into and out of the active condenser section; due to pressure changes in the heat pipe caused by low and high heat sources respectively. When the heating is high, the non-condensable gas is compressed and moves out of the active condenser section allowing for a higher heat transfer area. The opposite holds true. (Gilmore, 1994.)

Diode heat pipes are used in applications that require heat to flow only in one direction. In the liquid trap diode heat pipe, one end has a disconnected wick that leads to trapping or blocking the working fluid and thus shut off the operation if the condenser and evaporator reverse roles by changes in heat distribution (Karam, 1998). A typical application in a satellite would be to use the diode heat pipe to transfer heat from a subsystem to a radiator (that at times sees full sunlight), but not from the radiator back to the subsystem.

The capillary pumped loop (CPL) is a two-phase heat transfer loop that uses a capillary structure to return liquid to the evaporator. The CPL has the capacity to transfer heat over long distances with a very small temperature gradient. This device is essentially a heat pipe with the return flow of the condensate to the evaporator in a separate un-wicked tube. It utilizes the surface tension forces developed in the porous wick to circulate the working fluid. The wick is only needed in the evaporator section and the rest of the loop is made of smooth walled tubing (Gilmore, 1994). The absence of a wick in the transport lines of the CPL provides much greater flexibility for the loop design (spacescience.nasa.gov, 2000). A possible application in satellite thermal control would be to use the CPL to spread heat over a large area to reduce any effects of temperature gradients on subsystem performance.

Stellenbosch University http://scholar.sun.ac.za

The condenser duct for such an application would be looped back and forth over the area that requires equivalent distributed heating. Figure 4.5 shows such an application.

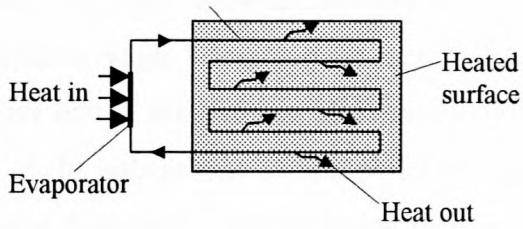

Figure 4.5 Capillary pumped loop application

SUNSAT did not use heat pipes as part of its thermal control system. It relied on conduction heat transfer along the natural tray structure of the satellite.

4.2.2 Refrigerators

Refrigerators on satellites are used primarily for subsystems that are unable to remove waste heat by passive mechanisms. They can also be used for heating components with the resulting waste heat from the radiator. Often a subsystem (e.g. RF receivers, or imager optics) may need to be kept at low temperatures to optimize their performance, and for this the use of refrigerators is made to induce the desired cooling effect.

A refrigerator operates on the following basis: The heat is transferred from the evaporator section (subsystem requiring cooling) to the working fluid (refrigerant) and then rejected at the condenser section. The condenser section may be a blackbody radiator facing space. Instead of rejecting the waste heat to space, it could also be redistributed to components that need to be heated and are operating at too low a temperature. A refrigerator would typically be required on a large satellite that has a high power rating. For this case, the cooling required outweighs the additional mass and cost of the refrigerator.

A practical example for the need for a refrigerator was on the Hubble Space Telescope, where a refrigerator was mounted in the telescope assembly to provide additional cooling to a set of sensors that are mounted on, but conductively isolated from, the primary focal plane (Gilmore, 1994).

Stellenbosch University http://scholar.sun.ac.za

4.2.3 Heaters

Due to variations in the satellite environment, component heat generation, and surface degradation, the temperature of certain subsystems (e.g. a battery and power regulator) may drop below their desired temperature range. For situations such as these, resistance heaters are added to regulate the temperatures of the subsystems. Heaters may also be used with thermostats to control the temperatures of the subsystems accurately. The most common type of heaters on spacecraft is the patch heater. It consists of an electrical resistance element sandwiched between two sheets of flexible electrical insulating material such as Kapton (Gilmore, 1994). These patches are then installed using film adhesives that bond the heater to the intended surface (Karam, 1998).

4.2.4 Louvers

Louvers are mechanical devices that are used on spacecraft to regulate the radiator area, and in doing so; regulate the rate at which internal heat is removed from the satellite. The louver surface would be coated with a flat reflector thermal finish. The type of louvers used most often is the venetian blind. The blinds are fitted to spring actuators on the radiator that opens and closes the louvers as required and this allows the radiator to radiate heat to space. The blinds are in effect thermal "rheostats" since they are able to adjust the resistance to thermal radiation. If it is required to reject waste heat from the radiator or take heat in from the environment, the blinds are opened. The opposite holds true. The temperature sensitive spring actuators open and close the blinds based on the temperature of the radiator. This variable radiator thermal radiation compensates for variable environmental and internal heat loads (Karam, 1998).

Stellenbosch University http://scholar.sun.ac.za

5 THERMAL MODELLING TECHNIQUES

An important aspect of the thermal analysis of a satellite requires the determination of the temperatures throughout the satellite. To determine the temperatures, the satellite is divided up into a number of finite control volumes. The temperature of each control volume is obtained by applying the conservation of energy in the form

$$\frac{\Delta U}{\Delta t} = \dot{Q} + \dot{Q}_{int} \tag{5.1}$$

where $\Delta U = mc\Delta T = \rho Vc\Delta T$.

5.1 Thermal Modelling Philosophy Details

Numerical methods commonly used in thermal modelling include finite-difference method, finite-element method and boundary-element method. Of these three, only the finite difference method will be used in this thesis. The finite-element method is used in stress analysis and the boundary-element method has yet to be established (Mills, 1999).

5.1.1 Finite Difference Method

Consider two-dimensional unsteady conduction with internal heat generation as shown in figure 5.1. The energy conservation principle, equation 5.1, is applied to the finite control volume over a time interval Δt, from time t to $t + \Delta t$.

$$\frac{\Delta U}{\Delta t} = \dot{Q}_W - \dot{Q}_E + \dot{Q}_S - \dot{Q}_N + \dot{Q}_{int} \tag{5.2}$$

The rate of change of internal energy is

$$\rho Vc\frac{\Delta T}{\Delta t} = \dot{Q}_W - \dot{Q}_E + \dot{Q}_S - \dot{Q}_N + \dot{Q}_{int} \tag{5.3}$$

It follows that the change in temperature from time t to $t + \Delta t$

$$\left(T_{m,n}^{t+\Delta t} - T_{m,n}\right) = \frac{\Delta t}{\rho(\Delta x \Delta y)c}\left(\dot{Q}_W - \dot{Q}_E + \dot{Q}_S - \dot{Q}_N + \dot{Q}_{int}\right) \tag{5.4}$$

Stellenbosch University http://scholar.sun.ac.za

Where $V = \Delta x \Delta y$. (Note that the superscript for temperature at time t is not included.)

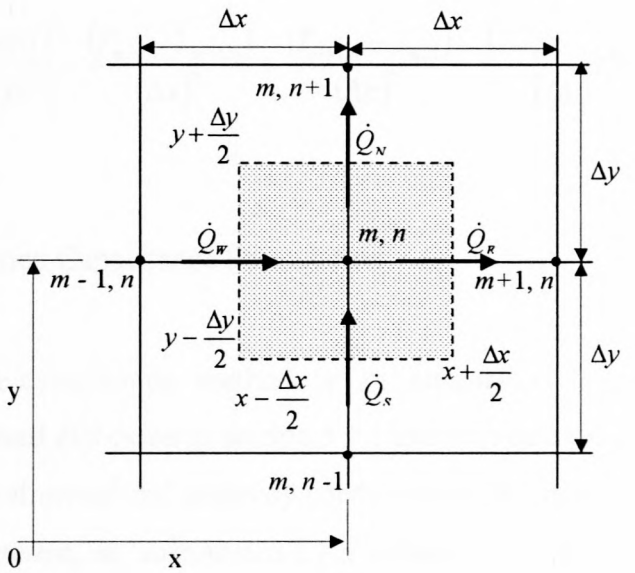

Figure 5.1 Two-dimensional control-volume

The heat transferred by conduction into the control volume over the time interval Δt is

$$\dot{Q}_W = -\frac{k\Delta y}{\Delta x}\left(T_{m,n} - T_{m-1,n}\right) \tag{5.5}$$

$$\dot{Q}_E = -\frac{k\Delta y}{\Delta x}\left(T_{m+1,n} - T_{m,n}\right) \tag{5.6}$$

$$\dot{Q}_S = -\frac{k\Delta x}{\Delta y}\left(T_{m,n} - T_{m,n-1}\right) \tag{5.7}$$

$$\dot{Q}_N = -\frac{k\Delta x}{\Delta y}\left(T_{m,n+1} - T_{m,n}\right) \tag{5.8}$$

After substituting for $\dot{Q}_W, \dot{Q}_E, \dot{Q}_S$ and $\dot{Q}_N$ into equation 5.4

$$\left(T_{m,n}^{t+\Delta t} - T_{m,n}\right) = \frac{\Delta t}{\rho(\Delta x \Delta y)c}\left[-\frac{k\Delta y}{\Delta x}\left(T_{m,n} - T_{m-1,n}\right) + \frac{k\Delta y}{\Delta x}\left(T_{m+1,n} - T_{m,n}\right) - \frac{k\Delta x}{\Delta y}\left(T_{m,n} - T_{m,n-1}\right) + \frac{k\Delta x}{\Delta y}\left(T_{m,n+1} - T_{m,n}\right) + \dot{Q}_{int}\right] \tag{5.9}$$

Stellenbosch University http://scholar.sun.ac.za

After simplification and rearranging

$$T_{m,n}^{t+\Delta t} = T_{m,n} + \frac{k\Delta t}{\rho c}\left[-\frac{\left(T_{m,n} - T_{m-1,n}\right)}{\left(\Delta x\right)^2} + \frac{\left(T_{m+1,n} - T_{m,n}\right)}{\left(\Delta x\right)^2} - \frac{\left(T_{m,n} - T_{m,n-1}\right)}{\left(\Delta y\right)^2} + \frac{\left(T_{m,n+1} - T_{m,n}\right)}{\left(\Delta y\right)^2} + \frac{\dot{Q}_{int}}{\Delta x \Delta y} \right] \tag{5.10}$$

5.1.2 Resistance-Capacitance Formulation

The resistance-capacitance method is an alternative formulation for the finite-difference numerical method discussed in section 5.1.1 and will be used in this thesis.

Consider three-dimensional unsteady conduction with internal heat generation. Figure 5.2 shows the node of interest, *m*, surrounded by a volume ΔV_m of thermal capacitance $C_m = \rho_m c_m \Delta V_m$. The surrounding nodes are denoted *n*, and conduction from the volume ΔV_n into the volume ΔV_m is expressed in terms of a thermal resistance R_{mn}.

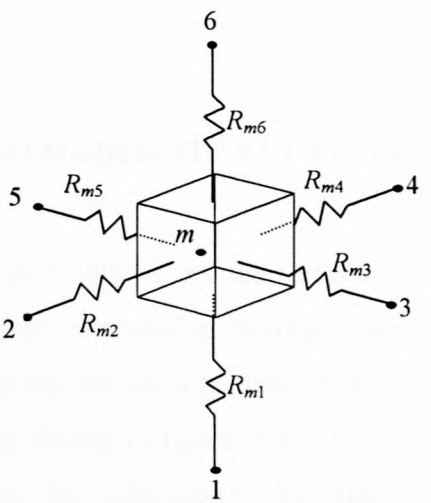

Figure 5.2 Finite control-volume, ΔV_m, surrounding node *m*

An energy balance on volume ΔV_m over the time interval Δt gives

$$C_m \frac{T_m^{t+\Delta t} - T_m}{\Delta t} = \sum_{n=1}^{6} \frac{T_n - T_m}{R_{mn}} + \dot{Q}_{\text{int}}''' \Delta V_m \tag{5.11}$$

where $\dot{Q}'''$ is the volumetric heat generation.

Stellenbosch University http://scholar.sun.ac.za

Equation 5.11 is an explicit formulation and although written for an interior node, can also be applied to boundary nodes.

Rearranging equation 5.11 gives

$$T_m^{t+\Delta t} = T_m + \frac{\Delta t}{C_m}\left(\sum_1^6 \frac{T_n - T_m}{R_{mn}} + \dot{Q}_{int}^{'''}\Delta V_m\right) \tag{5.12}$$

A satisfactory condition for stability is that

$$1 - \frac{\Delta t}{C_m}\sum_{n=1}^{6}\frac{1}{R_{mn}} \geq 0 \tag{5.13}$$

The stability criterion must be evaluated for each node, and a time step Δt chosen such that

$$\Delta t \leq \left(\frac{C_m}{\sum \frac{1}{R_{mn}}}\right)_{min} \tag{5.14}$$

5.2 Numerical Thermal Model of SUNSAT's Batteries

The NiCd batteries used in SUNSAT are the focus of interest in trying to determine the reasons for this satellite subsystem overheating during space operation. To determine the operating temperatures of the batteries, an explicit numerical thermal resistance model is generated. The schematic of SUNSAT is shown in figure 5.3. The SUNSAT body has been divided up into a number of lumped-masses. No solar panels have been included as it is assumed that no heat is transferred through the solar panels into the main body. The overall dimensions are 0.45 x 0.45 x 0.49 m; and the total mass is 50 kg.

The two battery packs have been combined into a single battery, located on the bottom-tray enclosure. The remaining trays have been combined into two lumped-mass trays 2 and 3. The bottom-plate includes the bottom-plate of SUNSAT and the UHF and VHF amplifiers. The top-plate represents the top-plate of SUNSAT and the telemetry components.

SUNSAT internal heating occurs predominantly in the bottom-plate due to the UHF and VHF amplifiers, and from the batteries and tray 2 and 3 electrical circuit boards.

Stellenbosch University http://scholar.sun.ac.za

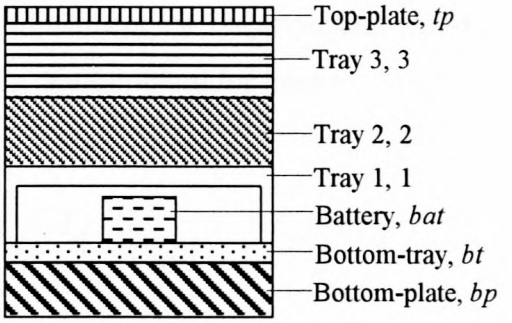

Figure 5.3 SUNSAT as 7 lumped-masses

The top and bottom-plate surface temperatures are taken to be equivalent to the top and bottom lumped-mass temperatures respectively. The bottom surface is coated with a flat-reflector and the top with a solar reflector (refer to section 4.1). Figure 5.4 shows the relevant thermal resistances and nodal temperatures. This figure does not account for direct and reflected solar radiation and only the thermal radiation heat load is shown. All the relevant heating loads are added to the top and bottom-plates. To determine the heat loads, the computer program "ORBIT-FLUX" was developed. (The theory for the program is discussed in Appendix C.)

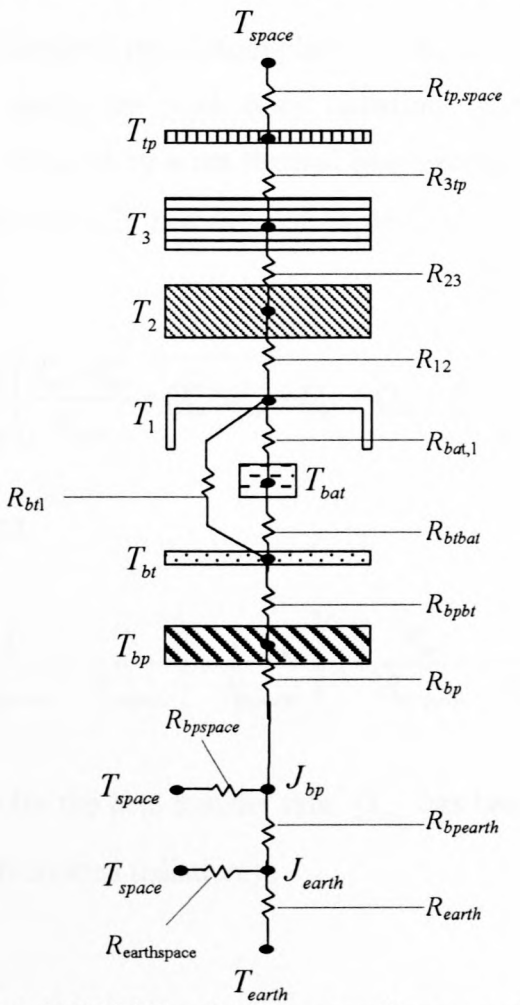

Figure 5.4 SUNSAT resistance-capacitance model

Stellenbosch University http://scholar.sun.ac.za

From equation 5.12, with adjustment for radiation heat transfer and the incoming solar heating loads, the temperature of the bottom-plate for time $t + \Delta t$ is derived in terms of the temperatures at time t as

$$T_{bp}^{t+\Delta t} = T_{bp} + \frac{\Delta t}{C_{bp}}\left(\frac{T_{bt} - T_{bp}}{R_{bpbt}} + \dot{Q}_{\text{int}}^{\prime\prime\prime}\Delta V_{bp} + \frac{J_{bp} - \sigma T_{bp}^4}{R_{bp}} + \dot{Q}_{ds} + \dot{Q}_{er}\right) \tag{5.15}$$

where, $\dot{Q}_{ds}$ is the direct solar radiation on the bottom-plate, $\dot{Q}_{er}$ is the earth reflected solar radiation heat load on the bottom-plate; also, $C_{bp} = \rho_{bp} c_{bp} \Delta V_{bp}$ and J_{bp} is the radiosity of the bottom-plate. The thermal resistance R_{bpbt} is determined as

$$R_{bpbt} = \left(\frac{2k_{bp}A_{bp}}{L_{bp}} + \frac{2k_{bt}A_{bt}}{L_{bt}}\right)^{-1} \tag{5.16}$$

where A is the cross-sectional area, and L the length, in the direction of heat transfer.

The infrared radiation between the bottom-plate, the earth and space is described in equation 5.15 by the radiosity minus the black body radiation divided by the surface resistance to radiation. This term is replaced by a net thermal heat exchange with the environment from the bottom-plate, $\dot{Q}_{bp}$. (This term is derived and explained in appendix B.) It follows then that equation 5.15 becomes

$$T_{bp}^{t+\Delta t} = T_{bp} + \frac{\Delta t}{C_{bp}}\left(\frac{T_{bt} - T_{bp}}{R_{bpbt}} + \dot{Q}_{\text{int}}^{\prime\prime\prime}\Delta V_{bp} + \dot{Q}_{bp} + \dot{Q}_{ds} + \dot{Q}_{er}\right) \tag{5.17}$$

where from equation B13

$$\dot{Q}_{eebp} = \left[E_{bp}\left(\frac{1}{R_{bpearth}} + \frac{1}{R_{bpspace}}\right) - \frac{E_{earth}}{R_{bpearth}}\right]\left(1 + \frac{R_{bp}}{R_{bpspace}} + \frac{R_{bp}}{R_{bpearth}}\right)^{-1} \tag{5.18}$$

(**Note**: the subscript *bp* for the heat transfer rate, $\dot{Q}_{bp}$, has been dropped for the subscript *eebp*, since this indicates earth-emitted radiation.)

Stellenbosch University http://scholar.sun.ac.za

And from equations B7, B8 and B9

$$R_{bp} = \frac{(1-\varepsilon_{bp})}{\varepsilon_{bp} A_{sp}},\ R_{bpearth} = \frac{1}{A_{bp} F_{bp,earth}} \text{ and } R_{bpspace} = \frac{1}{A_{bp} F_{bpspace}} \tag{5.19}$$

The general equation for each of the lumped-masses, m, is derived from equation 5.15 for time $t + \Delta t$ as

$$T_m^{t+\Delta t} = T_m + \frac{\Delta t}{C_m}\left(\sum \frac{T_n - T_m}{R_{mn}} + \dot{Q}_{\text{int}}''' \Delta V_m + \dot{Q}_{eem} + \dot{Q}_{dsm} + \dot{Q}_{erm}\right) \tag{5.20}$$

The environmental heat loads $\dot{Q}_{dsm}$, $\dot{Q}_{erm}$, and $\dot{Q}_{eem}$ in equation 5.17 are only relevant to the surfaces exposed to the environment, i.e., the top and bottom-plates. (Note that the top and bottom-plates also receive direct solar radiation during the orbit around the earth.) From these equations, a computer program named "BATTERY", is generated to predict the temperatures of the 7 lumped-masses for specific orbit path parameters.

Equation 5.17 serves to explain the theory, but for the purpose of the computer program, the thermal radiation from the bottom-plate and top tray is added to the direct and earth reflected solar radiation heat loads in the computer program ORBIT-FLUX; which results in the overall environmental heat load for each radiating surface. From this, equation 5.20 then becomes

$$T_m^{t+\Delta t} = T_m + \frac{\Delta t}{C_m}\left(\sum \frac{T_n - T_m}{R_{mn}} + \dot{Q}_{\text{int}}''' \Delta V_m + \dot{Q}_m\right) \tag{5.21}$$

where $\dot{Q}_m$ is the total environmental heating load on surface m.

The results of the numerical thermal model are compared to the TAS (outsourced thermal software) model results in order to establish the useability, accuracy and consistency of the TAS software. The details of the numerical model are given in appendix D.

Stellenbosch University http://scholar.sun.ac.za

5.3 TAS Thermal Model of SUNSAT's Batteries (Outsourced Program)

This section serves as an introduction into thermally modelling with TAS, and to show the difference between a numerically developed thermal model and a similar TAS thermal model, for the 7 lumped-mass model of SUNSAT previously discussed.

5.3.1 TAS Background

As the SUNSAT models become more advanced, so the need for a comprehensive software program becomes necessary to thermally model the complex geometries. TAS (Thermal Analysis Systems) is an outsourced software program from Harvard Thermal (Harvard Thermal, 2000). TAS is a general-purpose tool used to computer-simulate thermal problems.

A single environment provides model generation, execution and post processing of results. TAS uses a finite difference solution to solve the models. Full three-dimensional geometry can be created using two dimensional *plate* and three-dimensional *brick* and *tetrahedron* elements. The program then solves for the temperatures at element nodes that are generated as part of the geometry shown below in figure 5.5.

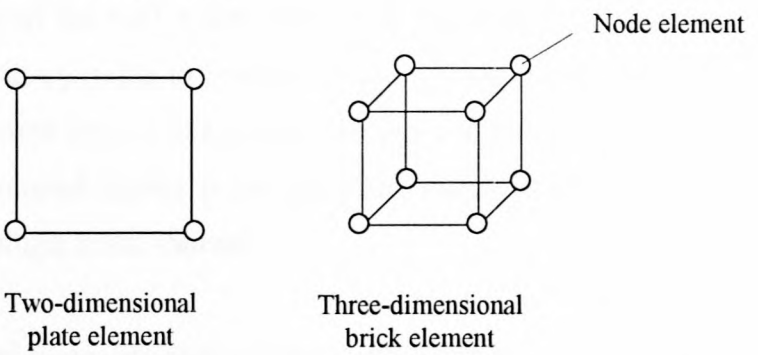

Figure 5.5 TAS two-dimensional and three-dimensional geometric elements

5.3.2 TAS Modelling

The equivalent SUNSAT-body lumped-mass model generated in TAS to that shown in figure 5.3 would be made up of brick elements and plate elements. Referring to figure 5.6, the bottom-plate is created from nine brick elements.

Stellenbosch University http://scholar.sun.ac.za

The bottom-tray is very thin compared to the bottom-plate and for this reason is generated from a plate element on the surface of the brick elements and shares common nodes. The battery is then constructed from a single brick element by extruding the centre plate element.

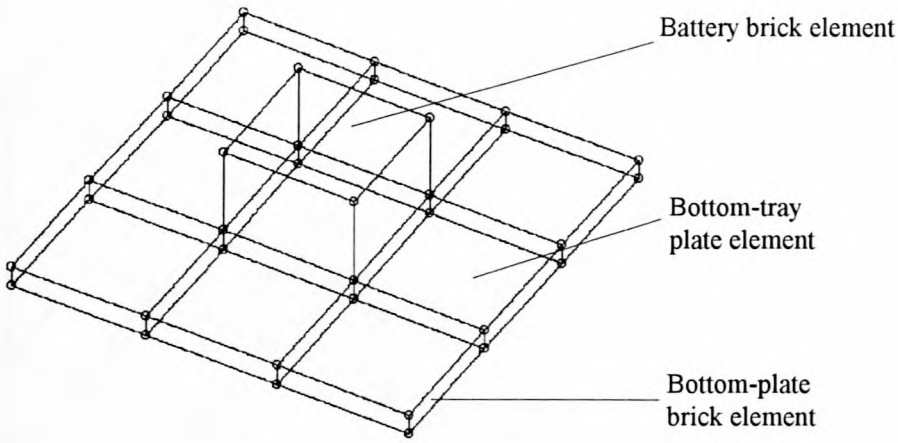

Figure 5.6 TAS model of the bottom-plate, bottom-tray and battery geometry

The overall TAS model of the SUNSAT-body is shown in figure 5.7. The walls of the battery enclosure (tray 1) are thin enough to assume there is no temperature gradient through them and are therefore created as plate elements (lumped-mass 1). The reason for the bottom-tray nodes not corresponding to the wall nodes is because the number of radiating surfaces on the walls surrounding the battery needs to be reduced to improve calculation time. The lumped-masses 2 and 3 are each created from a single brick element and placed on top of the lumped-mass tray 1. On top of these lumped-masses is the top-plate, which is reasonable thick and for that reason generated from a single brick element.

The top and bottom-plates are each given a surface coating property. On these radiating surfaces, surface-to-node radiating elements are created. This property allows for radiation from the surface to a boundary-node at 0 K representing space. The external heating loads on the top tray and bottom-plate are imported into TAS as array data from the text files generated from the ORBIT-FLUX program. These heat load properties are then applied as surface heating in TAS to the relevant surfaces. The view factors between the battery surface and the surrounding enclosure are determined by exporting the geometry, with predefined radiating surfaces, to the built-in sub-program TRASYS; where the view factors are determined and imported back into TAS. The program is then run for transient analysis. Using the plotting and graphic tools in TAS, the temperatures of the nodes can be analysed and presented as desired.

Stellenbosch University http://scholar.sun.ac.za

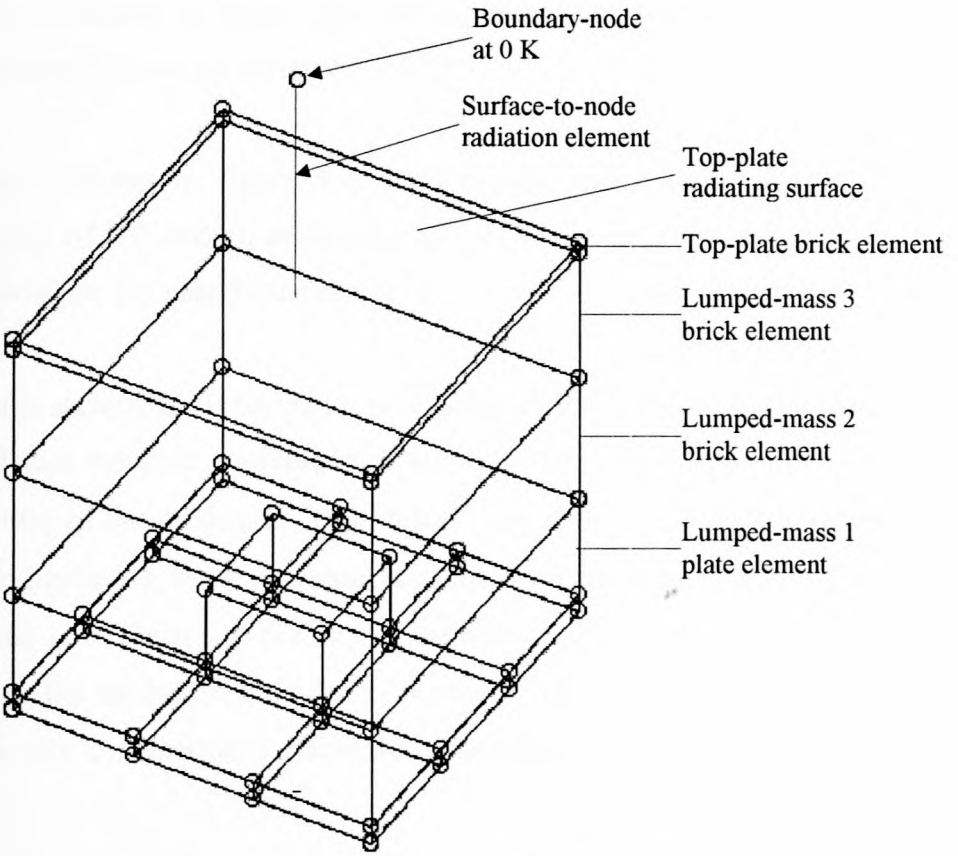

Figure 5.7 TAS model of the SUNSAT-body

5.4 Comparison of Numerical and TAS Models of SUNSAT's Batteries

A comparative temperature response of the combined battery is generated from the numerical and the TAS thermal models. In each case, the input variables are identical. The models are subjected to a polar sun-synchronous orbit with a β-angle = 0°. The model is subjected to ten orbits around the earth and simultaneously, four rotations around the SUNSAT Z-axis per orbit. The total internal heating rate was taken as 30 W. A break down of the heating rates is as follows:

- Bottom-plate, 18 W
- Battery, 4 W
- Tray 2, 4 W
- Tray 3, 4 W

Two comparison test cases were done. The difference between the two is that the surface properties selected for the top and bottom-plates differ for each run. Factors such as processing time, accuracy, dynamic steady state time and response of the battery to heating and cooling are all considered in determining the performance and consistency of the two models.

Stellenbosch University http://scholar.sun.ac.za

For case 1 shown in figure 5.8, the top-plate and bottom-plate were each given a solar absorptivity of 0.5 and an emissivity of 0.8.

For case 2 shown in figure 5.9, the top-plate and bottom-plate were each given a solar absorptivity of 0.7 and an emissivity of 0.8. The expected result being that the temperatures would be higher for case 2 than case 1.

The results show that the temperature response of the batteries for the two models is similar. It is assumed that dynamic equilibrium is attained after 60000 s. For the results in figure 5.8, the temperature of the models at "equilibrium" are within 3°C of each other. For the second case shown in figure 5.9, the temperature at equilibrium are within 2°C of each other. The variation in the results is attributed to the approximations made with regard to radiation from the battery surface to the enclosure. For the TAS model, 10 surfaces were modelled. For the numerical program only 2 isothermal surfaces were modelled.

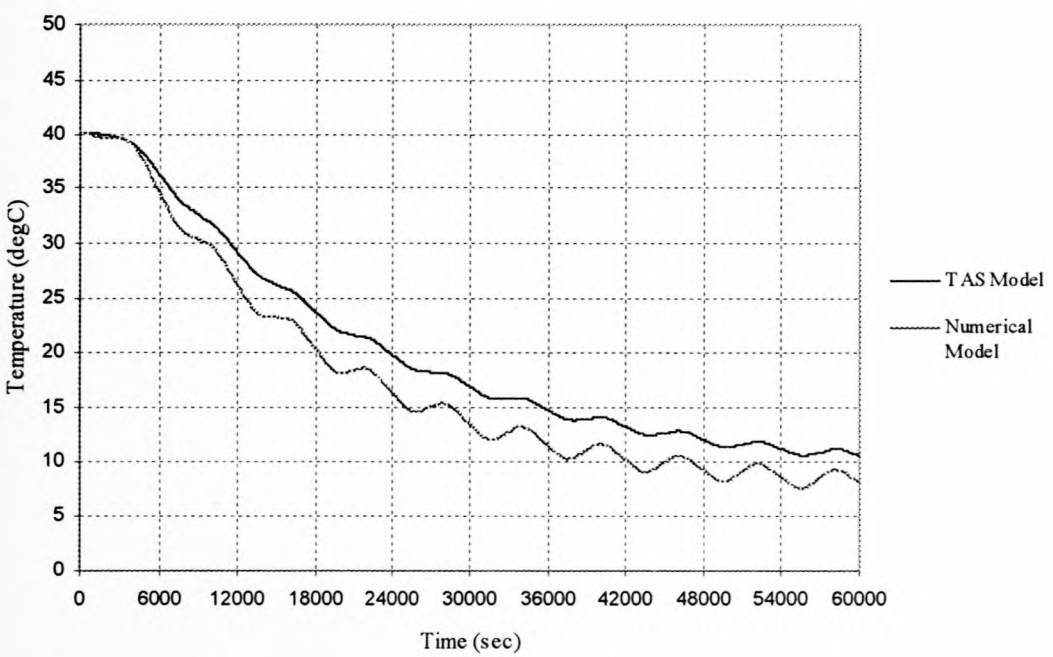

Figure 5.8 Temperature responses of the batteries used in SUNSAT for the numerical and TAS models with radiators of medium ($\alpha = 0.5$, $\varepsilon = 0.8$) solar absorptivity

Stellenbosch University http://scholar.sun.ac.za

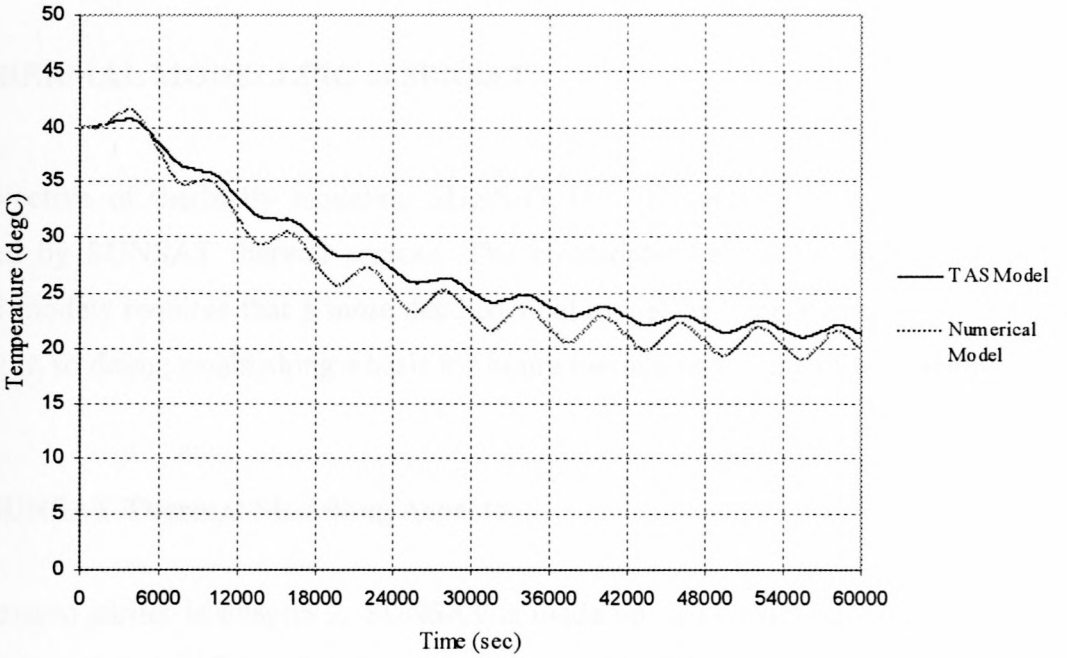

Figure 5.9 Temperature responses of the batteries used in SUNSAT for the numerical and TAS models with radiators of high ($\alpha = 0.7$, $\varepsilon = 0.8$) solar absorptivity

Stellenbosch University http://scholar.sun.ac.za

6 THERMAL MODELLING of SUNSAT

The objective of thermally modeling SUNSAT is to theoretically simulate temperature data recorded by SUNSAT thermal sensors. The philosophy behind the generation of SUNSAT thermal models requires that a more detailed final model be generated than previously simpler models; in so doing, establishing a basis for future thermal modelling of microsatellites.

6.1 SUNSAT Thermal Modelling Aspects

As discussed earlier in chapter 2, SUNSAT is made up of 11 aluminum trays with bottom and top-plates as shown in figure 6.1. Each tray is packed tightly with bus-equipment. SUNSAT can be approximated as being made up out of 11 solid material trays with average physical and thermal properties. For the purpose of thermal modelling, these trays can be combined into sections with averaged thermal properties. Four solar panels provide the satellite subsystems with power and insulation from the environmental heating loads. The total mass of SUNSAT is taken to be 60 kg and the overall dimensions as 0.45 x 0.45 x 0.49 m.

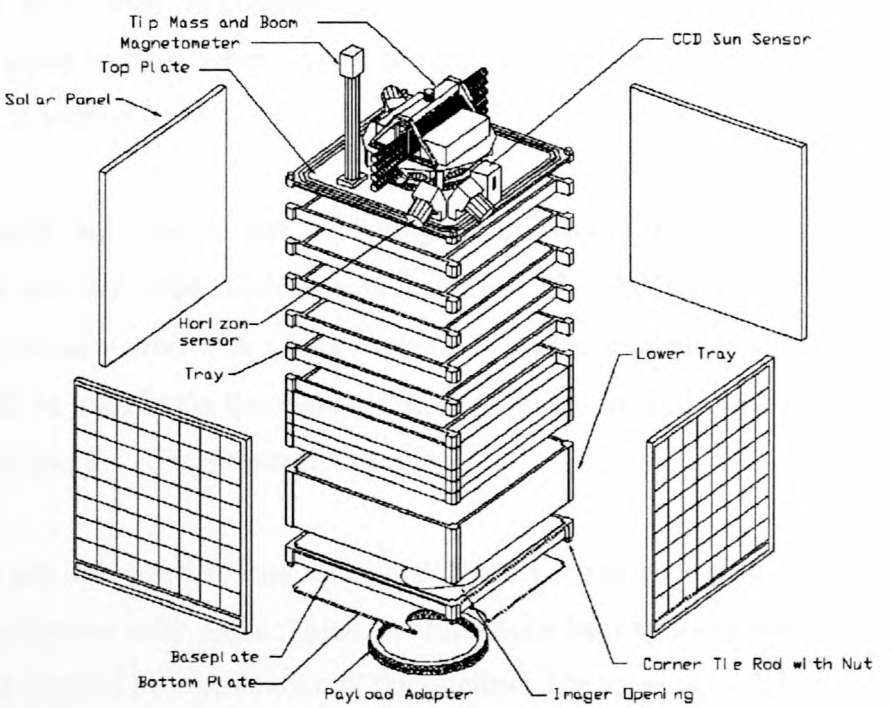

Figure 6.1 Exploded-view of SUNSAT (Schoonwinkel, 1997) (Figure 2.13 repeated for convenience)

Stellenbosch University http://scholar.sun.ac.za

For the solid model configuration used in the thermal modelling of the trays, conduction is the only heat transfer mechanism between the trays. Although radiation does occur in reality, due to insufficient computing and TAS capability, it is not introduced into the thermal models of SUNSAT in this thesis. Heat is assumed to be predominately conducted along the corner columns of the aluminum trays to the top or bottom-plate and then radiated to space. If this is the case, then only the outer surfaces of the top and bottom-plates are considered to be radiators.

The emissive and absorptive properties of the surfaces of SUNSAT are dependant on the thermal properties of the surface coatings, which in turn are dependant on directional properties, and temperature of the surface and the intensities of the spectrum of wavelengths (Modest, 1993). For modelling purposes, only hemispherical averaged properties will be used in this thesis.

The solar panels are approximated as having a BOL total hemispherical emittance equal to 0.8 and a total hemispherical absorptance equal to 0.8. The top of SUNSAT consists of telemetry equipment and this equipment is coated with a Kapton layer to protect it from direct solar radiation and overheating, by having a fairly low absorptance and a high emittance. Alodine surface treatment alone would not suffice for the top-plate as it did for the bottom-plate due to the high solar loads received on the top-plate, and the need for a high emittance. The Kapton layer has a BOL total hemispherical emittance equal to 0.73 and a total hemispherical absorptance equal to 0.41. After 3 years of orbit, the performance of this kapton layer degrades as discussed in section 4.1.1.

Two orbit-paths are used in the modelling of SUNSAT. The first is a circular polar sun-synchronous circular orbit with a beta angle of 0°. The second is a circular polar sun-synchronous circular orbit with a beta angle of 90° (refer to chapter 3, figures 3.3 and 3.4). The first orbit will be used in the thermal modelling up to the final SUNSAT model, where both will be considered and the effects thereof discussed.

The models are subjected to environmental heating loads as would be experienced in space operation for the two orbit paths. These environmental heating loads are illustrated in figure 6.2, as well as the internal heat generation of the satellite. The value of each heat load on each surface is dependant on the position of the satellite relative to the earth and the sun for each position in its orbit around the earth as well as the optical and geometric properties of the satellite surfaces. These heat loads are determined by the computer program ORBIT-FLUX for each of the 6 surfaces and are discussed in appendix C.

Stellenbosch University http://scholar.sun.ac.za

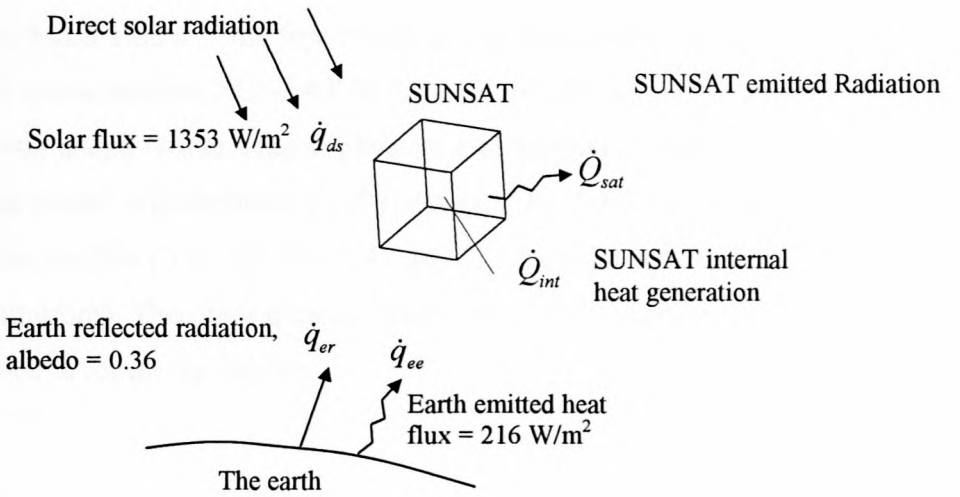

Figure 6.2 Heating loads on SUNSAT in orbit

The total internal heat load for SUNSAT is averaged as 30 W (Schoonwinkel, 1997) when all the subsystems are operating as normal. The biggest contributors include the batteries (approximately 4 W) and the UHF and VHF amplifiers (approximately 18 W). The remaining heat (8 W) is produced by the ohmic heating in the resistance of electrical circuits. A peak internal heat generation of 80 W occurs for a maximum of 2 minutes per orbit. This is when the imager is used to take pictures of the earth.

The SUNSAT co-ordinate system is illustrated in figure 6.3. The +Z direction always points to the centre of the earth; the opposite of which is the –Z or *top*-plate that never sees the earth. The surfaces of the satellite are numbered from 1 to 6. Numbers 1 and 6 represent the +Z (bottom-plate) and –Z (top-plate) surfaces respectively, 2 and 4 the +Y and -Y (solar panels) surfaces and 3 and 5 the +X and –X (solar panels) surfaces respectively.

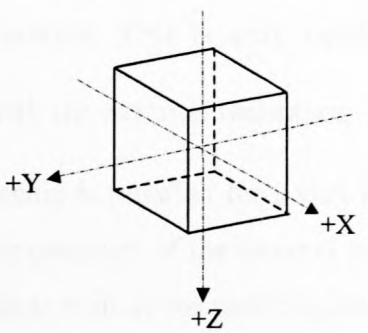

Figure 6.3 SUNSAT co-ordinate axis

Stellenbosch University http://scholar.sun.ac.za

6.2 SUNSAT Lumped-Mass Model

The Lumped-Mass model is the first theoretical model used to predict the operating temperature of the micro space satellite SUNSAT in orbit. SUNSAT is firstly modeled as a lumped-mass of material of box shape with averaged physical and thermal properties. The average density of the lumped-mass model is determined as 604.69 kg/m^3 by dividing the satellite mass of 60 kg by the volume of the satellite (0.45 x 0.45 x 0.49 m). The thermal capacitance is taken to be 1000 J/kgK (close to aluminum). The outer dimensions of the lumped-mass model are consistent with that of SUNSAT, as it is for all the models.

6.2.1 Numerical Lumped-Mass Model

The numerical lumped-mass SUNSAT model consists of a single control volume $\Delta x \Delta y \Delta z$. The control volume has a single interior node that represents the temperature of the entire lumped-mass. Figure 6.4 shows the geometry of the numerical lumped-mass model.

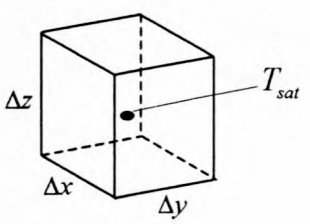

Figure 6.4 SUNSAT lumped-mass model

This approximation is more commonly referred to as a lumped thermal capacity model (Mills, 1997). For this type of model to be valid, there needs to be negligible temperature gradients within the system. This is only possible if the internal resistance to heat transfer is small compared with the external resistance, i.e. $\frac{L}{kA} << R_{spspace}$, between the satellite panel and space. This relationship is satisfied for a very high thermal conductivity of *satellite material*. The result is that the temperature of the internal node of the model represents the temperature of the entire lumped-mass as well as the radiating satellite surfaces.

Stellenbosch University http://scholar.sun.ac.za

The thermal resistance diagram for the numerical lumped-mass SUNSAT model is shown in figure 6.5 (refer to appendix B). The four solar panels and bottom-plate interact thermally with the earth while the top-plate does not since it always points away from the earth during orbit. The view factors F_{ij} (embedded in the space resistance $R_{ij} = \frac{1}{F_{ij} A_i}$) for the solar panels and bottom-plate to the earth are determined from equations B26 and B27 in appendix B respectively.

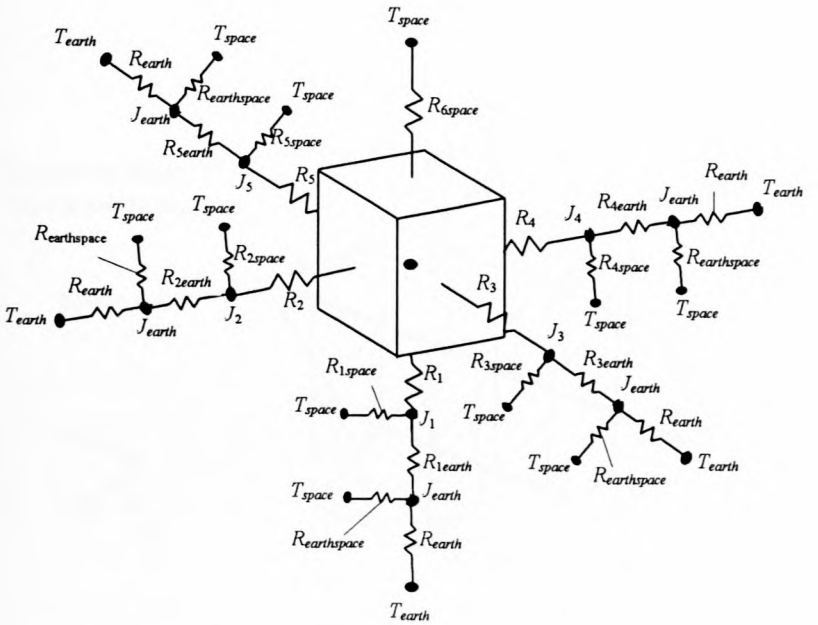

Figure 6.5 Thermal resistance diagram of lumped-mass SUNSAT model

From general equation (5.20), the explicit formulation for the temperature of the single interior node at time t is derived as

$$T_{sat}^{t+\Delta t} = T_{sat} + \frac{\Delta t}{C_{sat}} \left(\frac{T_{space} - T_{sat}}{R_{1space}} + \dot{Q}_{\text{int}}^{m} \Delta V_{sat} + \sum_{m=1}^{6} \dot{Q}_m + \sum_{m=1}^{6} \left(\dot{Q}_{dsm} + \dot{Q}_{erm} \right) \right) \tag{6.1}$$

where, $\dot{Q}_{dsm}$ is the direct solar radiation on surface m, $\dot{Q}_{erm}$ is the earth reflected solar radiation on surface m, $\dot{Q}_m$ is the net thermal radiation heat exchange of the surface m at temperature T_m with the environment, for m = 1, 2…6 surfaces.

Equation 6.1 is used to predict the operating temperatures of the numerical lumped-mass SUNSAT model. The results of the model are given in appendix E.

Stellenbosch University http://scholar.sun.ac.za

6.2.2 TAS Lumped-Mass Model

The lumped-mass model generated in TAS is not identical to the previous numerical model. Figure 6.6 below shows the TAS lumped-mass SUNSAT model. TAS is not able to model a lumped-mass with a single interior node. Nodes are automatically generated as part of the structure and for the case of a block; nodes are generated at each of the corners. To determine average temperature of the lumped-mass, a node needs to be placed at the centre of the block. The model is made up of 8 TAS brick elements

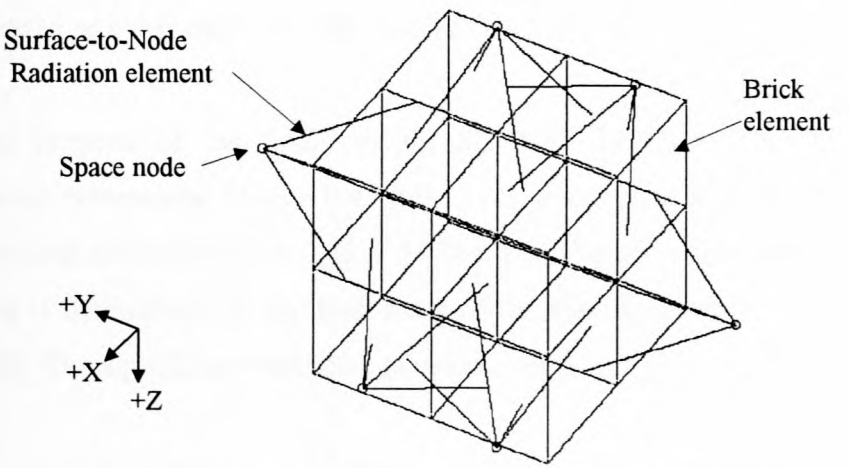

Figure 6.6 TAS lumped-mass model architecture

The internal heat load of 30 W is divided equally between the 8 bricks as a volumetric heat load. The same is done for the peak internal heat load of 80 W. The four solar panels all have the same surface properties, while the top and bottom-plates are coated with a layer of Kapton for this particular model.

The total environmental heat loads for each of the 6 surfaces are given a specific surface-heat property in TAS. The heat loads are then imported from text files that were generated from the ORBIT-FLUX program and applied to the specific properties.

To simulate the surfaces radiating to space using TAS, it is necessary to generate boundary nodes and create surface-node radiation elements (indicated in figure 6.6). The boundary nodes are fixed temperature nodes, in this case space at 0 K. The surface-to-node radiation property simulates the interaction between a single surface and a boundary node.

Stellenbosch University http://scholar.sun.ac.za

For the TAS lumped-mass model, each side consists of 4 radiating surfaces and thus 4 surface-to-node elements are defined for each of the surfaces. The results of the TAS lumped-mass SUNSAT model are given in appendix E.

6.3 Progressive SUNSAT Models using TAS

The next step in thermally modelling SUNSAT is to include the effect of solar panels. The solar panels play a significant role in thermally insulating the satellite from the environmental heating loads. Evolving from the lumped-mass model, the next model, SUNSAT 2, should have more brick elements to improve the accuracy of the results; and also certain subsystems can be represented as brick elements and thus making the model more realistic.

For the purpose of the TAS models, SUNSAT is divided up into three body sections of equivalent dimensions (0.45 x 0.45 x 0.15 m), a top-plate section (0.45 x 0.45 x 0.014 m) and a bottom-plate section (0.45 x 0.45 x 0.024 m) as shown in figure 6.7. The mass of each of these sections is determined by the total mass of the significant components in each section (refer to table J5). The significant components in each section is given as follows:

- Tray 11, which consists of the optics, batteries, reaction wheels and circuitry, makes up the lower-body.

- Trays 7 – 10, which includes; the GPS tray, the VHF tray, the UHF tray, and the power tray respectively, make up the middle-body.

- Trays 1 – 6, which include; the ADCS tray, the RAM tray, the OBC2 tray, the OBC1 tray, the TCMD tray, and the TLM tray respectively, make up the top-body.

- The top-plate section consists of the top-plate, boom, sun sensors, antennas, magnetometer and horizon sensors

- The bottom-plate section consists of the base plate, amplifiers, bottom-plate and payload adaptor.

Each body and plate section is made up of TAS brick elements with averaged thermal properties equal to those for the numerical lumped-mass model.

Stellenbosch University http://scholar.sun.ac.za

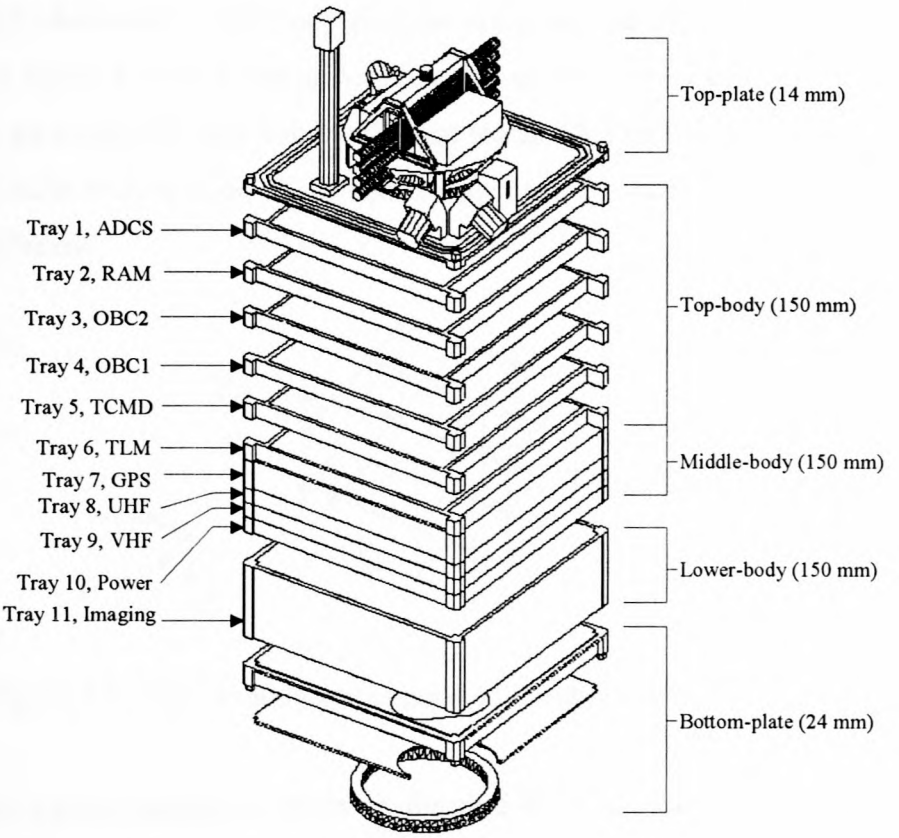

Figure 6.7 TAS model divisions of SUNSAT

6.3.1 SUNSAT 2 Model

For the SUNSAT 2 model, each section is further broken up into 9 brick elements of equivalent properties. Internal heating of the batteries can now be localised at specific brick elements. The TAS model of the lower-body section of SUNSAT 2 is shown in figure 6.8. The two SUNSAT batteries are represented by bricks *a* and *b*. The reason for isolating the batteries is so as to allow for the addition of volumetric heat generation to these specific brick elements. The heat load in each of bricks *a* and *b* is 2 W. The temperature of the battery is taken to be equal to the temperature of the TAS node, indicated in figure 6.8 as T_{bat}.

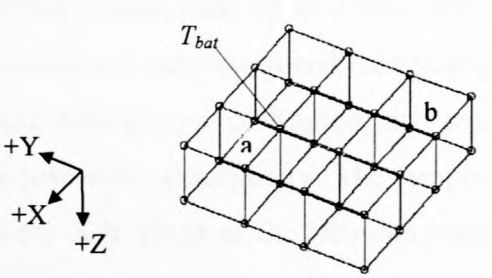

Figure 6.8 Lower-body section of the SUNSAT 2 model

Stellenbosch University http://scholar.sun.ac.za

The middle-body and upper-body sections are given the same average properties, and they are shown in figure 6.9. The heat generation that occurs from trays 1-10 is added to the 18 brick elements as evenly divided volumetric heat loads. This total heat load is 8 W. The temperatures of the middle-body section ($T_{mb.}$) and the upper-body section ($T_{ub.}$) are measured at the nodes indicated below.

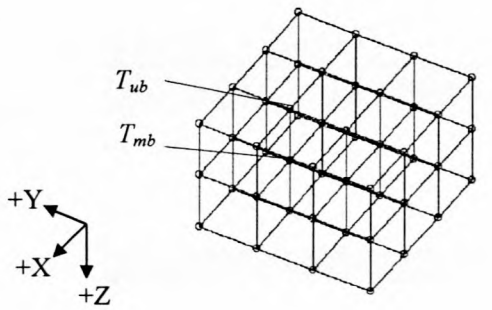

Figure 6.9 Middle-body and upper-body sections of SUNSAT 2 model

The bottom-plate section is shown in figure 6.10. Since the amplifiers for the UHF and VHF transmitters are located in the base plate, a volumetric heat load equivalent to a total of 18 W is applied to all 9 bricks. The +Z face of the bottom-plate is surface treated with Alodine to reduce solar and infrared absorptance. The temperature of the bottom-plate (T_{bp}) and the +Z surface (T_{+Z}) is measured at the nodes as indicated below. The bottom-plate is taken to be 24 mm thick.

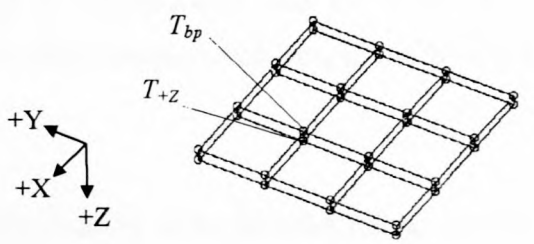

Figure 6.10 Bottom-plate section of the SUNSAT 2 model

The top-plate section is also made up of 9 brick elements. It is assumed that the heat generation of the telemetry sensors is very small and thus heat generation negligible. The –Z surface of the top-plate is coated with a layer of Kapton, and equivalently in TAS, is given a high thermal emissivity and a low solar absorptivity. The temperature of the –Z surface is measured at the same location in the X-Y plane as the previous measurements, except, on the –Z surface of the top-plate. The top-plate is taken to be 14 mm thick.

Stellenbosch University http://scholar.sun.ac.za

A detailed sketch of the construction of the solar panel used on SUNSAT is shown in figure 6.11. On the sides of the SUNSAT body, four solar panels are mounted. They perform two critical thermal tasks; they convert solar radiation to electrical energy and they provide thermal insulation from the environment to the satellite body. The task of insulation is reversed when the satellite passes through eclipse and the satellite body heat is not allowed to escape.

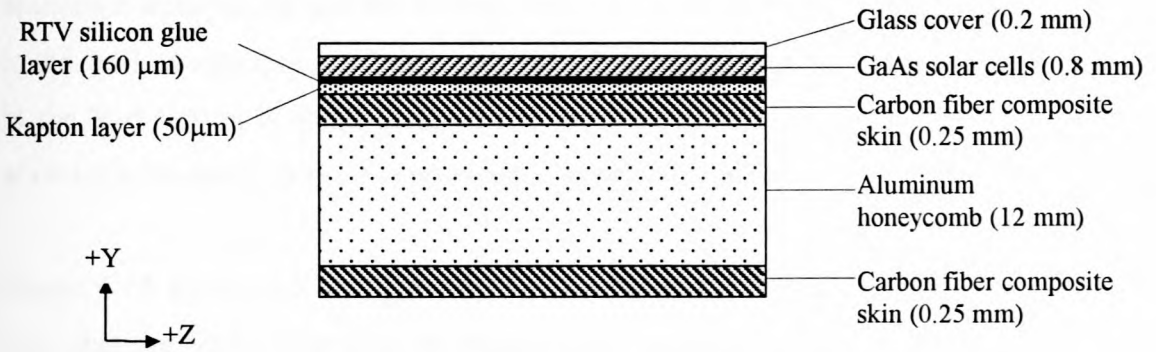

Figure 6.11 SUNSAT solar panel construction

Each solar panel is mounted to two aluminum columns that form part of the tray corner structure. They are mounted on either ±Y ends or ±X ends with 4 x M4 bolts per panel side connected through a brass collar to each aluminum column (Blom, 2002). The contact resistances associated with these mountings are expected to reduce the rate of heat flow from the solar panels, through the mountings and into the satellite body. (The effect of the contact resistance of the mountings is incorporated into the TAS SUNSAT 3 model, by reducing the thermal conductivity of the aluminum columns in the X and Y-directions by three times (from 120 to 40 W/mK).)

As a first approximation of the SUNSAT solar panels for modelling purposes of SUNSAT 2, it is assumed that the solar panels are attached to the body with a mass-less, zero thermal resistance layer of adhesive. (The modelling of the actual attachment with M4 bolts is more detailed and will be considered in the SUNSAT 3 model.) To simulate the high resistance property of the solar panel mountings, a layer of high thermal resistance material is added to the solar panel/ satellite body interface. This serves to reduce the rate at which heat is transferred from the solar panels to the satellite body. This thermal resistance layer replaces the layer of carbon fibre on the satellite body side of the solar panel.

The layer of RTV silicon and Kapton in the SUNSAT solar panel is not included in the SUNSAT 2 model of the solar panel. The GaAs solar cells are generated as plate elements on the honeycomb.

Stellenbosch University http://scholar.sun.ac.za

The layer of glass is not included in this model. (The reason for the exclusion of these layers is due to computational errors that occur in TAS when multiple layers like these are placed one on top of the other as plate elements.)

The honeycomb is modelled in TAS with brick elements that have the equivalent density of the aluminum honeycomb and the thermal conductivity in each of the three directions as determined in the worked example in appendix A. The effect of radiation heat transfer across the honeycomb in the Y-direction is small compared to the heat transfer by conduction (figure A6) and thus allows the honeycomb to be approximated as brick elements.

Figure 6.12 shows the configuration for the SUNSAT 2 solar panel that is modelled in TAS. Note that the GaAs solar cells are modelled as a single layer of material of thickness equivalent to the total thickness of the glass, solar cells, RTV silicon layer, kapton layer and carbon fiber added together. (The reason for this assumption is based on the computational errors that occur in TAS when the same node is shared by more than two TAS plate elements.) The total thermal resistance of the layers is determined as

$$R_{tot} = \left(\frac{1}{R_{glass}} + \frac{1}{R_{GaAs}} + \frac{1}{R_{RTV}} + \frac{1}{R_{kap}} + \frac{1}{R_{cf}} \right)^{-1} \tag{6.2}$$

where $R = \frac{kA}{L}$, and k is the thermal conductivity, A the cross sectional area and L is the thickness.

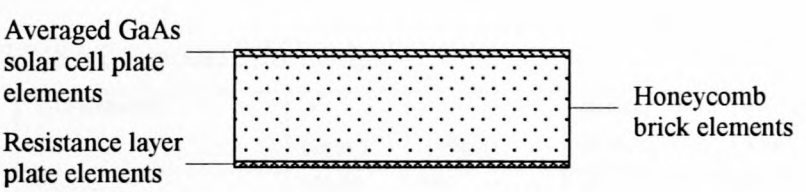

Figure 6.12 TAS SUNSAT 2 thermal model solar panel construction

The relevant environmental heating loads on each of the six surfaces are determined in the program ORBIT-FLUX. These are then added to each of the surfaces of the satellite in TAS as *surface-power* heat loads. Each surface radiates to deep space (as discussed in the lumped-mass model) which is represented by a single boundary node at 0 K. The resistance to the surface-to-node radiation is determined by the values of emissivity given to the averaged solar cell material surface. The TAS model of the four solar panels is shown in figure 6.13.

Stellenbosch University http://scholar.sun.ac.za

Each panel looks like a single layer, but that is because it is not possible to distinguish between the outside plates on the brick, since they share common nodes. The temperatures of each of the solar panels are measured at a similar position as shown for the +Y panel temperature (T_{+Y}) below.

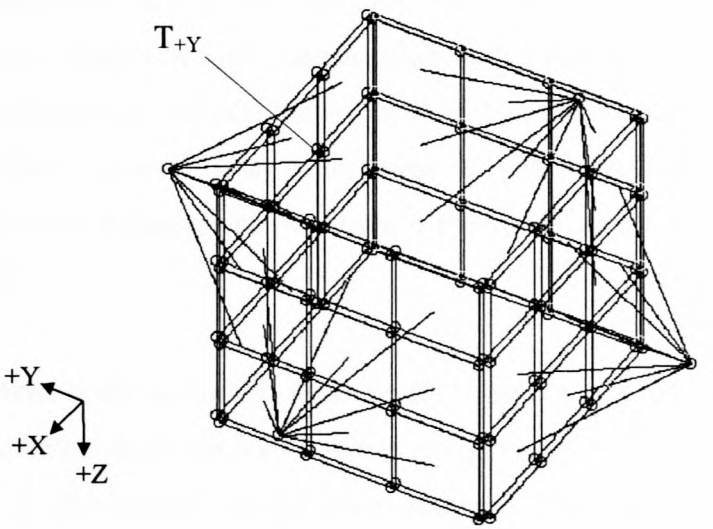

Figure 6.13 TAS SUNSAT 2 model sketch

The model details are presented in Table 6.1 below, and the model results in appendix F. The density values correspond to the mass and volume distributions of SUNSAT, and the specific heat has been estimated as well as the thermal conductivity for the model components, except for the solar panel and Kapton.

Table 6.1 SUNSAT 2 model information

TAS description	TAS element/s	ρ (kg/m^3)	c (J/kgK)	k_x, k_y, k_z (W/mK)	Internal Heat Load (W)	α (BOL)	ε (BOL)
Lower-body	9 bricks	571.55	500	15	4	-	-
Middle-body	9 bricks	470.12	500	30	4	-	-
Upper-body	9 bricks	470.12	500	30	4	-	-
Top-plate	9 bricks	2673.72	500	30	0	-	-
Bottom-plate	9 bricks	720.16	500	50	18	-	-
Solar-panels	9 plates, resistance layer 9 bricks, honeycomb 9 plates, GaAs averaged	750 35 2300	1000 903 750	0.0001 9.3, 1.16, 5.24 1.3	0	- - 0.8	- - 0.8
Kapton layer (2mil*)	9 plates	1420	1090	0.12	0	0.41	0.73

(***Note**: 1mil = 1 millionth of an inch)

Stellenbosch University http://scholar.sun.ac.za

6.3.2 SUNSAT 3 Model

Evolving from the SUNSAT 2 model, SUNSAT 3 has more body brick elements, solar panel mountings, and solar panels similar to those of SUNSAT 2. The higher number of body brick element increases the calculation time (time for 1 simulation run ≈ 30 min), but improves the accuracy of the results since the control volumes are smaller. The solar panel mounting on the body is approximated by vertical plate elements. This isolates the body from the solar panel and the result of this is that the solar panel temperature will fluctuate more; and the average body temperature will be higher since heat cannot readily escape from the body via the solar panels and into space.

Each of the three body sections is made up of 16 bricks of averaged material. The geometry for the case of the lower-body section is shown in figure 6.14. The outer dimensions are the same as for SUNSAT 2. The batteries in the lower-body are represented by TAS brick elements *c* and *d* with a 2 W internal heat generation rate for each brick. The equivalent battery temperature (T_{bat}) is taken to be equal to the temperature of the centre node as indicated below.

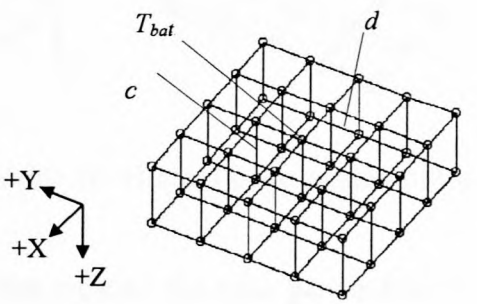

Figure 6.14 SUNSAT 3 lower-body section

The middle-body and upper-body sections are identical in size and TAS geometry as the lower-body section. The internal heat load of 8 W is added to the 32 bricks that make up the middle-body and upper-body sections as a volumetric heat load in TAS. The TAS geometry of the middle-body and upper-body sections is shown in figure 6.15. The temperatures of the middle-body and upper-body are measured at the nodes in the centre of the brick configuration, on the same X-Y plane as for the SUNSAT 2 model in figure 6.9.

Stellenbosch University http://scholar.sun.ac.za

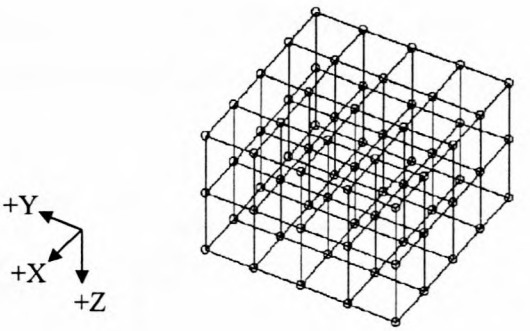

Figure 6.15 Middle-body and upper-body sections of SUNSAT 3 model

The top and bottom-plates are each made up of 16 brick elements of averaged material. Figure 6.16 shows the bottom-plate of SUNSAT 3. The 18 W internal heat generation by the amplifiers in the bottom-plate is added to the 16 bricks as a volumetric heat load. The temperature of the bottom-plate (T_{bp}) and the +Z surface (T_{+Z}) is measured at the nodes as indicated below.

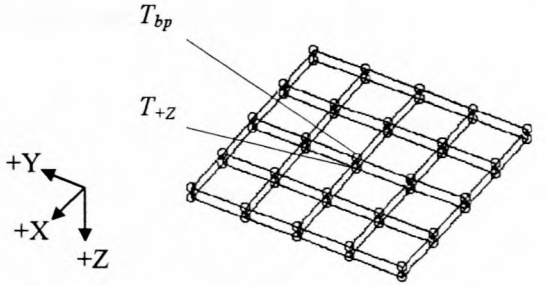

Figure 6.16 Bottom-plate section of the SUNSAT 3 model

The four spacers that separate the solar panels from the body of the satellite replaces the 32 M4 bolts that connect the four panels to the body corner aluminum columns (four bolts per solar panel per corner). These aluminum columns are essentially the corners of the trays that have been joined together by tie-rods when the satellite body is assembled. The tie-rods pass through the center of the columns. The aluminum columns played a crucial thermal role in SUNSAT by allowing heat to flow from the trays to the top or bottom-plates. The negative side of these four columns in terms of thermal performance is the contact resistance that exists at the interface of each tray corner when they are assembled with the tie-rods. (The effect of these multiple contact resistances is introduced into the model by reducing the thermal conductivity of the aluminum column in the Z-direction by six fold (from 120 to 20 W/mK).)

The spacers are generated in TAS as plate elements with equivalent cross-sectional area to the M4 bolts. The spacers are 0.45 m in length (same as the body), have a width of 3.5 mm and a thickness of 0.342 mm.

Stellenbosch University http://scholar.sun.ac.za

The exaggerated top view of the SUNSAT 3 model is shown in figure 6.17. Radiation heat exchange occurs between the body and the backside of the solar panel (carbon fiber layer).

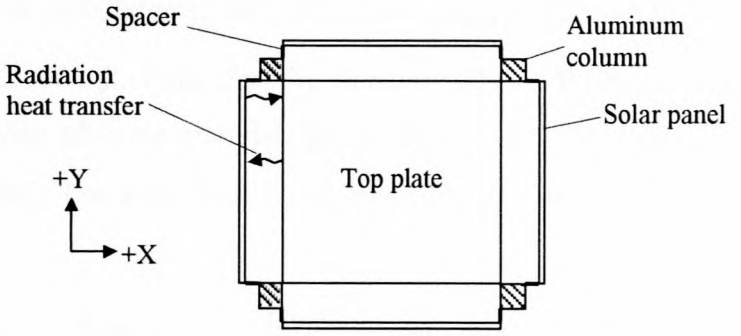

Figure 6.17 SUNSAT 3 top-view sketch

The model of an aluminum column with two spacers attached at the opposite corners and solar panels attached to the spacers is shown in figure 6.18 below.

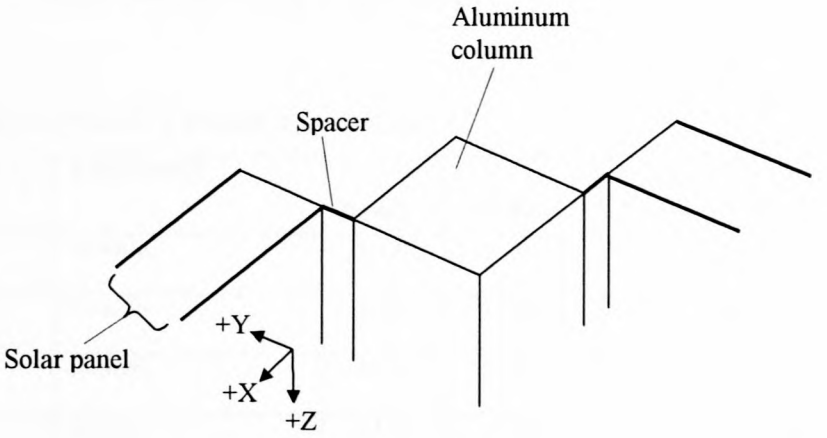

Figure 6.18 Model of SUNSAT 3 aluminum column, spacers and solar panels

The solar panels used in the SUNSAT 3 model are the same as for SUNSAT 2. The relevant heat loads are added to the 6 surfaces using the ORBIT-FLUX program. Each of the surfaces radiates to space. The details of the model properties are given in table 6.2. The densities are determined from the knowledge of the volume and mass, the specific heat values are estimated, and the thermal conductivities are calculated for the body sections.

To calculate the effective thermal conductivities for the body sections for each of the directions requires knowledge of the SUNSAT cross-sectional areas for the different directions so that the fraction of area that is aluminum and that which is essentially vacuum, can then be determined. Consider for example, the Y-direction in the middle-body section.

Stellenbosch University http://scholar.sun.ac.za

The middle-body consists of SUNSAT trays 7-10. Each "tray base plate" is approximately 2.2 mm thick, and 450 mm in width. The sides of each tray are also 2.2 mm thick. The summed height of the four trays is 150 mm. The total cross-sectional area of the aluminum in the Y-direction is calculated to be 0.00462 m^2 (A_{trays}) Aluminum 7075-T6 has a thermal conductivity of 121.25 W/mK (van der Westhuizen, 1995). What is required is the equivalent thermal conductivity of some material, for the SUNSAT 3 middle-body section. The SUNSAT 3 model middle-body has a cross-sectional area of 0.0675 m^2 ($A_{mod\ el}$, 0.45 m x 0.15 m). It follows then that

$$k_{eq} = \frac{A_{trays}}{A_{mod\ el}} k_{trays} = \frac{0.00462}{0.0675} 121.25 = 8.30 \text{ W/mK}$$

In a similar manner, the remaining equivalent thermal conductivities are determined. (**Note**: these thermal conductivities have been adjusted in the development of the SUNSAT 3 model and serve only as a benchmark.) All the properties are given in table 6.2. The results from the SUNSAT 3 model are presented in appendix F.

Table 6.2 SUNSAT 3 model information

TAS description	**TAS element/s**	ρ (kg/m^3)	c (J/kgK)	k_x, k_y, k_z (W/mK)	**Internal Heat Load (W)**	α (BOL)	ε (BOL)
Lower-body	16 bricks	571.55	300	5, 1, 5	4	-	-
Middle-body	16 bricks	470.12	400	5, 1, 5	4	-	-
Upper-body	16 bricks	470.12	500	5, 1, 5	4	-	-
Top-plate	16 bricks	2673.72	1000	5, 1, 5	-	-	-
Bottom-plate	16 bricks	720.16	300	30, 10, 30	18	-	-
Body surface coating	12 plates on each body ± Y, ± X surface	1420	1090	5	-	0.4	0.4
Aluminum column	3 bricks	2702	903	40, 40, 20	-	-	-
Spacer	3 plates	2702	903	121.15	-	-	-
Solar-panel	6 plates, carbon layer 6 bricks, honeycomb 6 plates, GaAs averaged	750 35 2300	1000 903 750	11, 11, 1 9.3, 1.16, 5.24 5	- - -	0.5 - 0.8	0.5 - 0.8
Kapton layer (2mil)	16 plates	1420	1090	0.12	-	0.41	0.73

Stellenbosch University http://scholar.sun.ac.za

7 THERMAL MANAGEMENT and CONTROL TECHNIQUES – A CASE STUDY

This chapter is aimed at showing how thermal control can influences the flow of heat, and thus the operating temperature of a system and its subsystems. An investigative approach is taken to illustrate the effect of thermal control hardware in managing temperature. Passive techniques such as thermal surface finishes and insulation will be investigated. The implication of an active method of thermal control, such as the use of heat pipes is also demonstrated in this chapter. The results are established and used in a case study that looks at a more defined thermal control scenario.

7.1 Defining the System

The focus is set on a system that comprises of a cubic box structure and an internal solid cubic block as shown in figure 7.1 below. The cubic box is 0.45 m in dimension and the cubic block is 0.15 m in dimension. A single external surface of the box is subjected to solar irradiation equivalent to 1353 W/m^2 and the block has internal heat generation. The ±Y and ±X external surfaces of the box radiate to a space environment. The sides of the cubic-box (plates) are labelled according to the co-ordinate system shown in figure 7.1. The +Y plate is the side that receives the irradiation. The block is centrally positioned inside the box and is in contact with the bottom (+Z) side of the cubic box.

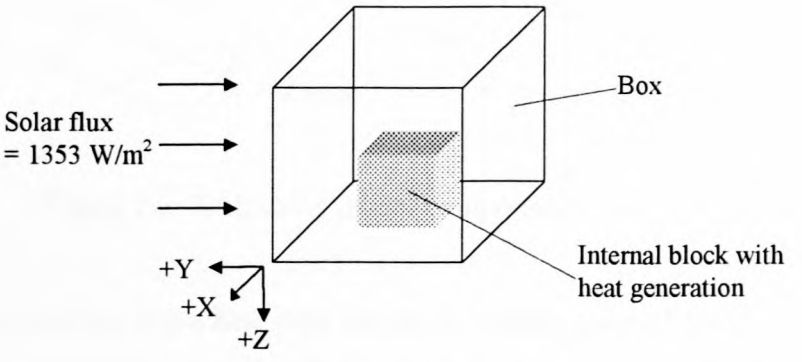

Figure 7.1 Cubic-model set-up

The material used for the box is aluminum 7075-T6, and the block is made up from some averaged material. The optical properties of the box internal and external surfaces as well as for the block surface is set as variables in the thermal analysis.

Stellenbosch University http://scholar.sun.ac.za

The model is generated and analyzed using TAS. Each of the 6 sides of the box are each made up of 9 TAS plate elements and the block is a single brick element. The properties of the box and block are given in table 7.1.

Table 7.1 Cubic-model property table

	Model Properties				
Model Components	**TAS Element/s**	**ρ (kg/m^3)**	**c (J/kgK)**	**k (W/mK)**	**Dimensions (m)**
+Z box plate	9 plates	2794.64	963.16	121.15	0.45 x 0.45 x 0.003
-Z box plate	9 plates	2794.64	963.16	121.15	0.45 x 0.45 x 0.003
+Y box plate	9 plates	2794.64	963.16	121.15	0.45 x 0.45 x 0.003
-Y box plate	9 plates	2794.64	963.16	121.15	0.45 x 0.45 x 0.003
+X box plate	9 plates	2794.64	963.16	121.15	0.45 x 0.45 x 0.003
-X box plate	9 plates	2794.64	963.16	121.15	0.45 x 0.45 x 0.003
Internal block	1 brick	1000	500	10	0.15 x 0.15 x 0.15

The block and +Z plate generated in TAS is illustrated in figure 7.2 on the left, and the –Z, ±X and ±Y plates are shown on the right. The –Y box surface can be expected to be the coldest since it is furthest from the heat sources. In practical space applications, a heat sink can be used to remove heat from components more effectively (than by conduction through the structure) by coupling the heat sink and the heat source with a heat pipe.

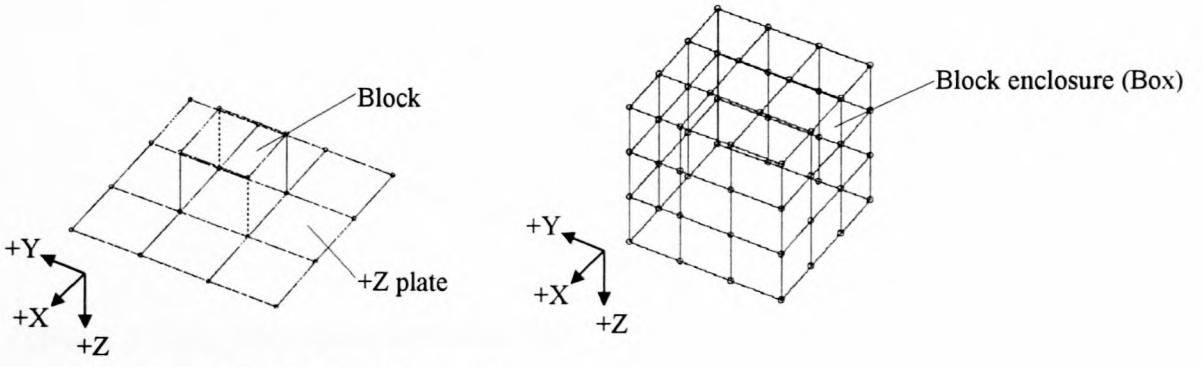

Figure 7.2 TAS cubic model components

To investigate the effect that a heat pipe has on the temperature of the block in the cubic-model, a second cubic-model is developed in TAS, which includes a heat pipe. A heat pipe is placed on top of the block and extends to the –Y surface as shown in figure 7.3. The heat pipe is constructed from three 2 mm thick TAS plate elements, and the material selected is aluminum (k = 237 W/mK, ρ = 2702 kg/m^3, c = 903 J/kgK, Mills, 1995). To simulate the effect that a heat pipe has in its ability to transfer heat with very low thermal resistance, convective heat transfer is included in the model.

Stellenbosch University http://scholar.sun.ac.za

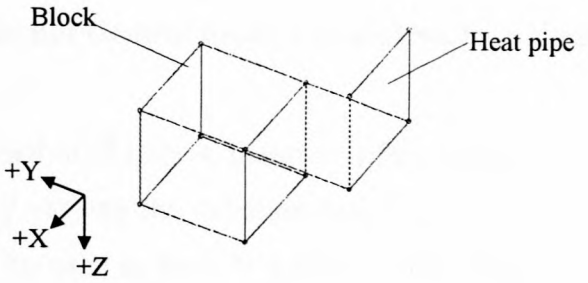

Figure 7.3 TAS cubic-model block with heat pipe

The temperature of the working fluid in a heat pipe can be approximated as being uniform throughout. Thus, a single node in TAS can represent the temperature of the heat pipe fluid. Conduction along the heat pipe wall is represented by the plate elements. The overall heat transfer coefficient through the heat pipe wall is approximated as 450 W/m^2K, as determined experimentally by Swanepoel (2001). The convection elements simulate the resistance of heat transfer into and out of the heat pipe, which has a single temperature. The TAS configuration for the heat pipe is shown in figure 7.4 below.

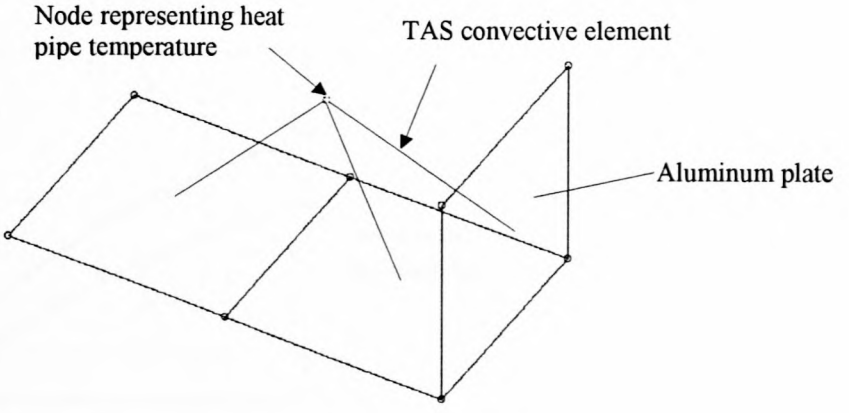

Figure 7.4 Heat pipe representation in TAS

The block is the subsystem under investigation in the thermal management and control of the cubic model system. For specific set conditions, the block will attain some average steady state temperature. By controlling these conditions, the block temperature can be thermally managed to attain the desired effect. The test results are tabulated in appendix H.

Stellenbosch University http://scholar.sun.ac.za

7.2 Thermal Control using Thermal Surface Finishes and Heat Pipes

As discussed in chapter 4, thermal surface finishes are a passive means of controlling the "flow" of heat, by varying the radiation heat transfer of the surfaces. An active technique such as heat pipes can be used to provide a low thermal resistance heat transfer path between a hot and cold area.

Tests 1 & 2

Consider the cubic-models with and without a heat pipe. The external solar irradiated surface of the box receives a heat load that is dependant on the solar absorptivity of the surface. By varying the solar absorptivity, the heat load is varied, and the sensitivity of the block temperature to the change in absorptivity can be established. The model with the heat pipe is analyzed in an identical manner and the effect of the heat pipe on reducing the block temperature is also established. The results are given in tables H1 and H2. The average block temperature is plotted against the box external solar absorptivity for the model with and without the heat pipe, as shown in figure 7.5 below.

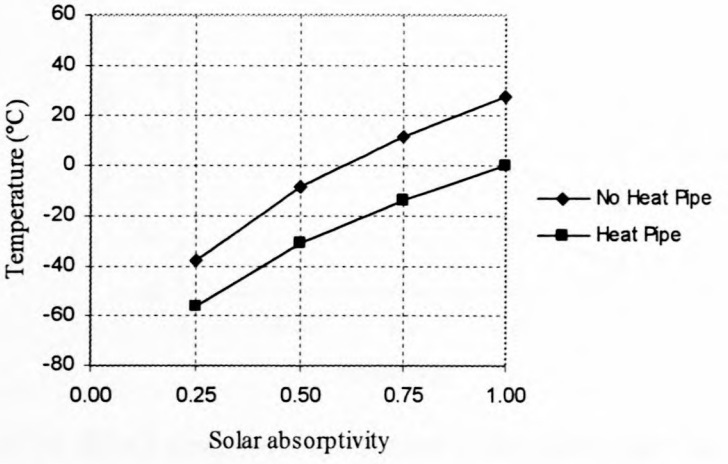

Figure 7.5 Block temperature variation with external surface solar absorptivity for cases with and without a heat pipe

The results show that the temperature of the block is very sensitive to the variation of the external surface solar absorptivity. The sensitivity is amplified by the fact that the system structure allows for a high rate of heat transfer by conduction. For this particular case, the internal surface of the box and the surface of the block were treated with Alodine.

Stellenbosch University http://scholar.sun.ac.za

This meant that the influence of radiation on the outcome of the results was very small. The responses are clearly non-linear. The results also show that the heat pipe necessitates the transfer of heat from the block to the radiator, and this results in a lower block temperature than for the case of no heat pipe. The effect of the heat pipe becomes more pronounced at higher temperatures.

Tests 3 & 4

In a similar manner as with the solar absorptivity, the external surface emissivity is varied and the effect of this variation on the system, and more particular the block, is established. The comparison for the TAS cubic-model with and without a heat pipe is also made. Note that in the previous case, the change in solar absorptivity only affected the irradiated surface while in this case; all the radiating surfaces are directly influenced. The results of the test are given in tables H3 and H4. The average block temperature is plotted against the external surface emissivity in figure 7.6 below.

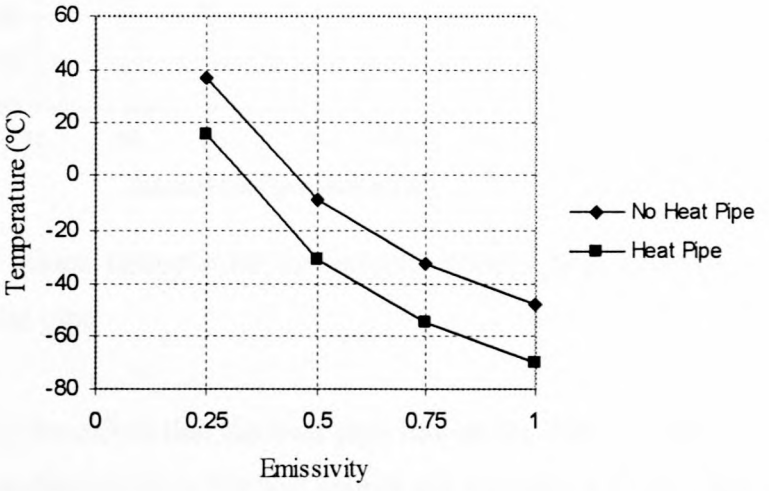

Figure 7.6 Block temperature variation with external surface emissivity for cases with and without a heat pipe

A high radiator emissivity significantly reduces the temperature of the block for the cubic-model with and without a heat pipe. The heat pipe is consistent with the results from tests 1 & 2 in that it allows for a higher rate of heat removal from the block. The effect of the heat pipe compared to none, is more significant at lower temperatures for this case.

Stellenbosch University http://scholar.sun.ac.za

Tests 5 & 6

The variation of the internal heat generation of the block could be attributed to different requirements of the block and its subsystems in some practical application. By varying the internal heat load of the block in the TAS models with and without a heat pipe, the effect of this on the temperature of the block can be established. These tests will show that by having the heat pipe at the source of heat, a more effective means of heat removal is possible. The structure does not play as big a role in the distributing the heat to the radiators, since the heat pipe is the lower thermal resistance path. The test results are given in tables H5 and H6. The block temperatures are plotted in figure 7.7.

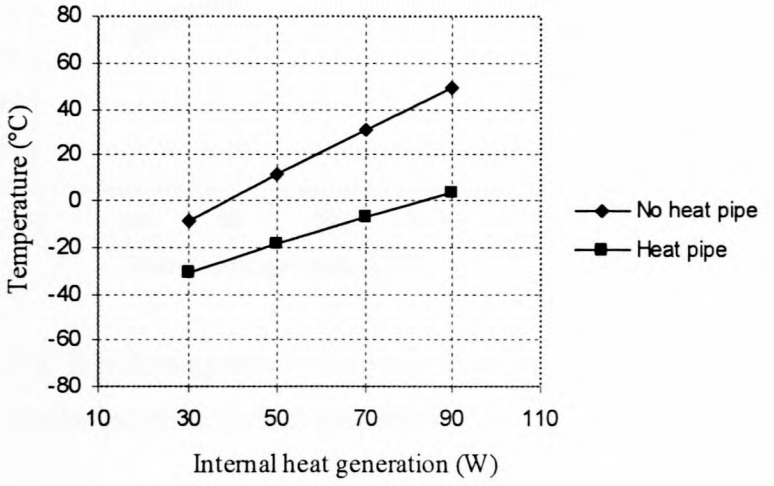

Figure 7.7 Block temperature for varying internal heat generation for cubic-model with and without a heat pipe.

As expected, the effect that the heat pipe has on the temperature of the block; is far greater if it removes heat directly from the heat source and transfers it to the radiator.

Tests 7, 8, 9 & 10

The internal surfaces are given various thermal surface finishes in order to establish the temperature affect of various combinations of infrared absorptivity and emissivity. In satellite applications, the selection of the correct coating can be significant in prolonging the life of specific components, since it ensures the temperature of the components does not exceed the design temperature range.

Stellenbosch University http://scholar.sun.ac.za

For the *first case* the block and box inside surfaces are treated with Alodine. For the *second case* the block and the box inside surfaces are coated with black paint (ε = 0.9, α_{IR} = 0.9). For the *third case*, the block surface is coated with black paint (ε = 0.9, α_{IR} = 0.9) and the box inside surface is treated with Alodine. For the *fourth case*, the block is treated with Alodine and the box inside surface is coated with black paint (ε = 0.9, α_{IR} = 0.9. The internal heat generation of the block is varied and the average block temperature recorded and plotted in figure 7.7 below. The results are given in tables H7, H8, H9, and H10.

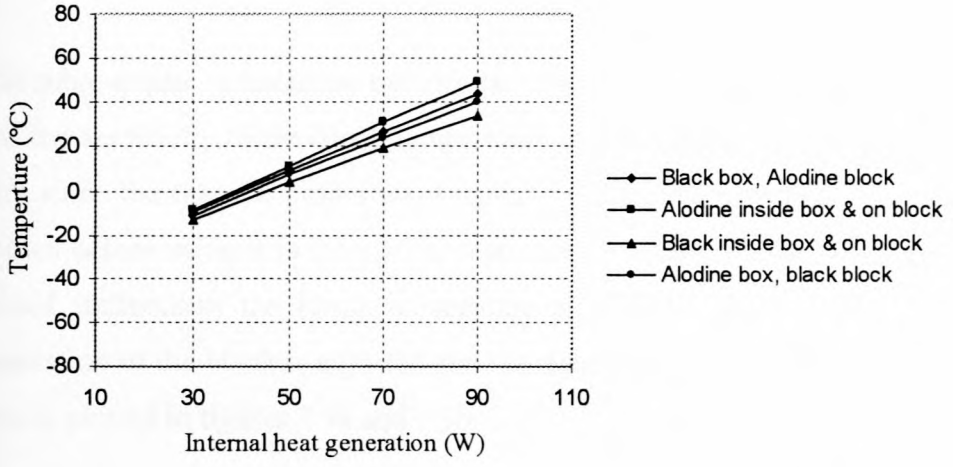

Figure 7.8 Block temperature for varying internal heat generation and for combinations of cube-model internal surface optical properties

The results show that for the first case, the block temperatures are the highest. Almost no radiation takes place since Alodine is a flat-reflector, and very little heat is absorbed or emitted. For the second case, the temperatures are the lowest. The black surface allows for heat sharing, and thus heat is radiated from the block and absorbed by the radiators and radiated to space. The third case results in temperatures in-between the previous two cases. The box shares heat with the surroundings and this enables a reduction in its temperature compared to the first case. The heat sharing is not that effective because the surroundings does not allow for effective heat sharing. For the fourth case, there is a slight reduction in the block temperature from the first case. This can be attributed to the fact that the block shares heat with the box, not by radiation, but because the box allows for heat sharing, which reduces the box temperature and thus improves the transfer of heat by conduction from the block to the box radiators. As the internal heat load increases, so the differences between the four cases become more pronounced. This is because, as the temperatures of the block increases with increasing heat load, so more heat is radiated at a rate proportional to the fourth power of the absolute temperature.

7.3 Thermal Control using Insulation Materials

For the cubic-model, a thin layer of insulation material was added to the base of the block, thus uncoupling the direct physical and thermal contact between the block and the box. In thermal management of satellites, it is often necessary to implement thermal control hardware that significantly reduces the transfer of heat by conduction, such as insulating materials, and MLI.

Tests 11 & 12

The cubic-model is tested for two insulation materials; rubber (Neoprene) and plastic (Phenolic), and the sensitivity of the block temperature to the materials is analysed. (MLI is not considered here since the thermal properties, such as the effective emittance, would need to be accurately known before using it in TAS.) The materials (see table 7.2) are used as 5mm sheets, which are placed underneath the block to separate it from the box. For each case the internal heat generation of the block is adjusted and the results are given in tables H11 and H12. The resulting data is plotted in figures 7.9a and 7.9b.

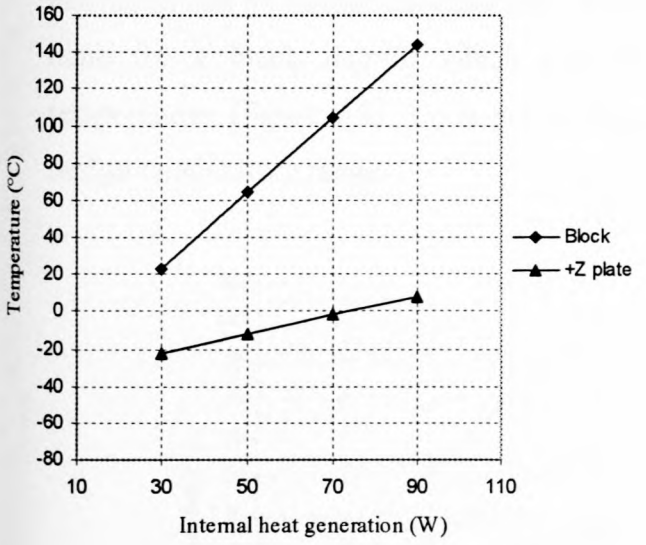

(a) Rubber (Neoprene) insulation

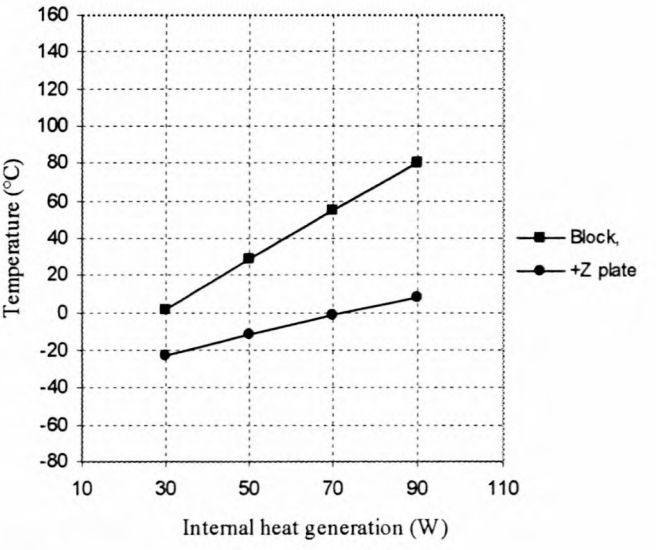

(b) Plastic (Phenolic) insulation

Figure 7.9 Block and +Z plate temperatures for varying internal heat generation, and for two different insulation materials

Table 7.2 Insulation material property table (Mills, 1995)

	Model Properties				
Model Components	**TAS Element/s**	**ρ (kg/m^3)**	**c (J/kgK)**	**k (W/mK)**	**Dimensions (m)**
Rubber insulation	1 brick	1250	1930	0.19	0.15 x 0.15 x 0.005
Plastic insulation	1 brick	1760	1260	0.50	0.15 x 0.15 x 0.005

The results from tests 11 and 12 show that the type of insulation material used plays a significant role in the temperature of the block. Since the dimensions are the same for both insulating sheets, the thermal conductivity is the property that affects the thermal resistance ($R = \frac{L}{kA}$) and ultimately the rate of heat transfer from the block. The resistance to heat transfer through the rubber sheet is 2.63 times greater than for the plastic sheet. The result of which is a considerably higher block temperature using the rubber. The average +Z plate temperature is also plotted in figure 7.9 to illustrate how effective the insulation is in reducing heat transfer to the +Z plate. Meaning, the gradient at which the block temperature increases compared to the +Z surface, is much larger. Figure 7.10 is a direct comparison of the case for rubber insulation, plastic insulation and no insulation (table H8). What may not be that apparent is that all these tests were done for a black interior which provides maximum heat sharing, and thus the lowest temperatures (figure 7.8), yet is not alone sufficient to keep the block temperature within the design temperature range.

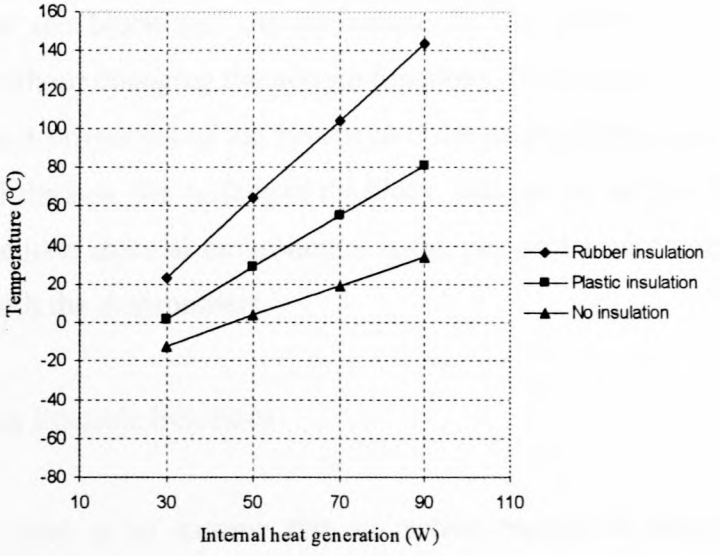

Figure 7.10 Block temperature direct comparison for different insulation materials, and also for the case without insulation

7.4 Numerical Example

Defining the Situation

Consider the case of the cubic-model with no heat pipe. Assume that the block consists of equipment critical to the operation of the system, and this equipment has a design operational temperature range of between 0 and 20 °C, and is sensitive to temperature gradients of 10 °C and greater across the block. The block at peak loads can generate 60 W of heat, and during normal operation 30 W. The external solar irradiation on the +Y surface is fixed at 1353 W/m^2. The external surface properties on the radiators (±Y and ±X external surfaces) are the same as that of some fictitious solar panels (α_{IR} = 0.8, ε = 0.8). The physical and thermal properties of the system are fixed, and are given by table 7.1. What thermal surface coatings on the inside of the box and on the block, would be sufficient to ensure the block operates within its design temperature range? Is it necessary to include insulation material, or possibly a heat pipe?

Two operating cases are considered. The "cold case" will be the operational mode for 30 W internal heat generation and the "hot case" for 60 W internal heat generation. The heat generation of the block is the thermal design driver for this problem since it requires the focus of the thermal management techniques. The external surface finish is determined by the need for solar panels to provide the system with power, and can thus not be influenced by the TCS. The "zone" of influence from a thermal management perspective, is inside the box. This includes the box internal surfaces, and the block. The blocks physical properties cannot be altered, only the surface of the block and the immediate (inside the cube-model) block environment can be altered, without changing the system functions. In summary, the thermal management is focused at altering 3 properties of the system in order to attain the desired block temperatures: the inside surface of the box, the surface of the block, and the immediate thermal environment of the block. The immediate thermal environment is the physical environment that sets the block in thermal contact with the environment.

Generating Possible Solutions

The first step is to assume that no active control is required, that is to say, the desired temperatures can be attained just by using thermal surface finishes or insulation material.

This is usually the first assumption in satellite thermal design, unless the system has significant internal heat generation or very stringent operating temperature limits, in which case, active control is considered from the beginning.

An initial assumption about the internal surface coatings needs to be made and the resultant temperatures determined. Therefore, it is assumed that all the internal surfaces are coated with a black paint ($\varepsilon = 0.9$, $\alpha_{IR} = 0.9$). The model is tested for the cold and hot case. The resulting block temperatures are summarised in table 7.3 below.

Table 7.3 Block temperature using a black interior thermal surface finish

	Block Temperatures (°C)		
Case	Maximum	Minimum	Average
Hot	12.27	-7.16	3.72
Cold	-12.56	-25.62	-17.89

The cold case temperature falls outside the desired temperature range, and the hot case is in the desired range. The gradient across the block is also too large. The temperatures are too low and need to be increased. As shown earlier, Alodine results in higher temperatures of the block than black paint. After applying Alodine to the inside of the cubic-model, the model is tested for the hot and cold cases. The resulting block temperatures are given in table 7.4.

Table 7.4 Block temperature using Alodine as an interior thermal surface finish

	Block Temperatures (°C)		
Case	Maximum	Minimum	Average
Hot	22.79	-1.36	12.05
Cold	-8.57	-23.74	-14.74

Although the temperatures did increase using the Alodine as an interior thermal surface finish, the cold case still results in too low a temperature. The conclusion of these results is that standard thermal surface finishes is not sufficient for thermal control of the block subsystem. The temperature gradients are also *too* high.

A New Plan of Action

The block loses too much heat by conduction through the block and into the structure. To alleviate this problem, it is decided to use insulation material under the block.

From the tests done previously, it was clear that the selection of the correct material with the right thermal conductivity is critical. It may be expected that the temperature of the block can be increased using insulation, but it may also be too high.

For this reason, the black paint is initially used to allow for better heat sharing and may be able to alleviate the expected higher temperatures. Through trial and error, an insulation material conductivity is selected so as to ensure that the cold case is at the lower end of the temperature range (0 °C). The deciding factor is the thermal conductivity, and it was set at 0.39 W/mK. The results are tabulated below. (Insulation material thickness is not adjusted since this would require a new TAS model.)

Table 7.5 Block temperature using black paint as an interior thermal surface finish, and insulation of some averaged material

	Block Temperatures (°C)		
Case	Maximum	Minimum	Average
Hot	50.96	30.20	41.08
Cold	5.48	-6.06	0.24

The results show that the insulation material results in too high a block temperature for the hot case. The sensitivity of such a system to small changes in block internal heat generation was illustrated in figure 7.9 and is again noted here. A point that should be mentioned is that in the selection of the insulation material, it may be difficult to obtain a non-standard material with a specific thermal conductivity of 0.39 W/mK. Since a thermal conductivity 0.39 W/mK is closer to that of plastic than rubber, the non-standard insulation material in the model is replaced with plastic. (Another alternative would be to vary the thickness of the plastic or rubber insulation, which has a direct influence on the thermal resistance; but this requires a new model to be generated.)

The black interior is still used, even though it is expected to lower the cold case below the lower end of the range. The idea is to get the average block temperature difference between the cold and hot case lower than before, and then adjust the thermal surface finish to increase the temperatures as required. The model is tested for the plastic insulation and black interior, and the results are summarized in table 7.6.

Table 7.6 Block temperature using black paint as an interior thermal surface finish, and plastic insulation

	Block Temperatures (°C)		
Case	Maximum	Minimum	Average
Hot	43.77	22.72	33.82
Cold	1.93	-9.91	-3.39

The difference between the block temperature for the hot and cold case is lower than before, but the hot case is still too high. It would appear that thermal surface finishes are not sufficient to alleviate the problem of over-heating with insulation. A decision to include a heat pipe is made.

An Active Solution

The heat pipe will provide the block with a thermal path to remove excess heat from overheating as well as reduce temperature gradients. The heat pipe needs to be attached to a surface whose average temperature is similar to that of the block requirements. The temperatures of the box plates are listed below for the previous test.

Table 7.7 Box plate temperatures using black paint as an interior thermal surface finish, and plastic insulation

	Temperatures, hot case (°C)			Temperatures, cold case (°C)		
Component	Maximum	Minimum	Average	Maximum	Minimum	Average
+Z box plate	5.47	-38.50	-15.28	-4.74	-48.59	-28.15
-Z box plate	-5.59	-47.79	-30.80	-10.25	-53.69	-36.26
+Y box plate	8.80	-14.51	**-3.35**	2.81	-19.23	**-9.55**
-Y box plate	-33.22	-51.00	-45.17	-45.30	-57.55	-53.05
+X box plate	-6.75	-50.21	-30.63	-14.82	-56.52	-37.79
-X box plate	-6.80	-50.13	-30.61	-14.72	-46.46	-37.78

The only plate that has a temperature high enough and close enough to the block requirements is the +Y box plate. The heat pipe is thus attached (in similar fashion as to that shown in figure 7.3) to the block and connected to the +Y box plate. The heat pipe is identical to the one used in the tests H2, H4 and H6. The model with the plastic insulation and the heat pipe is tested, and the results given in table 7.8.

Table 7.8 Box plate temperatures using black paint as an interior thermal surface finish, plastic insulation, and a heat pipe

	Block Temperatures (°C)		
Case	Maximum	Minimum	Average
Hot	13.69	5.50	10.33
Cold	1.09	-9.85	-3.58

With the inclusion of the heat pipe, the hot and cold case temperatures have stabilized around the desired range, and the gradients are far less than before. The cold case average block temperature is still just outside the desired range. In an attempt to increase the hot and cold case temperatures, the rubber insulation is reintroduced into the model to replace the plastic insulation. The new model is tested, and the results given in table 7.9.

Table 7.9 Box plate temperatures using black paint as an interior thermal surface finish, rubber insulation, and a heat pipe

	Block Temperatures (°C)		
Case	Maximum	Minimum	Average
Hot	18.73	16.93	17.65
Cold	4.09	-1.1	1.92

The results show that all the thermal design requirements are satisfied for the particular system under investigation. The average temperatures are within the 0 to 20 °C range, and the gradient is at most 5.19 °C for the cold case.

7.5 Case Study Results and Conclusions

The effect of altering the external surface solar absorptivity was shown to result in large changes in the block temperature. An increase in the solar absorptivity caused an increase in the temperatures of the system. The effect of altering the external surface emissivity was also significant in changing the systems temperatures. The emitting power of the radiators is directly proportional to the surface emissivity, and to the temperature in Kelvin to the fourth power. By increasing the emissivity, more heat was allowed to emit to space. The change in the block temperature with emissivity (as shown in figure 7.6) was initially high and then gradually decreased as the emissivity increased.

The results from the tests H1 through to H12 for the cubic-model, helped to illustrate the effect of thermal surface finishes, insulation materials, and heat pipes, on a systems thermal behaviour to thermal control mechanisms. The system analysed in this chapter served only to illustrate the concept of thermal management using the correct thermal control techniques. This is a direct result of lowering the emissive power by lowering the temperature of the radiator, by increasing the emissivity.

The tests with the heat pipe showed that removing heat from the heat source, and transferring it through the heat pipe directly to the radiator lowered the overall temperatures of the block and the box sub-systems. In other words, a heat pipe is able to transfer heat from a hot area to a cold area with minimum thermal resistance.

The changes made to the internal surface did not result in significantly large variations in the block temperature for a specific heat load. This was largely due to the fact that the high conductive path through the structure allowed for most of the heat to be transferred at low thermal resistance. What was however apparent was that the black interior thermal surface coating, gave the lowest temperatures and reduced temperature gradients. This is due to the high rate of heat sharing induced by the high infrared absorptivity and emissivity of the surfaces. As the internal heat loads increased, and the temperatures increased, so the effect of the surface coating became more evident. The flat-reflector surface such as Alodine has the opposite effect: low heat sharing because of the low infrared absorptivity and emissivity, and essentially suppressing the effect of radiative heat transfer. With Alodine, the system distributes heat internally mainly by conduction. The other tests on internal surfaces involved combinations of black and Alodine thermal surface finishes, and these showed results that fell between the cases for just black or just Alodine thermal surface finish.

The insulation material tests showed that the effect of insulation is to thermally isolate a subsystem from the immediate system. If managed correctly, this can provide more predictability in the thermal design, since there are fewer factors influencing the temperatures of the subsystem. What was shown in the tests is that if a subsystem with internal heat generation is being isolated from the system, high temperatures can be a problem. It was also shown that the change in the block temperature was sensitive to the change in internal heat generation. This sensitivity is far greater when the block is thermally isolated from the environment.

8 DISCUSSIONS and CONCLUSIONS

The thesis, "Thermal Management and Control of Space Satellite Systems and Subsystems in Orbit", presented the background theory, the thermal management philosophy and thermal control methods, the thermal modelling techniques, and the hardware requirements necessary to manage and control the temperatures of the systems and subsystems of a satellite in orbit.

The background research gave an introduction into the philosophy behind the thermal management of satellites and the role of thermal control in ensuring the satellite subsystems operate within their design temperature ranges. The background research also provided information about the environment of the satellite and the role of each significant form of heating experienced by the satellite in orbit as well as an introduction into heat transfer.

SUNSAT was used as an example for illustrating thermal management and control practices through the thermal modelling of SUNSAT for two particular orbits. Before this could be done, the SUNSAT mission and subsystem makeup were briefly highlighted and discussed in the thesis, with emphasis placed on the physical structure of SUNSAT, the possible orbit paths, the internal heat generation and the total environmental heat loads on each of the six surfaces. These environmental heat loads were determined using the computer program "ORBIT-FLUX", for known thermal and physical surface properties as well as the orientation of the satellite in space relative to the sun and the earth. The two orbit paths that could be used in the ORBIT-FLUX program were approximations of possible SUNSAT orbits for July 1999 and June 2000. (The validity of the computer program ORBIT-FLUX is established in tandem with the validity of the final thermal model of SUNSAT.)

Data that was retrieved from the ESL ground station was extrapolated and presented in the thesis. Of the 35 temperature sensors that were used, only several were operational. The centre solar panel sensors, the bottom-plate sensor, and battery sensors gave the most consistent data. Data from these sensors were not always reading data, due to power regulation requirements. During the period of high battery temperature until battery failure (May 2000 to February 2001), most of the temperature sensor data was erratic and the frequency of readings too low. The accuracy of the temperature readings was limited by the analogue-to-digital converter, which could only handle temperature changes of 0.5°C.

The thermistor sensors used on the solar panels, did not allow for measurement of below –30°C as the reading became saturated, and this limited the minimum temperature reading.

Both the resistance-capacitance numerical method for generating in-house programs and an outsourced software program TAS were used for the thermal modelling of SUNSAT. The TAS software provided a means of generating more complex thermal models as the modelling became more detailed with the knowledge of SUNSAT and also that of TAS. For both the numerical and TAS modelling, the resistance-capacitance formulation method was used. The first models were for SUNSAT modelled as 7 lumped-masses. This model served as a means to compare the numerical theory applied to a computer program, with the outsourced program TAS, and did not serve to accurately model SUNSAT. The ORBIT-FLUX computer program was used to determine the heat loads on the top and bottom plates of the satellite model. It was assumed for this model that the four sides were made of insulation material and thus no heat transfer was possible through the sides of the model. (At this point in time in the thesis, it was understood that the solar panels acted as thermal barriers between the SUNSAT body and space, and for this reason assumed so in the SUNSAT 7 lumped-mass model.) The results of the numerical and TAS models showed good correlation (see figures 5.8 and 5.9) for two specific tests. For each case, the temperatures of the batteries at dynamic thermal equilibrium (thermal equilibrium repeated for each successive orbit) were within 3°C of each other. The difference in the results can be possibly attributed to the radiation heat transfer approximations made for the numerical model, as well as the number of control volumes used for the TAS model was significantly higher. Based on the results attained, a confidence in the TAS software use and results was gained. Although the results have little value in the modelling of SUNSAT because of the many approximations made, it did show that the effect of adjusting the solar absorptance of a satellite surface by 0.2 (from $\alpha = 0.5$ to $\alpha = 0.7$) can significantly change the temperature of the satellite subsystems.

The next model of SUNSAT, the lumped-mass model, was numerically modelled as well as with TAS. This model allowed for the interaction of each of the six sides of the satellite with the environment. The results showed a significant difference between the numerical and the TAS models. This was expected because of the higher number of control volumes of the TAS model which resulted in a difference in the temperatures of the emitting surfaces. The surface properties used were not identical to SUNSAT's due to limited information at that point in time, and therefore the results did not represent SUNSAT accurately.

It can be accepted that the TAS model gave the better results because of the higher detail (more control volumes) of the TAS model compared to the numerical model. The models were tested and the results presented in appendix E (tables E1 to E4, and figures E1 to E8) for the polar sun-synchronous orbit of beta-angle = 0°. The results showed that the effect of lowering the surface emissivity of all the outside surfaces from 0.8 to 0.6 resulted in a significant change in the temperature of the TAS lumped-mass model equivalent to ± 18 °C (from –3.42 to 14.49°C). The higher the emissivity, the lower the lumped-mass temperature and visa versa. The change in internal heat generation from 30 to 80 W resulted in a change in the TAS lumped-mass model temperature from –3.42 to 6.61°C (± 10°C). It can be concluded that although the results showed good consistency with the changes in surface property and internal heat generation, the lumped-mass model is still not an accurate physical representation of SUNSAT. For this reason, a TAS SUNSAT 2 model was generated.

The TAS SUNSAT 2 model was a better representation of the physical structure of SUNSAT since the model included more control volumes as well as an averaged solar panel structure. The control volumes were generated based on the physical structure and were divided and labelled according to the SUNSAT subsystems they represented. Physical elements of the model that could be associated with included: the bottom-plate, the battery, middle-body section, upper-body section, top-plate section and the four solar panels. The reason for the averaged solar panels was due to a limitation identified in TAS. The TAS software does not support multiple (more than two) plate element construction at common nodes, or two plates or more constructed on a brick element. This causes errors in the output results as well as a significantly longer solving time. The solar panels used in the model were attached to the body of the satellite model by means of some insulation material. This was intended to reduce the flow of heat in and out of the satellite body. (At this point in time, an understanding of how the solar panels were attached to the body was limited.). The model was run and the results presented in appendix F (table F1, and figures F1 to F10) for the polar sun-synchronous orbit of beta-angle = 0°. What was evident from the results was that the thin layer of insulation material had little effect on reducing the flow of heat to and from the satellite body. The result of which is that the solar panel temperatures did not fluctuate significantly with the varying environmental heat loads. The solar panel temperatures averaged around 3°C, and the body temperature was highest at the +Z surface (average = 5.05°C), lowest at the –Z surface (average = 3.3°C), with the battery temperature in-between (average = 4.04°C). The gradient in temperature through the body can be concluded to be due to the heating of the amplifiers in the bottom-plate, as well as the batteries.

The results also showed that the +Z surface did not easily allow for heat removal, and thus did not act as a "radiator". This was due to the low emitting properties of the Alodine-treated +Z surface.

In conclusion of the TAS SUNSAT 2 model: the solar panel attachment method was not a proper representation of how the solar panels on SUNSAT were attached. The result of the model was that the solar panels temperature did not rise and fall as quickly or by as much as expected (comparing to actual SUNSAT data). Another effect of this was that the internal heat as well as heat from the environment passed easily through the interface between the body and the solar panels and then was radiated to space, thus resulting in lower satellite body temperatures than expected. For the next model, SUNSAT 3, a better approximation of the solar panel/body interface was initiated.

The TAS SUNSAT 3 model was based on the SUNSAT 2 model with a few important adjustments. The number of control volumes of the body was increased to create a more realistic representation of the batteries, and improve the accuracy of the model. The solar panels on the model were mounted to the satellite body with thin TAS plate elements that represented the equivalent cross-sectional area of the M4 bolts used on SUNSAT. The result of which was that the flow of heat from the body and space would be lower and the body temperatures higher. These expectations were verified by the results given in appendix F (tables F2 to F5, and figures F11 to F50). The model was run for two specific orbits that corresponded approximately to the SUNSAT mission for two specific periods in SUNSAT's life: a polar sun-synchronous orbit for a beta-angle = 0° (July 1999) and beta-angle = 90° (June 2000). The results for the case of beta-angle = 0° showed that the temperature responses for the model solar panels correlated well to actual SUNSAT data. The only significant deviation was for the saturation of the SUNSAT data at –30°C. The results for the body of the satellite showed good consistency with the expected temperature gradient from the bottom to the top. The average battery temperature for the various test runs varied around 28°C. The actual battery temperature for SUNSAT averaged around 20°C. For the case of the orbit with beta-angle = 90°, the results from the model correlated well to the actual data for the battery temperature (36°C) but poorly for the solar panel temperatures.

The significant difference in the solar panel temperatures can be attributed to the fact that the orbit of SUNSAT during June 2000 did have a partial eclipse, yet the model could not include the effect of this partial eclipse using the ORBIT-FLUX program; and was run for a close approximation at full sunlight conditions.

The software Nova that tracks objects in space established this initial estimation of full sunlight conditions in June 2000. A discrepancy between SUNSAT data and the Nova results exists, and the reason is unknown. One would have to believe that the data is correct and an error in the Nova software occurred. This limitation of the ORBIT-FLUX program hindered the accuracy of the TAS SUNSAT 3 model.

The modeling of SUNSAT was a process of evolution, from the most basic thermal model, to a more detailed one that gave a good representation of SUNSAT. The process of modeling change was driven by the actual SUNSAT data, which provided a goal post to aim for. This goal could not have been achieved without an established software program such as TAS. TAS enabled a model to be generated that not only resembled the physical size and properties of SUNSAT, but also included modeling (bulk models) of subsystems such as the batteries, solar panels etc.

Limitations on how complex the final TAS SUNSAT model could be was dictated by the number of control volumes which influenced the computational time; as well as the detailed knowledge of the physical and property make-up of all the SUNSAT subsystem components. For this reason, averaged lumped masses (brick and plate elements in TAS) were used to represent subsystems and there components. The problem associated with this approach is that the properties such as specific heat, and thermal conductivity used for the model, were not an exact representation of the SUNSAT properties. For a satellite in orbit, the dynamic thermal equilibrium that it achieves is dependent on these properties, which makes their selection crucial.

The orbit approximations that were made for the ORBIT-FLUX computer program carried a heavy weighting on the results of all the models. This is because the temperature of the satellite and its subsystems are very dependant on the radiation heat transfer between the outer surfaces of the satellite and the space environment, which depends on the position of the satellite in space relative to the sun and the earth. The orbit approximation for SUNSAT in maximum eclipse (beta-angle = 0°), gave the most accurate solar panel temperature results for the SUNSAT 3 model; which shows that the heat loads determined using the ORBIT-FLUX program were fairly accurate. For the other orbit approximation (beta-angle = 90°), the ORBIT-FLUX program could not model the SUNSAT orbit accurately enough. For this orbit condition to be modeled correctly, a more advanced program would be necessary. Possibly the use of an established program for determining the heating on the satellite surface for defined orbit parameters could be used.

Such a program is currently in use for a new satellite under development at the company SUNSpace in Stellenbosch. "Nevada" is used to determine the heat fluxes on a satellite for complex orbits.

Is TAS a sufficient thermal program for modeling satellites in orbit? Although it is possible to generate fairly detailed models of satellites using TAS, there is a limit to how much detail is possible because of computer processing time required to model detailed models. A balance between model detail and time available needs to be achieved according to the requirements of the project. A significant limitation of TAS is that the program is not designed for detailed modeling of satellites in orbit. The heat fluxes for the TAS SUNSAT 3 model needed to be determined using the numerical program ORBIT-FLUX. A possible solution to the problem would be the future use of a recognized satellite-modeling program such as "SindaG", which is used extensively by the space industry (and by SUNSpace) in conjunction with Nevada (a built in interface) to develop detailed models of satellites.

The case study on thermal management and control presented in the thesis, gives valuable insight into the use of hardware to passively and actively control the temperatures of a system, and its subsystems. Using TAS, a simple case-study model was developed, tested and analyzed for various combinations of thermal surface properties, of insulation materials, and the use of a heat pipe. The results showed that the temperature of the block inside the box was very sensitive to changes in the solar absorptivity and the emissivity of the external surfaces. This shows how important it is to select the correct surface properties for the outer radiating surfaces of a satellite.

The effect of surface property degradation due to the space environment needs to be carefully considered and the EOL properties designed for. A heat pipe was also added to the system to remove heat generated internally (by the block) by providing the heat with a low thermal resistance path to the space radiator. The result of the inclusion of a heat pipe was a decrease in the temperature of the block. This effect of decreased temperature also perpetuated throughout the other components of the system. For this particular example, the radiator to which the heat pipe was attached, did not receive any environmental heating and was thus at the lowest temperature of the system. Such a situation in a space application might not be suitable, since the radiator might receive solar radiation, heat up, and reverse the role of the heat pipe, i.e. take heat to the block. Considering diode heat pipes might alleviate this problem.

Various combinations of surface coatings were used to alter the distribution of internal heating by radiation. It can be concluded that black paint on the interior surfaces aids in the redistribution of internal heat, and thus reduces hot spots. The temperature of the block was the lowest for this case. For the case of all the interior surfaces treated with Alodine, the temperature of the block was the highest. The effect of the low emitting and absorbing surfaces is to lower the heat sharing, and thus limit the flow of heat out of the system and into space. With increasing internal heat generation, the effect of black paint in heat sharing becomes more pronounced.

The effect of insulation materials such as rubber (Neoprene) and plastic (Phenolic) was investigated and the effect thereof on the system and subsystems established. It was found that insulation material thermally isolated a subsystem from the immediate system and gave more predictability in thermal control of a subsystem because there are fewer influencing factors. For a possible satellite application, insulation might be used to thermally insulate a tray from the other trays and the rest of the satellite, and a refrigerator used to remove the necessary excess heat generated by the subsystem.

In closure, it can be said that the thermal management of satellites in orbit requires detailed knowledge of a satellite system and subsystems and their workings, and the satellite environment. To manage and control the temperatures of a satellite requires the additional knowledge of heat transfer theory as well as the attributes and limitations of thermal control hardware.

9 RECOMMENDATIONS

The thermal management and control for the SUNSAT microsatellite was limited in the fact that no thorough thermal management system was set in place in the design process, and this limited the thermal control system. The selection of passive thermal control was the correct one, if one considers the fact that SUNSAT was a LEO microsatellite and had low internal heating. But based on the findings in this thesis, more detailed consideration could have been given to the selection of the passive thermal control hardware or possibly even the use of heat pipes to reduce the overheating of the batteries. Note that even in the "cooler" period of SUNSAT's life, the batteries were still operating at the upper design range for NiCd batteries (±20°C). One noticeable problem from the thermal design was the fact that the amplifiers, which have the highest heat generation, were placed in the bottom-plate to allow for the heat to be emitted by the +Z surface; yet this surface was treated with Alodine, which has a very low BOL emittance (0.15). The result was high bottom-plate temperatures, and because this plate was just below the battery tray (tray 11), the battery was also a little warmer than it should have been. Possibly another type of thermal surface finish with a higher emissivity should have been used on the +Z surface that faced earth. Based on the findings in the thermal management and control case study, it may have been better to coat the inside of the bottom-plate and the amplifiers, and the inside of tray 11 with black paint, to improve heat sharing and thus lower the temperature of the batteries.

Another solution to the overheating battery would have been the use of heat pipes to remove excess heat from the battery to an area of the satellite that was on average cooler than the battery. Diode heat pipes could have been attached from the battery to the solar panels, and thus when the solar panel temperature dropped below that of the battery for some period of time, heat could be removed from the battery. The correct sizing of the heat pipes would be required to insure the battery does not get too cold.

Based on the thermal modelling done in this thesis as well as the extrapolation and interpretation of SUNSAT data, it would appear that the positioning, the monitoring, and the type of temperature sensors used on satellites, plays a critical role in the understanding of how heat is distributed and flows throughout the satellite structure. All the components of the respective satellite subsystems critical to the outcome of the mission need to be constantly monitored by temperature sensors, to ensure their thermal health.

Considering SUNSAT as an example. The temperature sensors for tray 11 should have been placed on the base-plate of the tray to monitor the temperature gradients across the plate and from this the actual heat transferred to and from the battery and the camera. The information gained from this data could have helped to determine if the net flow of heat was from the bottom-plate (with the amplifiers), from the solar panels, or from tray 10 (tray above tray 11). It can be recommended that each of the trays of SUNSAT should have had sensors on each tray base-plate corner as well as in the centre. Components sensitive to thermal gradients and large components, such as the camera, batteries, reaction wheels etc, should have more than a single temperature sensor to measure temperature gradients and give an indication of the *true* average temperature of the component. The positioning of the temperature sensors in the solar panels under the kapton layer was appropriate for measuring the solar panels temperature, but the number of sensors as well as the position should be re-considered for future satellites. Five sensors positioned on each of the corners as well as in the centre of the solar panels should be used. This will highlight thermal gradients that might exist across the solar panels. It is recommended that temperature sensors that are able to read as low as –45°C should be used on the solar panels in the future.

The thermal modelling using TAS provided the means to generate moderately detailed models of SUNSAT, but was limited in the fact that the heat loads needed to first be determined from another numerical program that was limited to only two specific orbit paths. Another possible limitation of TAS from a confidence perspective would be that it is not intensively used by the space industry, which places its accreditation under scrutiny. It is recommended that a more advanced and well-established thermal modelling program such as SindaG, in conjunction with the built-in orbital-heating program Nevada, be used for future thermal analysis of satellites in orbit. For other thermal management scenarios such as during ground operations, pre-launch, and launch, TAS could possibly be used to thermally model the satellite and its various subsystems.

Recommendations for future projects or theses that may follow on from this thesis, would be that a more detailed investigation into determining the optical surface properties of thermal surface finishes, and the implications thereof on satellite thermal performance be made. This recommendation is substantiated by the importance of thermal optical properties in passively controlling the temperatures of LEO satellites.

Appendix A: Honeycomb Thermal Analysis

Honeycomb composites of various types are commonly used on satellites as solar-array substrates. Due to its construction, honeycomb has directionally dependant conductivities. The thermal conductivities are presented in this appendix for each of the three directions for a general hexagonal structure. An effective thermal conductivity will be established for each. It will be shown in the analysis that follows that the effect of radiative heat transfer is negligibly small in comparison to conductive heat transfer through the honeycomb material for all three directions. It should be noted that this analysis deals exclusively with the core material and does not in any way include the face-sheets that will be bonded to the core.

Consider the sketch of a typical honeycomb structure below. The figure gives the general dimensions of a typical honeycomb structure. Three conductive heat transfer paths are shown: two in the honeycomb panel (paths 1-2 and *a*-*b*) and one perpendicular to it (path *i*-*ii*).

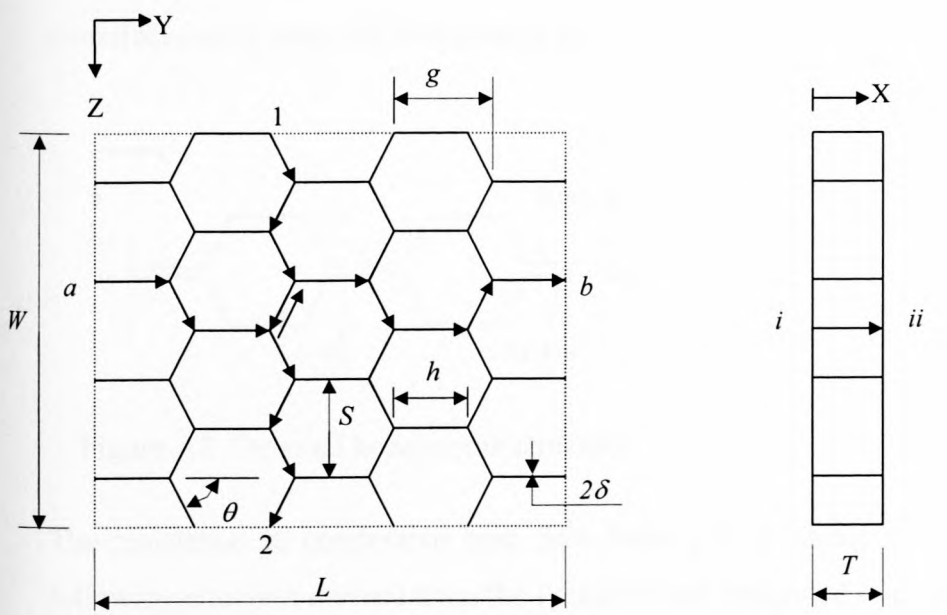

Figure A1 Honeycomb structure and conductive heat transfer paths

The heat transfer rate through the honeycomb by conduction is given by equation A1 as

$$\dot{Q} = \frac{\Delta T}{R} \tag{A1}$$

For the case of heat transfer between two sides of the honeycomb for each dimension, the temperatures of the sides will typically be known and assumed to be uniform along the length of the side. But what won't be known is how the heat is being transferred to the opposite side. In other words how easily is the heat being transferred and which is the dominant mode of heat transfer.

The role that conduction and radiation play in the transfer of heat through the honeycomb and just how significant this role is, will be established later in this appendix. First of all however, the equivalent thermal conductivity for each of the directions needs to be determined.

Conduction in the Y-direction

The path for conduction in the Y-direction is shown in figure A1 as path *a*-*b*. There are two possible conduction paths from *a* to *b*, but only the one is shown in figure A1. Each of these paths is along a section of the structure that forms a "ribbon". Figure A2 below shows two ribbons that are of equal thickness δ. The common sides of the ribbons are pressed together when manufactured to form the honeycomb structure.

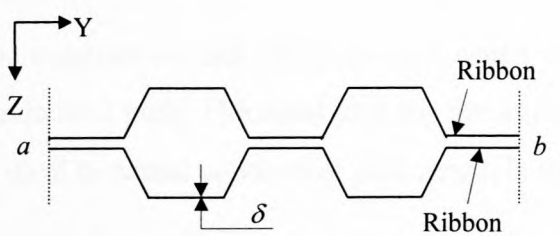

Figure A2 Detailed honeycomb structure

The resistance to conductive heat flow from *a* to *b* along a single ribbon, is given by the following equation derived from the Fourier's law integrated over the length *x*

$$R_{ab} = \frac{x}{kA} \tag{A2}$$

Where *x* is the total length of the ribbon, *A* is the cross-sectional area of the ribbon and *k* is the thermal conductivity of the ribbon material.

The area and total length are defined as

$$A = \delta T \tag{A3}$$

$$x = \eta L \tag{A4}$$

where η is the extension factor.

The extension factor is used to bring into account the extra distance of the conductive path in the Y-direction due to the angle θ relative to the ideal path direction (the Y-direction). Consider the detail of a single cell with sides of length h.

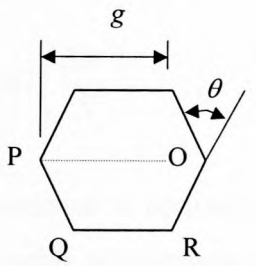

Figure A3 Single honeycomb cell details

The length g shown in the figure is common to every cell and is determined by the following equation

$$g = h + h\cos\theta \tag{A5}$$

The conductive path along the cell wall P-Q-R is equivalent in length to 2h. This is the actual conductive path. The ideal path for the same Y-direction would be P-O of length g. The fraction of ideal to actual conductive path length is the extension factor η, and is given as

$$\eta = \frac{2h}{h + h\cos\theta} = \frac{2}{1 + \cos\theta} \tag{A6}$$

It follows after substitution of equation A3 and A4 into equation A2 that

$$R_{ab} = \frac{\eta L}{k\delta T} \tag{A7}$$

Now for n number of ribbons in the Y-direction, we assume that the net heat interchange between ribbons is negligible for this directional calculation. This is to say that the heat flow rate is combined in common conduction paths and then equally divided at branches.

Then based on this assumption, the number of ribbons or conduction paths, n, in the Y-direction can be determined by the equation A8.

$$n = \frac{2W}{S} \tag{A8}$$

where *W/S* is the number of cells in the Z-direction.

The total frontal area through which conductive heat transfer takes place is then

$$A = \delta T n \tag{A9}$$

And after substitution for *n* ribbons

$$A = \delta T\left(\frac{2W}{S}\right) \tag{A10}$$

The total resistance to conductive heat transfer through n number of ribbons in the Y-direction is then derived after substitution as

$$R_Y = \frac{\eta L}{k\delta T\left(\frac{2W}{S}\right)} \tag{A11}$$

The equivalent resistance to conductive heat transfer through a solid plate with the same outer dimensions as the honeycomb in figure 1 is

$$R_{Yeq} = k_{Yeq}\frac{WT}{L} \tag{A12}$$

But since $R_{Yeq} = R_Y$, by definition, it follows that

$$\frac{L}{k_{Yeq}WT} = \frac{\eta L}{k\delta T\left(\frac{2W}{S}\right)}$$

Rearranging and solving for k_{Yeq} gives

$$k_{Yeq} = \frac{2k\delta}{\eta S} \tag{A13}$$

Conduction in the Z-direction

For the one path conduction from 1 to 2, it is assumed that the net heat interchange between paths is negligible for conduction in the Z-direction.

It can be shown that the contact resistances at the ribbon interfaces along the path are also negligible compared to the material resistance (Gilmore, 1994). The resistance from 1 to 2 is given as

$$R_{12} = \frac{x}{kA} \tag{A14}$$

where k is the honeycomb material thermal conductivity, A is the cross-sectional area of the conductive path and x is the total path length. As before, A (the cross-sectional area) is determined from equation A3. The total conductive path length is determined from

$$x = nh \tag{A15}$$

where n is equivalent to 2W/S. It follows then that

$$x = \frac{2Wh}{S} \tag{A16}$$

The number of paths in the Z-direction, m is determined as

$$m = \frac{L}{g} \tag{A17}$$

The total cross-sectional area for the m paths can the be calculated from

$$A = m\delta T \tag{A18}$$

The total resistance to conduction in the Z-direction, after substituting equations A18 and A16 into equation A14 is

$$R_Z = \frac{2Wh}{km\delta TS} \tag{A19}$$

Simplifying this equation using previous definitions and equations

$$R_Z = \frac{2Wh}{km\delta TS} = \frac{2Wh}{k\left(\frac{L}{g}\right)\delta TS} = \frac{2Wh}{k\left(\frac{L}{h+h\cos\theta}\right)\delta TS} = \frac{2Wh^2(1+\cos\theta)}{kL\delta TS}$$

Further simplification gives

$$R_Z = \frac{2W\left(\frac{S}{2}\sin\theta\right)^2(1+\cos\theta)}{kL\delta TS} = \frac{WS\sin^2\theta\left(\frac{1+\cos\theta}{2}\right)}{kL\delta T}$$

And finally

$$R_Z = \frac{WS\sin^2\theta}{kL\delta T\eta} \tag{A20}$$

The equivalent resistance for a plate in the Z-direction of the same dimensions as the honeycomb is

$$R_{Zeq} = \frac{W}{k_Z LT} \tag{A21}$$

But since $R_{Zeq} = R_Z$ by definition, it follows that

$$\frac{W}{k_{Zeq}LT} = \frac{WS\sin^2\theta}{kL\delta T\eta}$$

Rearranging and solving gives

$$k_{Zeq} = \frac{k\delta\eta\sin^2\theta}{S} \tag{A22}$$

Conduction in the X-direction

For a single ribbon from location *i* to *ii* in figure A1, the resistance to conduction is defined as

$$R_{iii} = \frac{x}{kA} \tag{A23}$$

The cross-sectional area for one ribbon is

$$A = \sigma L\delta \tag{A24}$$

The path length is equivalent to *T*. Substituting equation A24 into equation A23 gives

$$R_{iii} = \frac{k\sigma\delta L}{T} \tag{A25}$$

Now for *n* number of ribbons, it is assumed that the net heat interchange between ribbons is negligible for this directional calculation. The total cross-sectional area for conduction in the X-direction is given as

$$A = n\sigma\delta L \tag{A26}$$

The total resistance for n ribbons is extrapolated as

$$R_X = \frac{ST}{2k\sigma\delta LW} \tag{A27}$$

The equivalent total resistance in the X-direction for a solid plate of outer-dimensions equivalent to those of the honeycomb is given as

$$R_{Xeq} = \frac{T}{k_{Xeq}LW} \tag{A28}$$

But since $R_{Xeq} = R_X$ by definition, it follows that

$$\frac{T}{k_{Xeq}LW} = \frac{ST}{2k\sigma\delta LW}$$

After rearranging and solving

$$k_{Xeq} = \frac{2k\sigma\delta}{S} \tag{A29}$$

Radiation Considerations

For the purpose of simplifying the calculations for radiation in the X-direction of the honeycomb, the six-sided shape is replaced by a cylinder with an average internal radius (r_i). Only one cell is considered (shown in figure A4 below). At end 1, a fictitious cover plate is placed over the opening, as this would be the case for cover plates in a solar panel used for space applications. The same is assumed for bottom end, 2. In other words, an enclosure with three surfaces is under consideration.

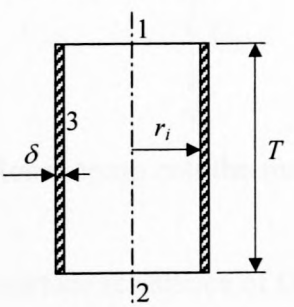

Figure A4 Cylindrical honeycomb cell approximation details

The equivalent internal radius is determined by equating the equivalent cross-sectional area for the hexagonal honeycomb cells. It follows after the calculation that

$$r_i = \frac{\left(\frac{6h\delta}{\pi}\right) - \delta^2}{2\delta} \tag{A30}$$

The idea is to calculate the amount of heat exchanged due to radiation in the cylinder for specified temperatures and then to compare these values to the case of pure conduction for the same geometric and thermal set-up. The temperature of the top plate, bottom plate and side of the cylinder is taken to be constant throughout. The top plate is taken to be a constant higher temperature than the bottom plate and the sidewall temperature, 3, is taken to be at an average of the top and bottom plate temperatures. The sidewalls are taken to be an adiabatic, or refractory surface. That is to say, it is well insulated and no net heat exchange takes place to or from side 3. The only heat being exchanged is that between side 3 and the other two surfaces in the enclosure. Consider the thermal resistance diagram in figure A5 for the enclosure. The relevant net heat transfers to or from each of the surfaces is shown. Since the sidewalls are adiabatic, it follows that $\dot{Q}_3 = 0$. The result of this is that: $\dot{Q}_1 = \dot{Q}_2$.

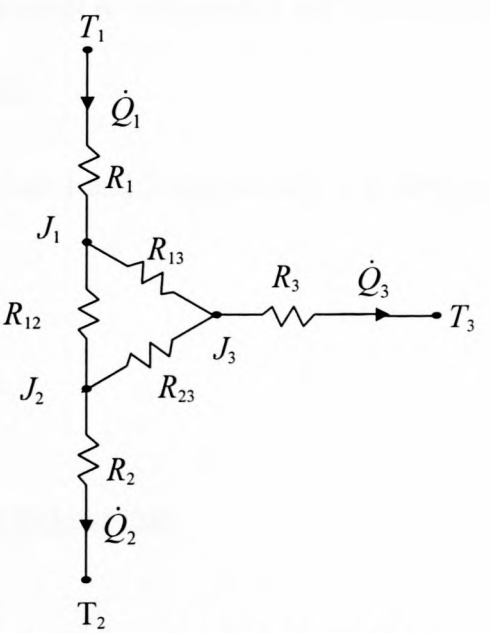

Figure A5 Honeycomb cell thermal radiation resistance model

The general surface resistance of the three surfaces is given by

$$R_i = \frac{1-\varepsilon_i}{\varepsilon_i A_i} \tag{A31}$$

And the general resistance due to the view factors of the surfaces is given as

$$R_{ij} = \frac{1}{A_i F_{ij}} \tag{A32}$$

The equation (Mills, 1995) used to calculate the heat exchange between 1 and 2 for the specific case of $\dot{Q}_3$ equal to zero, is given as

$$\dot{Q}_{12} = \frac{E_1 - E_1}{R_1 + R_2 + R_{//}} \tag{A33}$$

where E_1 and E_2 is the emissive power of surfaces 1 and 2 respectively, and $R_{//}$ is the parallel thermal resistance between surface 1 and 2, and is solved as follows

$$R_{//} = \left(\frac{1}{R_{12}} + \frac{1}{R_{13} + R_{23}} \right)^{-1} \tag{A34}$$

It is also known that

$$Q_{12} = \frac{J_1 - J_2}{R_{//}} \tag{A35}$$

Setting the equations equal to one another and rearranging gives

$$J_1 = J_2 + R_{//}\dot{Q}_{12} \tag{A36}$$

The heat leaving surface 1 and 2 respectively is determined from

$$\dot{Q}_1 = \frac{E_1 - J_1}{R_1} \tag{A37}$$

$$\dot{Q}_2 = \frac{E_2 - J_2}{R_2} \tag{A38}$$

But since $\dot{Q}_1 = \dot{Q}_2$, it follows that

$$\frac{E_1 - J_1}{R_2} = \frac{E_2 - J_2}{R_2}$$

And after rearranging

$$J_1 = E_1 - R_1\left(\frac{E_2 - J_2}{R_2} \right) \tag{A39}$$

Setting the radiosity J_1 from equations A37 and A35 equivalent

$$E_1 - R_1\left(\frac{E_2 - J_2}{R_2} \right) = J_2 + R_{//}\dot{Q}_{12}$$

Rearranging and solving for J_2

$$J_2 = \frac{\left(\frac{E_2 R_1}{R_2}\right) - E_1 + R_{//}\dot{Q}_{12}}{\left(\frac{R_1}{R_2} - 1\right)} \tag{A40}$$

The radiosity of surface 2 can then be used to calculate the net heat transferred by radiation into surface 2 (surface 1 is at a higher temperature than 2), by using equation A37.

Now to determine the net heat transfer rate to surface 2 by conduction through the sidewall of the cylinder represented in figure A4, consider the conduction resistance model in figure A6

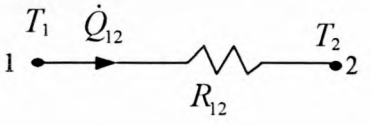

Figure A6 Honeycomb cell thermal conductive resistance model

It is assumed that conduction between sides 1 and 2 take place only through the wall 3 of thickness δ. The net heat transfer rate into side 2 by conduction is then determined from the restructured equation A1.

$$\dot{Q}_{12} = \frac{T_1 - T_2}{R_{12}} \tag{A41}$$

The net heat transfer rate by conduction is then compared to the net heat transfer rate by radiation to determine whether or not radiation in the X-direction is negligible for honeycomb thermal analysis. A Microsoft Excel Spreadsheet was generated and the results plotted to show the relevance of radiation compared to conduction heat transfer. The honeycomb used was the same as that used for SUNSAT (dimensions given in worked example further on in the appendix). The temperature of the one end (side 1) was kept at 350 K and the temperature of the other end (side 2) adjusted higher from 270 K in increments of 10 K. The results are shown in figure A7. It is evident from the results for the SUNSAT honeycomb that the heat transfer in the X-direction by conduction is significantly higher than that by radiation heat transfer, and the assumption that the radiation heat transfer is negligible would not cause significant loss of accuracy.

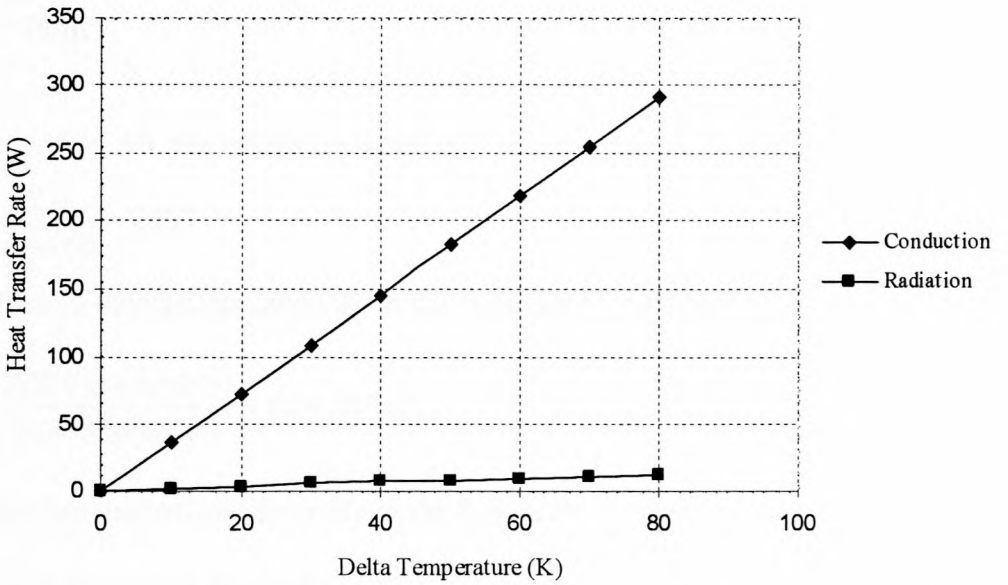

Figure A7 The effect of radiation heat transfer in the SUNSAT honeycomb for the X-cell-direction

Radiation Consideration in the Y-direction and the Z-direction

From an initial look at the honeycomb pattern (as seen in figure A1), it is apparent that each of the walls of the different cells, form radiation shields or barriers (similar to MLI). The effect of these shields is to reduce the heat transfer rate due to a larger resistance to radiation heat flow. It is known (Mills, 1995) that the net radiation heat transfer rate can be halved between two parallel plates by inserting a third identical plate between the other two (that is for three parallel black plates with view factors of approximately 1). This essentially means that for a honeycomb structure with multiple "barriers", the radiation heat transfer in the Y and Z-direction has a path of high thermal resistance and this induces a low rate of heat transfer; almost negligible.

Worked Problem for SUNSAT Honeycomb

$L = 0.383$ m

$W = 0.374$ m

$T = 0.012$ m

$\delta = 140$ μm

$h = 0.006$ m

$S = 0.0095$ m

$\theta = 60$ °

k = 237 W/m K

From equation A6, the extension factor is

$$\eta = \frac{2}{1+cos\,60} = 1.333$$

The effective thermal conductivity in the Y-direction is determined from equation A13 as

$$k_{Yeq} = \frac{2(237)(140x10^{-6})}{(1.333)(0.0095)} = 5.24 \text{ W/mK}$$

The effective thermal conductivity in the Z-direction is determined from equation A22 as

$$k_{Zeq} = \frac{(237)(140x10^{-6})(1.333)(sin^2\,60)}{0.0095} = 1.164 \text{ W/mK}$$

The effective thermal conductivity in the X-direction is determined from equation A29 as

$$k_{Xeq} = \frac{2(237)(1.333)(140x10^{-6})}{0.0095} = 9.311 \text{ W/mK}$$

Appendix B: Thermal Radiation

Radiation in Space

Consider the radiation heat exchange between a satellite panel, the earth and deep space. The panel is at a temperature T_{sp}, the earth is at some average earth temperature T_{earth} and space is at the temperature T_{space}. The satellite emits infrared radiation and reflects solar radiation to the earth as well as space. The net amount of radiation absorbed, reflected and emitted on the panel surface is dependant on its surface properties.

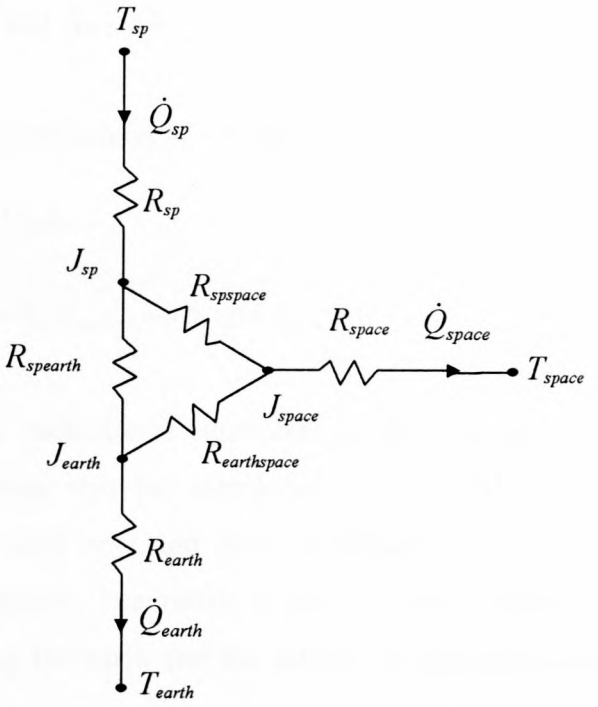

Figure B1 Conceptual blackbody thermal resistance diagram of radiation in space

Space can be considered to be a vacuum at ≈ 0 K. Space can be imagined as being an infinitely large sphere that surrounds both the earth and the satellite with a surface that has a zero value for emissivity and absorptivity equivalent to 1. If the absorptivity is equal to one, it follows that the reflectivity is equal to zero (equation 2.7).

The radiosity of the *i*'th surface can be determined using the following equation (Mills, 1997)

$$J_i = \varepsilon_i E_i + (1-\varepsilon_i)\sum_{k=1}^{n} J_k F_{i,k} \qquad i = 1, 2, \ldots, n \text{ surfaces} \qquad \text{(B1)}$$

Where $E_i = \sigma T_i^4$.

After analysis and reduction of equation B1 for the satellite panel, the earth and space, the radiosity is solved for each of the "surfaces". It follows that for the space radiosity

$J_{space} = 0$, since $F_{space,sp} \to 0$, $F_{space,earth} \to 0$, $F_{space,space} = 0$ and $E_{space} \approx 0$.

For the satellite panel radiosity it follows then that

$$J_{sp} = \varepsilon_{sp} E_{sp} + (1 - \varepsilon_{sp})(J_{earth} F_{sp,earth}) \tag{B2}$$

where $F_{sp,sp} = 0$ and $J_{space} = 0$.

For the earth approximated as a black body ($\varepsilon_e = 1$), the earth radiosity is determined as

$$J_{earth} = E_{earth} \tag{B3}$$

where $F_{earth,earth} = 0$, $F_{earth,sp} \to 0$ and $J_{\text{space}} = 0$.

Since the space radiosity is equivalent to zero, no reflected or re-emitted radiation can leave space. This means that the interaction of the earth and the satellite with space is a single interaction for each case and thus no radiation can be re-radiated to either the earth or the satellite from space. The result is that for the resistance diagram shown in figure B1, the radiation leaving the earth and the satellite is uncoupled for the radiosity J_{space}. It follows that the resistance diagram of figure B1 reduces to that shown in figure B2.

The energy balance on the satellite panel with reference to figure B2 is as follows

$$\dot{Q}_{sp} = \dot{Q}_{spearth} + \dot{Q}_{spspace} \tag{B4}$$

where

$$\dot{Q}_{spearth} = \frac{J_{sp} - J_{earth}}{R_{spearth}} \tag{B5}$$

and

$$\dot{Q}_{spspace} = \frac{J_{sp}}{R_{spspace}} \tag{B6}$$

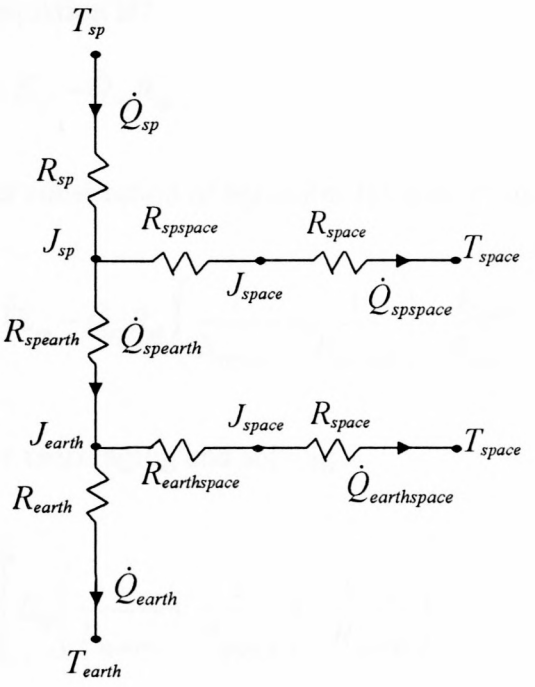

Figure B2 Thermal resistance diagram illustrating radiation in space

The resistances to radiation are defined as

$$R_{sp} = \frac{\left(1-\varepsilon_{sp}\right)}{\varepsilon_{sp} A_{sp}} \tag{B7}$$

$$R_{spearth} = \frac{1}{A_{sp} F_{sp,earth}} \tag{B8}$$

$$R_{spspace} = \frac{1}{A_{sp} F_{spspace}} \tag{B9}$$

where $F_{spearth} + F_{spspace} = 1$.

Substituting equation B5 and B6 into equation B4

$$\dot{Q}_{sp} = J_{sp}\left(\frac{1}{R_{spearth}} + \frac{1}{R_{spspace}}\right) - \frac{J_{earth}}{R_{spearth}} \tag{B10}$$

It is also known that

$$\dot{Q}_{sp} = \frac{E_{sp} - J_{sp}}{R_{sp}} \tag{B11}$$

Rearranging equation B7

$$J_{sp} = E_{sp} - \dot{Q}_{sp} R_{sp} \tag{B12}$$

It follows after substitution of equations B3 and B9 into equation B7

$$\dot{Q}_{sp} = \left(E_{sp} - \dot{Q}_{sp} R_{sp}\right)\left(\frac{1}{R_{spearth}} + \frac{1}{R_{spspace}}\right) - \frac{E_{earth}}{R_{spearth}}$$

It follows after rearranging and solving

$$\dot{Q}_{sp} = \left[E_{sp}\left(\frac{1}{R_{spearth}} + \frac{1}{R_{spspace}}\right) - \frac{E_{earth}}{R_{spearth}}\right]\left(1 + \frac{R_{sp}}{R_{spspace}} + \frac{R_{sp}}{R_{spearth}}\right)^{-1} \tag{B13}$$

Gilmore (1994) explains how equation B13 above is replaced with a more simple approach to radiation in space. The earth is ignored in the infrared radiation from the satellite, and the infrared radiation from the earth is then added back as shown in equation B14.

$$\dot{Q}_{sp} = \varepsilon_{sp} A_{sp} \sigma T_{sp}^4 - \varepsilon_{sp} A_{sp} F_{sp,earth} \sigma T_{earth}^4 \tag{B14}$$

To prove that equation B13 and B14 are equivalent, example B1 is introduced:

Example B1.

Consider the following situation: $T_{space} = 0$ K, $T_{sp} = 300$ K, $T_{earth} = 248$ K, $\varepsilon_{sp} = 0.7$, $F_{sp,earth} = 0.8$ and $A_{sp} = 0.25$ m^2.

It follows from equations B7 - B9 that: $R_{spearth} = 5$ m^{-2}, $R_{spspace} = 20$ m^{-2}, and $R_{sp} = 1.714$ m^{-2}.

After substituting all relevant variables into equation B13

$$\dot{Q}_{sp} = \left[\sigma 300^4\left(\frac{1}{5} + \frac{1}{20}\right) - \frac{\sigma 248^4}{5}\right]\left(1 + \frac{1.714}{20} + \frac{1.714}{5}\right)^{-1}$$

Which equates to

$$\dot{Q}_{sp} = 50.345 \text{ W}$$

From equation B14 it follows after substituting for the necessary variables

$$\dot{Q}_{sp} = (0.7)(0.25)\sigma 300^4 - (0.7)(0.25)(0.8)\sigma 248^4$$

This equates to

$$\dot{Q}_{sp} = 50.345 \text{ W}$$

The result proves that equation B13 correlates exactly with equation B14 and that equation B13 is indeed the un-simplified form of the Gilmore approach to radiation from a surface in space.

View Factor Details

The calculation of the radiation view factor between any two finite surfaces as shown in figure B3, requires the solution to a double area integral, or fourth-order integration. The equation used to determine the view factor between two finite areas is given by equation B15 (Mills, 1995) with reference to figure B3.

$$F_{1,2} = \frac{1}{A_1} \int_{A_1} \int_{A_2} \frac{\cos\theta_1 \cos\theta_2}{\pi s^2} dA_2 dA_1 \tag{B15}$$

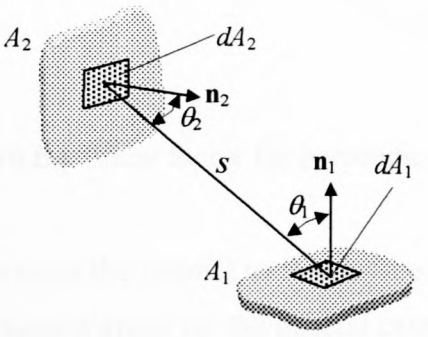

Figure B3 Geometry for shape factor formulation

The analytical procedure required to setup a fourth-order integral from equation B15 for the view factor between two perpendicular rectangular finite surfaces A_1 and A_2 (figure B4); is explained as follows: The distance between the two surfaces is determined as

$$s^2 = z_2^2 + \left[(y_1 - y_2)^2 + x_1^2\right] \tag{B16}$$

Assume that the local surface normals are also known in terms of the unit vectors $\hat{\mathbf{i}}$, $\hat{\mathbf{j}}$ and $\hat{\mathbf{k}}$, then it follows that

$$\hat{\mathbf{n}} = l\hat{\mathbf{i}} + m\hat{\mathbf{j}} + n\hat{\mathbf{k}}$$

where l, m and n are the direction cosines for the unit vector **n**, i.e., $l = \mathbf{n} \cdot \mathbf{i} = \cos\theta_x$ is the cosine of the angle between **n** and the x-axis, etc. (Modest, 1993).

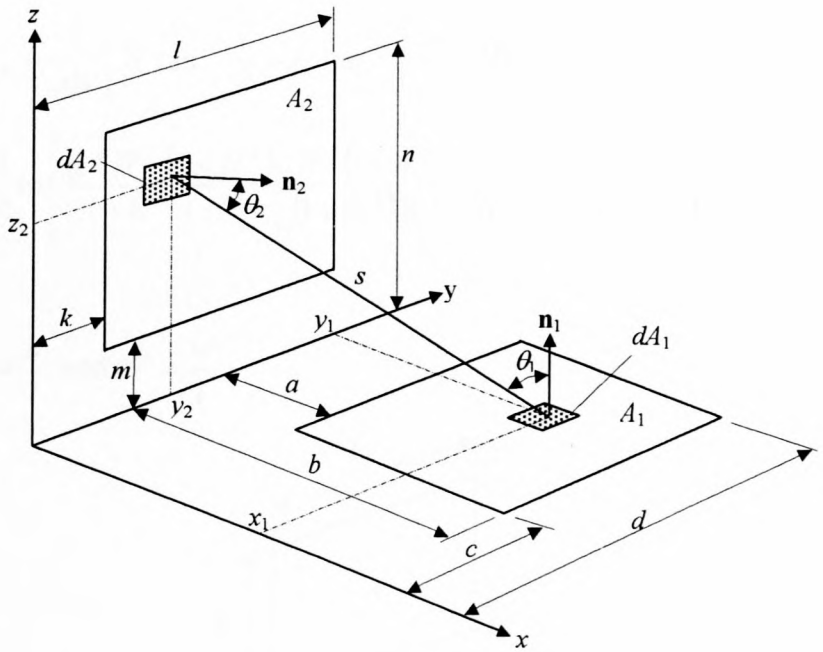

Figure B4 View factor for perpendicular finite surfaces

The angles between the normal to the surfaces and the line connecting the distance between the elemental surfaces is given for the general case as (Modest, 1993)

$$\cos\theta_i = \frac{1}{s}\left[(x_j - x_i)l_i + (y_j - y_i)m_i + (z_j - z_i)n_i\right] \qquad \text{(B17)}$$

After substitution and simplification for the case in figure B4 it follows that,

$$\cos\theta_1 = \frac{z_2}{s} \text{ and } \cos\theta_2 = \frac{x_1}{s}$$

Substituting for s, $\cos\theta_1$, $\cos\theta_2$ and the relevant integral boundary conditions into equation B15 and simplifying gives the form factor between two perpendicular finite surfaces A_1 and A_2 as

$$F_{1,2} = \frac{1}{\pi A_1} \int_c^d \int_a^b \int_k^l \int_m^n \frac{z_2 x_1}{\left(z_2^2 + (y_1 - y_2)^2 + x_1^2\right)^2} dz_2 dy_2 dx_1 dy_1 \tag{B18}$$

Such integrals are difficult to evaluate analytically except for very simple geometries. The view factor for various geometric configurations is often available in tables.

For two finite rectangles of the same length, having one common edge, and perpendicular to each other (as shown in figure B5), the view factor is given as (Modest, 1993)

$$\begin{aligned} F_{1,2} = \frac{1}{\pi W}\Bigg(& W \tan^{-1}\frac{1}{W} + H \tan^{-1}\frac{1}{H} - \sqrt{H^2 + W^2}\tan^{-1}\frac{1}{\sqrt{H^2 + W^2}} \\ & + \frac{1}{4}\ln\left\{\frac{(1+W^2)(1+H^2)}{1+W^2+H^2}\left[\frac{W^2(1+W^2+H^2)}{(1+W^2)(W^2+H^2)}\right]^{W^2}\left[\frac{H^2(1+H^2+W^2)}{(1+H^2)(H^2+W^2)}\right]^{H^2}\right\}\Bigg) \end{aligned} \tag{B19}$$

where $H = \frac{h}{l}$ and $W = \frac{w}{l}$.

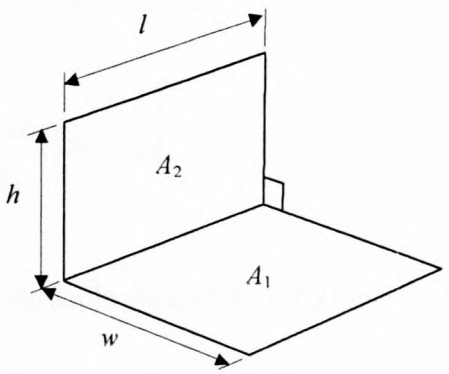

Figure B5 Two perpendicular plates of equal length and a common edge

Consider the configuration in figure B6. To determine the view factor between areas A_1 and A_6, the rules of reciprocity and summation are firstly applied in the following manner

$$\begin{aligned} (A_5 + A_6)F_{(5+6),(1+2)} &= (A_5 + A_6)(F_{(5+6),1} + F_{(5+6),2}) \\ &= A_1(F_{1,5} + F_{1,6}) + A_2(F_{2,5} + F_{2,6}) \\ &= A_1(F_{1,(3+5)} - F_{1,3}) + A_2(F_{2,(4+6)} - F_{2,4}) \\ &\quad + A_1F_{1,6} + A_2F_{2,5} \end{aligned}$$

And it is also known that

$$(A_5 + A_6)F_{(5+6),(1+2)} = (A_1 + A_2)(F_{(1+2),(3+4+5+6)} - F_{(1+2),(3+4)})$$

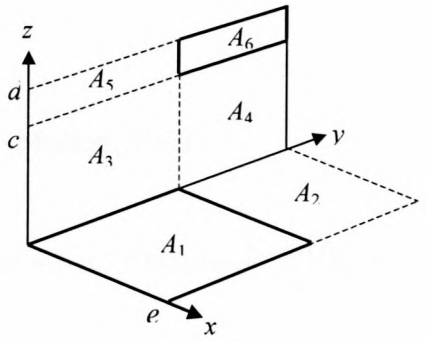

Figure B6 Generalized rectangular surfaces on perpendicular planes

In both the expressions all view factors, with exception of $F_{1,6}$ and $F_{2,5}$, are of the type given in figure B5. These two view factors may be related to one another, as is easily seen from their integral forms. From equation B15

$$F_{2,5} = \frac{1}{A_2}\int_{A_2}\int_{A_5}\frac{\cos\theta_2 \cos\theta_5}{\pi s^2} dA_5 dA_2 \qquad \text{(B20)}$$

For the coordinate system shown in figure B6, it follows that

$$s^2 = x_2^{\,2} + (y_2 - y_5)^2 + z_5^{\,2}$$

and $\cos\theta_2 = \frac{z_5}{s}$ and $\cos\theta_5 = \frac{x_2}{s}$. Substituting for s, θ_2, θ_5 into equation B20

$$F_{2,5} = \frac{1}{\pi A_2}\int_{x_2=0}^{e}\int_{y_2=a}^{b}\int_{y_5=0}^{a}\int_{z_5=c}^{d}\frac{z_5 x_2}{\left[z_5^2 + (y_2 - y_5)^2 + x_2^2\right]} dz_5 dy_5 dy_2 dx_2$$

Similarly, for s, θ_1, θ_6

$$F_{1,6} = \frac{1}{\pi A_1} \int_{x_2=0}^{e} \int_{y_1=a}^{a} \int_{y_6=a}^{b} \int_{z_6=c}^{d} \frac{z_6 x_1}{\left[z_6^2 + (y_1 - y_6)^2 + x_6^2\right]} dz_6 dy_6 dy_1 dx_1$$

From the law of reciprocity for diagonal opposed pairs of perpendicular rectangular plates, it follows that

$$A_2 F_{2,5} = A_1 F_{1,6}$$

And finally solving for $F_{1,6}$ (Modest, 1993)

$$F_{1,6} = \frac{A_1 + A_2}{2A_1}\left(F_{(1+2),(3+4+5+6)} - F_{(1+2),(3+4)}\right) - \frac{1}{2}\left(F_{1,(3+5)} - F_{1,3}\right) - \frac{A_2}{2A_1}\left(F_{2,(4+6)} - F_{2,4}\right) \qquad \text{(B21)}$$

Using similar arguments, one may also determine the view factor between two arbitrary orientated rectangular plates lying perpendicular planes as shown in figure B7. After considerable algebra, one finds that:

$$\begin{aligned} 2A_1 F_{1,2} = {} & f(x_2, y_2, z_3) - f(x_2, y_1, z_3) - f(x_1, y_2, z_3) + f(x_1, y_1, z_3) \\ & + f(x_1, y_2, z_2) - f(x_1, y_1, z_2) - f(x_2, y_2, z_2) + f(x_2, y_1, z_2) \\ & - f(x_2, y_2, z_3 - z_1) + f(x_2, y_1, z_3 - z_1) + f(x_1, y_1, z_3 - z_1) - f(x_1, y_1, z_3 - z_1) \\ & + f(x_2, y_2, z_2 - z_1) - f(x_2, y_1, z_2 - z_1) - f(x_1, y_2, z_2 - z_1) + f(x_1, y_1, z_2 - z_1) \end{aligned}$$

(B22)

where $f(w,h,l) = A_1 F_{1,2}$ is the product of area and view factor.

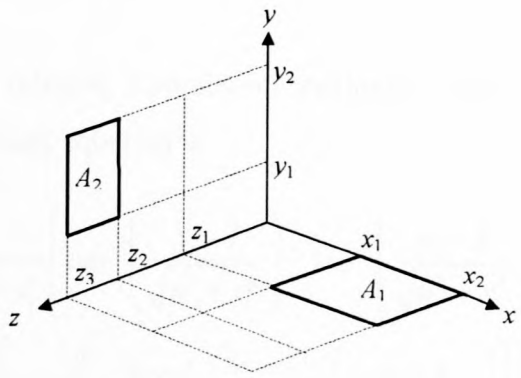

Figure B7 Arbitrary orientated perpendicular plates

An approximation can be made for the case solved by equation B21. If it is assumed that one of the areas is a differential size and there other finite for the situation described by figure B7, then equation B15 reduces to equation B23.

$$F_{1,2} = \int_{A_2} \frac{\cos\theta_1 \cos\theta_2}{\pi s^2} dA_2 \tag{B23}$$

It follows then that

$$F_{1,2} = \frac{1}{\pi} \int_k^l \int_m^n \frac{z_2 x_1}{\left[z_2^2 + (y_1 - y_2)^2 + x_1^2\right]^2} dz_2 dy_2 \tag{B24}$$

Solving this equation:

Let $z_2 + (y_1 - y_2)^2 + x_1^2 = p$. After substitution and simplification

$$F_{1,2} = \frac{1}{2\pi} \int_k^l \int_q^r \frac{x_1}{p^2} dp dy_2$$

where $q = \left(m^2 + (y_1 - y_2)^2 + x_1^2\right)$ and $r = \left(n^2 + (y_1 - y_2)^2 + x_1^2\right)$

It follows then that after integration and substitution that

$$F_{1,2} = -\frac{x_1}{2\pi} \int_k^l \left(\frac{1}{n^2 + (y_1 - y_2)^2 + x_1^2} - \frac{1}{m^2 + (y_1 - y_2)^2 + x_1^2} \right) dy_2$$

Let $(y_1 - y_2) = t$. After substitution and simplification

$$F_{1,2} = \frac{x_1}{2\pi} \int_{y_1 - k}^{y_1 - l} \left(\frac{1}{n^2 + t^2 + x_1^2} - \frac{1}{m^2 + t^2 + x_1^2} \right) dt$$

Using the appropriate integral formulation evaluated with inverse trigonometric functions (Finney, 1994), the resultant equation is

$$F_{1,2} = \frac{x_1}{2\pi} \left(\frac{1}{\sqrt{n^2 + x_1^2}} \left[\tan^{-1}\left(\frac{y_1 - l}{\sqrt{n^2 + x_1^2}} \right) - \tan^{-1}\left(\frac{y_1 - k}{\sqrt{n^2 + x_1^2}} \right) \right] - \frac{1}{\sqrt{m^2 + x_1^2}} \left[\tan^{-1}\left(\frac{y_1 - l}{\sqrt{m^2 + x_1^2}} \right) - \tan^{-1}\left(\frac{y_1 - k}{\sqrt{m^2 + x_1^2}} \right) \right] \right) \tag{B25}$$

For the specific case of determining the view factor between the satellite panel and the earth ($F_{sp,earth}$, equation B8), equations B26 and B27 (Modest, 1994) are used for the two specific panel orientations shown in figures B8 and B9 respectively.

It is assumed that the size of the satellite panel relative to the earth is small enough to be considered as a differential planar element.

$$F_{d1,2} = \left(\frac{r}{h}\right) \tag{B26}$$

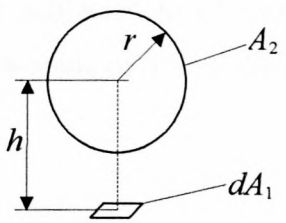

Figure B8 Differential planar element normal passes through center of sphere

When the differential planar element tangent passes through the center of the sphere (figure B9), the following equation is used

$$F_{d1,2} = \frac{1}{\pi}\left[\tan^{-1}\frac{1}{\sqrt{H^2-1}} - \frac{\sqrt{H^2-1}}{H^2}\right] \tag{B27}$$

where $H = \dfrac{h}{r}$

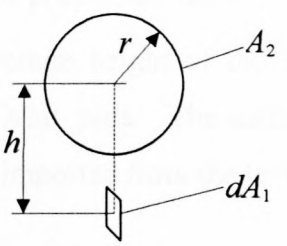

Figure B9 Differential planar element tangent passes through center of sphere

Appendix C: Orbital Heating Numerical Computer Program ORBIT-FLUX

The ORBIT-FLUX program provides a means of determining the amount of radiation incident on the satellite surfaces for a known orbit path. The program is limited to two orbit paths that SUNSAT could have been subjected to (discussed in section 3.2). The one is a polar sun-synchronous path with a beta-angle of 0° and the other a polar sun-synchronous path with a beta-angle of 90°.

The program uses variables that are imported into the program from text files. Figure C1 shows the geometric variables used to predict, for each of the 6 satellite surfaces, the earth thermal heat load, the earth reflected solar heat load and the direct solar heat load.

The angle of rotation of the satellite around the earth (θ) and the angle of rotation of the satellite around its own Z-axis (ϕ) are time dependant. The total orbit time is estimated at 100 min. From this, the rate of rotation, $\dot{\theta}$, is determined and then the angle of rotation for the specific time of the orbit. To model the orbit for no eclipse period (beta-angle equal to zero), $\dot{\theta}$ is set equal to zero in the program. The Z-axis spin rate $\dot{\phi}$ is set as required. The dimensions of the solar panels and the bottom and top plates are imported from text file "Length" and then used to determine the respective areas. The orbit properties: the albedo (a), the solar heat flux ($\dot{q}_{ds}$), the radius of the earth (R_{earth}) and the average height of the satellite above the earth surface (h), are all imported from the text file "Orbit_prop". The surface properties of the solar panels and those of the top and bottom plates are imported from the text file "Surface_prop".

Consider figure C1. From these previously mentioned variables, the angle of shadow, α, measured clockwise from the global z-axis, is determined for the geometry shown as

$$\alpha_1 = \cos\left(\frac{R_{earth}}{R_{earth}+h}\right) \tag{C1}$$

The earth emitted heat flux, $\dot{q}_{ee}$, is determined from chapter 2 using equation 2.20 as

$$\dot{q}_{ee} = \frac{(1-a)}{4}\dot{q}_{ds} \tag{C2}$$

The earth reflected radiation flux is determined from the knowledge of the albedo as

$$\dot{q}_{er} = a\dot{q}_{ds} \tag{C3}$$

The intensity of the earth reflected radiation on the satellite surface depends on the position of the satellite relative to the sun vector. It can be approximated (Piscane, 1994) that for theta equal to 0°, the earth reflected solar radiation is zero (refer to figure 3.4). This value increases as theta increases and is a maximum equal to $\dot{q}_{er}$ for theta equal to 90°. It then decreases again to zero for theta equal to 180°. The fraction of $\dot{q}_{er}$ that reaches the satellite expressed as a value between 0 and 1 is given by the factor

$$f_{er} = \sin\theta \tag{C4}$$

The view factors from the satellite bottom-plate to the earth is estimated using equation B26 in appendix B as

$$F_{bp,earth} = \left(\frac{R_{earth}}{R_{earth}+h}\right) \tag{C5}$$

The view factor for the solar panels to earth is determined from equation B27 as

$$F_{sp,earth} = \frac{1}{\pi}\left[\tan^{-1}\frac{1}{\sqrt{\left(\frac{R_{earth}+h}{R_{earth}}\right)^2-1}} - \frac{\sqrt{\left(\frac{R_{earth}+h}{R_{earth}}\right)^2-1}}{\left(\frac{R_{earth}+h}{R_{earth}}\right)^2}\right] \tag{C6}$$

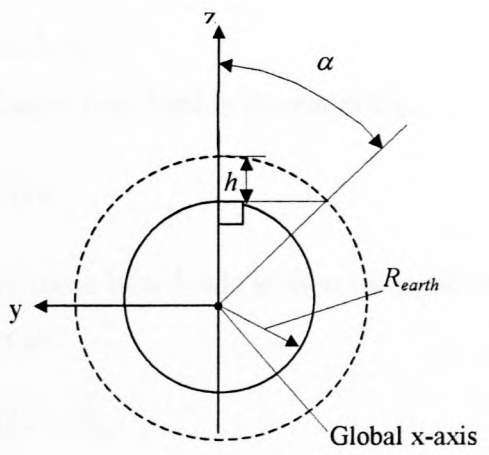

Figure C1 Shadow angle geometry

With reference to figure 3.6, the projected areas of the satellite surfaces in the direction of the sun vector **s** (PAS) are determined in terms of two parameters, θ and ϕ, for the starting position where surface 2 points to the sun.

$$PAS_1 = A_1 \sin(-\theta) \tag{C7}$$

$$PAS_2 = A_2(\cos\theta)\cos(\phi) \tag{C8}$$

$$PAS_3 = A_3(\cos\theta)\cos(\phi + 90) \tag{C9}$$

$$PAS_4 = A_4(\cos\theta)\cos(\phi + 180) \tag{C10}$$

$$PAS_5 = A_5(\cos\theta)\cos(\phi + 270) \tag{C11}$$

$$PAS_6 = A_6 \sin\theta \tag{C12}$$

If the value of *PAS* becomes negative, it means the surface is no longer receiving direct solar radiation since the *PAS* is in effect zero. (These equations are strictly speaking, for the simplified orbit paths discussed in chapter 3.2.) *PAS* is also zero when the satellite is in the earths shadow. The environmental heat loads on each of the surfaces can now be determined. The earth emitted heat load is determined for the surface *i* as

$$\dot{Q}_{ee} = \varepsilon_i F_{i,earth} A_i \dot{q}_{ee} \tag{C13}$$

where the view factor can be determined from either equations C4 or C5 depending on whether the surface is 1, or 2 to 5 respectively. The earth reflected heat load on the satellite surface *i* is determined as

$$\dot{Q}_{er} = \alpha_i F_{i,earth} f_{er} \dot{q}_{er} \tag{C14}$$

The direct solar radiation heat load is determined as

$$\dot{Q}_{ds} = \alpha_i PAS_i \dot{q}_{ds} \tag{C15}$$

The sum of all these three heat loads is then the total environmental heat load on each satellite surface, and is given as

$$\dot{Q}_e = \dot{Q}_{ds} + \dot{Q}_{er} + \dot{Q}_{ee} \tag{C16}$$

This heat load for each surface is then output as a text file and imported into TAS. Figure C2 shows the information flow diagram for the computer program ORBIT-FLUX.

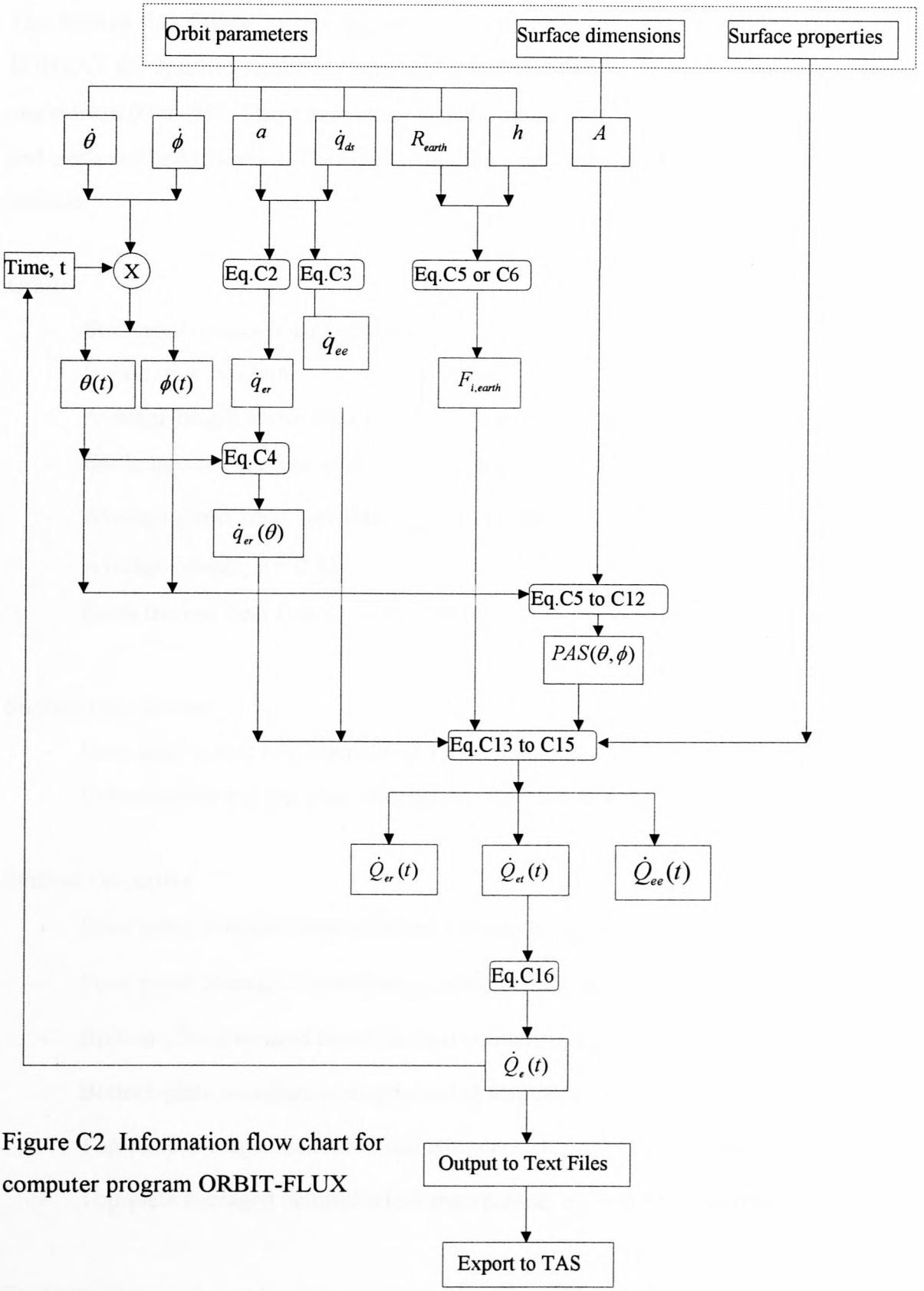

Figure C2 Information flow chart for computer program ORBIT-FLUX

Results

The figures that follow in this appendix show the heat load on each of the 6 surfaces of the SUNSAT for specific satellite missions i.e., different Z-axis rotation rates and change in the β-angle from 0° to 90°. These heat loads include the sum of the direct solar, earth reflected solar, and earth emitted radiation. The results are for a specific set of input parameters. These variables include:

Orbit

- Sun-synchronous polar circular orbit
- Period, $P = 100$ min
- Average height above the earth, $h = 700$ km
- Earth approximated as sphere with radius, $R_{earth} = 6371$ km
- Average direct solar heat flux, $\dot{Q}_{ds} = 1353$ W/m^2
- Average albedo, $a = 0.36$
- Earth thermal heat flux $\dot{Q}_{et} = 216$ W/m^2

Surface Dimensions

- Four solar panels of dimension: 0.45 x 0.45 m
- Bottom-plate and top-plate dimensions: 0.45 x 0.45 m

Surface Properties

- Solar panel averaged hemispherical emittance, $\varepsilon_{sp} = 0.8$ (±Y and ±X surfaces)
- Solar panel averaged hemispherical absorptance, $\alpha_{sp} = 0.8$ (±Y and ±X surfaces)
- Bottom-plate averaged hemispherical emittance, $\varepsilon_{bp} = 0.73$ (+Z surface)
- Bottom-plate averaged hemispherical absorptance, $\alpha_{bp} = 0.41$ (+Z surface)
- Top-plate averaged hemispherical emittance, $\varepsilon_{tp} = 0.41$ (-Z surface)
- Top-plate averaged hemispherical absorptance, $\alpha_{tp} = 0.41$ (-Z surface)

Four sets of surface heat loads are generated for four different rotation rates (2, 4, 6 and 8 Z-axis rotations per orbit) around the SUNSAT Z-axis. The objective being to show that the program is consistent and valid.

Note that the orbit starts at $\theta = 0$ and $\phi = 0$. The first satellite surface to see the solar radiation from the sun is surface 2 (+Y). The satellite then rotates around its Z-axis in the clockwise direction as seen from the earth.

The change in heating loads with a change in the orbit from a β-angle = 0° to a β-angle = 90° and a change in the Z-axis spin rate is also presented in this appendix. Table C1 summarizes the maximum, minimum and linearly averaged heat loads per orbit for each of the surfaces for the configuration previously described

Table C1 Summary of ORBIT-FLUX computer program results

		Heat Load for β-angle = 0° (W)						**Heat Load for β-angle = 90° (W)**					
		+Y	-Y	+X	-X	+Z	-Z	+Y	-Y	+X	-X	+Z	-Z
2 Z-axis Spins per Orbit	Max.	227.6	227.6	161.0	187.8	73.6	112.3	227.4	227.4	227.4	227.4	25.8	0
	Min.	8.2	8.2	8.2	8.2	25.8	0	8.2	8.2	8.2	8.2	25.8	0
	Avg.	48.6	48.6	26.4	60.6	39.6	35.8	78.0	78.0	78.0	78.0	25.8	0
4 Z-axis Spins per Orbit	Max.	227.4	227.4	211.7	218.4	73.6	112.3	227.4	227.4	227.4	227.4	25.8	0
	Min.	8.2	8.2	8.2	8.2	25.8	0	8.2	8.2	8.2	8.2	25.8	0
	Avg.	44.9	44.9	47.4	45.9	39.6	35.8	78.0	78.0	78.0	78.0	25.8	0
6 Z-axis Spins per Orbit	Max.	227.4	227.4	220.1	224.7	73.6	112.3	227.4	227.4	227.4	227.4	25.8	0
	Min.	8.2	8.2	8.2	8.2	25.8	0	8.2	8.2	8.2	8.2	25.8	0
	Avg.	44.9	44.9	54.6	42.4	39.6	35.8	78.0	78.0	78.0	78.0	25.8	0
8 Z-axis Spins per Orbit	Max.	227.4	227.4	223.1	226.7	73.6	112.3	227.4	227.4	227.4	227.4	25.8	0
	Min.	8.2	8.2	8.2	8.2	25.8	0	8.2	8.2	8.2	8.2	25.8	0
	Avg.	46.4	46.4	49.0	41.5	39.6	35.8	78.0	78.0	78.0	78.0	25.8	0

Discussions and Conclusions

It is evident from table C1 and the figures plotted, that the maximum, minimum and average total environmental heat loads on the solar panels for a β-angle = 0°, don't vary significantly from each other for varying Z-axis spin rates. What is however evident from the figures presented, is that the graphical area under the peaks is higher for low Z-axis spin than it is for a high Z-axis spin rate. The integration of this area would give the energy absorbed by the satellite solar panel in Joules and this would show that a higher quantity of energy is absorbed at peak loads for low Z-axis spin rate. The expected result is higher peak solar panel temperatures for lower Z-axis spin rate. This would explain the reason for using a higher spin rate to reduce solar panel peak temperatures by spreading the heat more evenly over the solar panels.

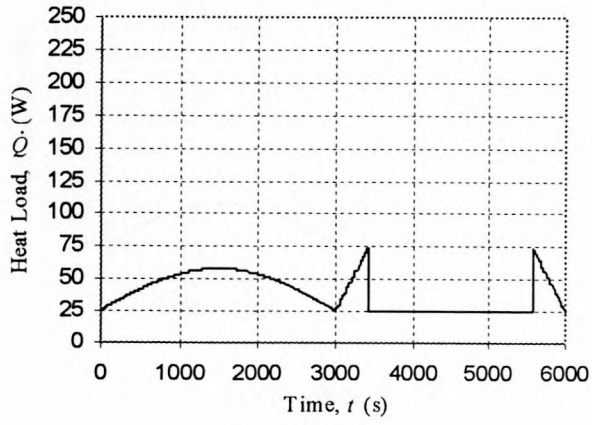

(a) Surface 1, +Z

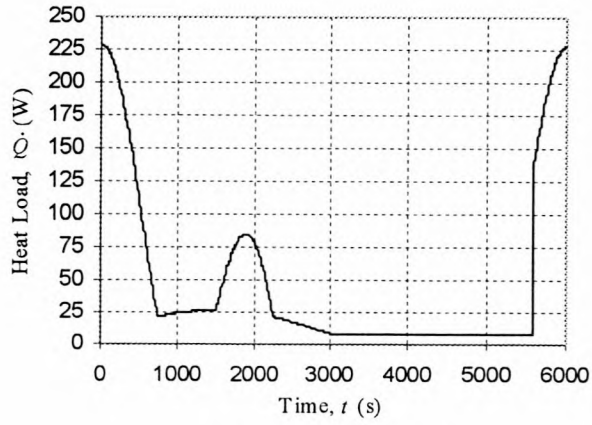

(b) Surface 2, +Y

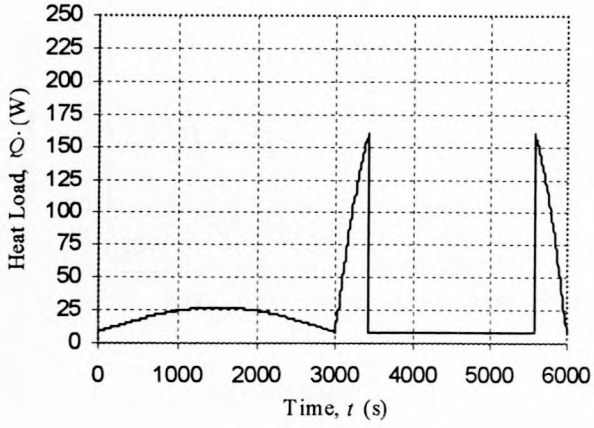

(c) Surface 3, +X

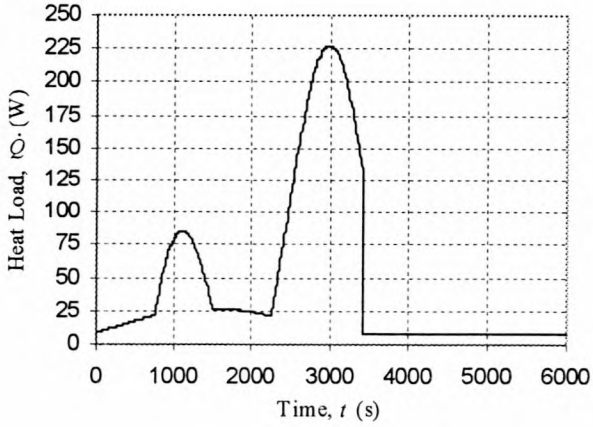

(d) Surface 4, -Y

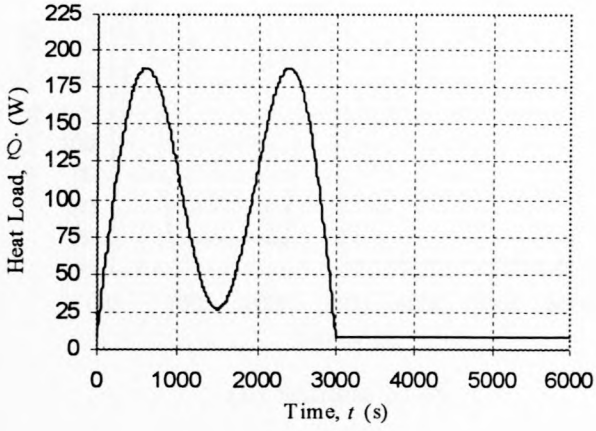

(e) Surface 5, -X

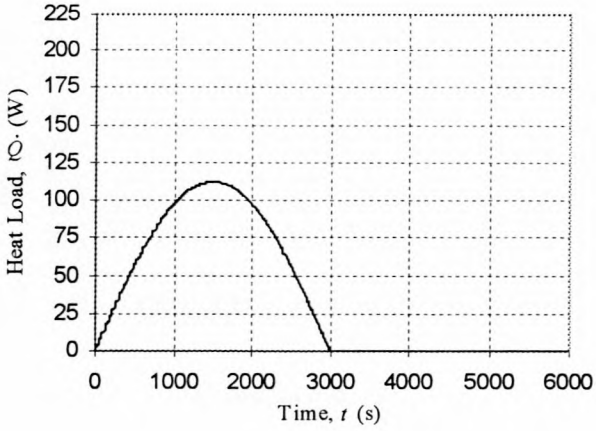

(f) Surface 6, -Z

Figure C3 Environmental heat loads on SUNSAT for a circular polar sun-synchronous orbit with a beta-angle of zero degrees and 2 rotations about the Z-axis per orbit

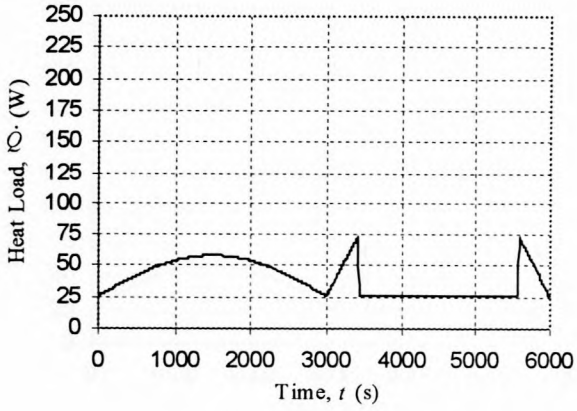

(a) Surface 1, +Z

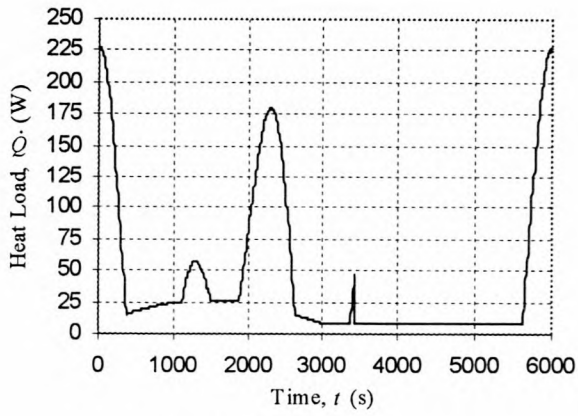

(b) Surface 2, +Y

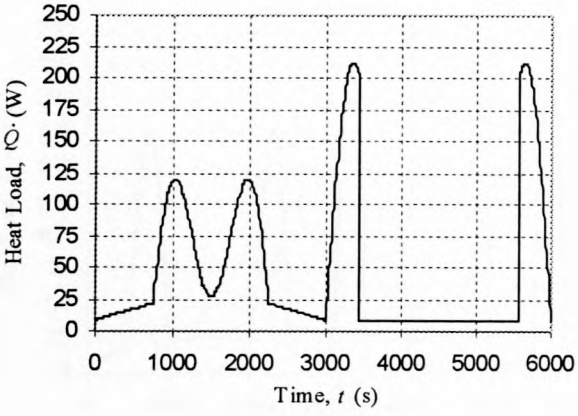

(c) Surface 3, +X

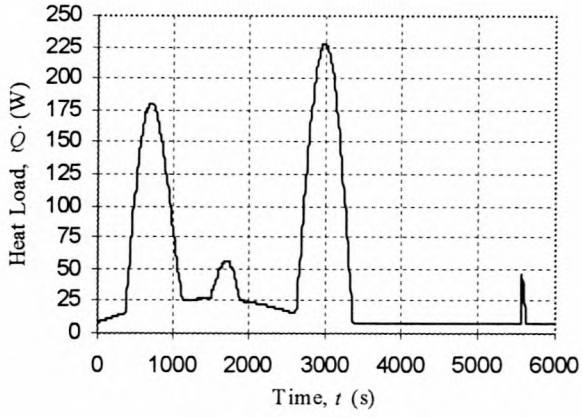

(d) Surface 4, -Y

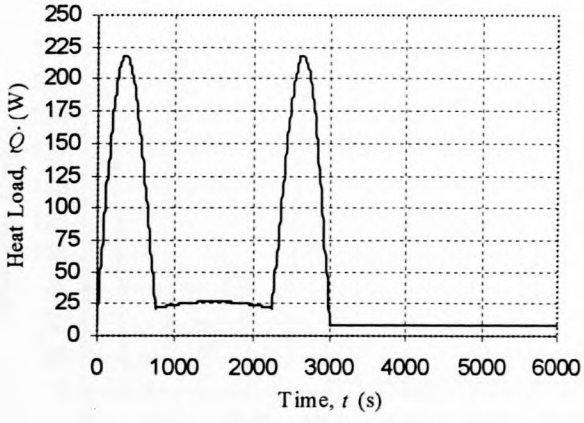

(e) Surface 5, -X

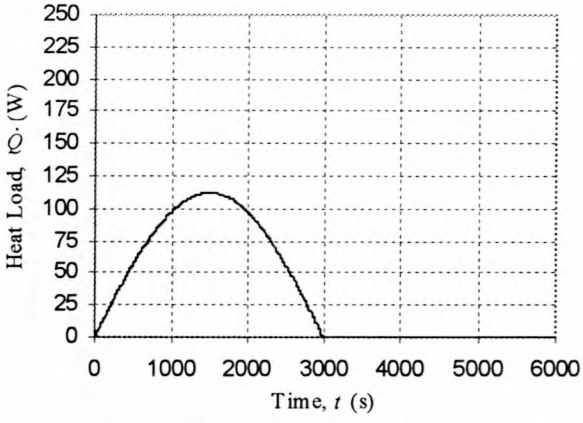

(f) Surface 6, -Z

Figure C4 Environmental heat loads on SUNSAT for a circular polar sun-synchronous orbit with a beta-angle of zero degrees and 4 rotations around the Z-axis per orbit

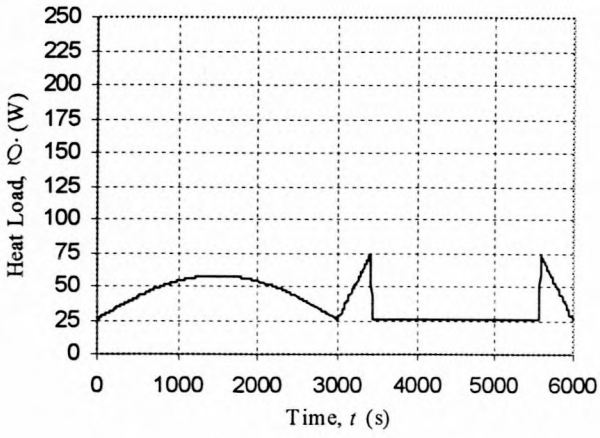

(a) Surface 1, +Z

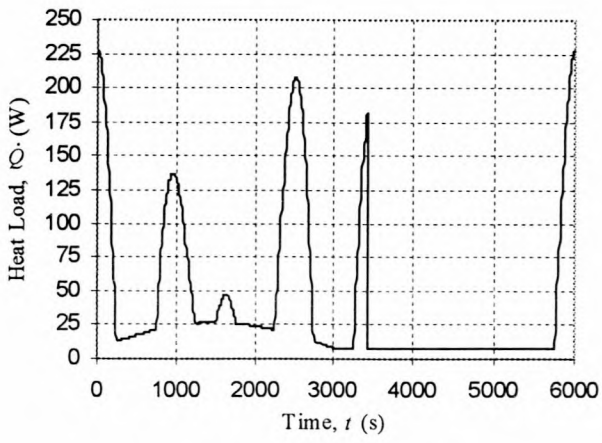

(b) Surface 2, +Y

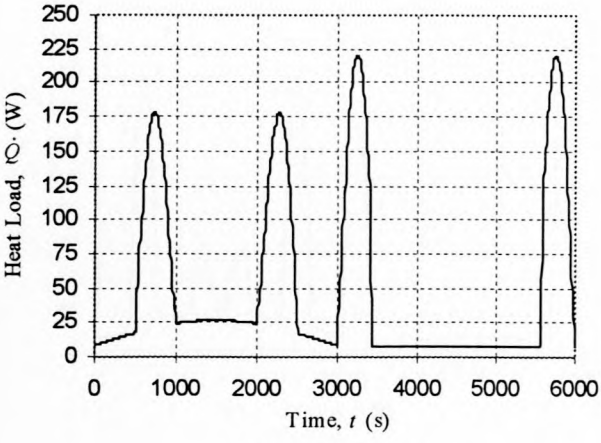

(c) Surface 3, +X

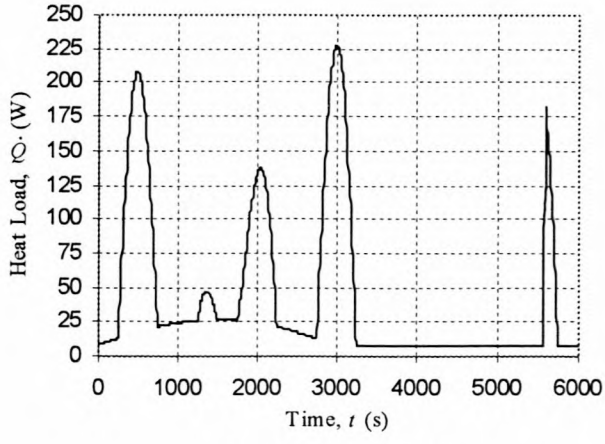

(d) Surface 4, -Y

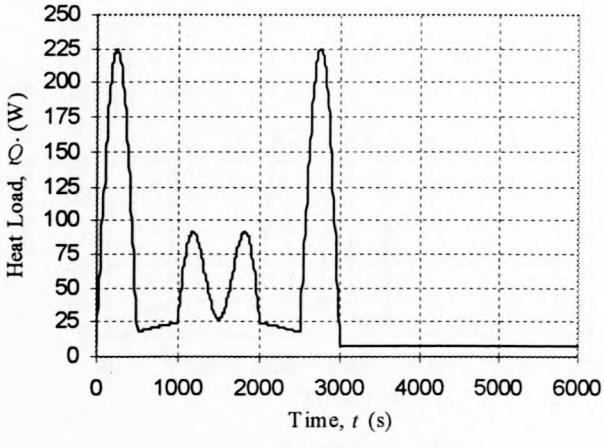

(e) Surface 5, -X

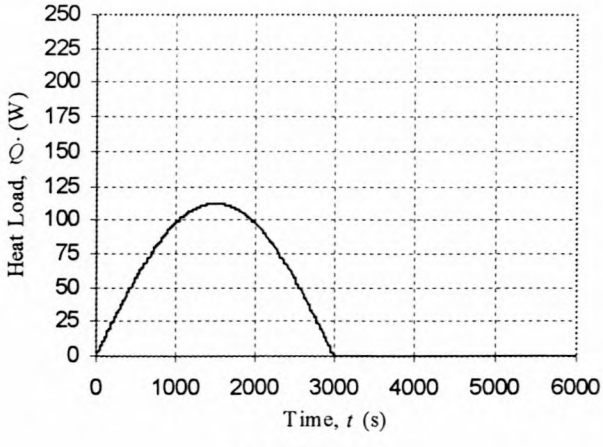

(f) Surface 6, -Z

Figure C5 Environmental heat loads on SUNSAT for a circular polar sun-synchronous orbit with a beta-angle of zero degrees and 6 rotations around the Z-axis per orbit

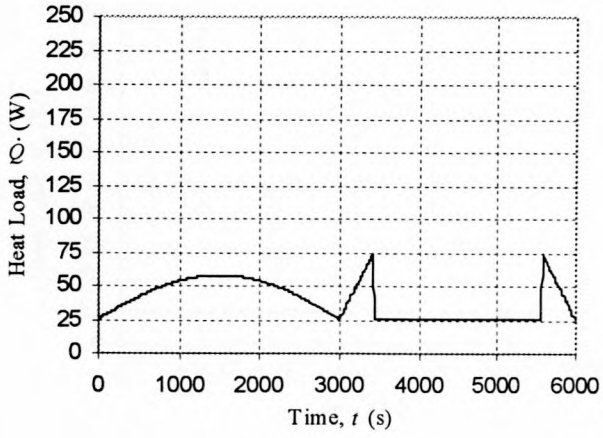

(a) Surface 1, +Z

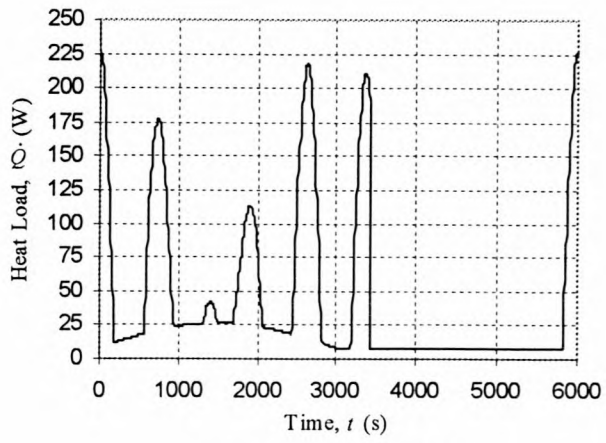

(b) Surface 2, +Y

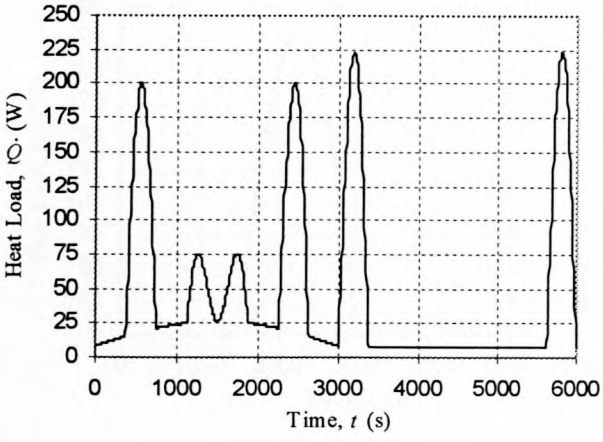

(c) Surface 3, +X

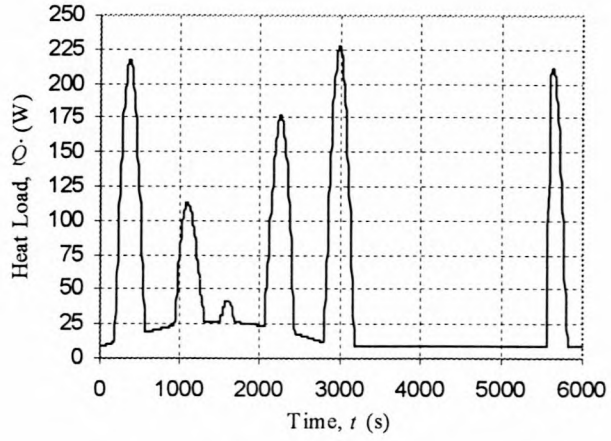

(d) Surface 4, -Y

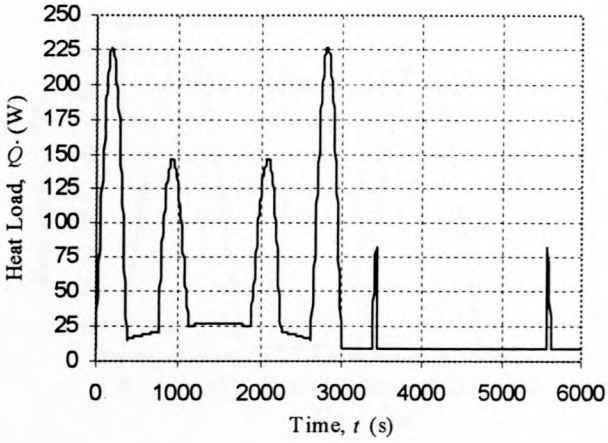

(e) Surface 5, -X

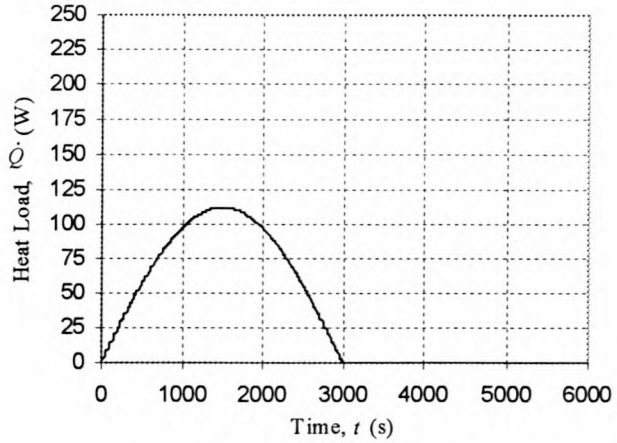

(f) Surface 6, -Z

Figure C6 Environmental heat loads on SUNSAT for a circular polar sun-synchronous orbit with a beta-angle of zero degrees and 8 rotations around the Z-axis per orbit

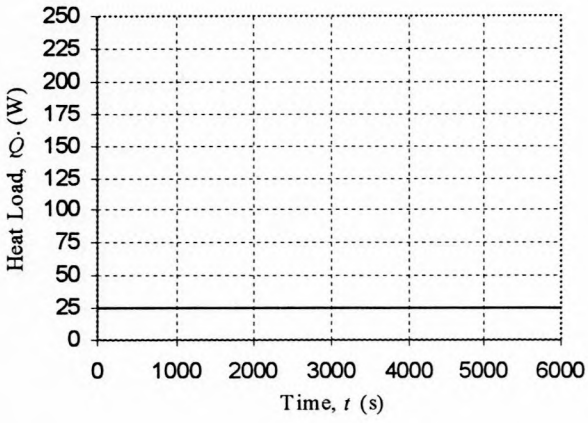

(a) Surface 1, +Z

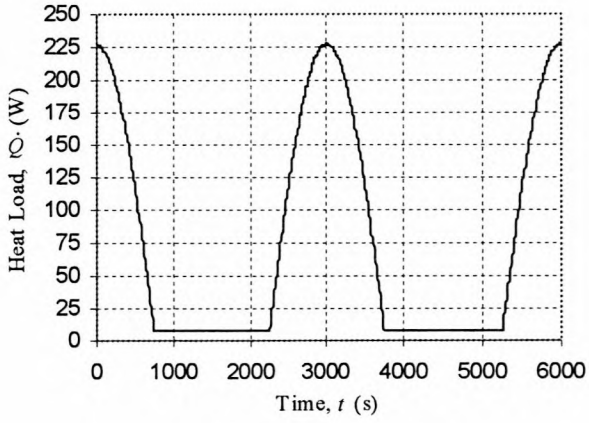

(b) Surface 2, +Y

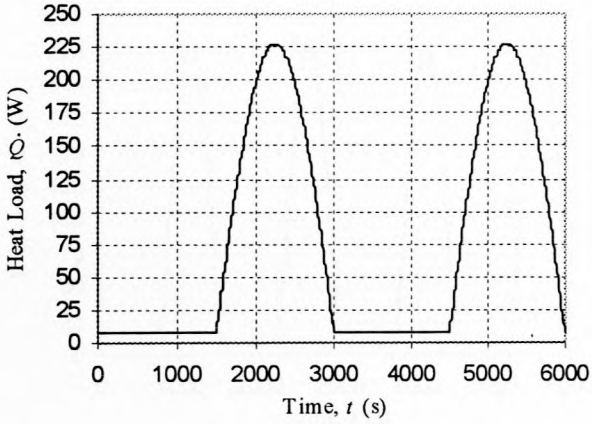

(c) Surface 3, +X

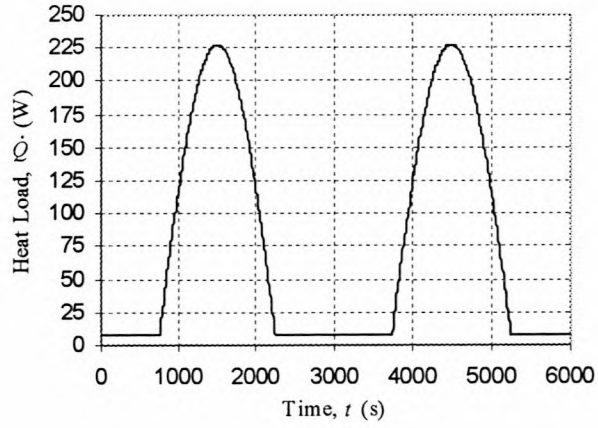

(d) Surface 4, -Y

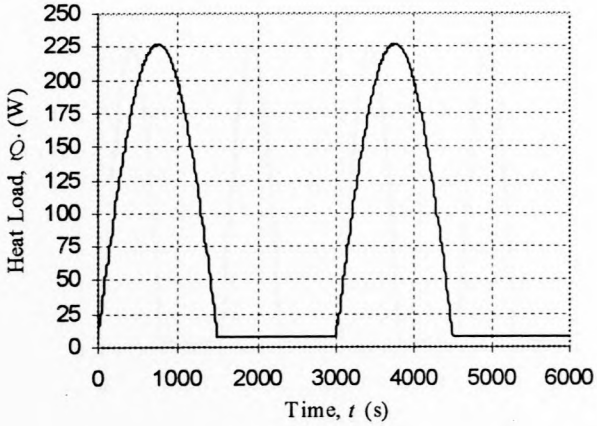

(e) Surface 5, -X

Figure C7 Environmental heat loads on SUNSAT for a circular polar sun-synchronous orbit with a beta-angle of ninety degrees and 2 rotations around the Z-axis per orbit

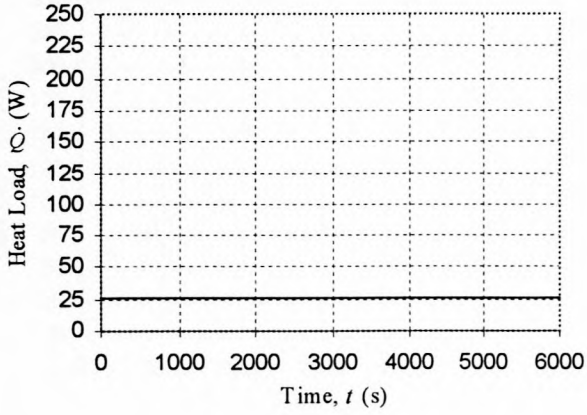

(a) Surface 1, +Z

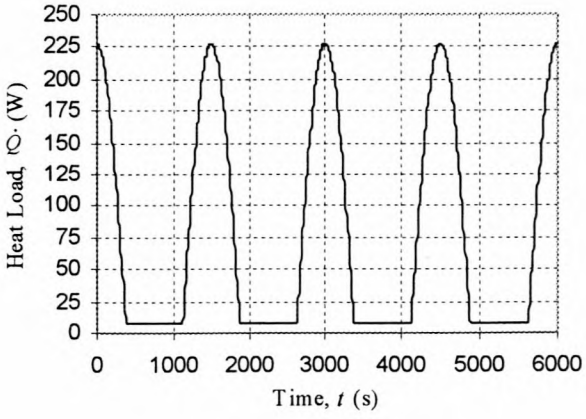

(b) Surface 2, +Y

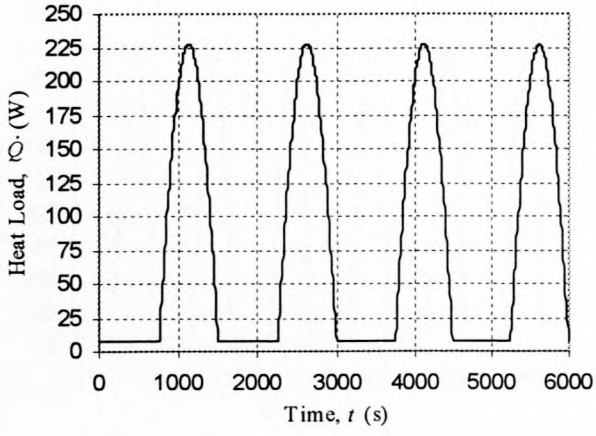

(c) Surface 3, +X

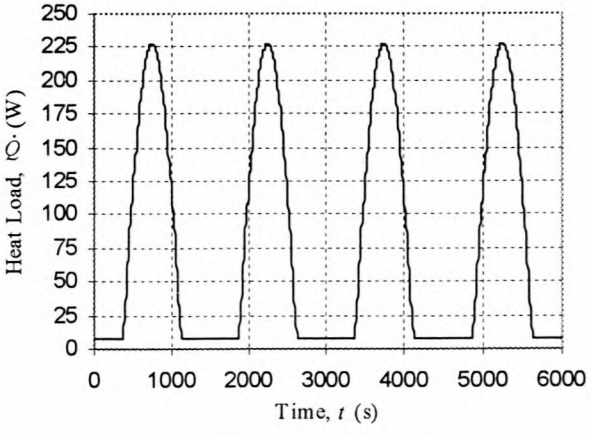

(d) Surface 4, -Y

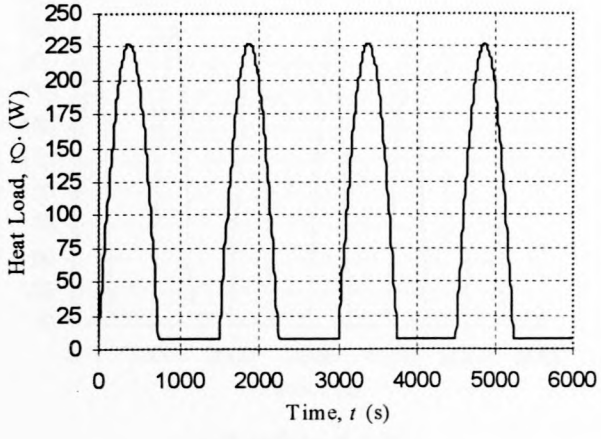

(e) Surface 5, -X

Figure C8 Environmental heat loads on SUNSAT for a circular polar sun-synchronous orbit with a beta-angle of ninety degrees and 4 rotations around the Z-axis per orbit

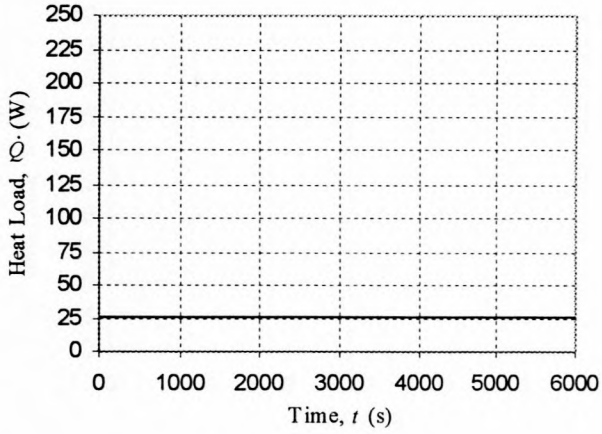

(a) Surface 1, +Z

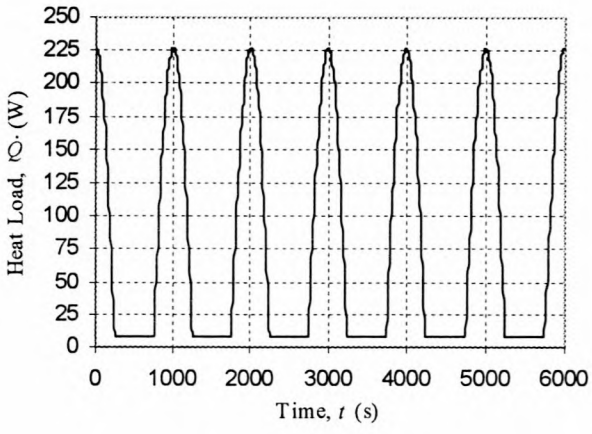

(b) Surface 2, +Y

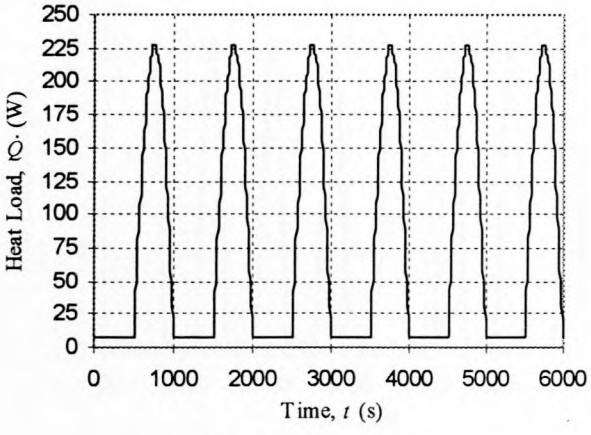

(c) Surface 3, +X

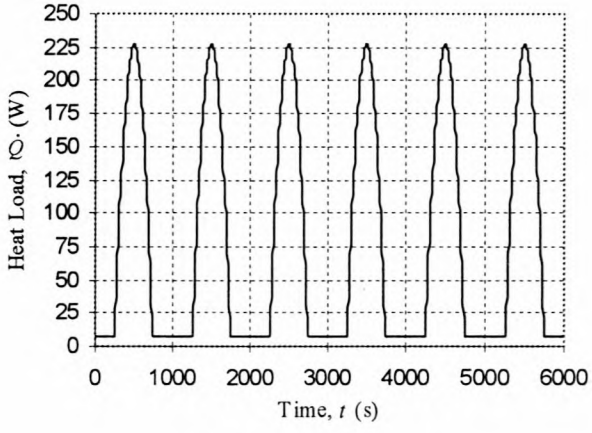

(d) Surface 4, -Y

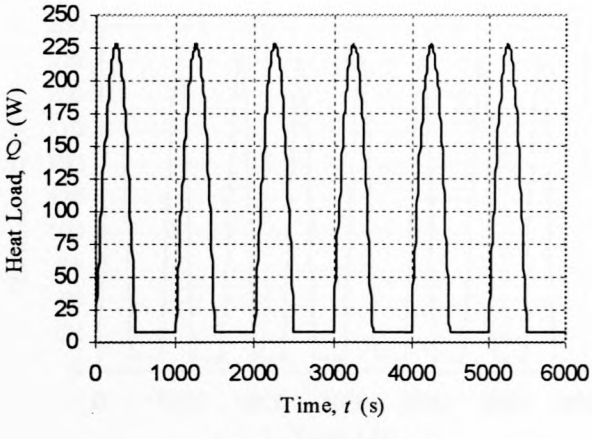

(e) Surface 5, -X

Figure C9 Environmental heat loads on SUNSAT for a circular polar sun-synchronous orbit with a beta-angle of ninety degrees and 6 rotations around the Z-axis per orbit

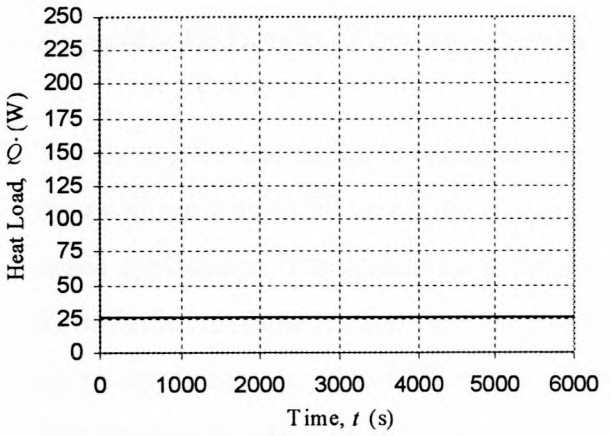

(a) Surface 1, +Z

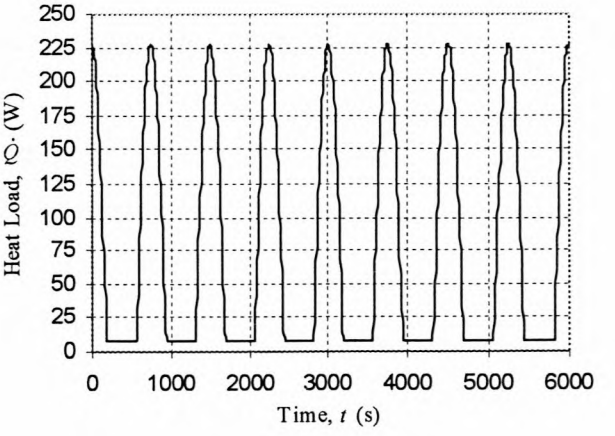

(b) Surface 2, +Y

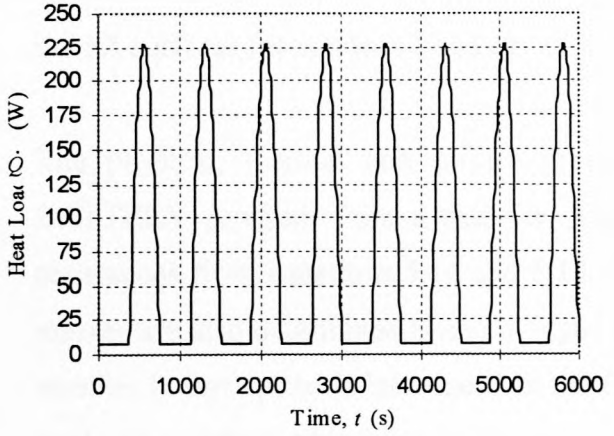

(c) Surface 3, +X

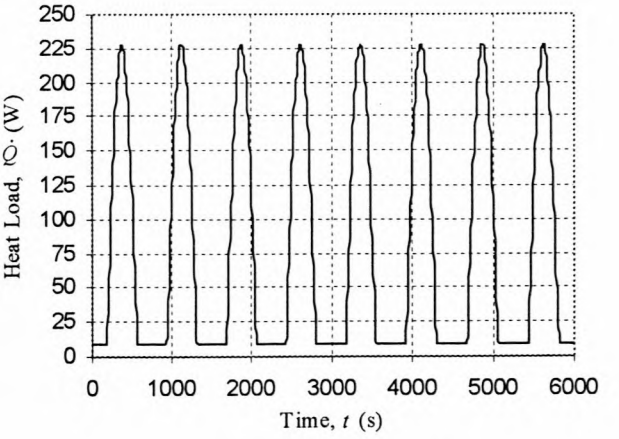

(d) Surface 4, -Y

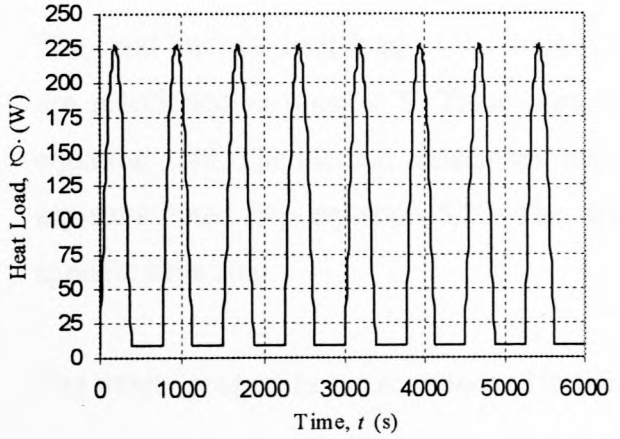

(e) Surface 5, -X

Figure C10 Environmental heat loads on SUNSAT for a circular polar sun-synchronous orbit with a beta-angle of ninety degrees and 8 rotations around the Z-axis per orbit.

Appendix D: Details of the Numerical Thermal Model of SUNSAT's Batteries

The theory for the computer program is presented in detail in chapter 5. The philosophy behind the program was to illustrate the use of theory and essential heat transfer principles in a simple space application. The numerical program, named "BATTERY", uses the resistance-capacitance formulation method to determine the transient temperature response of lumped-masses that make up an approximated SUNSAT model. The resistance-capacitance model is given by figure 5.4. The general equation used to solve the temperatures is given by equation 5.20. The BATTERY program is used in conjunction with the ORBIT-FLUX program. The environmental heat load inputs for the bottom and top-plates are obtained from the outputs from the ORBIT-FLUX for the ±Z surfaces (or surfaces 1 and 6).

The physical, thermal and surface properties of the lumped-masses are inputted into the BATTERY program from a text file. These properties are used in determining the thermal resistances from equations 5.16 and 5.19. The geometrical and mass properties of the lumped-masses are also determined from the input variables. The view factor of the earth as seen by the satellite bottom-plate is introduced in the ORBIT-FLUX program in determining the total heat load. The surface emissivity of the bottom-plate is relevant to both programs and thus not a "real" variable in the BATTERY program.

The total internal heat load of the bottom-plate, battery (combined batteries), tray 2 and tray 3 are mentioned in chapter 5. These replace the product of volumetric heating and volume in equation 5.20. The thermal resistances, mass, thermal capacitances and environmental heat loads are substituted into equation 5.20. The initial temperature is set and the iteration is run for a specific time step.

The model properties are summarized in table D1.

Table D1 Properties of numerical lumped-mass model of SUNSAT's batteries

Lumped-mass	Outer Dimensions (m)	ρ (kg/m^3)	c (J/kgK)	k_x, k_y, k_z (W/mK)	Internal Heat Load (W)	α (BOL)	ε (BOL)
Top-plate	0.45 x 0.45 x 0.014	2673	500	30	0	0.73	0.73
Tray 3	0.45 x 0.45 x 0.176	320	500	15	4	-	-
Tray 2	0.45 x 0.45 x 0.176	320	500	15	4	-	-
Tray 1	0.45 x 0.45 x 0.1	1470	500	100	0	0.15	0.15
Battery	0.15 x 0.15 x 0.1	2500	1000	5	4	0.5	0.5
Bottom-tray	0.45 x 0.45 x 0.01	1470	900	100	0	-	-
Bottom-plate	0.45 x 0.45 x 0.024	1132	500	30	18	0.15	0.15

Appendix E: SUNSAT Lumped-Mass Thermal Model Results

This appendix contains the results of the numerical lumped-mass model as well as the TAS lumped-mass model of SUNSAT (details in chapter 6) for various configurations.

The numerical lumped-mass model consists of a single interior node that represents the temperature of the model (figure 6.4). The TAS lumped-mass model consists of 27 nodes (figure 6.6) with the middle one representing the temperature of the model. The hemispherical emissivity of all the surfaces is used as a variable in the results that follow to show the effect that it has on the satellite temperature. The internal heat generation is also varied to investigate the effect thereof. The tables that follow summarize the variables used in each of the respective tests. The temperature data was also plotted versus time in figures E1 to E8. Test 1a corresponds to figures E1 and E2; Test 1b corresponds to figures E3 and E4 etc.

(**Note**: dynamic equilibrium is only approximately reached for the 6^{th} orbit and therefore between the time 30000 s to 36000 s, the correct average results are attained)

Conclusions of SUNSAT Lumped-Mass models, for Tests 1a, 1b, 1c and 1d

It is noticeable from all the results and figures that the TAS lumped-mass model temperatures are higher that that of the numerical model for all the tests. The difference in the temperatures fluctuates at about ±12°C for all the tests. This difference is possibly attributed to the fact that the numerical model emits radiation to space at the temperature of the single internal node as compared to the TAS model which emits heat at the temperature of the nodes on the outer surface; and the temperature of these outer surface nodes are lower than for the single node of the numerical model, and thus the heat radiated to space at the fourth power in Kelvin is higher for the numerical model.

The results also showed that the change in surface emissivity from 0.8 to 0.6 resulted in higher temperatures for the comparison of tests 1a with 1b, and tests 1c with 1d. The increase in internal heat generation from 30 to 80 W resulted in higher temperatures for the comparison of tests 1a with 1d and tests 1b with 1c. These differences were consistent for both the numerical and the TAS lumped-mass models.

When one compares the number of control volumes of each of the two models, it is evident the TAS model accounts for more model detail, and thus gives a better representation of the temperature response of the model. The numerical model can at best be used as a rough approximation of a satellite in orbit. The TAS model, although more accurate than the numerical model, is not a true physical representation of an actual satellite. For this reason another model would still need to be developed to represent SUNSAT more closely. This model is SUNSAT 2.

SUNSAT Lumped-mass, Test 1a

Table E1 Results of the Numerical and TAS Lumped-Mass models for a medium Z-axis spin rate, maximum eclipse, high surface emissivity and low internal heat generation

Model: SUNSAT Numerical and TAS Lumped-Mass					
Mission: Polar sun-synchronous circular orbit for β-angle = 0° and 4 Z-axis rotations per orbit					
Orbit Parameters					
Beta angle	Z-axis rot./orbit	Ht. above Earth	Orbit Period	Eclipse Period	
0°	4	700 km	100 min	± 36 min	
Heating					
Albedo	Solar Heat Flux	Earth Heat Flux	Internal Heat		
0.36	1353 W/m^2	216 W/m^2	30 W		
Surface avg. Heating as determined from ORBIT-FLUX Computer Program					
+Y	-Y	+X	-X	+Z	-Z
40.30 W	40.30 W	42.52 W	41.17 W	34.97 W	61.05 W
Surface Properties (BOL)					
ε_{sp}	ε_{bp}	ε_{tp}	α_{sp}	α_{bp}	α_{tp}
0.8	0.8	0.8	0.7	0.2	0.7
Results					
	Max. Temperature (°C)	**Min Temperature (°C)**	**Avg. Temperature (°C)**		
Numerical Model	-12.28	-19.63	-15.28		
TAS Model	-0.05	-7.10	-3.42		

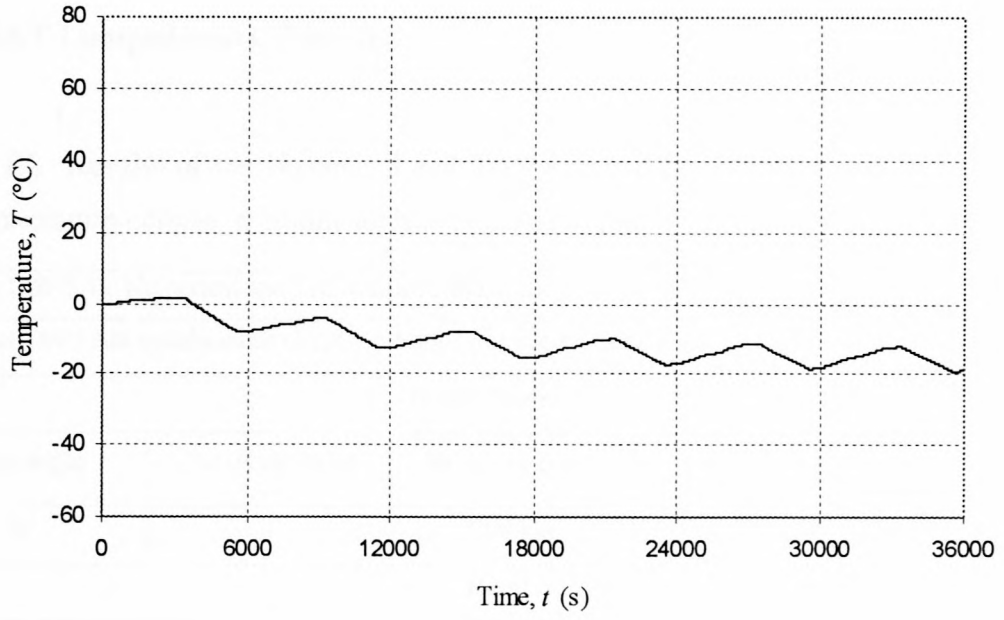

Figure E1 Numerical lumped-mass model temperature response for a 30 W orbit-averaged internal heat load and surface emissivity of 0.8

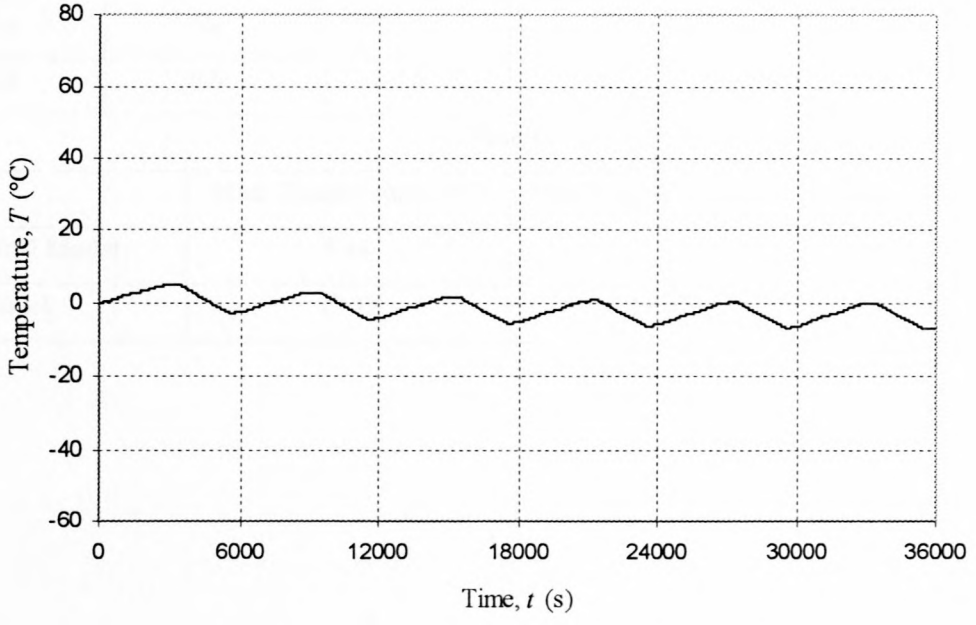

Figure E2 TAS lumped-mass model temperature response for a 30 W orbit-averaged internal heat load and surface emissivity of 0.8

SUNSAT Lumped-mass, Test 1b

Table E2 Results of the Numerical and TAS Lumped-Mass models for a medium Z-axis spin rate, maximum eclipse, medium surface emissivity and low internal heat generation

Model: SUNSAT Numerical and TAS Lumped-Mass					
Mission: Polar sun-synchronous circular orbit for β-angle = 0° and 4 Z-axis rotations per orbit					
Orbit Parameters					
Beta angle	Z-axis rot./orbit	Ht. above Earth	Orbit Period	Eclipse Period	
0°	4	700 km	100 min	± 36 min	
Heating					
Albedo	Solar Heat Flux	Earth Heat Flux	Internal Heat		
0.36	1353 W/m^2	216 W/m^2	30 W		
Surface avg. Heating as determined from ORBIT-FLUX Computer Program					
+Y	-Y	+X	-X	+Z	-Z
38.24 W	38.24 W	40.46 W	39.11 W	27.91 W	61.05 W
Surface Properties (BOL)					
ε_{sp}	ε_{bp}	ε_{tp}	α_{sp}	α_{bp}	α_{tp}
0.6	0.6	0.6	0.7	0.2	0.7

Results			
	Max. Temperature (°C)	**Min Temperature (°C)**	**Avg. Temperature (°C)**
Numerical Model	5.44	-1.70	2.40
TAS Model	17.93	11.07	14.49

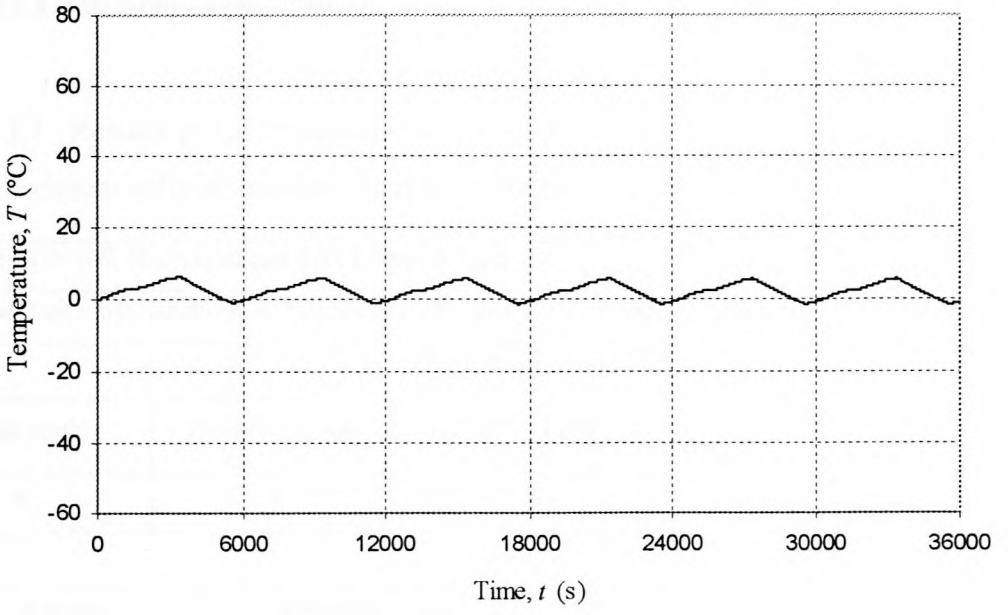

Figure E3 Numerical lumped-mass model temperature response for a 30 W orbit-averaged internal heat load and surface emissivity of 0.6

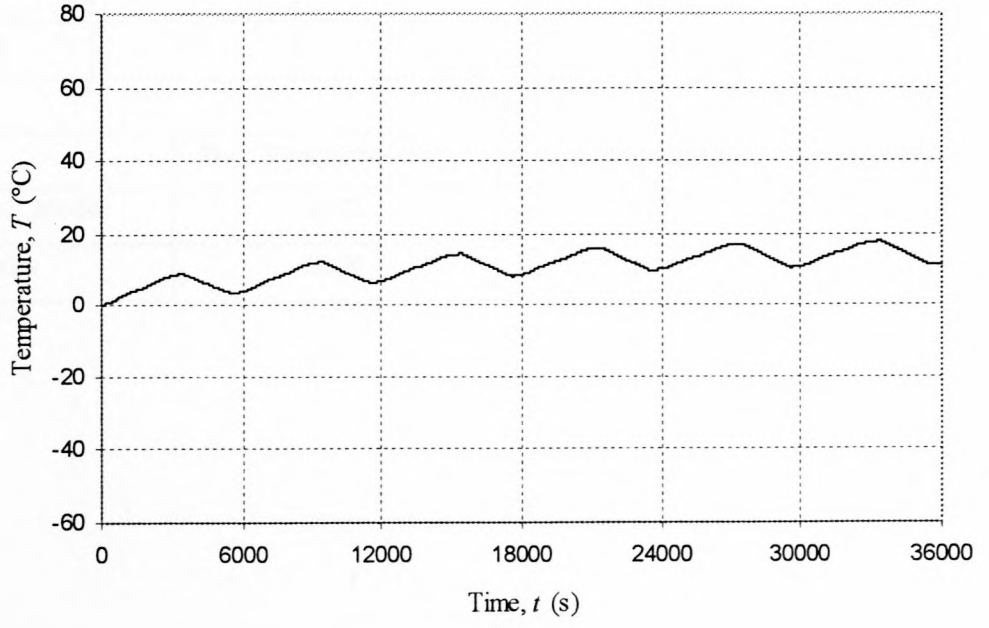

Figure E4 TAS lumped-mass model temperature response for a 30 W orbit-averaged internal heat load and surface emissivity of 0.6

SUNSAT Lumped-mass, Test 1c

Table E3 Results of the Numerical and TAS Lumped-Mass models for a medium Z-axis spin rate, maximum eclipse, medium surface emissivity and high internal heat generation

Model: SUNSAT Numerical and TAS Lumped-Mass					
Mission: Polar sun-synchronous circular orbit for β-angle = 0° and 4 Z-axis rotations per orbit					
Orbit Parameters					
Beta angle	Z-axis rot./orbit	Ht. above Earth	Orbit Period	Eclipse Period	
0°	4	700 km	100 min	± 36 min	
Heating					
Albedo	Solar Heat Flux	Earth Heat Flux	Internal Heat		
0.36	1353 W/m^2	216 W/m^2	80 W		
Surface avg. Heating as determined from ORBIT-FLUX Computer Program					
+Y	-Y	+X	-X	+Z	-Z
38.24 W	38.24 W	40.46 W	39.11 W	27.91 W	61.05 W
Surface Properties (BOL)					
ε_{sp}	ε_{bp}	ε_{tp}	α_{sp}	α_{bp}	α_{tp}
0.6	0.6	0.6	0.7	0.2	0.7
Results					
	Max. Temperature (°C)	**Min Temperature (°C)**	**Avg. Temperature (°C)**		
Numerical Model	15.78	8.77	12.73		
TAS Model	28.90	21.74	25.45		

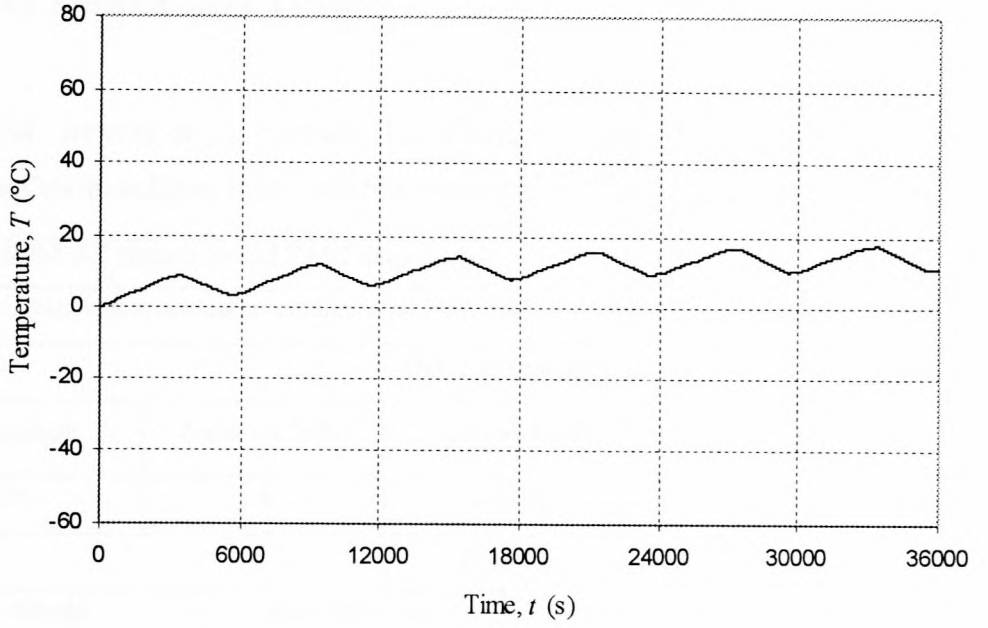

Figure E5 Numerical lumped-mass model temperature response for an 80 W orbit-averaged internal heat load and surface emissivity of 0.6

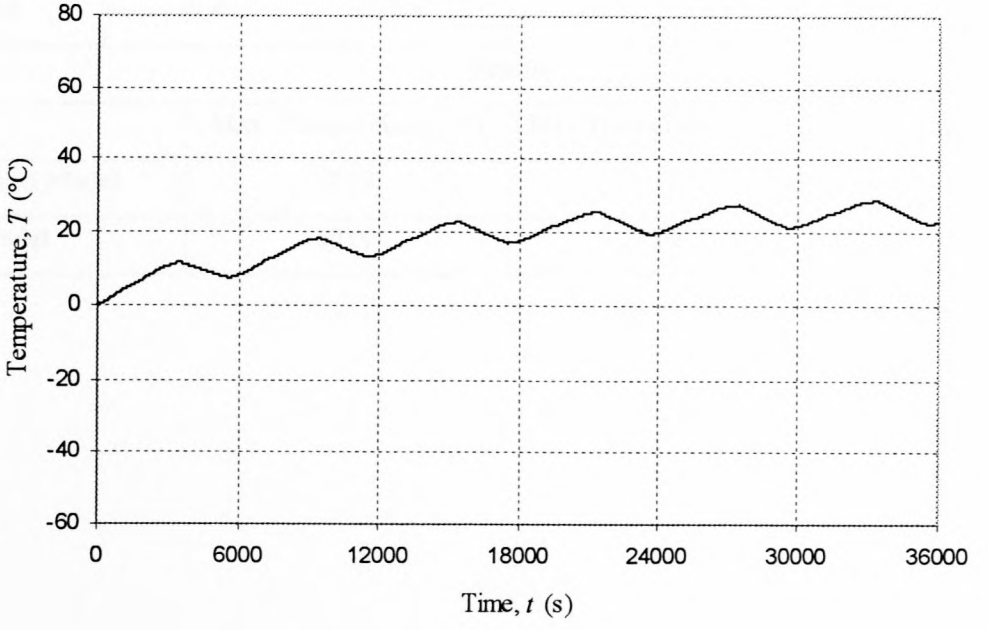

Figure E6 TAS lumped-mass model temperature response for an 80 W orbit-averaged internal heat load and surface emissivity of 0.6

SUNSAT Lumped-mass, Test 1d

Table E4 Results of the Numerical and TAS Lumped-Mass models for a medium Z-axis spin rate, maximum eclipse, high surface emissivity and high internal heat generation

Model: SUNSAT Numerical and TAS Lumped-Mass					
Mission: Polar sun-synchronous circular orbit for β-angle = 0° and 4 Z-axis rotations per orbit					
Orbit Parameters					
Beta angle	Z-axis rot./orbit	Ht. above Earth	Orbit Period	Eclipse Period	
0°	4	700 km	100 min	± 36 min	
Heating					
Albedo	Solar Heat Flux	Earth Heat Flux	Internal Heat		
0.36	1353 W/m^2	216 W/m^2	80 W		
Surface avg. Heating as determined from ORBIT-FLUX Computer Program					
+Y	-Y	+X	-X	+Z	-Z
40.30 W	40.30 W	42.52 W	41.17 W	34.97 W	61.05 W
Surface Properties (BOL)					
ε_{sp}	ε_{bp}	ε_{tp}	α_{sp}	α_{bp}	α_{tp}
0.8	0.8	0.8	0.7	0.2	0.7
Results					
	Max. Temperature (°C)	**Min Temperature (°C)**	**Avg. Temperature (°C)**		
Numerical Model	-2.78	-10.00	-5.79		
TAS Model	10.00	3.08	6.61		

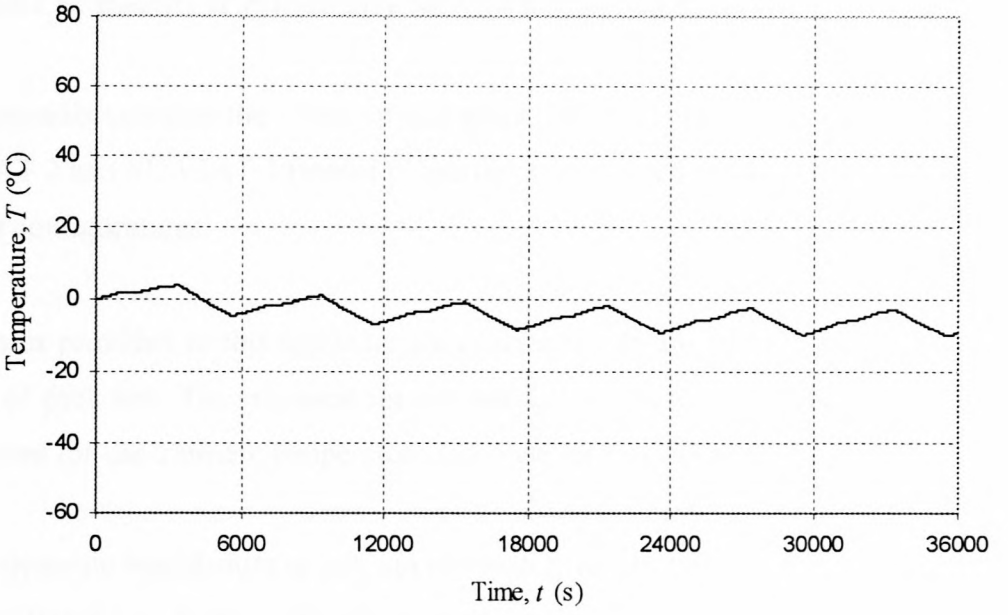

Figure E7 Numerical lumped-mass model temperature response for an 80 W orbit-averaged internal heat load and surface emissivity of 0.8

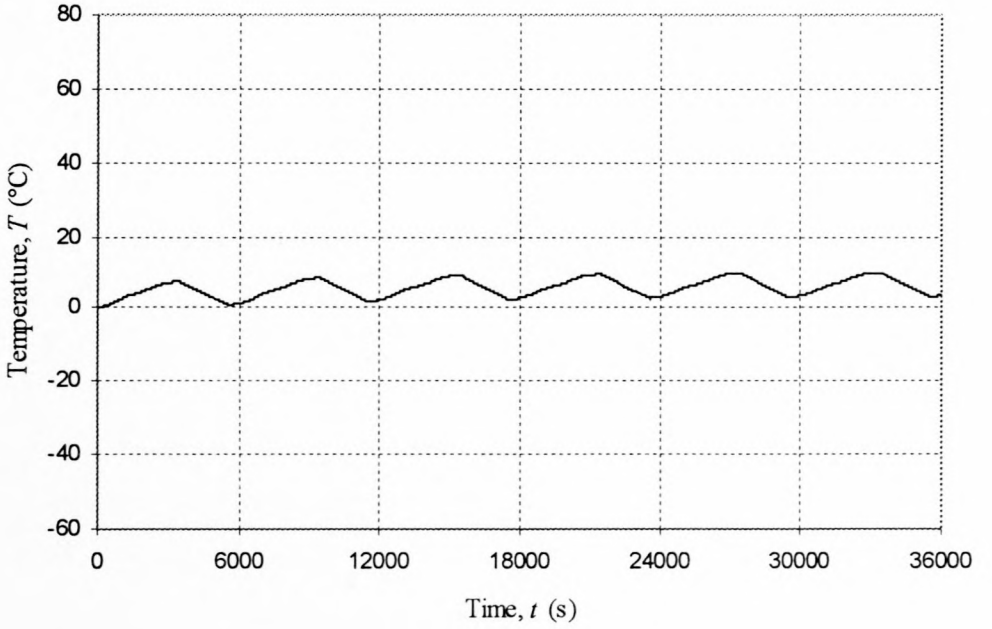

Figure E8 TAS lumped-mass model temperature response for an 80 W orbit-averaged internal heat load and surface emissivity of 0.8

Appendix F: Results of Progressive SUNSAT Thermal Models

This appendix contains the tabulated and graphical results of the TAS generated thermal models SUNSAT 2 and SUNSAT 3 (model properties summarized in tables 6.1 and 6.2 respectively) for various configurations.

The tables provided in this appendix summarize the details of the variables used as well as the results of each test. The graphical results that follow are for the specific tabulated variables and are plotted for the transient temperature response for 6 orbits around the earth.

(**Note**: dynamic equilibrium is only approximately reached for the 6^{th} orbit and therefore between the time 30000 s to 36000 s, the correct average results are attained)

SUNSAT 2, Test 2a

Table F1 Data and temperature results of the TAS SUNSAT 2 model for a medium Z-axis spin rate and maximum eclipse

Model: SUNSAT 2					
Mission: Polar sun-synchronous circular orbit for β-angle = 0° and 4 Z-axis rotations per orbit					
Orbit Parameters					
Beta angle	Z-axis rot./orbit	Ht. above Earth	Earth Radius	Orbit Period	Eclipse Period
0°	4	700 km	6371 km	100 min	± 36 min
Heating					
Albedo	Solar Heat Flux	Earth Heat Flux	Internal Heat		
0.36	1353 W/m^2	216 W/m^2	30 W		
Surface avg. Heating as determined from ORBIT-FLUX Computer Program					
+Y	-Y	+X	-X	+Z	-Z
44.88 W	44.88 W	47.41 W	45.88 W	8.00 W	35.76 W
Surface Properties (BOL)					
ε_{sp}	ε_{bp}	ε_{tp}	α_{sp}	α_{bp}	α_{tp}
0.80	0.15	0.73	0.80	0.08	0.41

Results			
	Max. Temperature (°C)	**Min Temperature (°C)**	**Avg. Temperature (°C)**
+Y solar panel	14.02	-6.67	2.94
-Y solar panel	18.25	-6.43	3.13
+X solar panel	11.36	-5.84	3.57
-X solar panel	11.59	-4.79	3.4
+Z surface	10.05	-2.08	5.06
-Z surface	8.26	-5.47	3.3
Bottom-plate	9.98	-2.09	5.05
Battery	9.22	-3.75	4.04
Middle-body section	8.85	-4.53	3.63
Upper-body section	8.33	-5.38	3.33

Conclusions of SUNSAT 2, Test 2a

What is noticeable from the figures is that the general pattern is one of a average temperature around 5 °C. The outer surface of the solar panels has a very low rate of response to the environmental heating. The upper and lower temperature bounds are also very low on the solar panels. This could be accredited to the fact that the layer of resistance material between the solar panels and the satellite body is not of high enough resistance to reduce the rate at which heat is transported from the solar panels to the main body, redistributed, and then reradiated to space.

The temperature response of the body sections is very similar to each other and to the solar panels. It would be expected that the temperature of the body would rise high with the very little insulation offered by the solar panels; but it doesn't because the body of satellite redistributes this heat efficiently to the cold solar panels which then radiate this heat to space.

In many ways, SUNSAT 2 has served only to establish the need for a more complicated lumped-mass model. The resistance to heat transport from the solar panels to the main body will be accounted for with the inclusion of an approximated SUNSAT solar panel mounting in the SUNSAT 3 model.

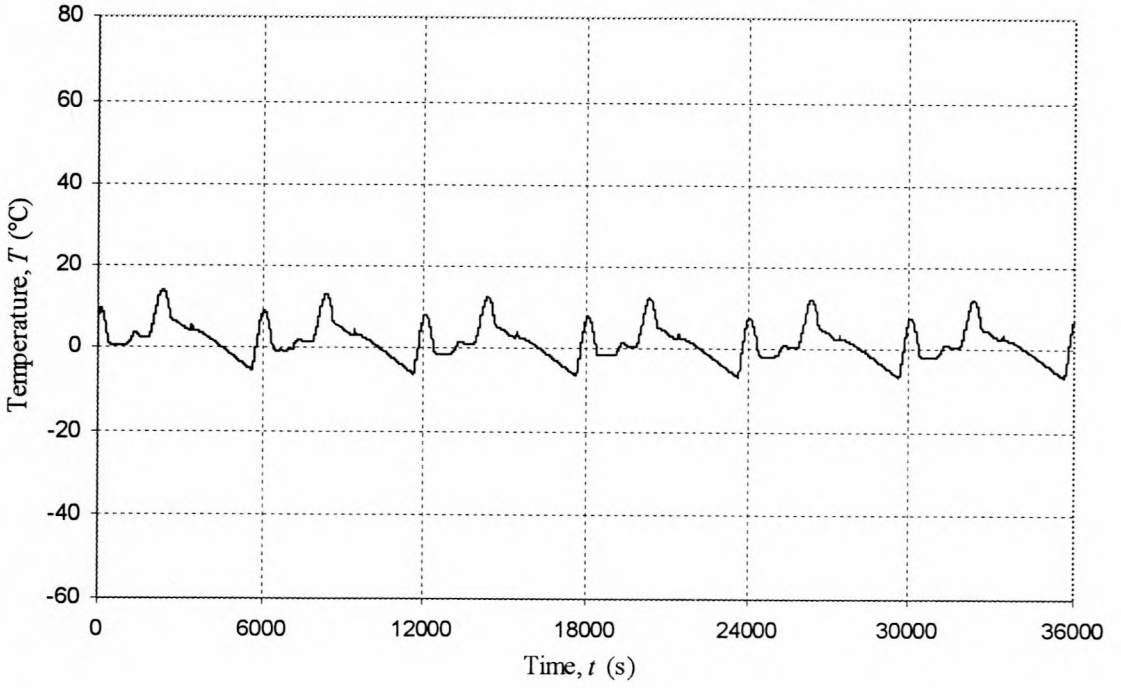

Figure F1 Temperature response of SUNSAT 2 +Y solar panel surface

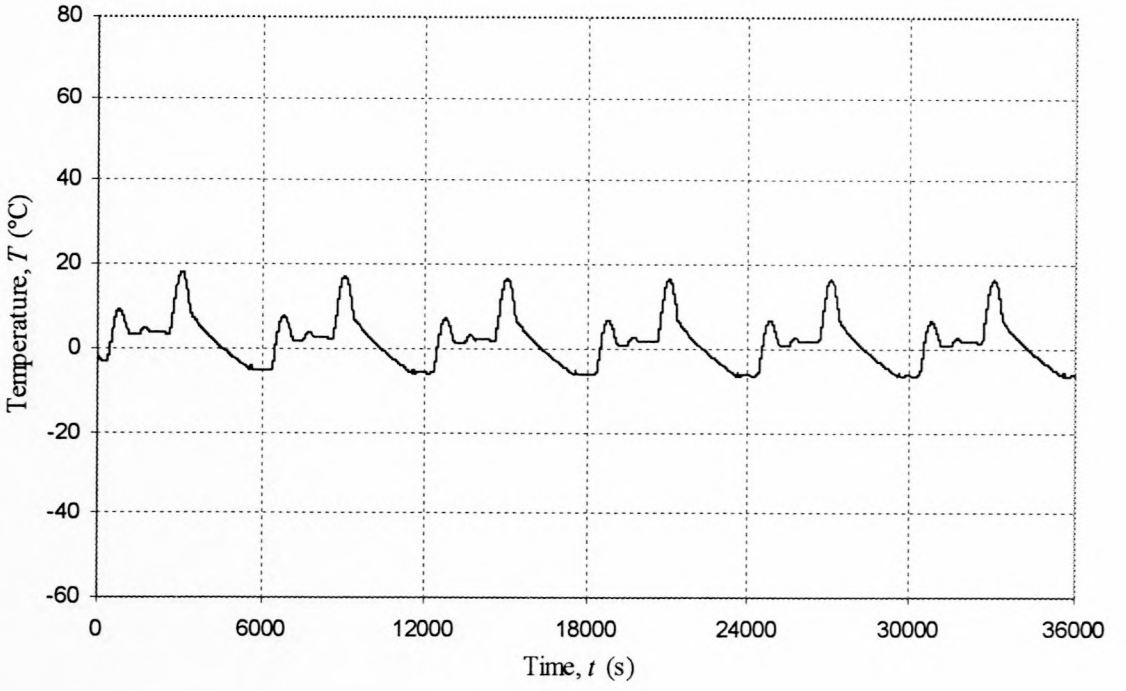

Figure F2 Temperature response of SUNSAT 2 -Y solar panel surface

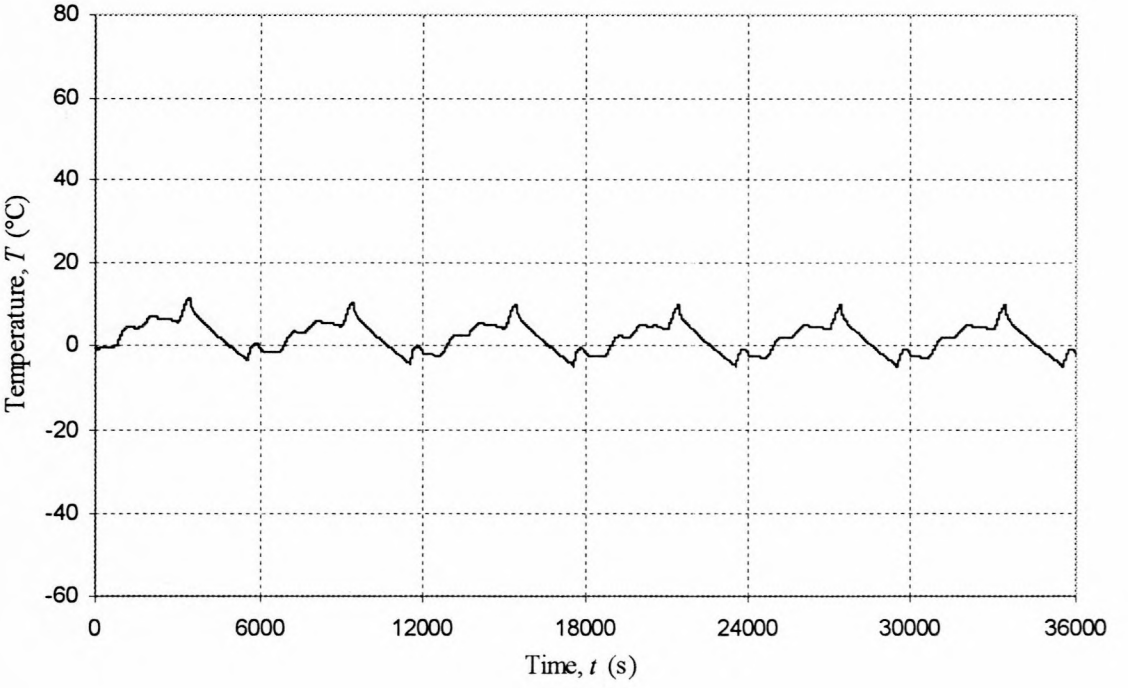

Figure F3 Temperature response of SUNSAT 2 +X solar panel surface

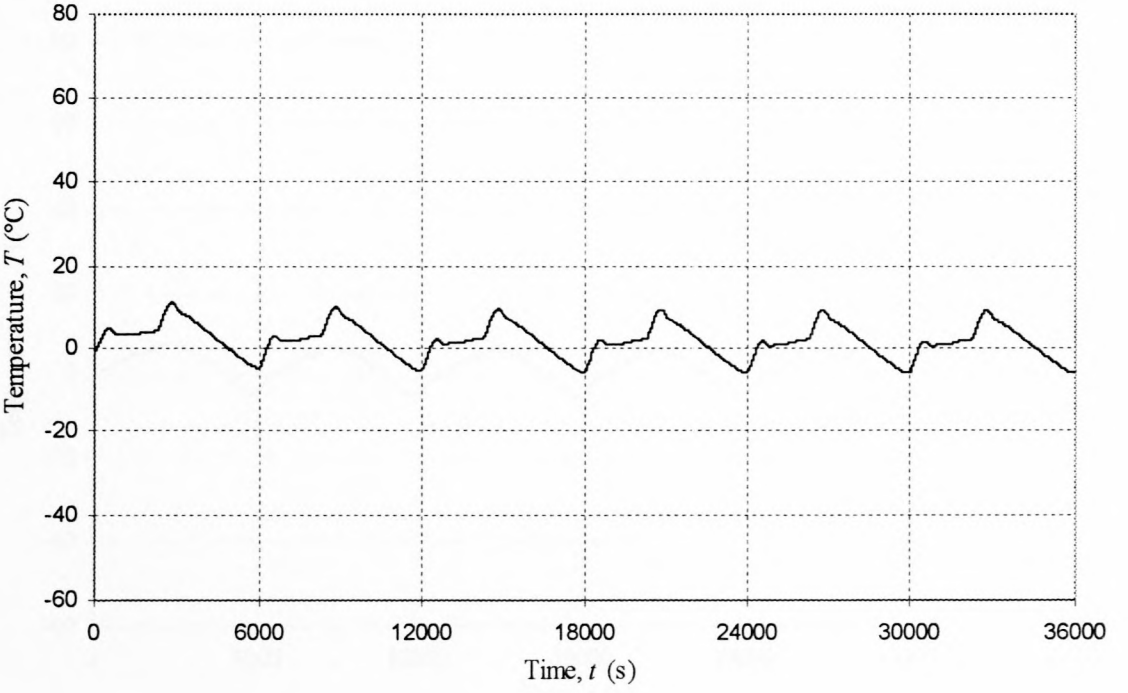

Figure F4 Temperature response of SUNSAT 2 -X solar panel surface

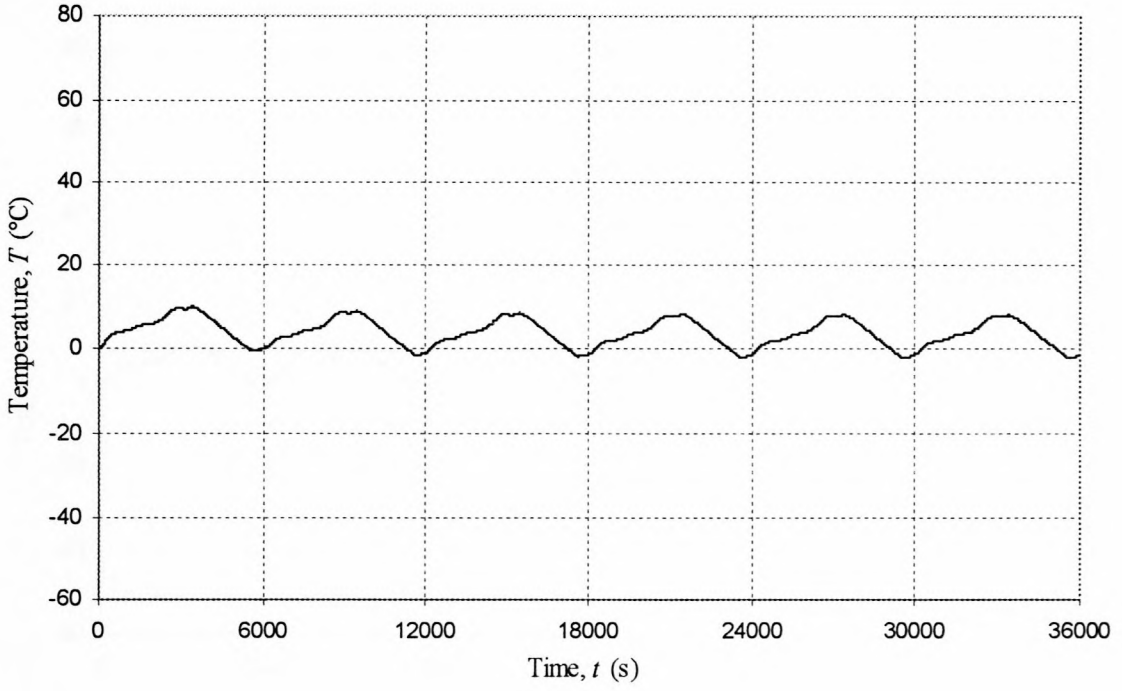

Figure F5 Temperature response of SUNSAT 2 top-plate +Z surface

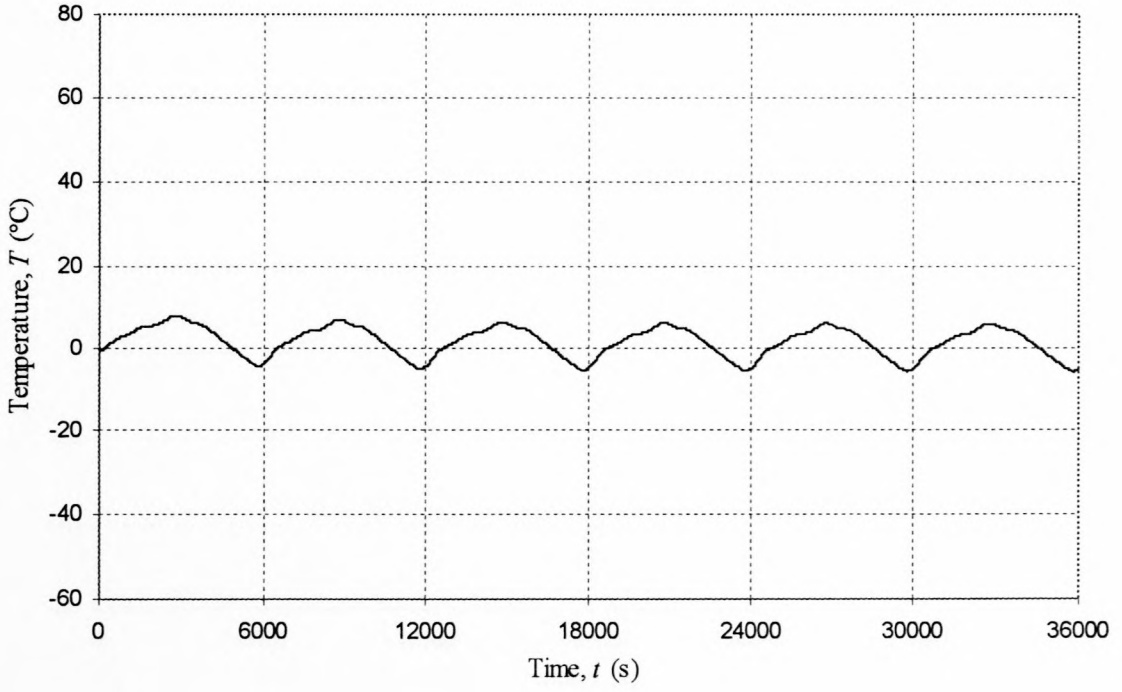

Figure F6 Temperature response of SUNSAT 2 bottom-plate -Z surface

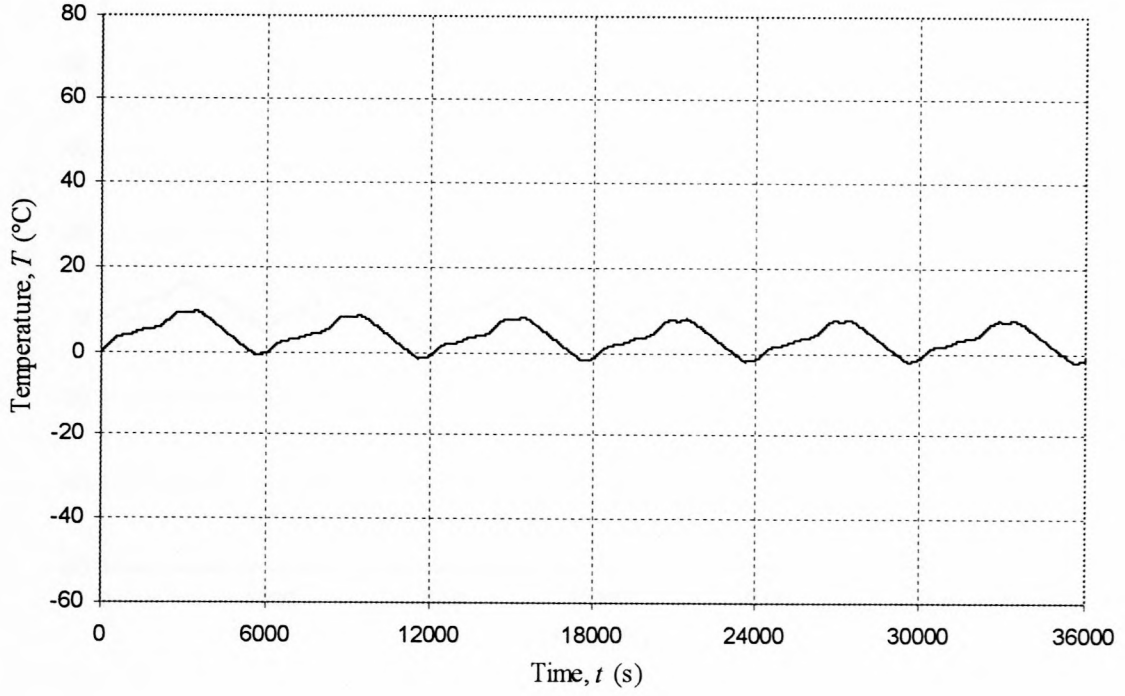

Figure F7 Temperature response of SUNSAT 2 bottom-plate

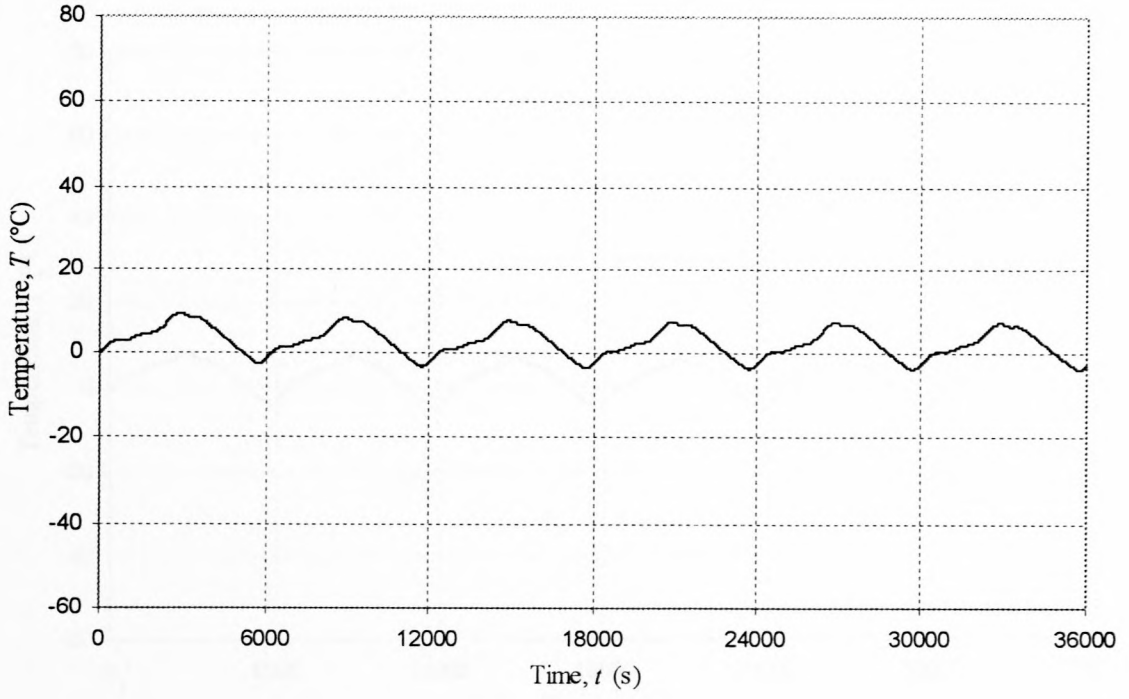

Figure F8 Temperature response of SUNSAT 2 battery

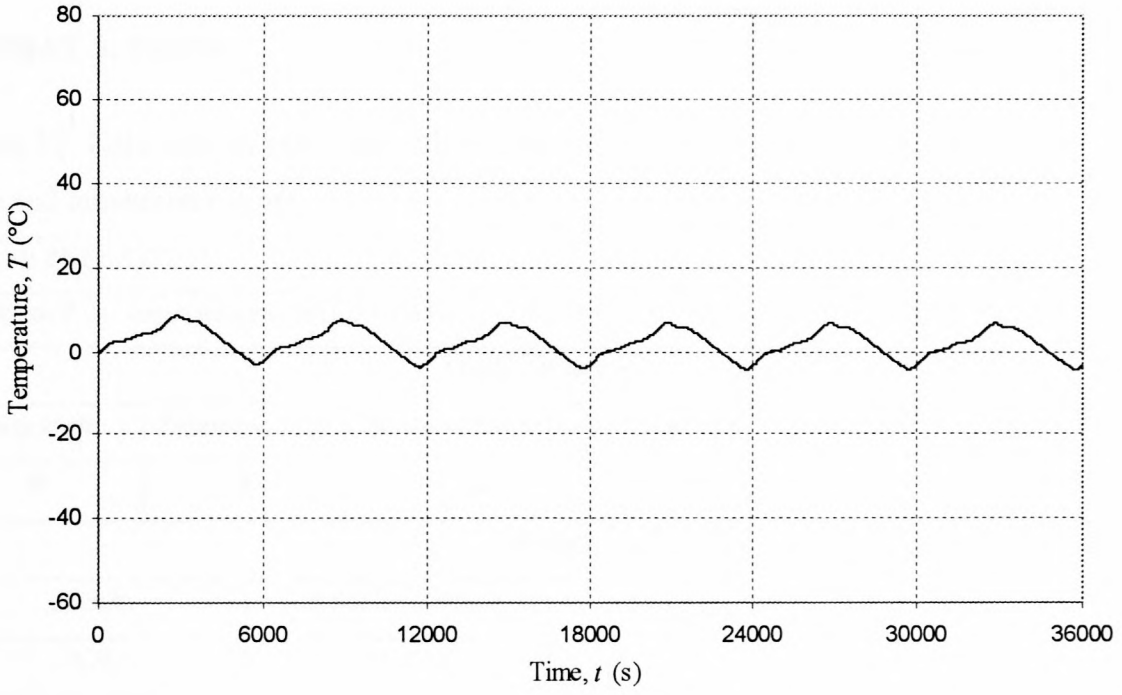

Figure F9 Temperature response of SUNSAT 2 middle-body section

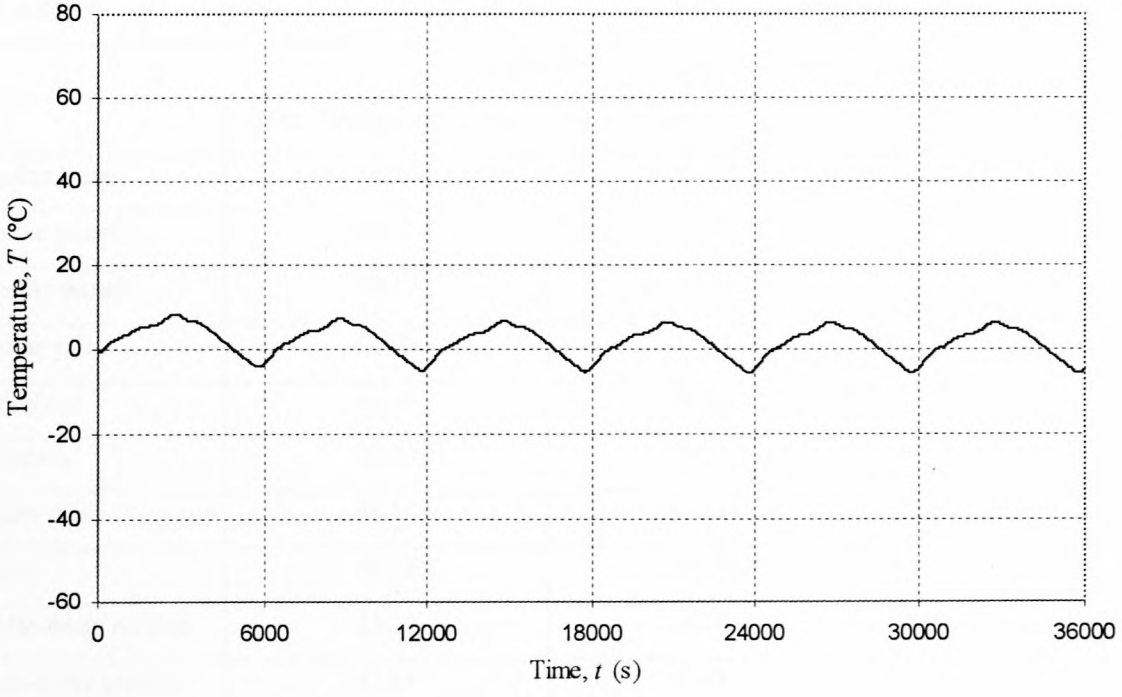

Figure F10 Temperature response of SUNSAT 2 upper-body section

SUNSAT 3, Test 3a

Table F2 Data and temperature results of the TAS SUNSAT 3 model for a medium Z-axis spin rate and maximum eclipse

Model: SUNSAT 3					
Mission: Polar sun-synchronous circular orbit for β-angle = 0° and 4 Z-axis rotations per orbit					
Orbit Parameters					
Beta angle	Z-axis rot./orbit	Ht. above Earth	Earth Radius	Orbit Period	Eclipse Period
0°	4	700 km	6371 km	100 min	± 36 min
Heating					
Albedo	Solar Heat Flux		Earth Heat Flux		Internal Heat
0.36	1353 W/m^2		216 W/m^2		30 W
Surface avg. Heating as determined from ORBIT-FLUX Computer Program (Appendix C)					
+Y	-Y	+X	-X	+Z	-Z
44.88 W	44.88 W	47.41 W	45.88 W	8.00 W	35.76 W
Surface Properties (BOL)					
ε_{sp}	ε_{bp}	ε_{tp}	α_{sp}	α_{bp}	α_{tp}
0.80	0.15	0.73	0.80	0.08	0.41

Results			
	Max. Temperature (°C)	**Min Temperature (°C)**	**Avg. Temperature (°C)**
+Y solar panel	56.89	-42.89	-11.09
-Y solar panel	68.12	-40.45	-10.98
+X solar panel	50.17	-41.73	-5.82
-X solar panel	64.55	-45.05	-12.84
+Z surface	44.37	38.59	40.86
-Z surface	35.89	10.22	21.03
Bottom-plate	44.13	37.41	40.64
Battery	30.52	25.37	27.95
Middle-body section	25.22	18.46	21.95
Upper-body section	32.85	11.88	21.46

Conclusions of SUNSAT3, Test 3a

The SUNSAT 3 model provides a more realistic approximation to the temperatures of the solar panel as direct result of including the spacer between the solar panel and the satellite body. The result of this effect is that the body temperatures are higher and more realistic since the heat flow rate out of the body is lessened. The body sections, battery, and top and bottom plates average ± 26°C, with a small gradient from the bottom surface to the top surface.

The low thermal capacitance of the solar panels allows them to respond very quickly to the varying environmental heat loads. The minimum temperature occurs during the eclipse period where the earth emitted heat is the only environmental heating incident on the satellite solar panels and bottom plate surface.

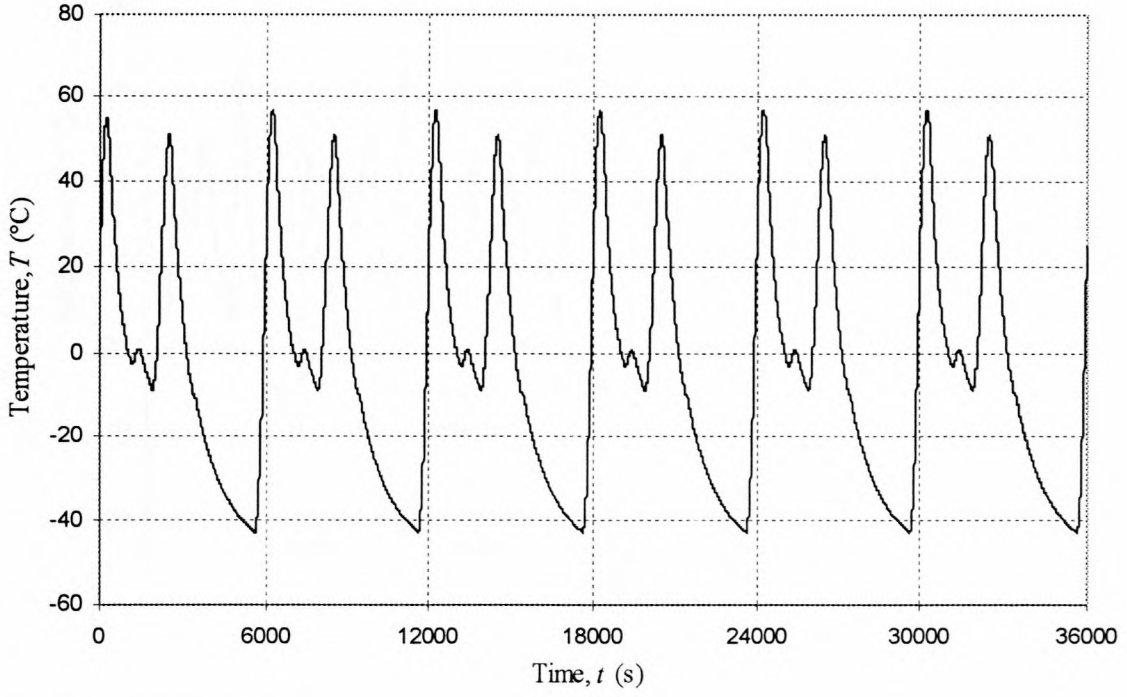

Figure F11 Temperature response of SUNSAT 3 +Y solar panel surface for β-angle = 0°

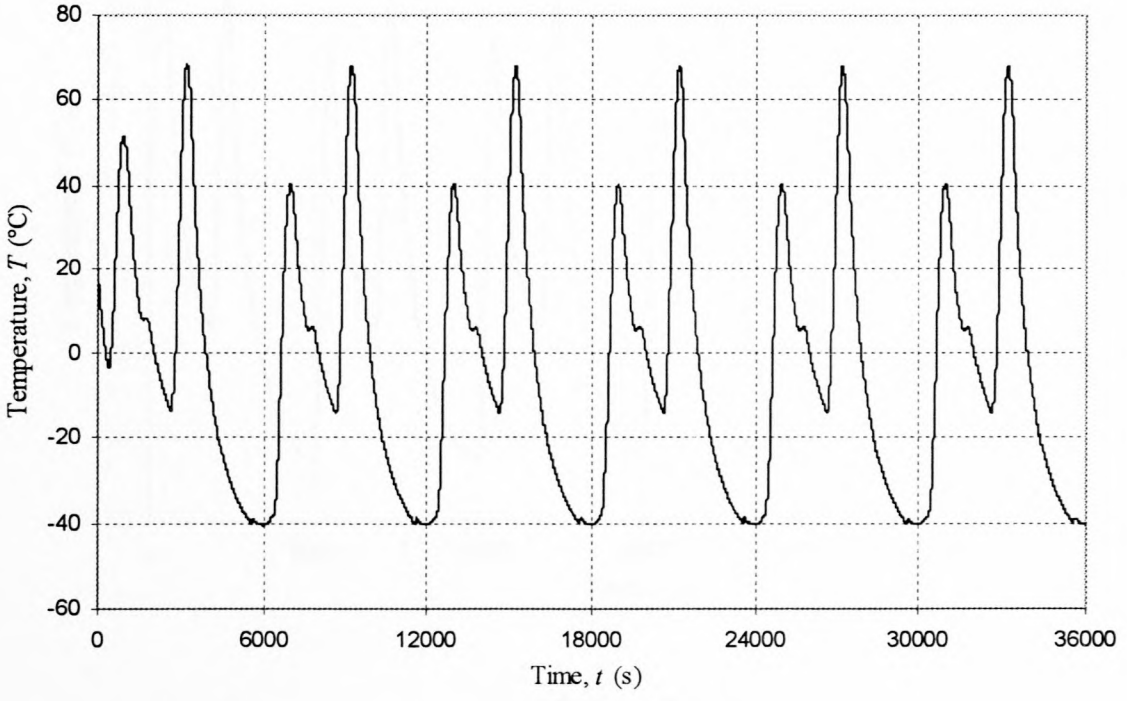

Figure F12 Temperature response of SUNSAT 3 -Y solar panel surface for β-angle = 0°

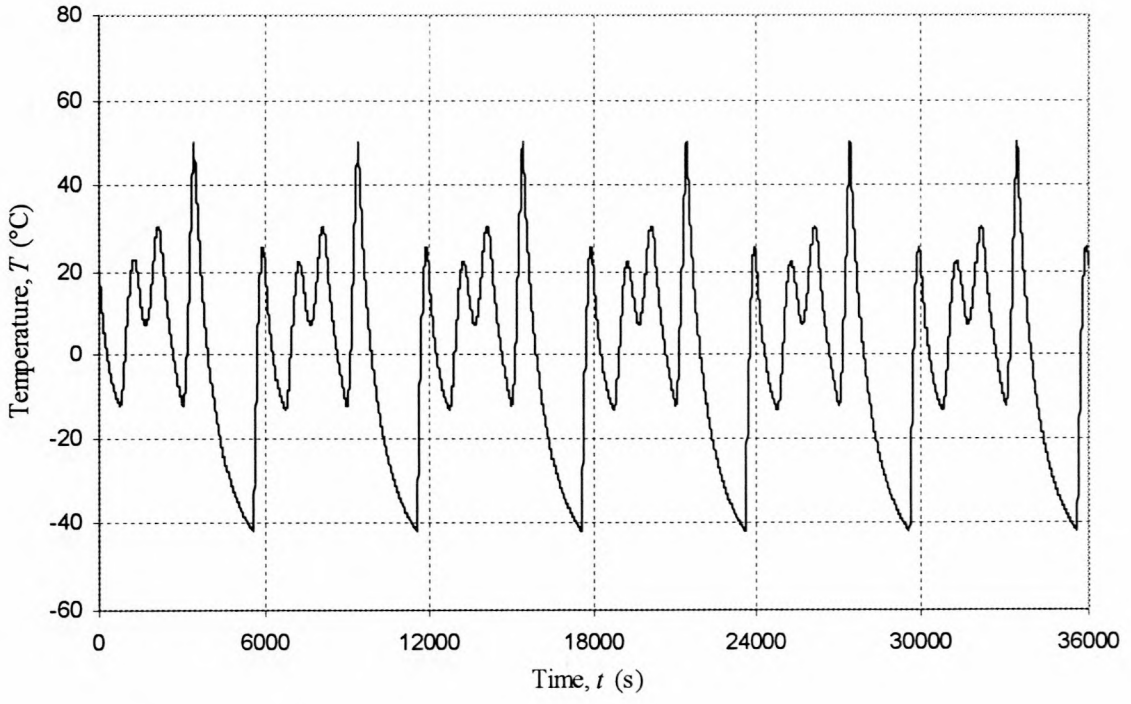

Figure F13 Temperature response of SUNSAT 3 +X solar panel surface for β-angle = 0°

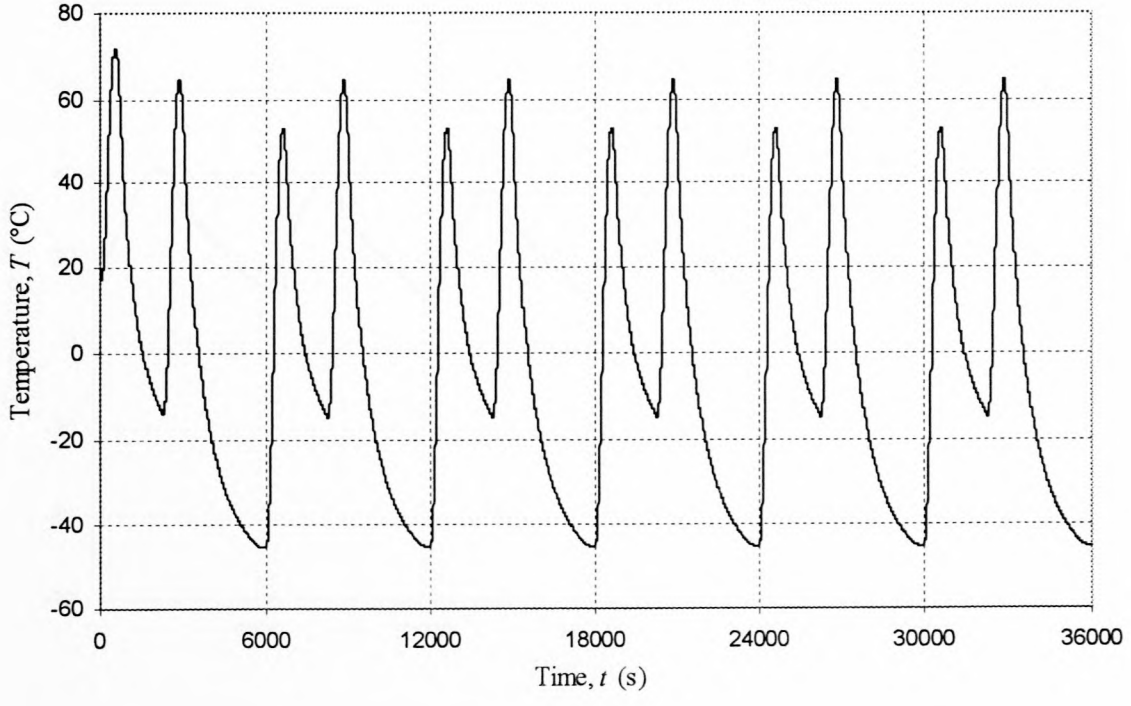

Figure F14 Temperature response of SUNSAT 3 -X solar panel surface for β-angle = 0°

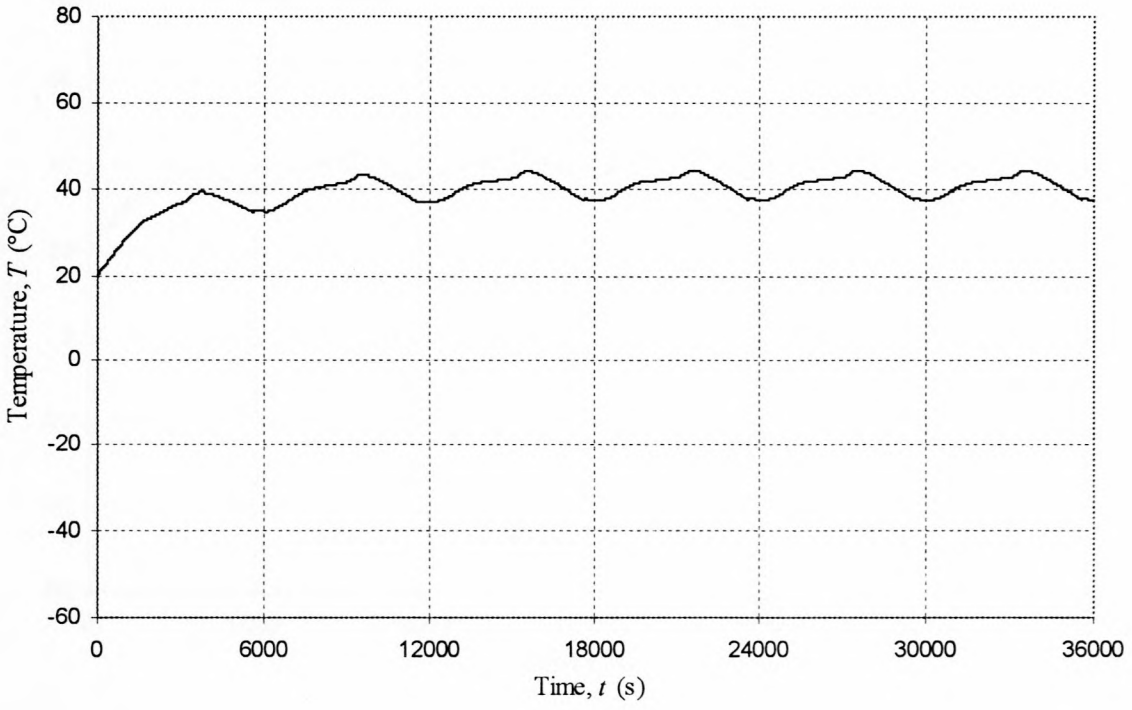

Figure F15 Temperature response of SUNSAT 3 +Z surface for β-angle = 0°

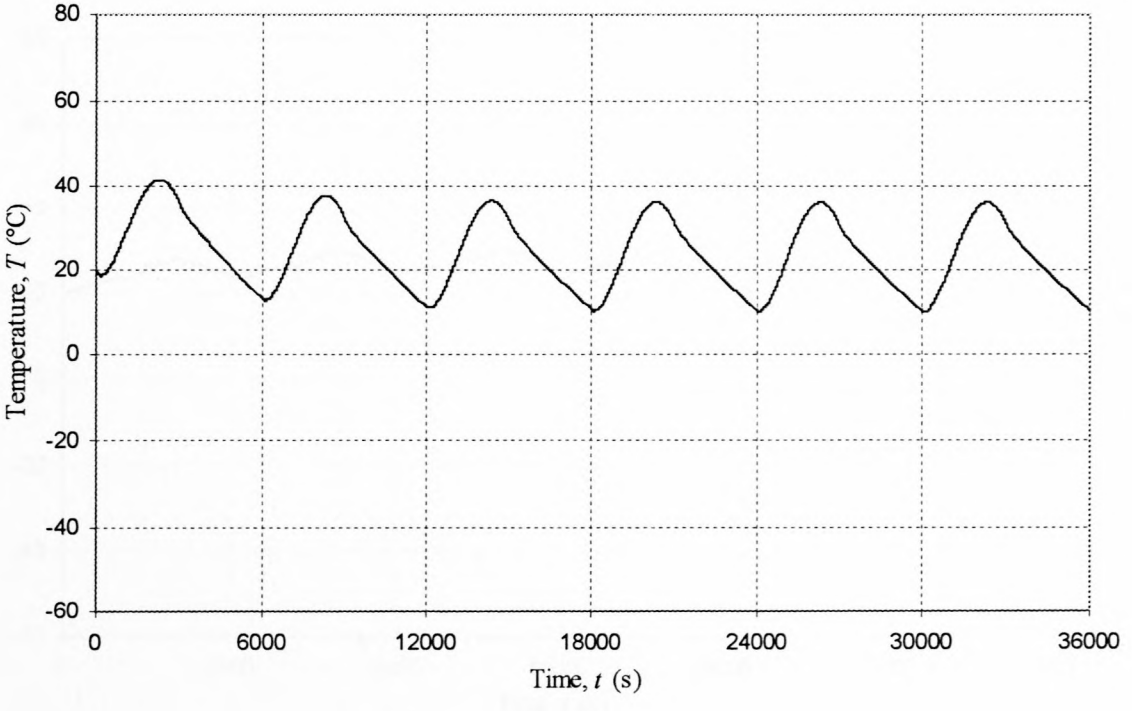

Figure F16 Temperature response of SUNSAT 3 -Z surface for β-angle = 0°

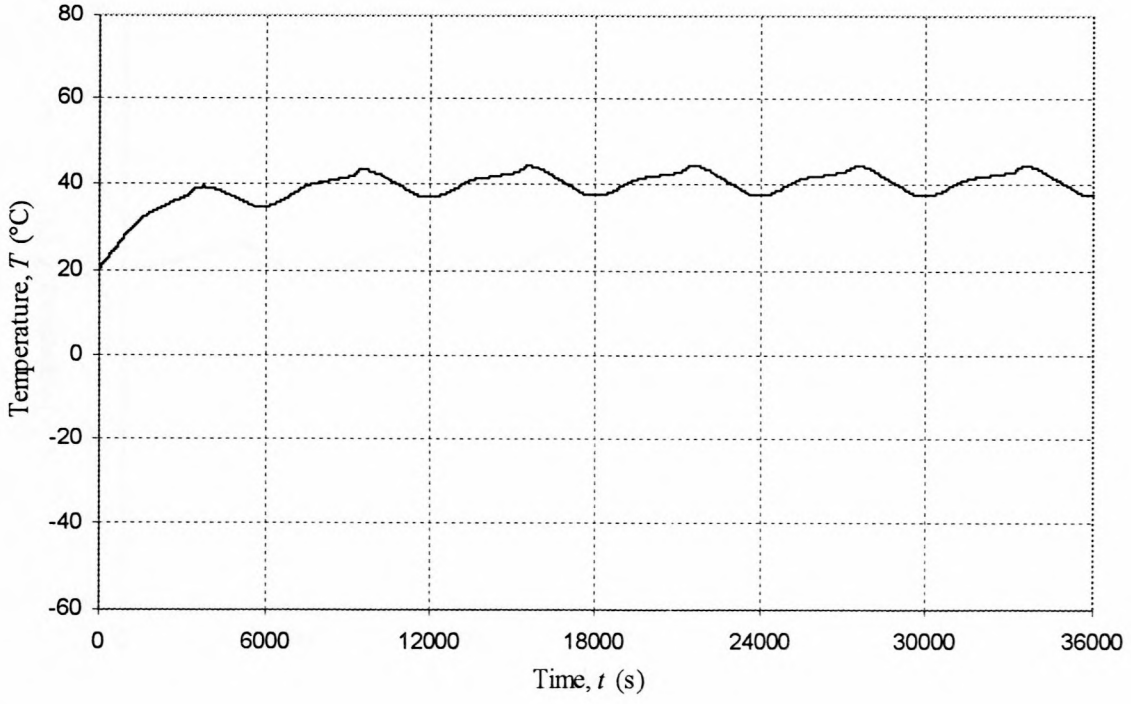

Figure F17 Temperature response of SUNSAT 3 bottom-plate for β-angle = 0°

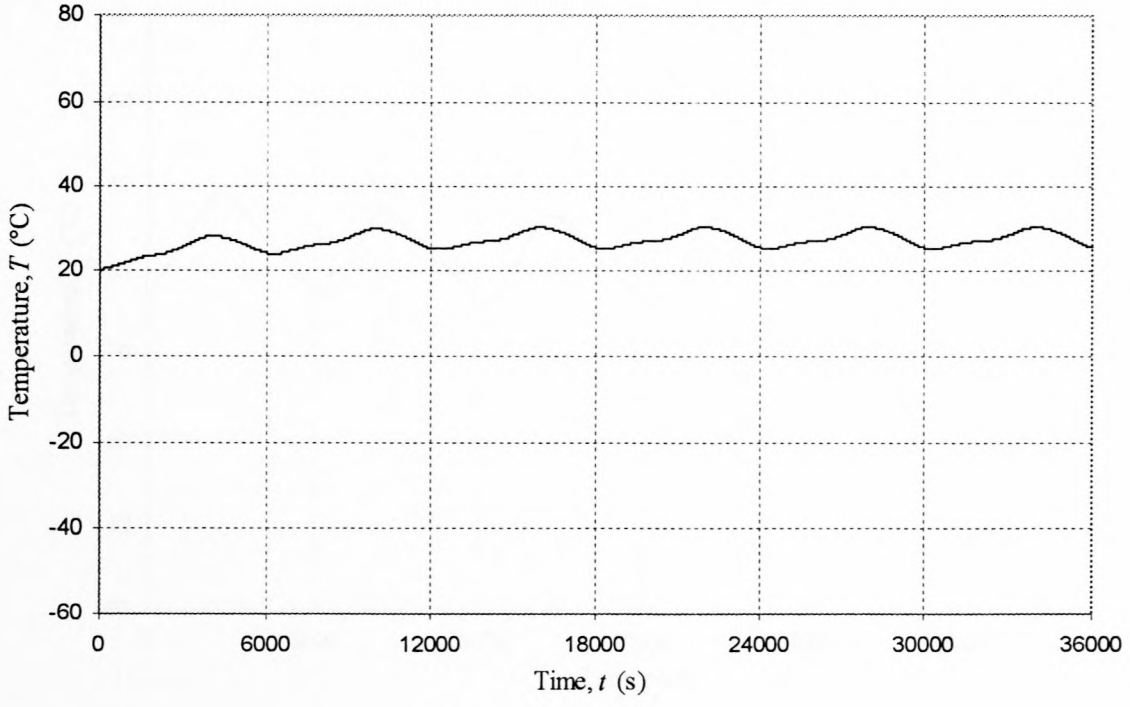

Figure F18 Temperature response of SUNSAT 3 battery for β-angle = 0°

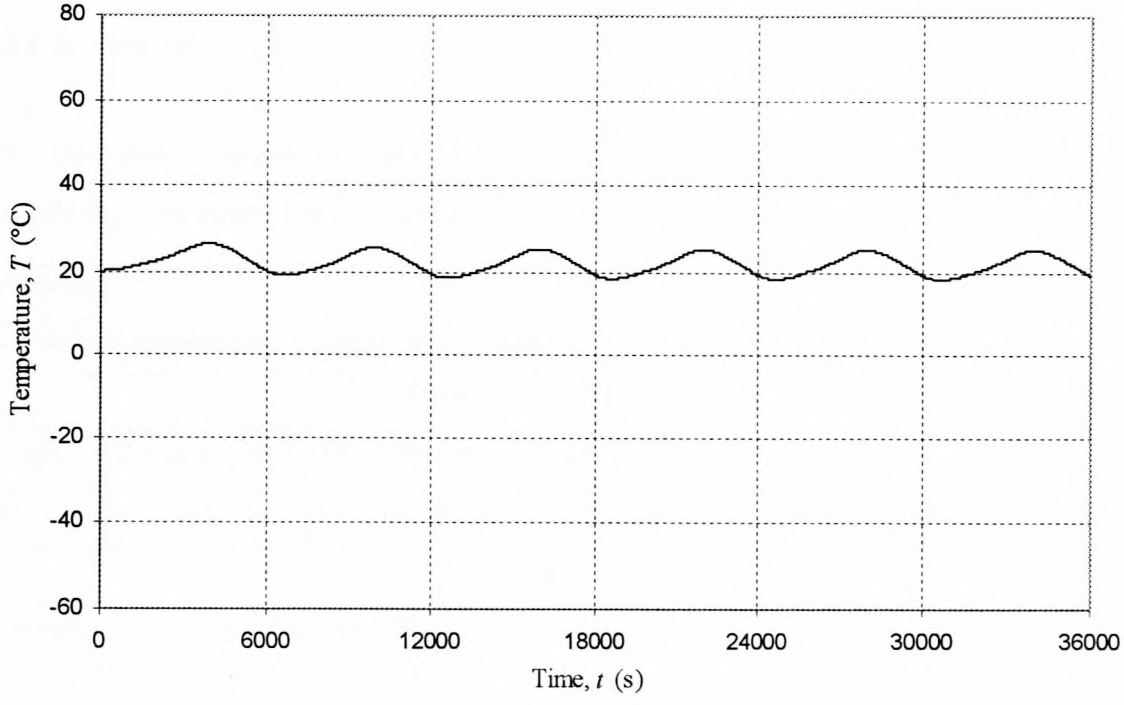

Figure F19 Temperature response of SUNSAT 3 middle-body section for β-angle = 0°

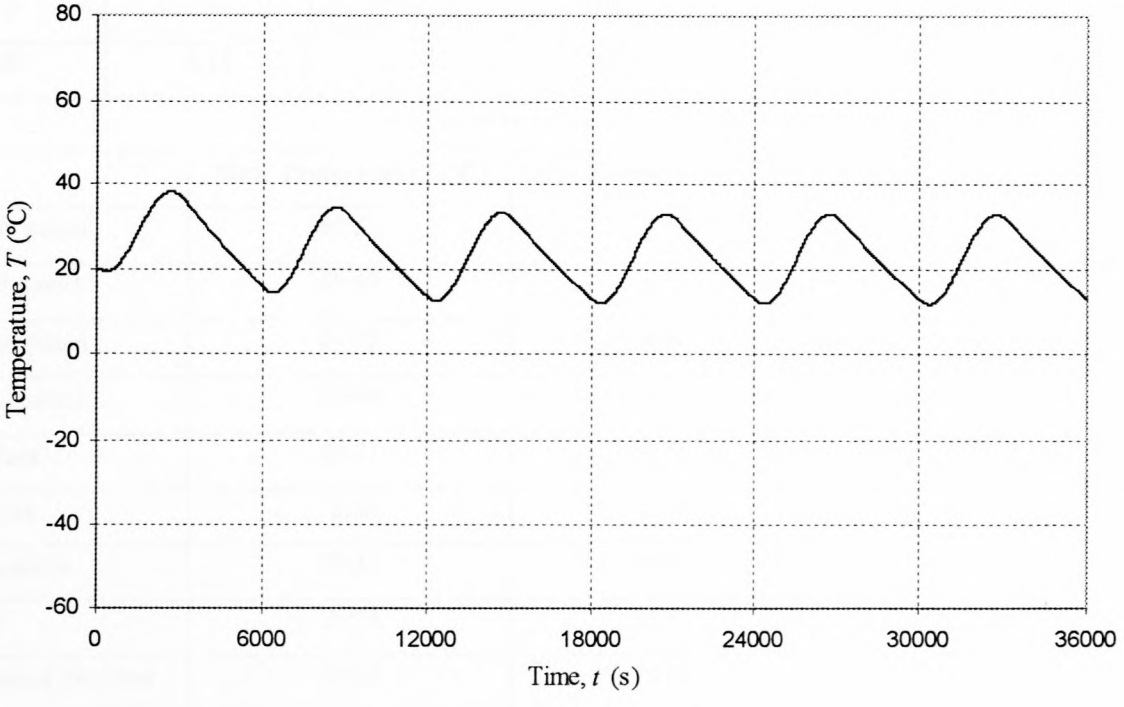

Figure F20 Temperature response of SUNSAT 3 upper-body section for β-angle = 0°

SUNSAT 3, Test 3b

Table F3 Data and temperature results of the TAS SUNSAT 3 model for a medium Z-axis spin rate and full sun conditions (zero eclipse)

Model: SUNSAT 3					
Mission: Polar sun-synchronous circular orbit for β-angle = 90 ° and 4 Z-axis rotations per orbit					
Orbit Parameters					
Beta angle	Z-axis rot./orbit	Ht. above Earth	Earth Radius	Orbit Period	Eclipse Period
90°	4	700 km	6371 km	100 min	0
Heating					
Albedo	Solar Heat Flux		Earth Heat Flux		Internal Heat
0.36	1353 W/m^2		216 W/m^2		30 W
Surface avg. Heating as determined from ORBIT-FLUX Computer Program					
+Y	-Y	+X	-X	+Z	-Z
78.00 W	78.00 W	77.99 W	77.99	5.30 W	0 W
Surface Properties (BOL)					
ε_{sp}	ε_{bp}	ε_{tp}	α_{sp}	α_{bp}	α_{tp}
0.80	0.15	0.73	0.80	0.08	0.41
Results					
	Max. Temperature (°C)		**Min Temperature (°C)**		**Avg. Temperature (°C)**
+Y solar panel	69.54		-8.43		25.23
-Y solar panel	69.59		-8.54		27.11
+X solar panel	69.79		-8.66		28.32
-X solar panel	69.74		-8.68		25.08
+Z surface	50.71		50.69		50.70
-Z surface	-6.66		-6.74		-6.71
Bottom-plate	50.53		50.52		50.53
Battery	35.75		35.73		35.74
Middle-body section	19.82		19.78		19.80
Upper-body section	-3.68		-3.76		-3.73

Conclusions of SUNSAT 3, Test 3b

The result of changing the orbit path from β-angle of 0° to one of 90° is an increase in the average solar panel temperature as well as the peak temperature. More importantly though, is the noticeable increase in the battery temperature of the satellite by ± 8°C from the previous Test 3a, as a direct result of the higher average external surface heating experienced by the solar panels. This heat cannot readily be emitted by the bottom-plate since this plate has a low emissivity, and therefore the battery gets hotter. The –Z surface is far colder than for the Test 3a due to the fact that it receives no solar radiation.

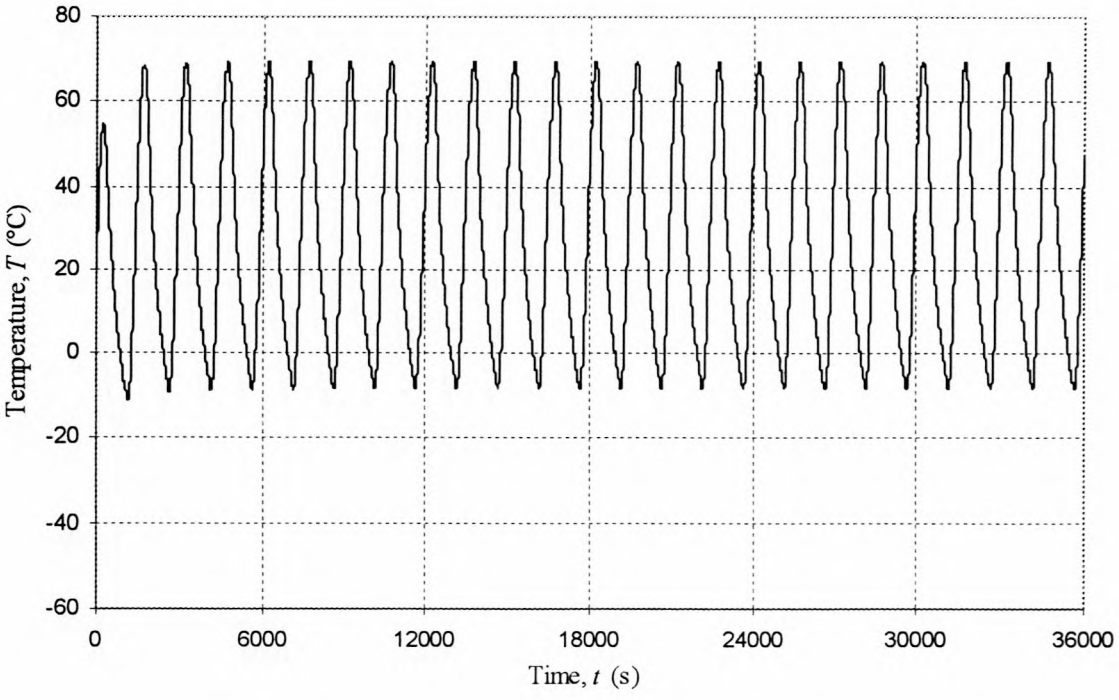

Figure F21 Temperature response of SUNSAT 3 +Y solar panel surface for β-angle = 90°

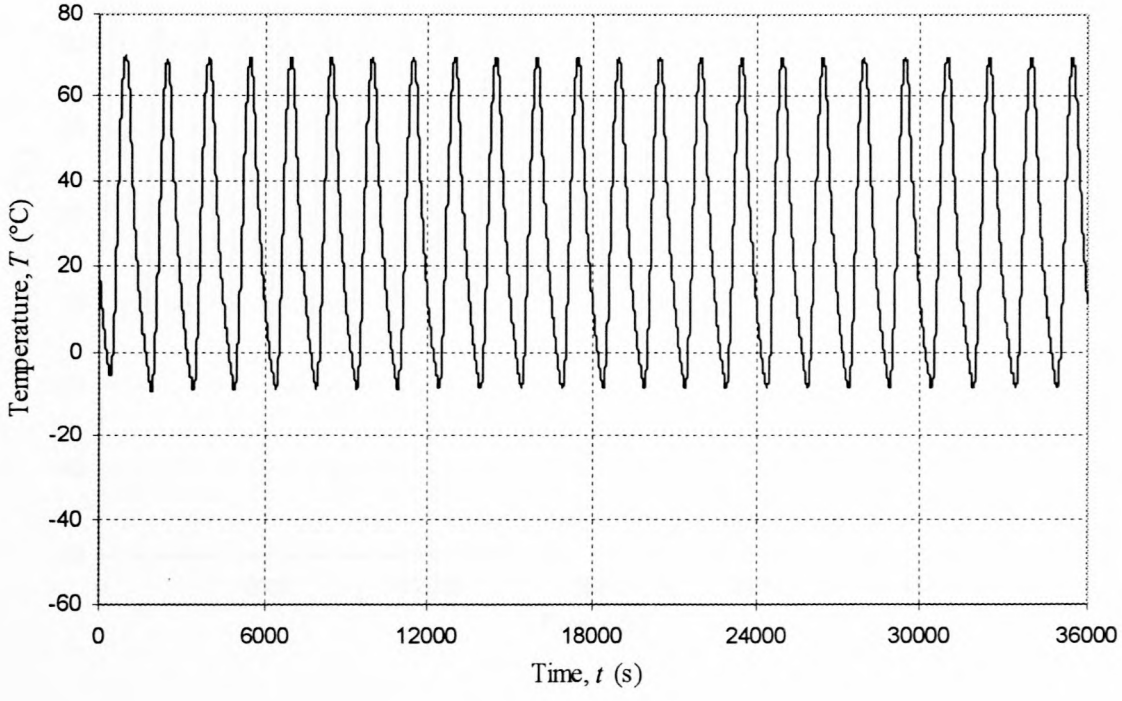

Figure F22 Temperature response of SUNSAT 3 -Y solar panel surface for β-angle = 90°

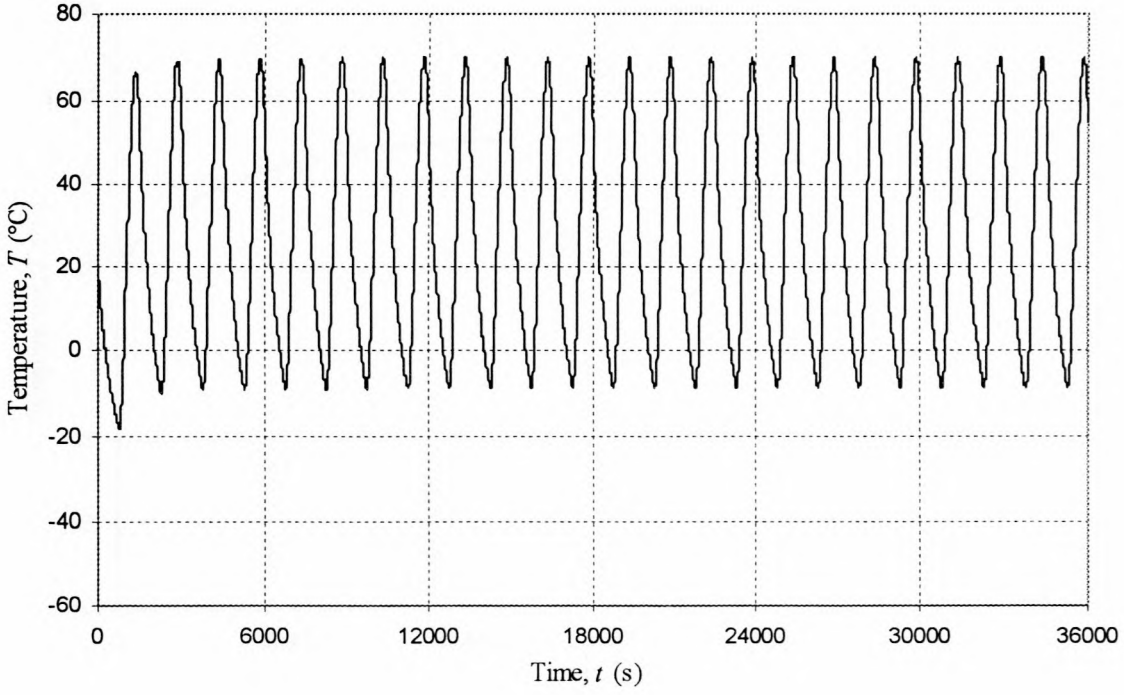

Figure F23 Temperature response of SUNSAT 3 +X solar panel surface for β-angle = 90°

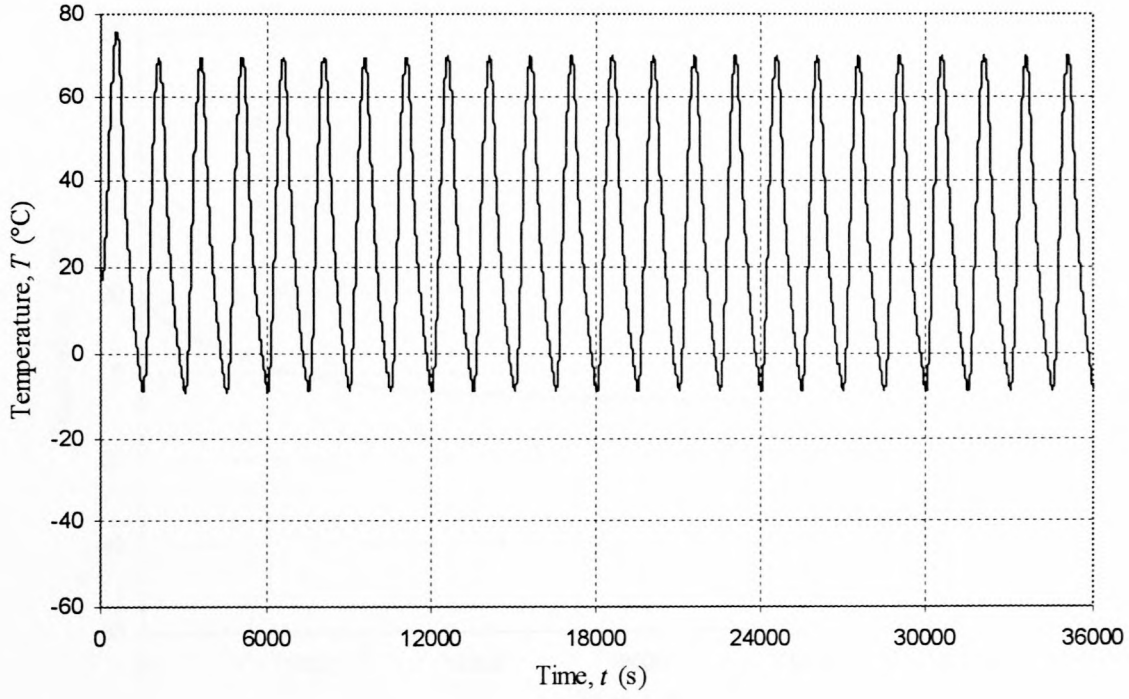

Figure F24 Temperature response of SUNSAT 3 -X solar panel surface for β-angle = 90°

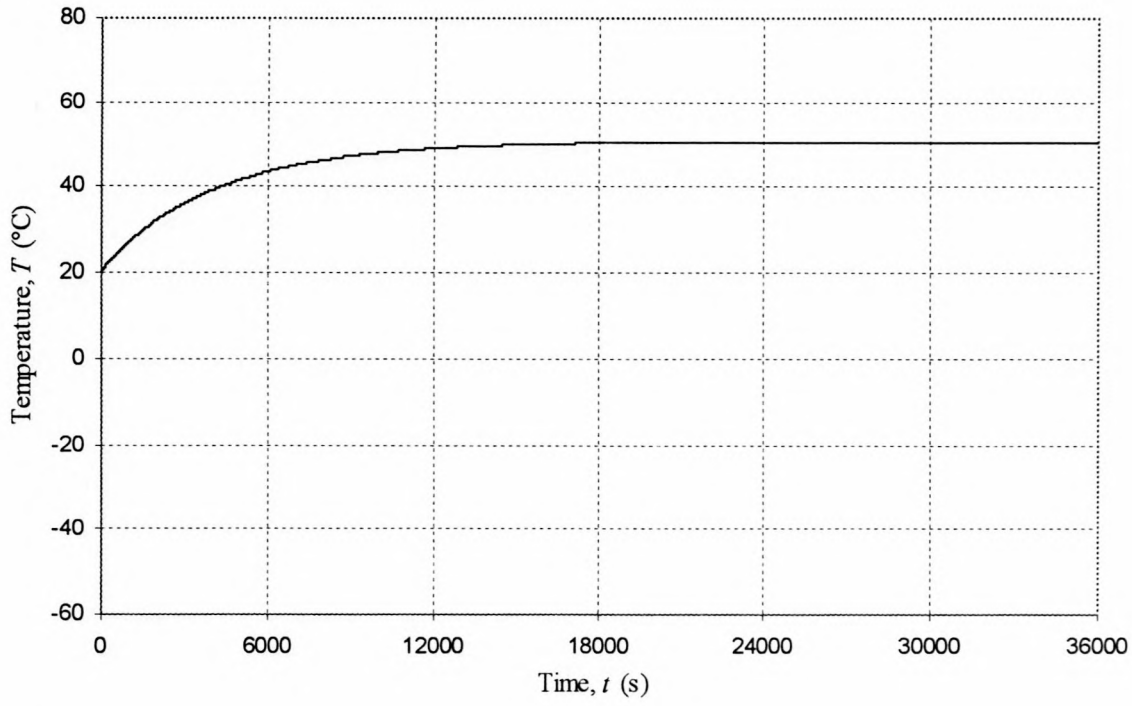

Figure F25 Temperature response of SUNSAT 3 +Z surface for β-angle = 90°

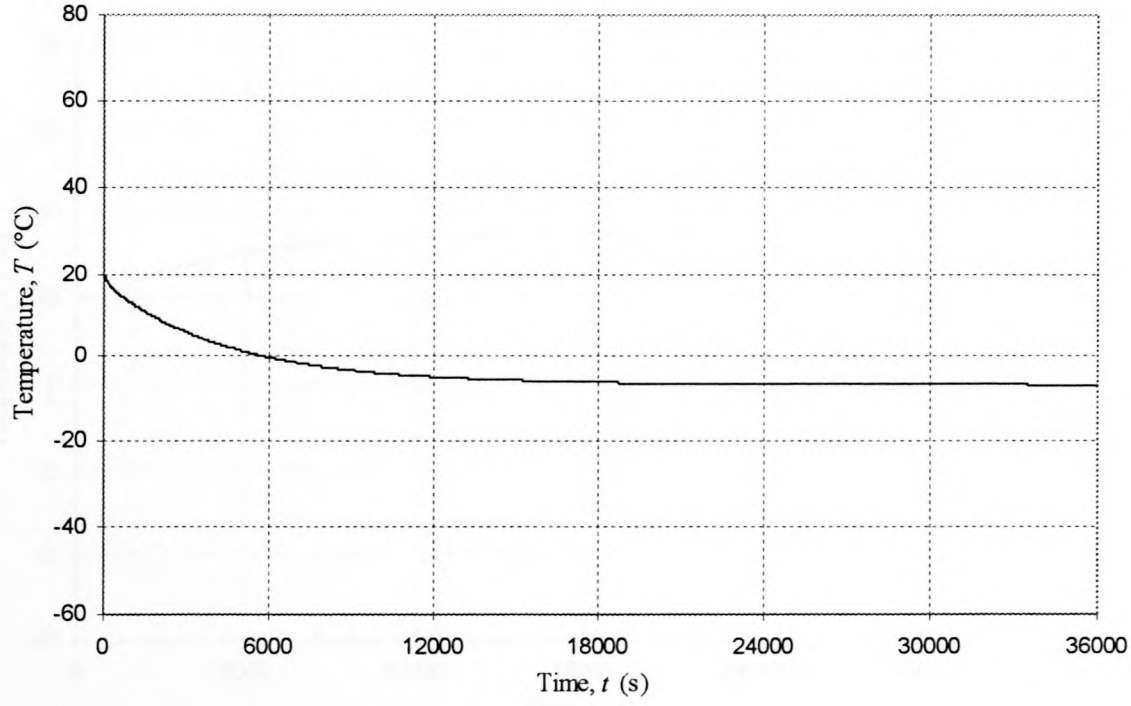

Figure F26 Temperature response of SUNSAT 3 -Z surface for β-angle = 90°

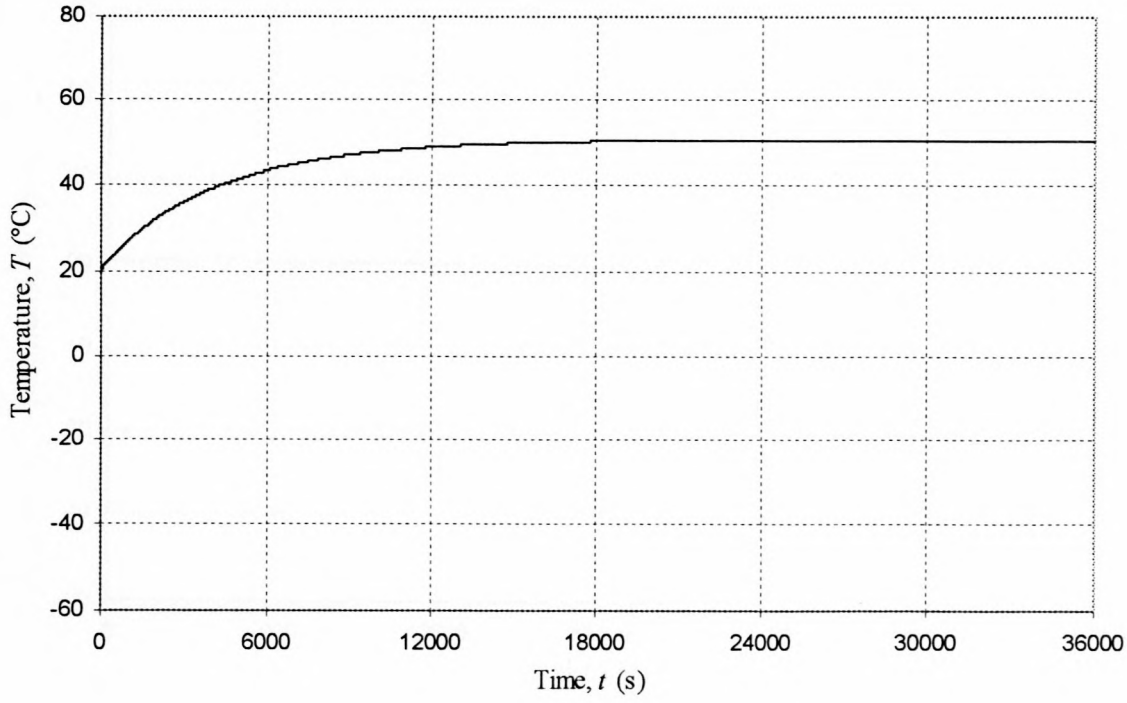

Figure F27 Temperature response of SUNSAT 3 bottom plate for β-angle = 90°

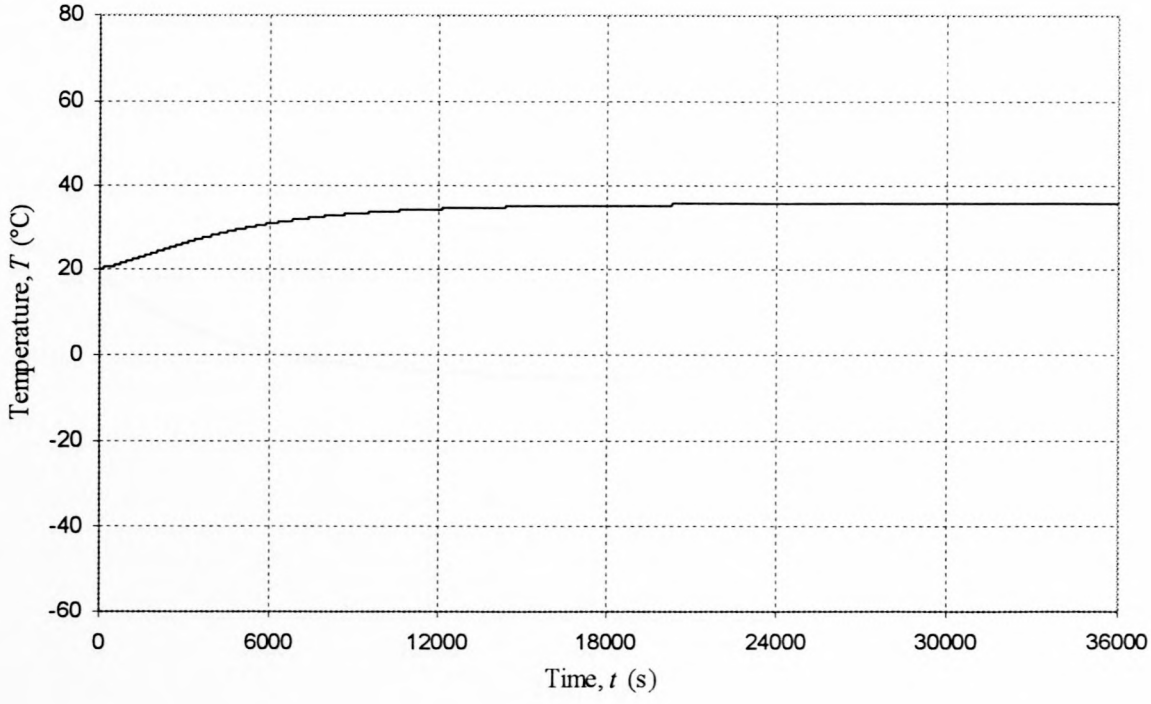

Figure F28 Temperature response of SUNSAT 3 battery for β-angle = 90°

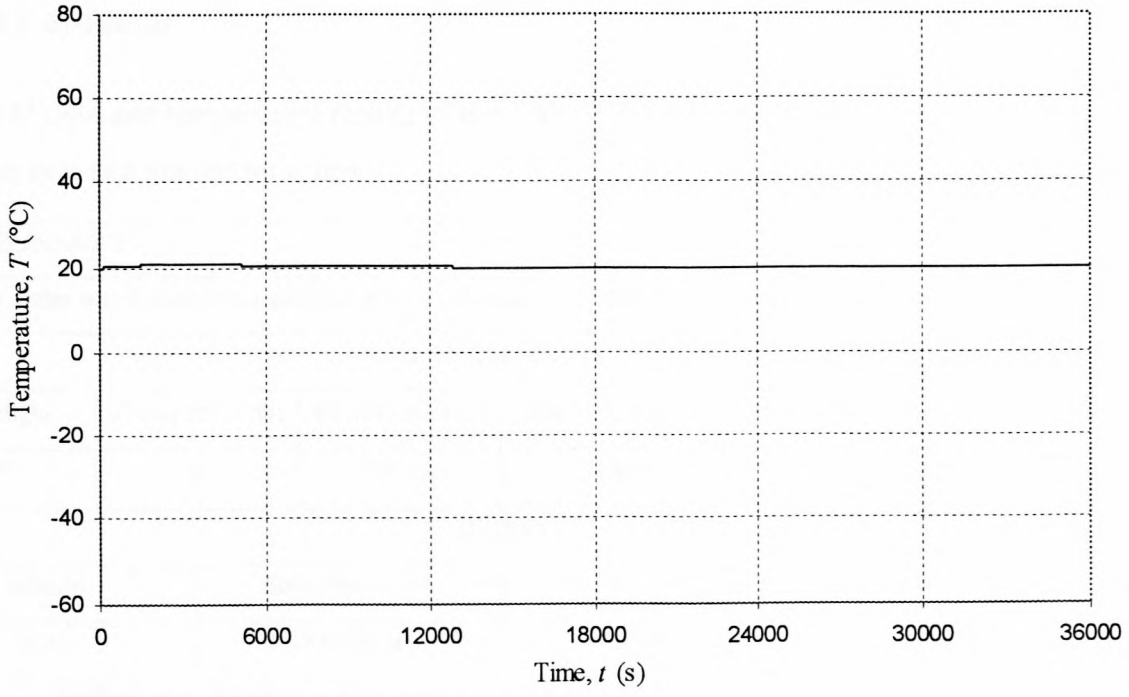

Figure F29 Temperature response of SUNSAT 3 middle-body section for β-angle = 90°

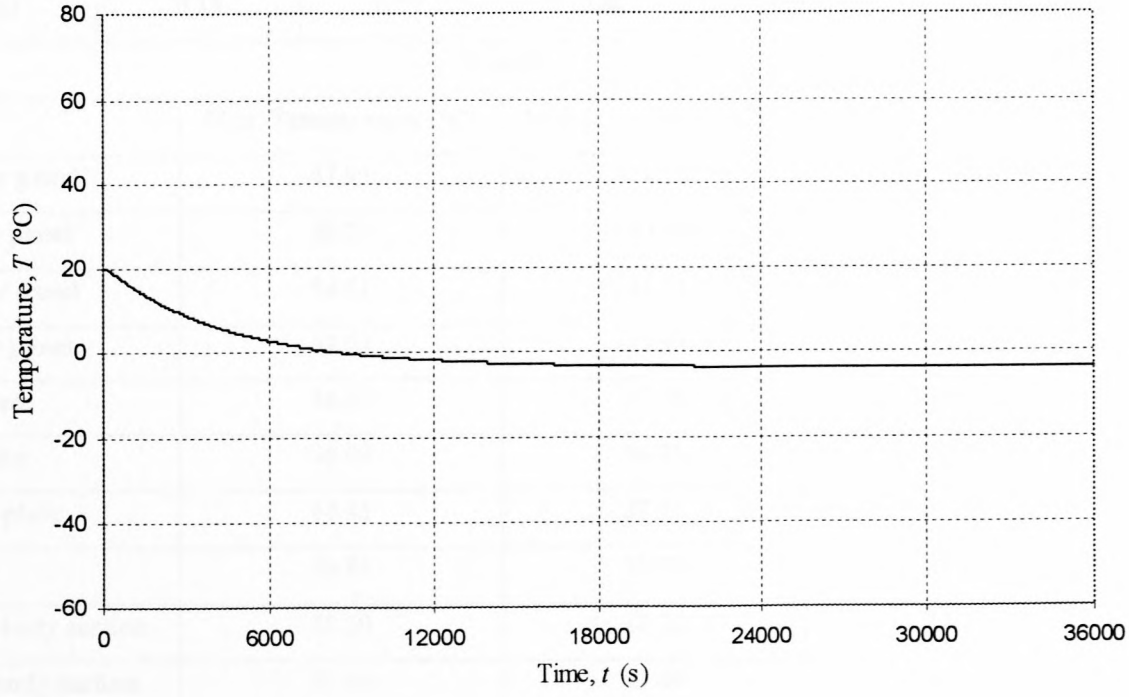

Figure F30 Temperature response of SUNSAT 3 upper-body section for β-angle = 90°

SUNSAT 3, Test 3c

Table F4 Data and temperature results of the TAS SUNSAT 3 model for a medium-to-high Z-axis spin rate and maximum eclipse

Model: SUNSAT 3					
Mission: Polar sun-synchronous circular orbit for β-angle = 0 ° and 6 Z-axis rotations per orbit					
Orbit Parameters					
Beta angle	Z-axis rot./orbit	Ht. above Earth	Earth Radius	Orbit Period	Eclipse Period
0°	6	700 km	6371 km	100 min	± 36 min
Heating					
Albedo	Solar Heat Flux	Earth Heat Flux	Internal Heat		
0.36	1353 W/m^2	216 W/m^2	30 W		
Surface avg. Heating as determined from ORBIT-FLUX Computer Program					
+Y	-Y	+X	-X	+Z	-Z
44.94 W	44.94 W	51.64 W	42.41 W	8.00 W	35.75 W
Surface Properties (BOL)					
ε_{sp}	ε_{bp}	ε_{tp}	α_{sp}	α_{bp}	α_{tp}
0.80	0.15	0.73	0.80	0.08	0.41

Results			
	Max. Temperature (°C)	**Min Temperature (°C)**	**Avg. Temperature (°C)**
+Y solar panel	47.95	-41.99	-9.91
-Y solar panel	56.24	-40.79	-9.36
+X solar panel	54.41	-41.45	-3.30
-X solar panel	54.04	-44.94	-14.14
+Z surface	44.69	37.95	41.15
-Z surface	36.09	10.41	21.19
Bottom-plate	44.45	37.77	40.94
Battery	30.83	25.72	28.25
Middle-body section	25.50	18.76	22.22
Upper-body section	33.06	12.09	21.64

Conclusion of SUNSAT 3, Test 3c

By increasing the number of rotations about the satellite Z-axis from 4 to 6 (Test 3a and Test 3c respectively) results in solar panel average temperatures that are within 1 or 2°C of each other. The maximum temperatures of the solar panels for Test 3c are several degrees lower than for those in Test 3a. In other words, the temperature gradients of the solar panels are lower for Test 3c than for Test 3a.

The average battery temperature however has not changed by much. A possible reason for this could be that by increasing the spin rate of the satellite, the heat does not have a chance to be transferred through the structure and then radiated to space by the un-illuminated solar panel, before the solar panel receives solar radiation again.

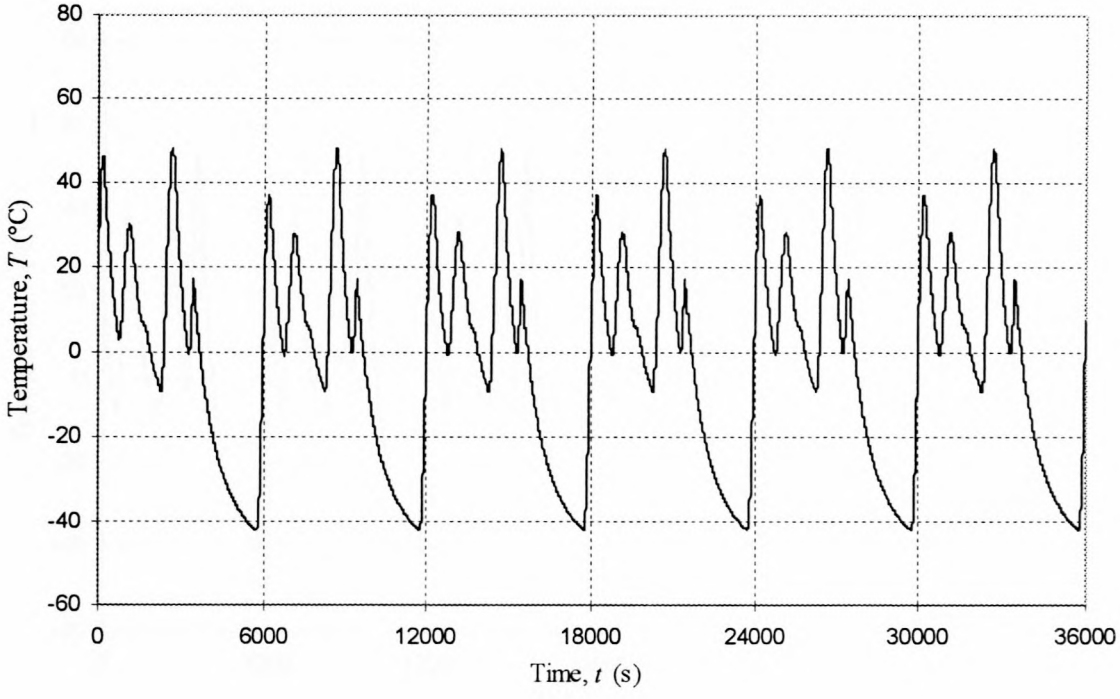

Figure F31 Temperature response of SUNSAT 3 +Y solar panel surface for 6 Z-axis spins

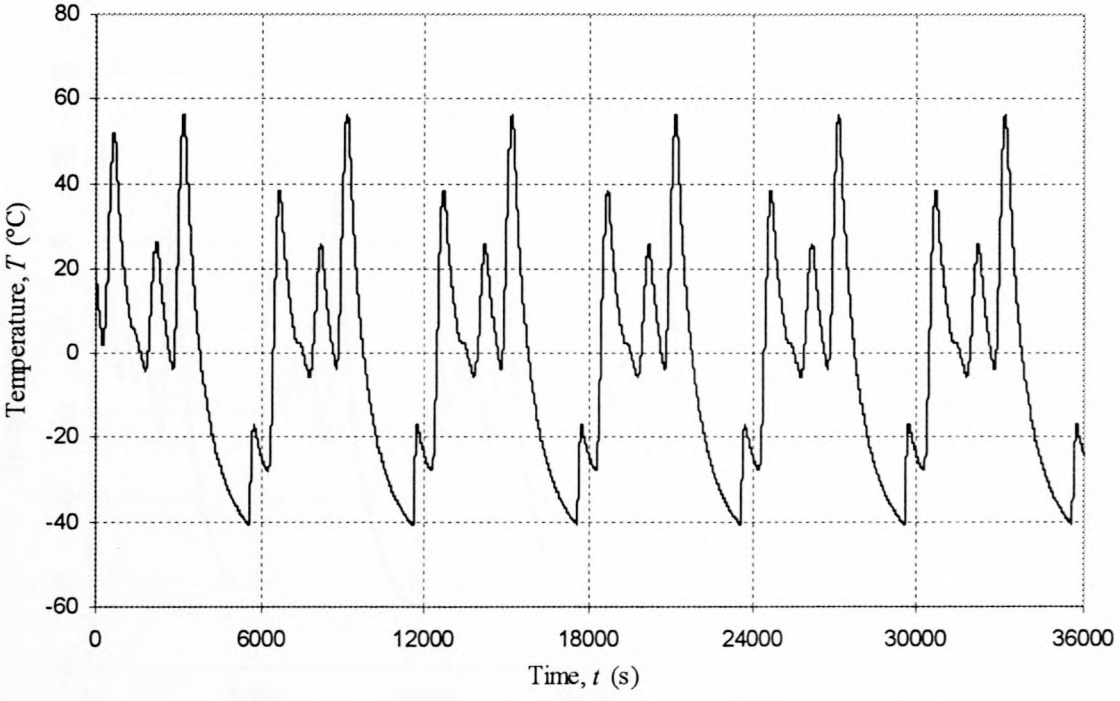

Figure F32 Temperature response of SUNSAT 3 -Y solar panel surface for 6 Z-axis spins

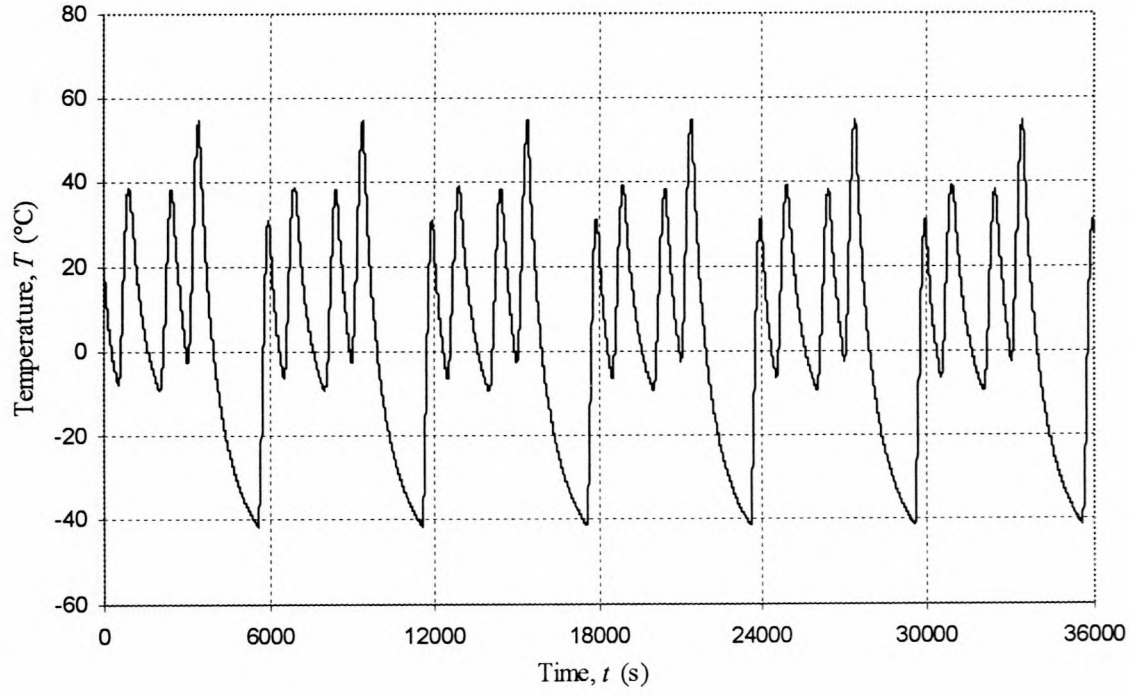

Figure F33 Temperature response of SUNSAT 3 +X solar panel surface for 6 Z-axis spins

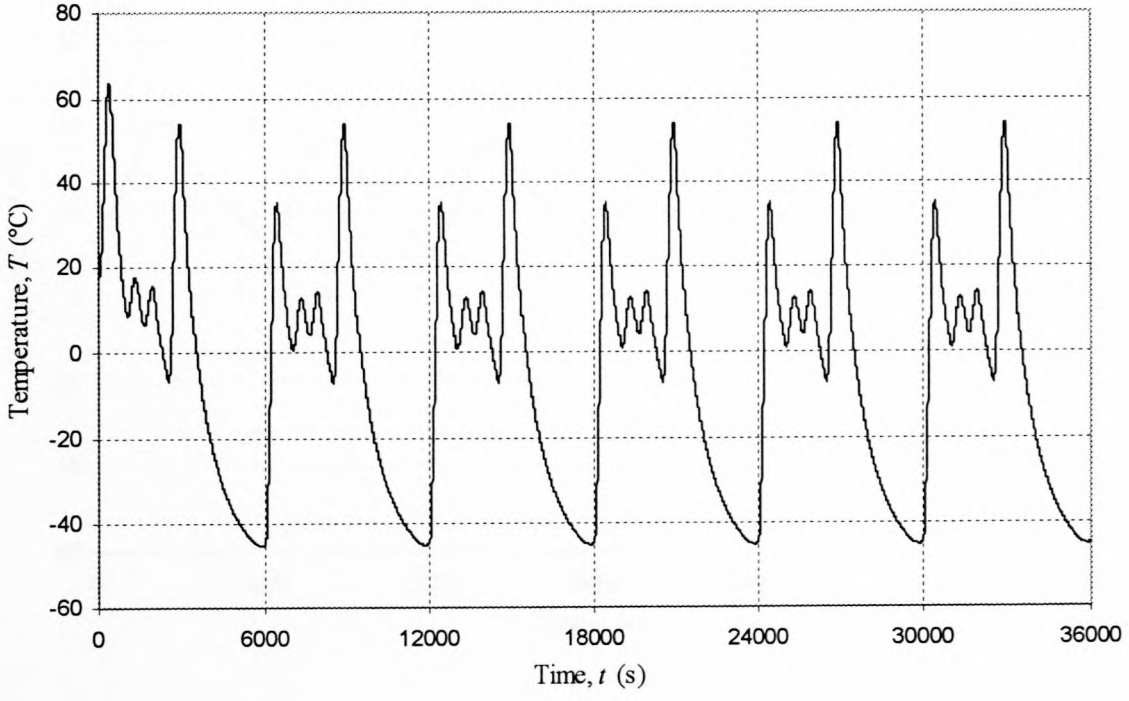

Figure F34 Temperature response of SUNSAT 3 -X solar panel surface for 6 Z-axis spins

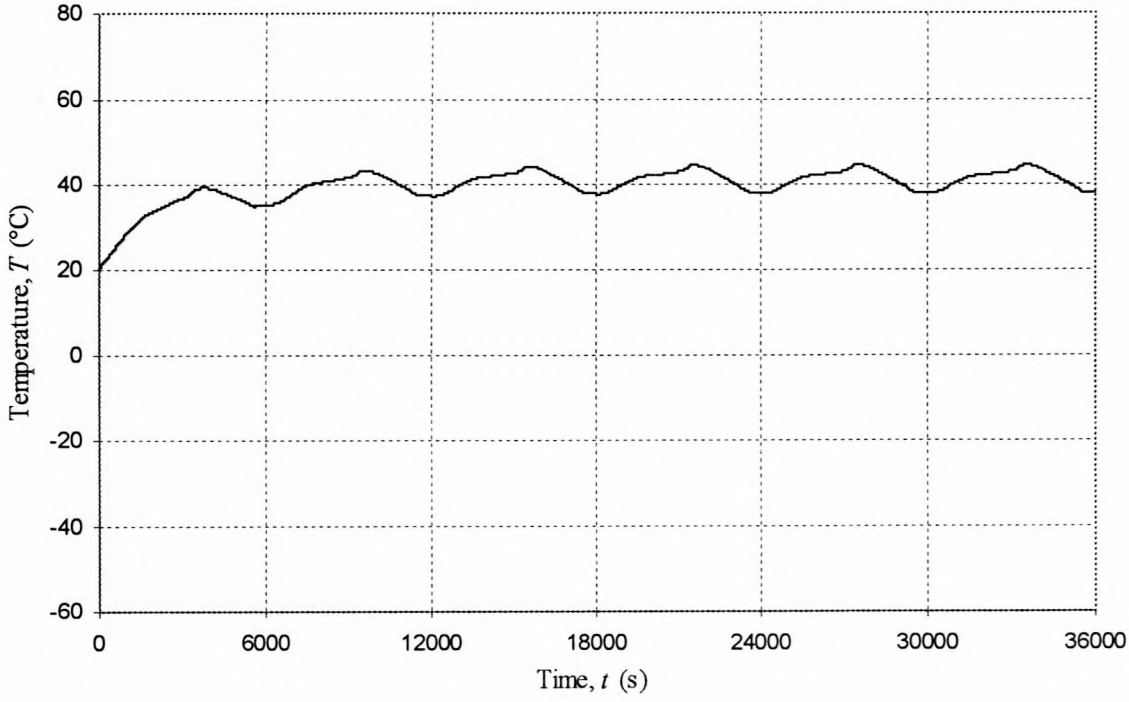

Figure F35 Temperature response of SUNSAT 3 +Z surface for 6 Z-axis spins

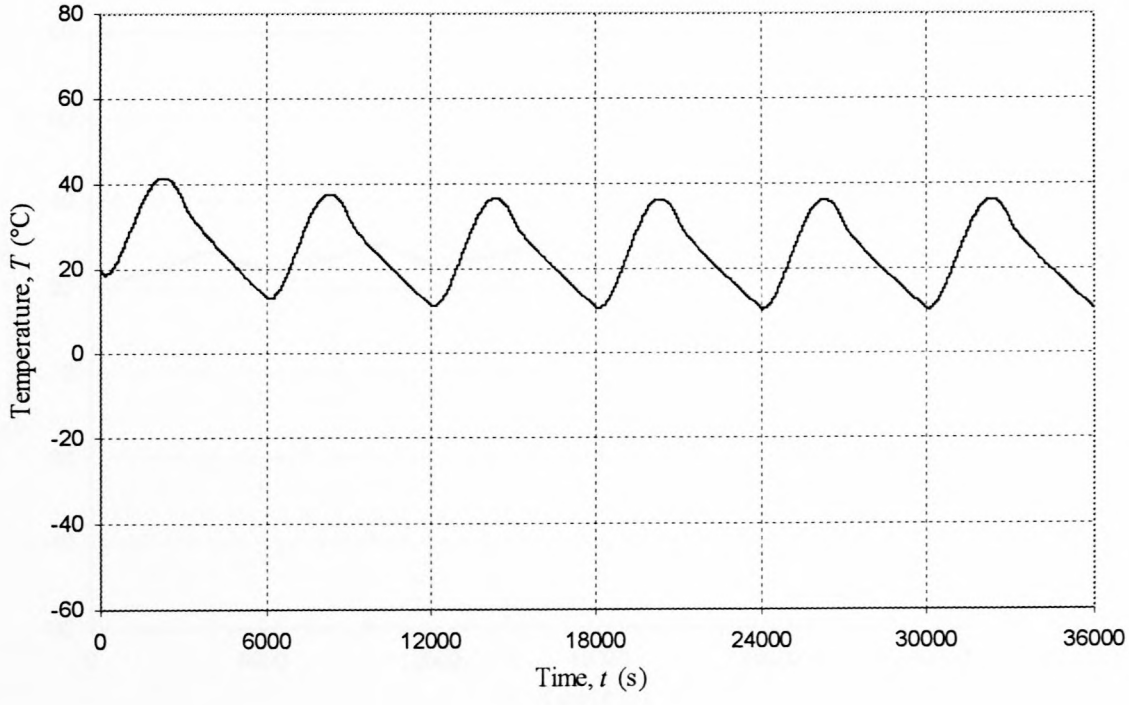

Figure F36 Temperature response of SUNSAT 3 -Z surface for 6 Z-axis spins

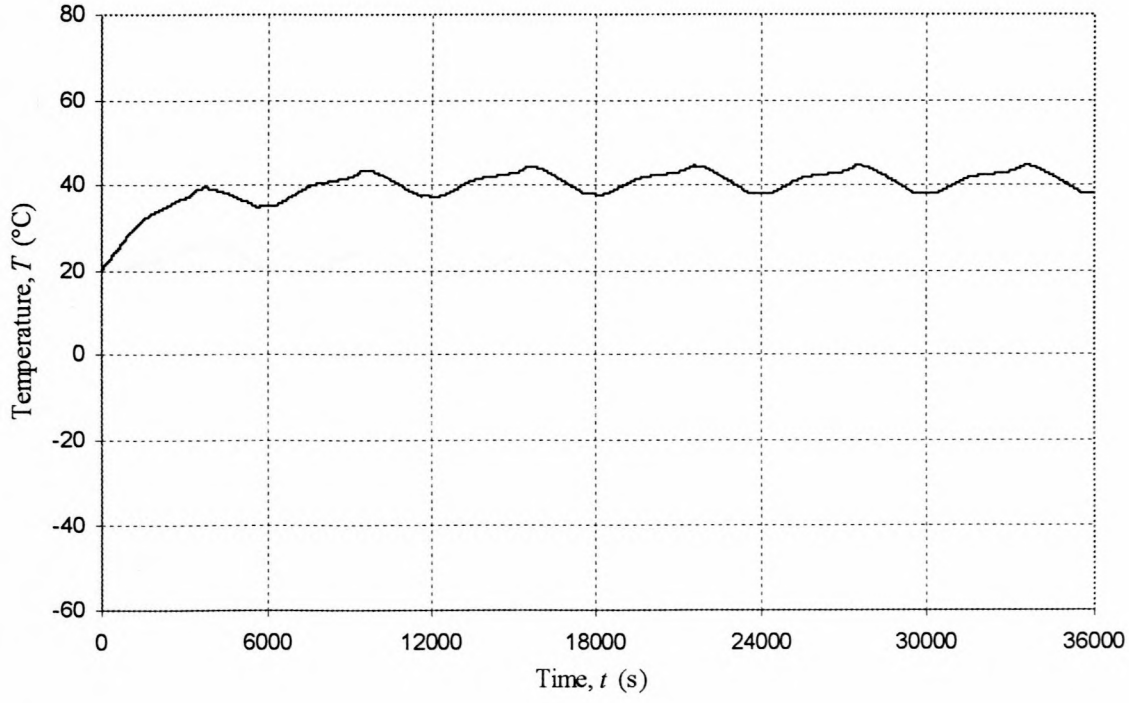

Figure F37 Temperature response of SUNSAT 3 bottom-plate for 6 Z-axis spins

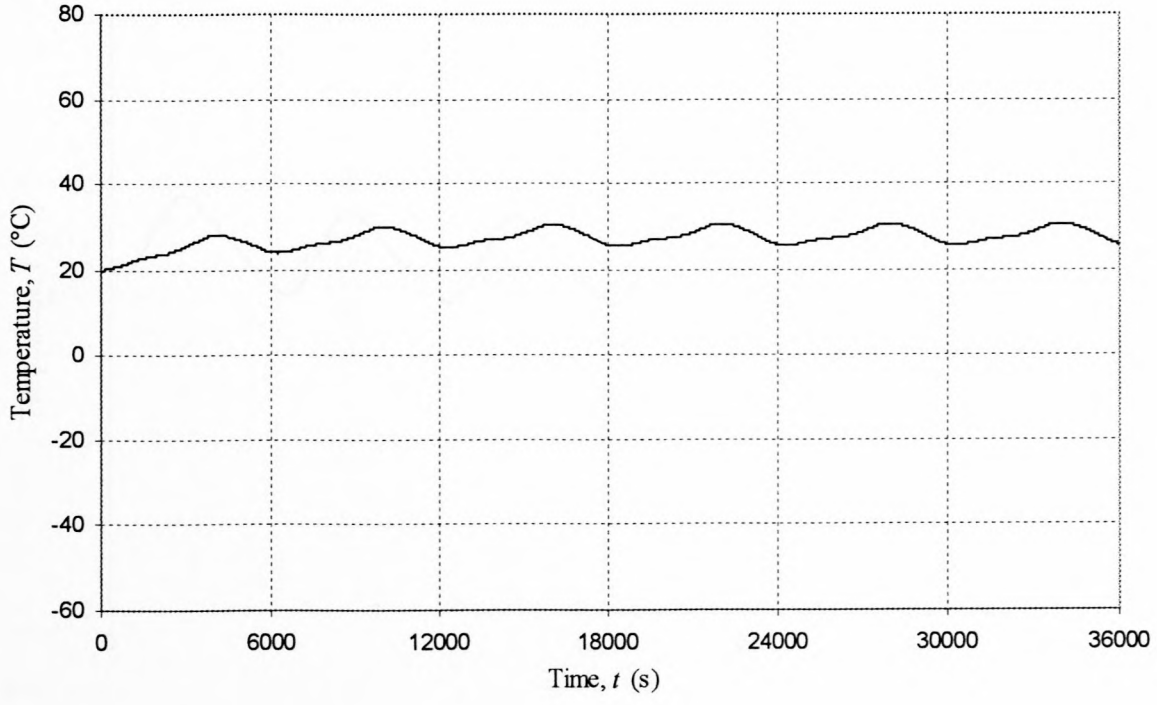

Figure F38 Temperature response of SUNSAT 3 battery for 6 Z-axis spins

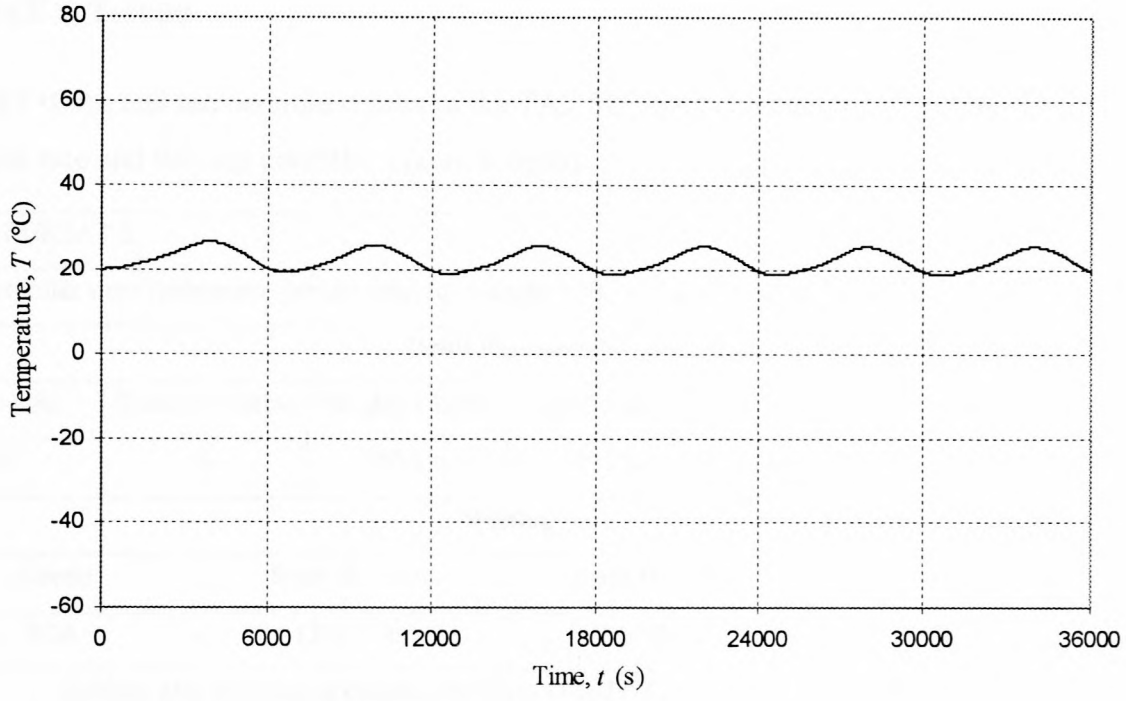

Figure F39 Temperature response of SUNSAT 3 middle-body section for 6 Z-axis spins

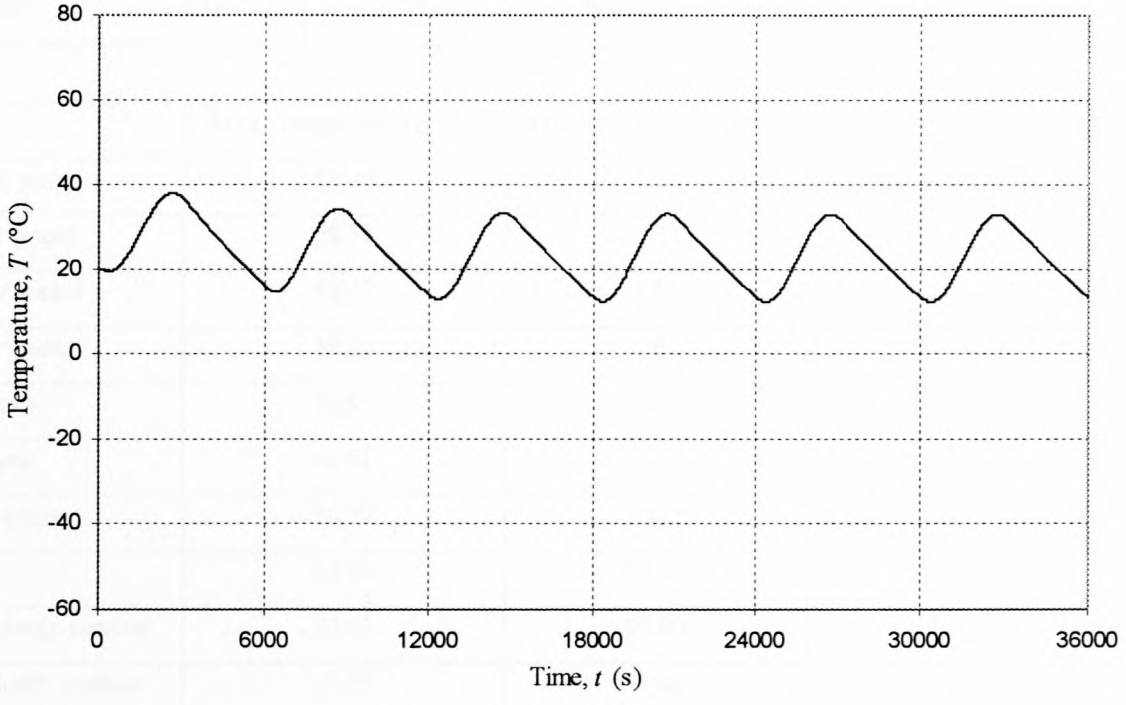

Figure F40 Temperature response of SUNSAT 3 upper-body section for 6 Z-axis spins

SUNSAT 3, Test 3d

Table F5 Data and temperature results of the TAS SUNSAT 3 model for a medium-to-high Z-axis spin rate and full sun conditions (zero eclipse)

Model: SUNSAT 3					
Mission: Polar sun-synchronous circular orbit for β-angle = 90 ° and 6 Z-axis rotations per orbit					
Orbit Parameters					
Beta angle	Z-axis rot./orbit	Ht. above Earth	Earth Radius	Orbit Period	Eclipse Period
90°	6	700 km	6371 km	100 min	± 36 min
Heating					
Albedo	Solar Heat Flux		Earth Heat Flux		Internal Heat
0.36	1353 W/m^2		216 W/m^2		30 W
Surface avg. Heating as determined from ORBIT-FLUX Computer Program					
+Y	-Y	+X	-X	+Z	-Z
77.97 W	77.97 W	77.97 W	77.97 W	5.29 W	0 W
Surface Properties (BOL)					
ε_{sp}	ε_{bp}	ε_{tp}	α_{sp}	α_{bp}	α_{tp}
0.80	0.15	0.73	0.80	0.08	0.41

Results			
	Max. Temperature (°C)	**Min Temperature (°C)**	**Avg. Temperature (°C)**
+Y solar panel	58.30	1.60	27.85
-Y solar panel	58.31	1.52	27.78
+X solar panel	58.47	1.63	28.00
-X solar panel	58.43	1.61	27.92
+Z surface	50.95	50.93	50.94
-Z surface	-6.51	-6.58	-6.55
Bottom-plate	50.77	50.75	50.77
Battery	35.98	35.98	35.98
Middle-body section	20.03	20.00	20.01
Upper-body section	-3.53	-3.60	-3.57

Conclusion of SUNSAT 3, Test 3d

As in the comparison of Tests 3a and 3c, the comparison of Test 3b with Test 3d has similarities. The increased spin rate decreases the solar panel maximum temperatures, but has little effect on the average solar panel temperatures. The average battery temperature doesn't vary by much either, with the change in spin rate. The comparison of Test 3c with Test 3d, shows similar results as in the comparison of Test 3a with Test 3b. The battery temperature is higher for Test 3d than for Test 3c. This is due to the higher surface heating of the solar panels.

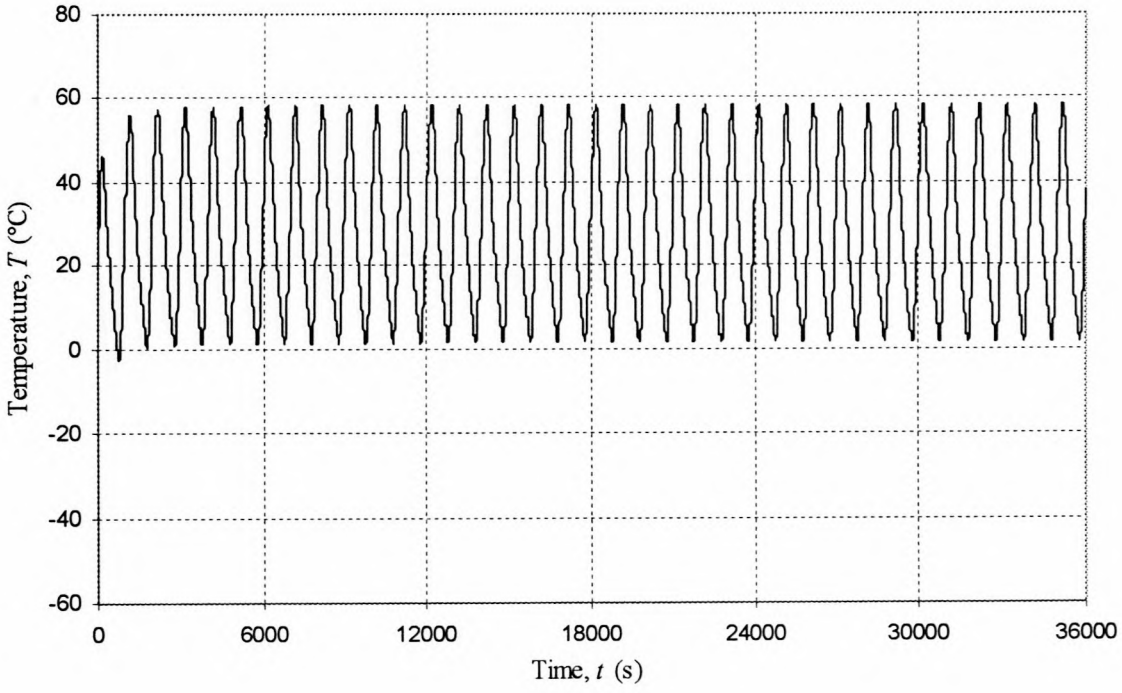

Figure F41 Temperature response of SUNSAT 3 +Y solar panel surface for 6 Z-axis spins

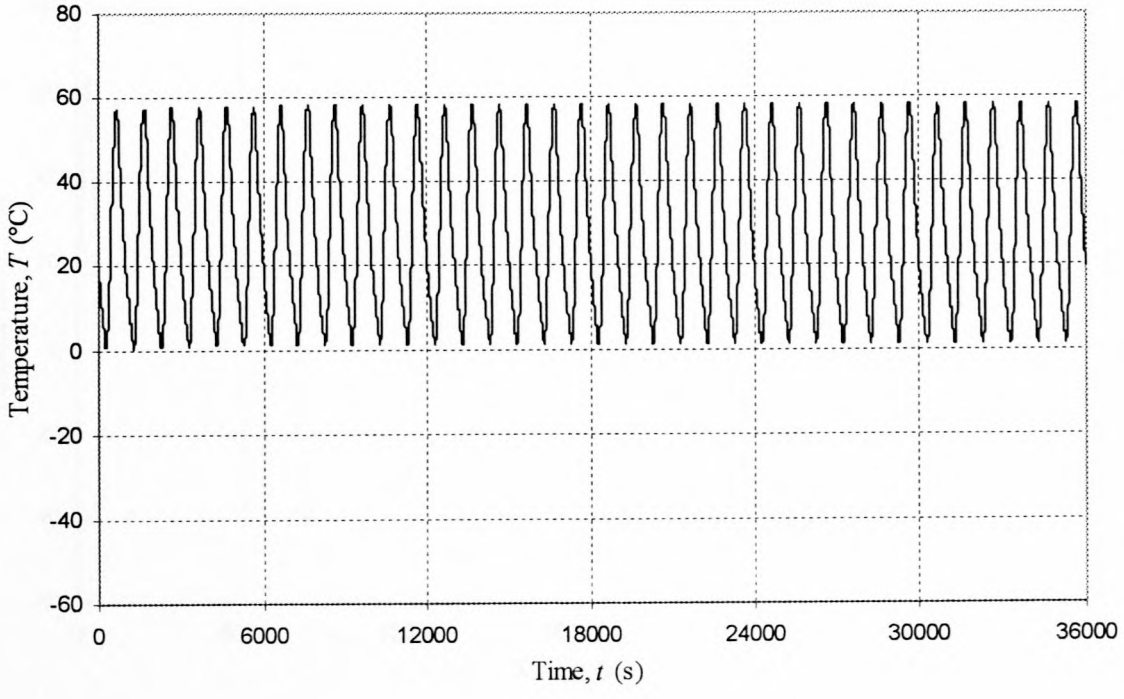

Figure F42 Temperature response of SUNSAT 3 -Y solar panel surface for 6 Z-axis spins

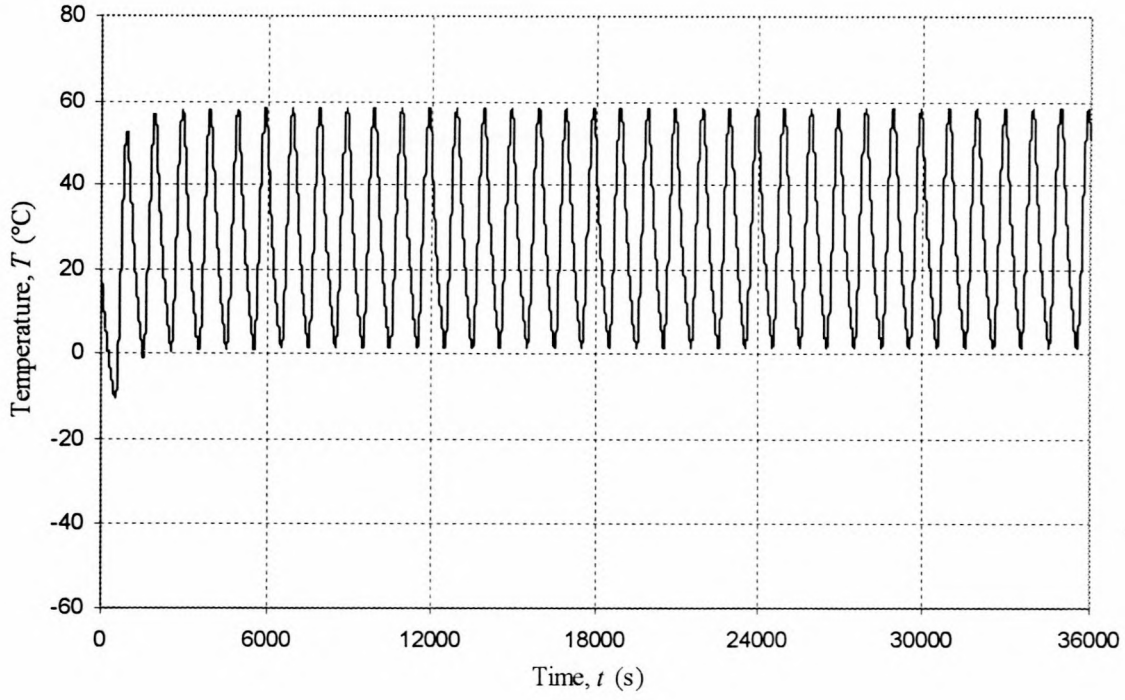

Figure F43 Temperature response of SUNSAT 3 +X solar panel surface for 6 Z-axis spins

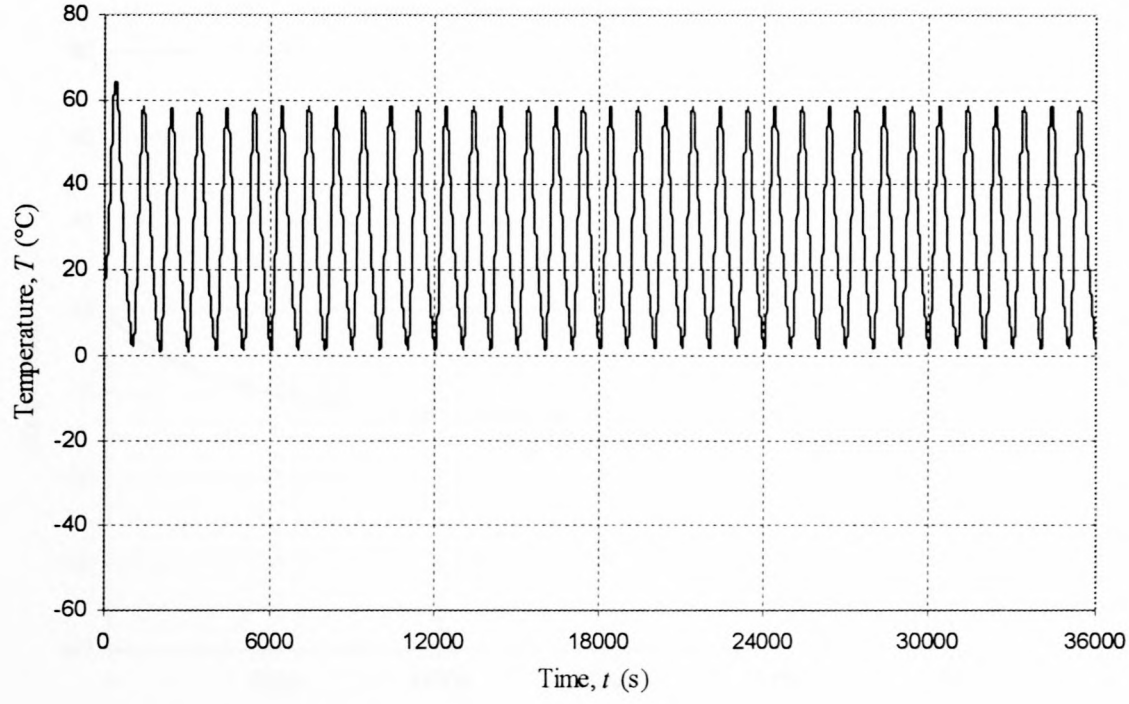

Figure F44 Temperature response of SUNSAT 3 -X solar panel surface for 6 Z-axis spins

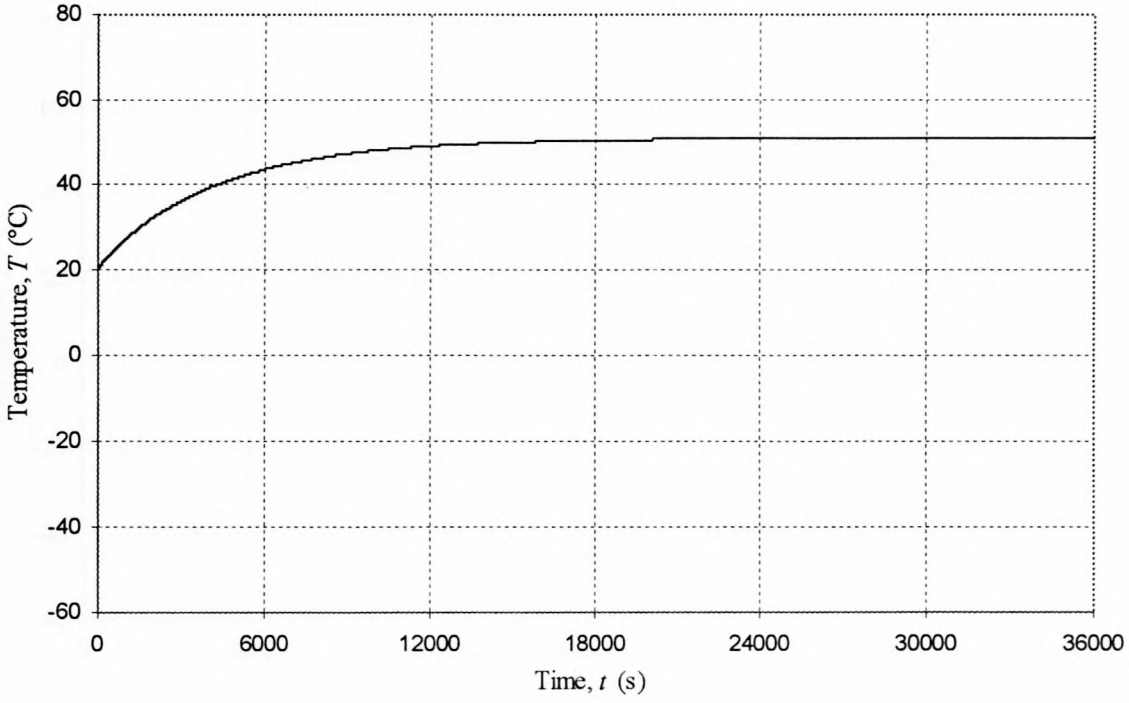

Figure F45 Temperature response of SUNSAT 3 +Z surface for 6 Z-axis spins

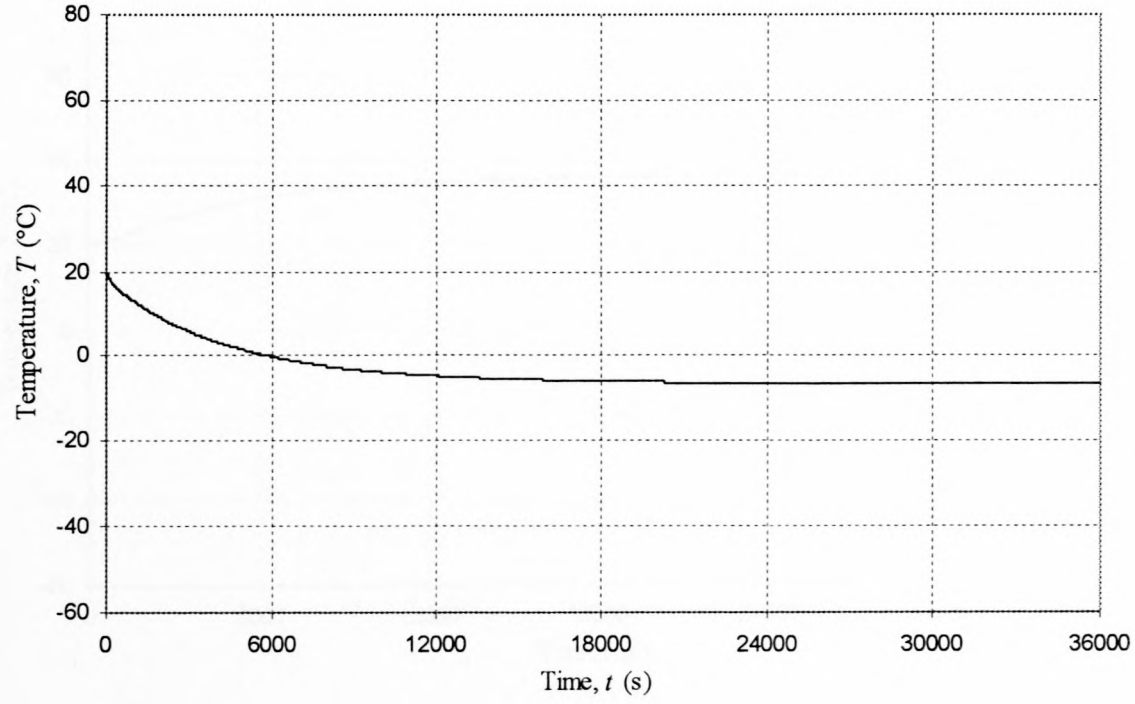

Figure F46 Temperature response of SUNSAT 3 -Z surface for 6 Z-axis spins

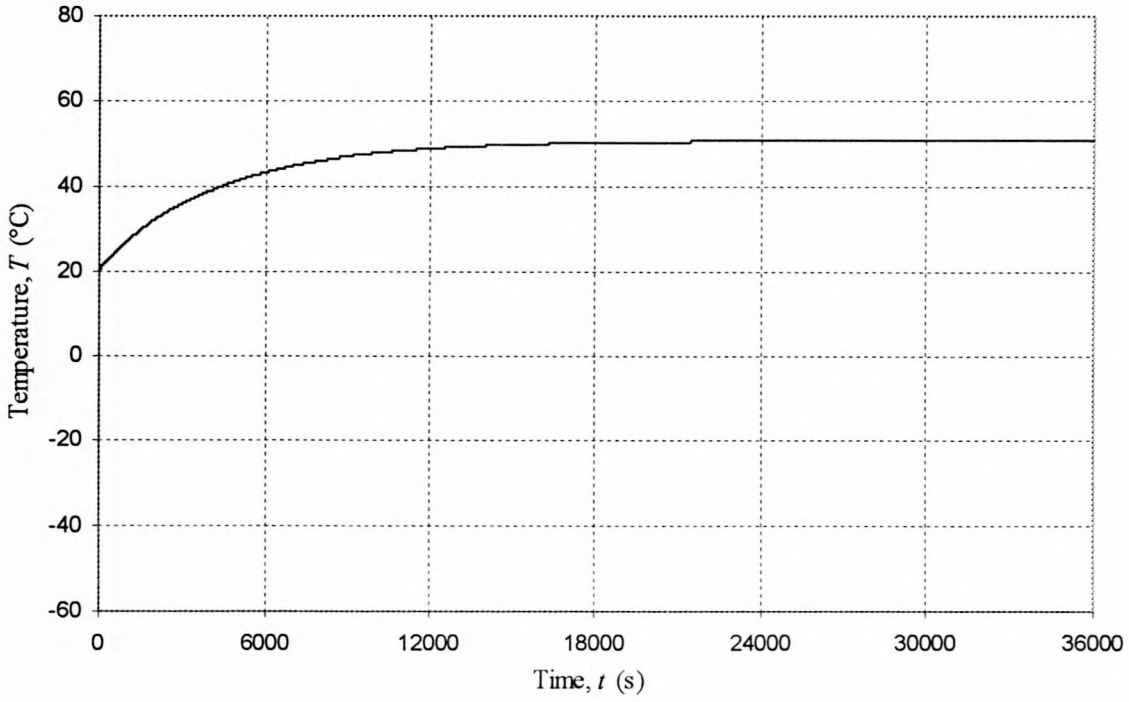

Figure F47 Temperature response of SUNSAT 3 bottom-plate for 6 Z-axis spins

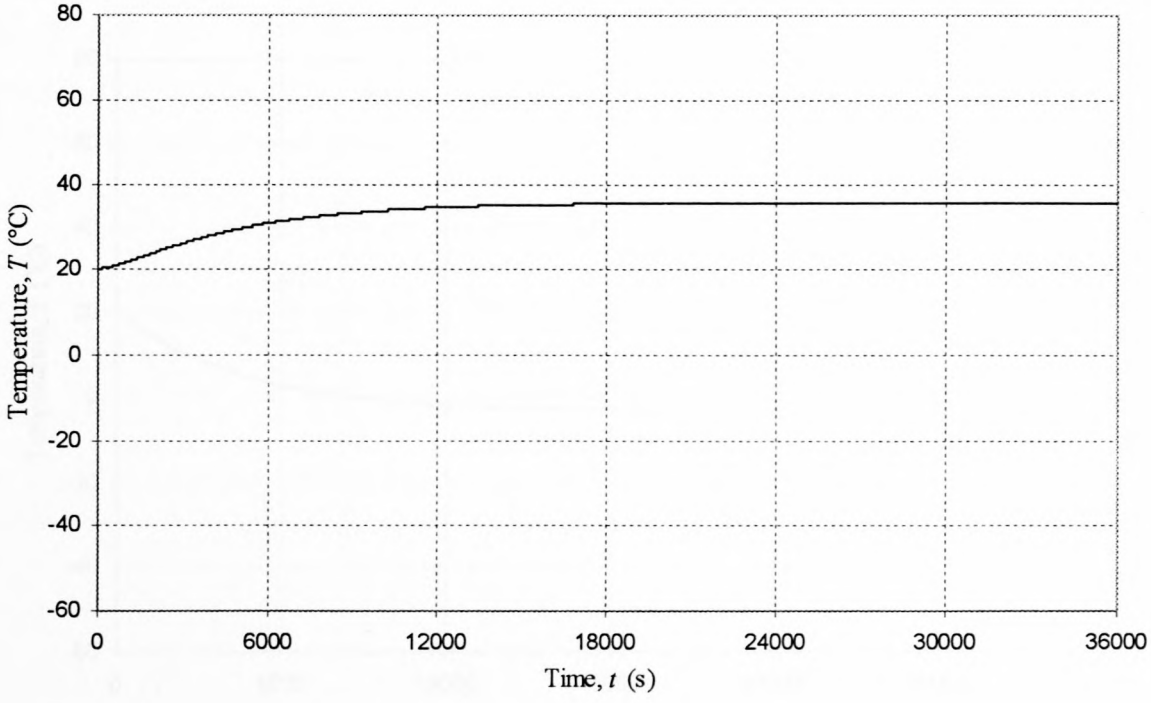

Figure F48 Temperature response of SUNSAT 3 battery for 6 Z-axis spins

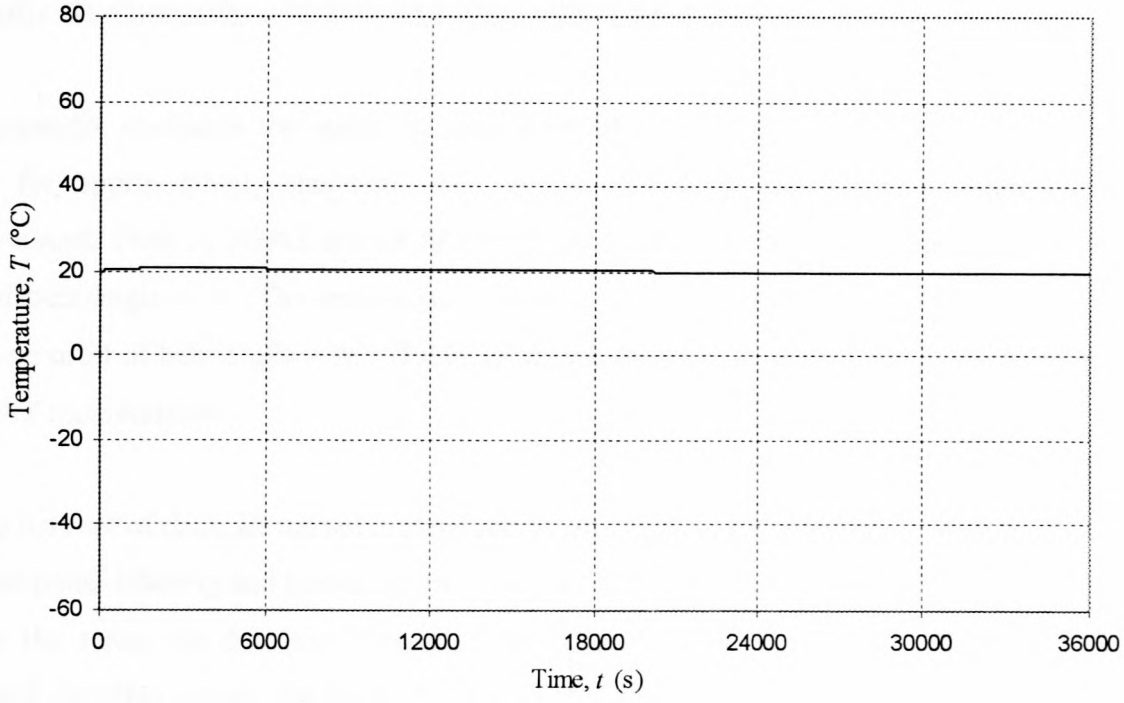

Figure F49 Temperature response of SUNSAT 3 middle-body section for 6 Z-axis spins

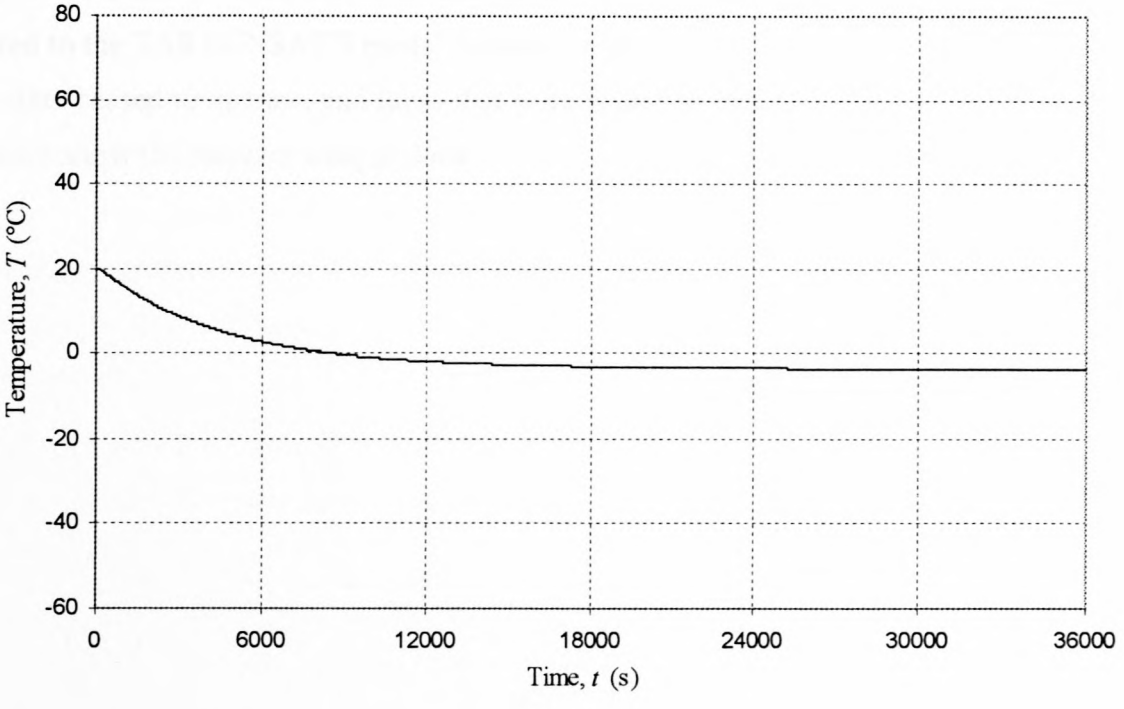

Figure F50 Temperature response of SUNSAT 3 upper-body section for 6 Z-axis spins

Appendix G: Comparison of SUNSAT Data with TAS SUNSAT 3 Model Results

This appendix compares the measured data from SUNSAT with that of the TAS SUNSAT 3 model for approximately the same two orbits with 6 spins per orbit. The first set of measurements from SUNSAT are for July 1999 when SUNSAT was in a polar sun-synchronous orbit of beta-angle = 0°. The second set of data is for June 2000 during which time SUNSAT was in an orbit of beta-angle = 90°. Table J6 shows the data channels used to attain the relevant SUNSAT temperatures.

For the first set of data, all the solar panel temperatures are compared for 1 orbit (6000 s). Since the solar panel labeling and identification used for SUNSAT and for the TAS SUNSAT 3 model are not the same, the data that correlated the best and was consistent with the labeling was compared. In other words, the SUNSAT +Y solar panel temperatures are compared to the TAS SUNSAT 3 model +X solar panel data; and the same for the SUNSAT –Y, +X, -X and the TAS SUNSAT 3 –X, -Y, +Y solar panels respectively. The bottom-plate and battery temperatures are also compared. Figures G1 to G6 show the relevant comparisons.

For the second set of data, only the SUNSAT +Y solar panel data and the battery data is compared to the TAS SUNSAT 3 model results due to the fact that most of the other sensors had by this time ceased to operate, and those that were operating had data that was unusable. Figures G7 and G8 show the relevant comparisons.

Discussions and Conclusions

Considering figures G1 to G4, the comparison of the solar panel temperatures showed good consistency in the maximum and minimum temperature ranges. The SUNSAT data saturated at low temperatures (discussed in chapter 3) due to sensor limitations. But if the minimum temperature were estimated, it would be around –40°C, the same as the TAS SUNSAT 3 model results. There is a noticeable period shift in the SUNSAT data. This is probably due to the fact that the SUNSAT orbit period was a little less than 100 min. The spin rate estimated at 6 per orbit shows to correlate fairly well with the actual SUNSAT data, as it is noticeable that the peaks that are caused by the direct solar radiation cause consistent temperature fluctuations that reflect on the TAS SUNSAT 3 model results.

The bottom-plate and battery comparisons in figures G5 and G6, showed consistency in the higher temperature of the bottom-plate compared to the battery for both cases. The difference in the temperatures is evident. The SUNSAT temperatures are lower than the model temperatures for both the bottom-plate and the battery by ± 8°C. This difference could be attributed to numerous reasons, but one might be that the internal heat generation that influences the bottom-plate and battery temperatures could have been estimated too high.

For the "hot" case shown in figures G7 and G8, the SUNSAT +Y solar panel data shows that the satellite was spinning approximately 18 times around its Z-axis per orbit. This was simulated in TAS to attain the desired effect. There is a significant difference in the results as it is evident that SUNSAT was still eclipsing (even though according to the software that tracked SUNSAT, Nova, it was in zero eclipse on 10 June 2000) and thus on average the temperatures are lower for the SUNSAT solar panel data than for the TAS SUNSAT 3 model results. The comparison of the battery temperatures in figure G8 shows good correlation. They both average a temperature of ± 36°C.

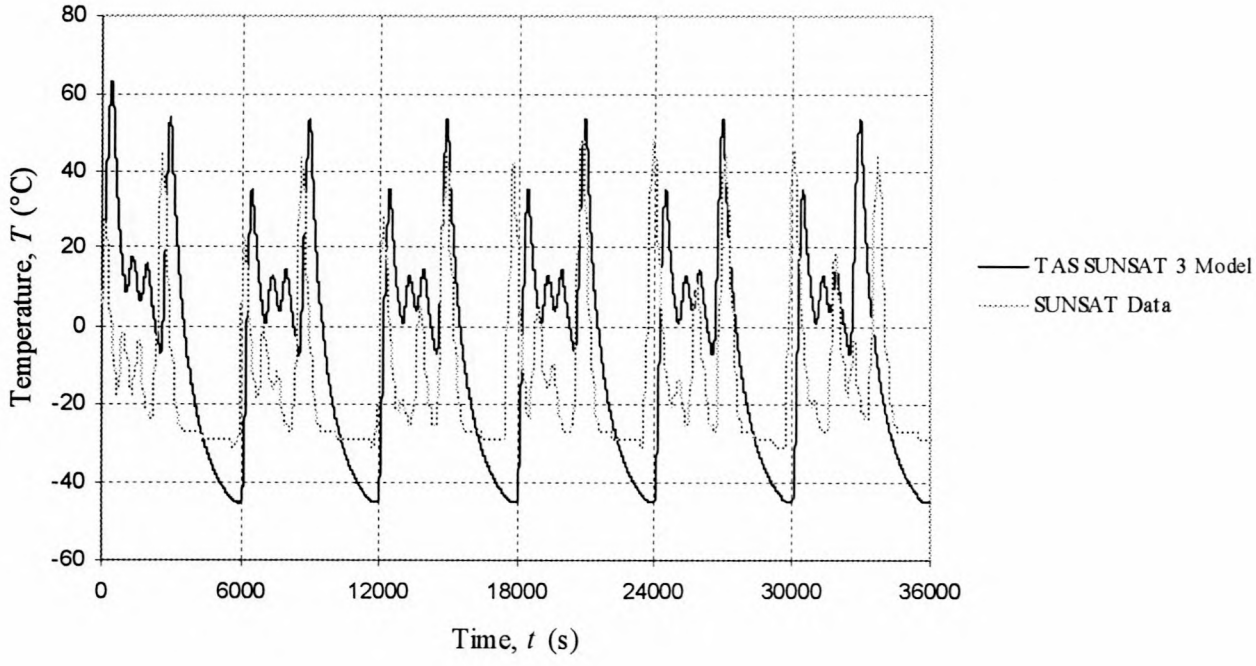

Figure G1 Comparison of SUNSAT +Y solar panel temperature data from 3 July 1999 with the TAS SUNSAT 3 model in a sun-synchronous polar orbit of β-angle = 0°

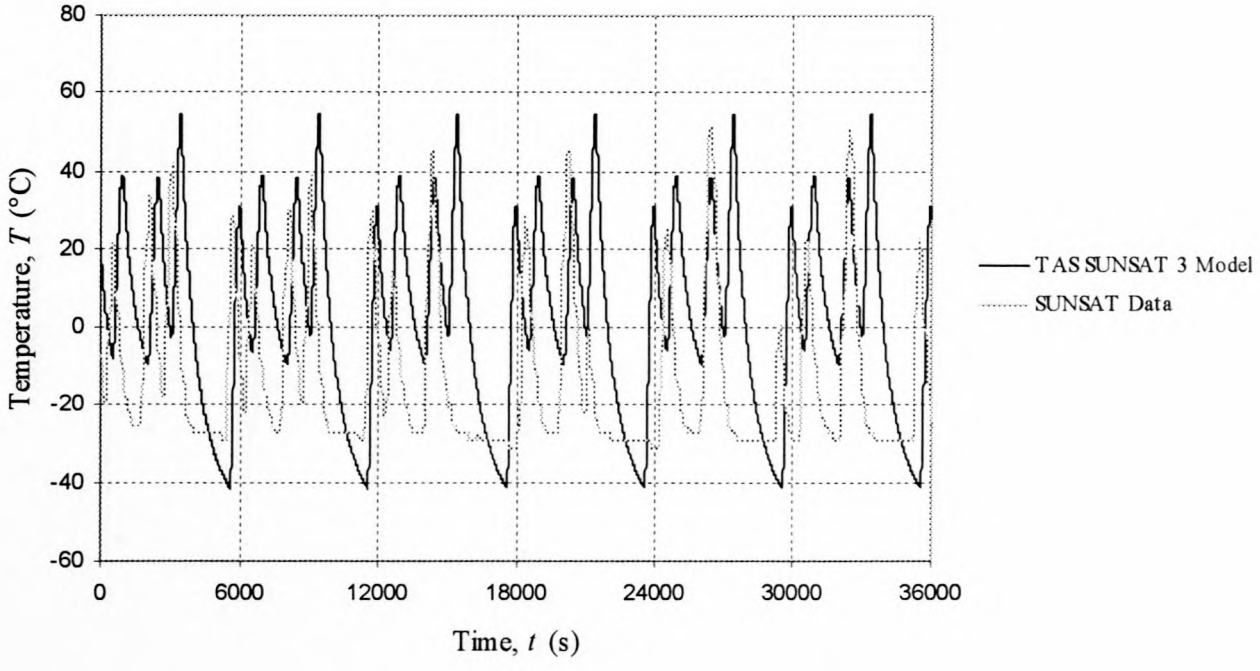

Figure G2 Comparison of SUNSAT -Y solar panel temperature data from 3 July 1999 with the TAS SUNSAT 3 model in a sun-synchronous polar orbit of β-angle = 0°

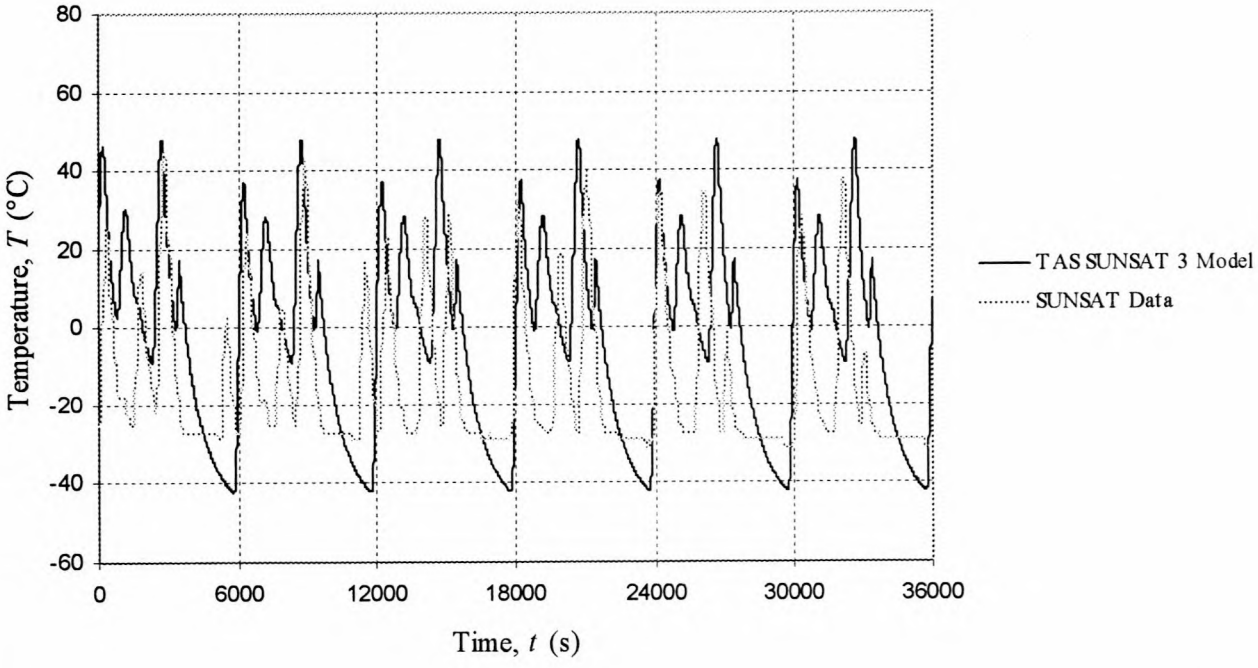

Figure G3 Comparison of SUNSAT +X solar panel temperature data from 3 July 1999 with the TAS SUNSAT 3 model in a sun-synchronous polar orbit of β-angle = 0°

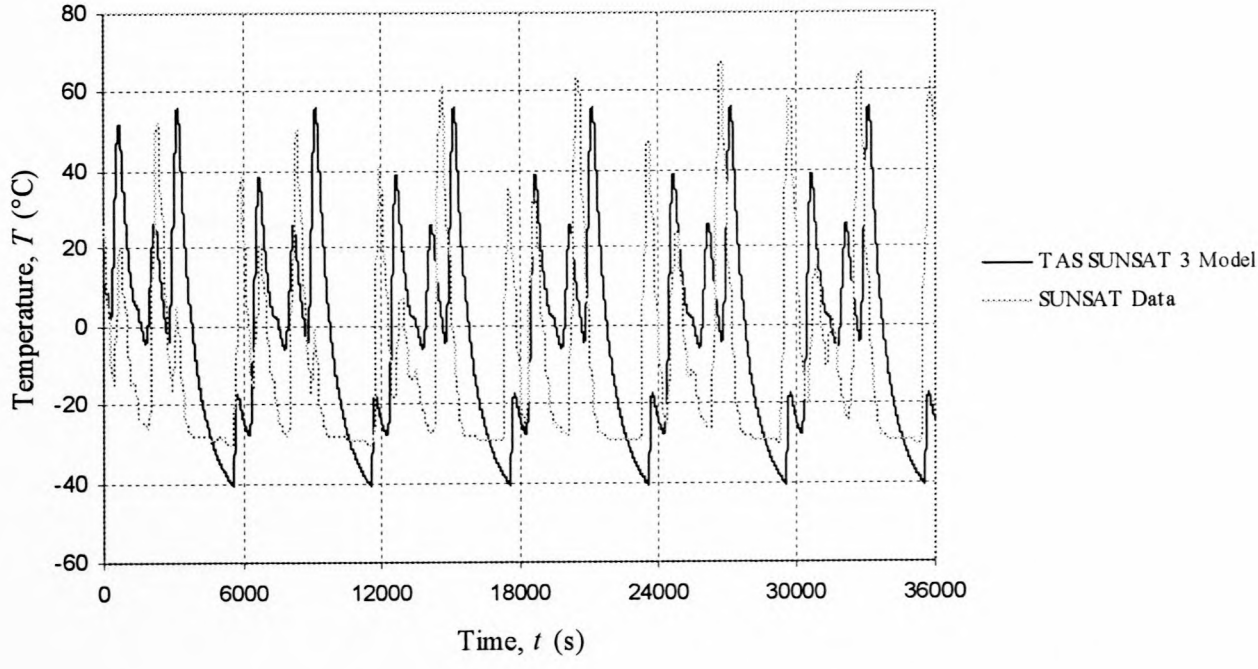

Figure G4 Comparison of SUNSAT -X solar panel temperature data from 3 July 1999 with the TAS SUNSAT 3 model in a sun-synchronous polar orbit of β-angle = 0°

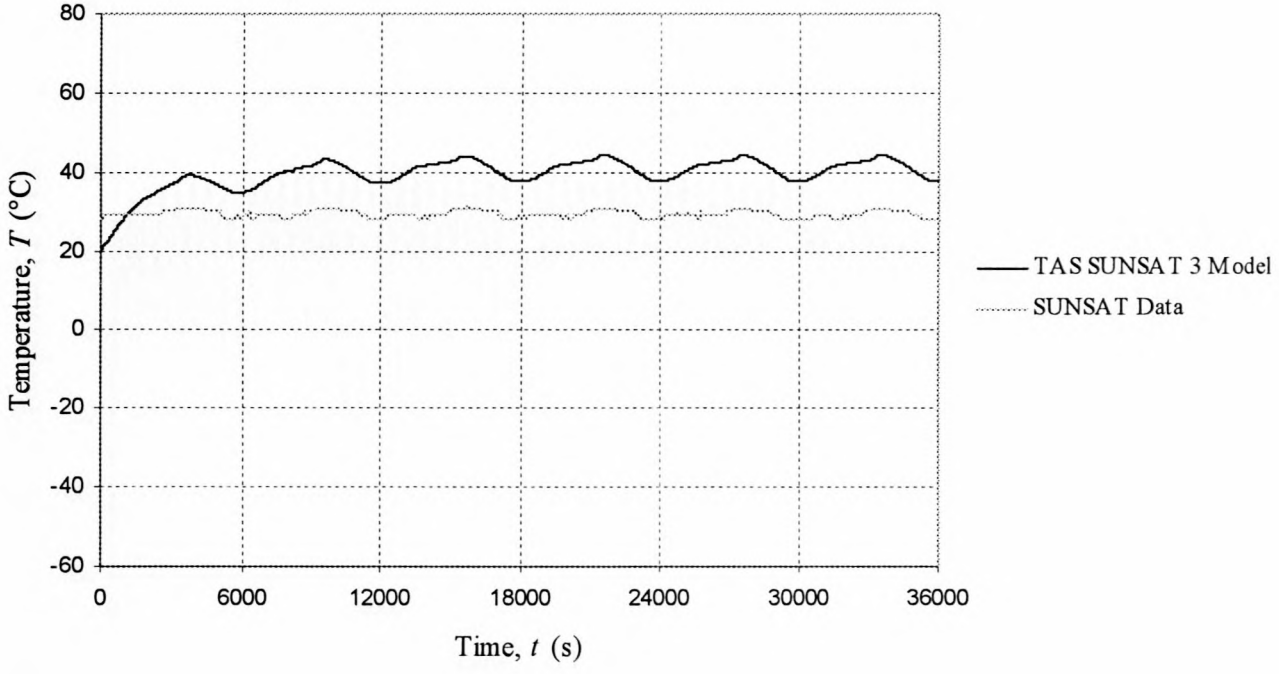

Figure G5 Comparison of SUNSAT bottom-plate temperature data from 3 July 1999 with the TAS SUNSAT 3 model in a sun-synchronous polar orbit of β-angle = 0°

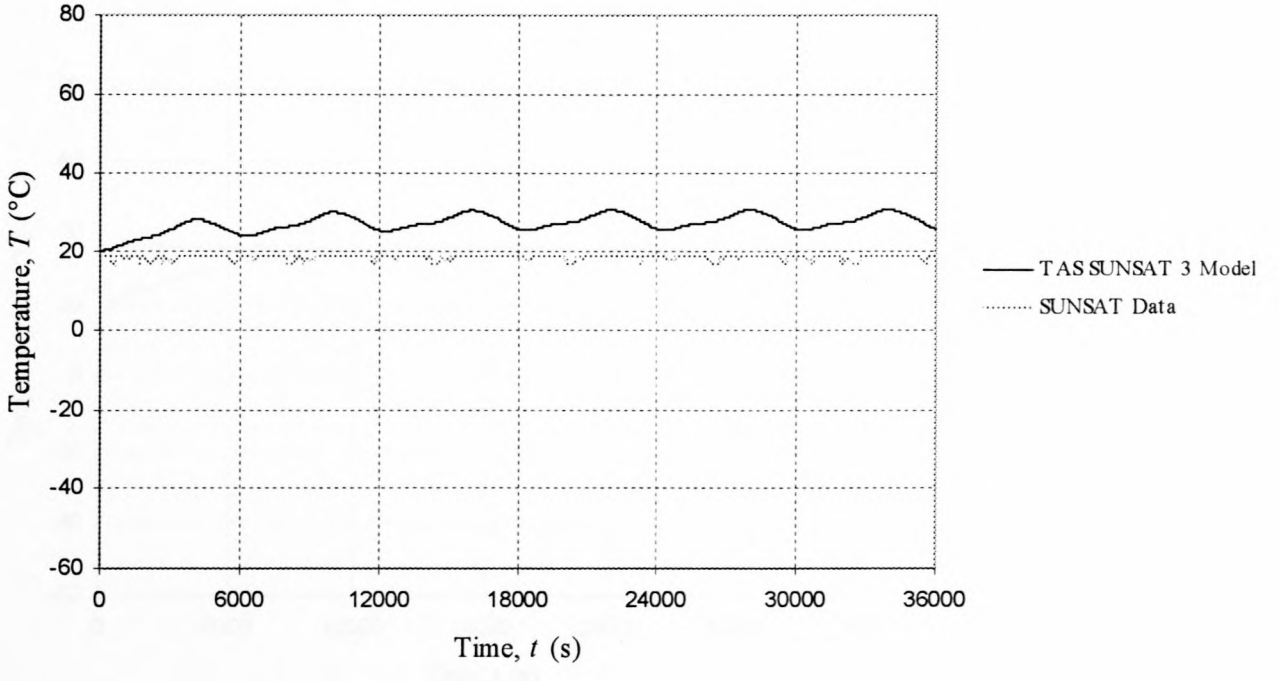

Figure G6 Comparison of SUNSAT battery temperature data from 3 July 1999 with the TAS SUNSAT 3 model in a sun-synchronous polar orbit of β-angle = 0°

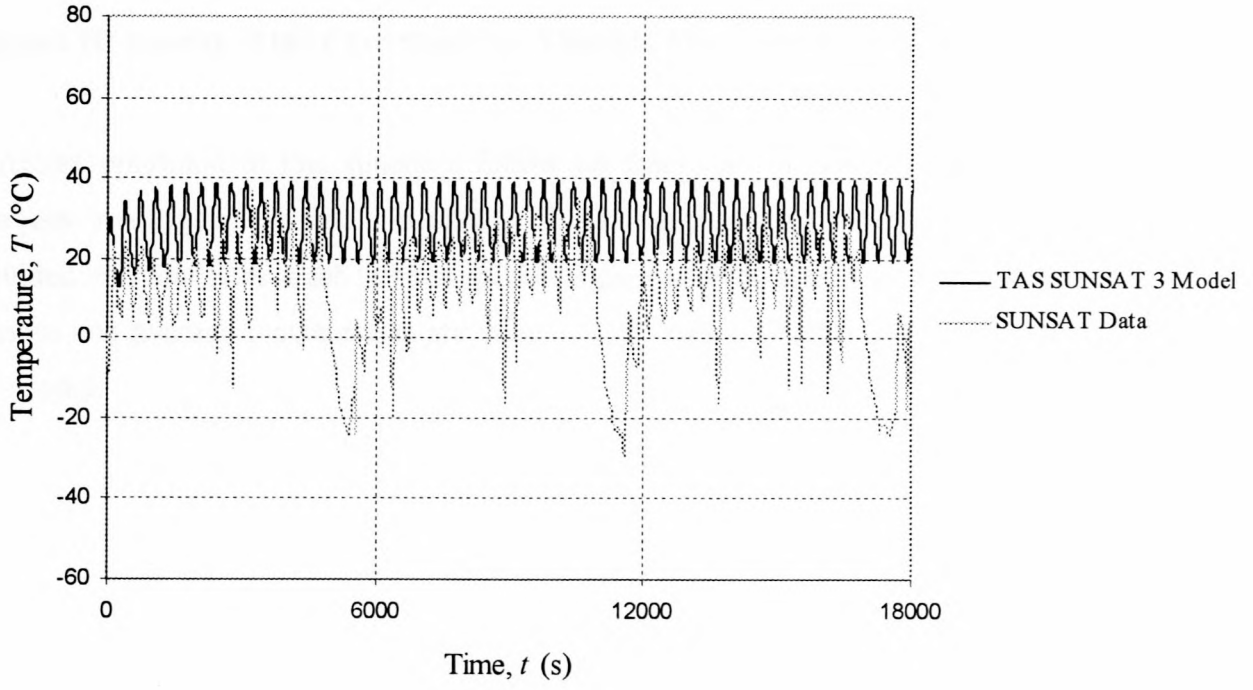

Figure G7 Comparison of SUNSAT +Y solar panel temperature from 16 June 2000 with the TAS SUNSAT 3 model in a sun-synchronous polar orbit of β-angle = 90°

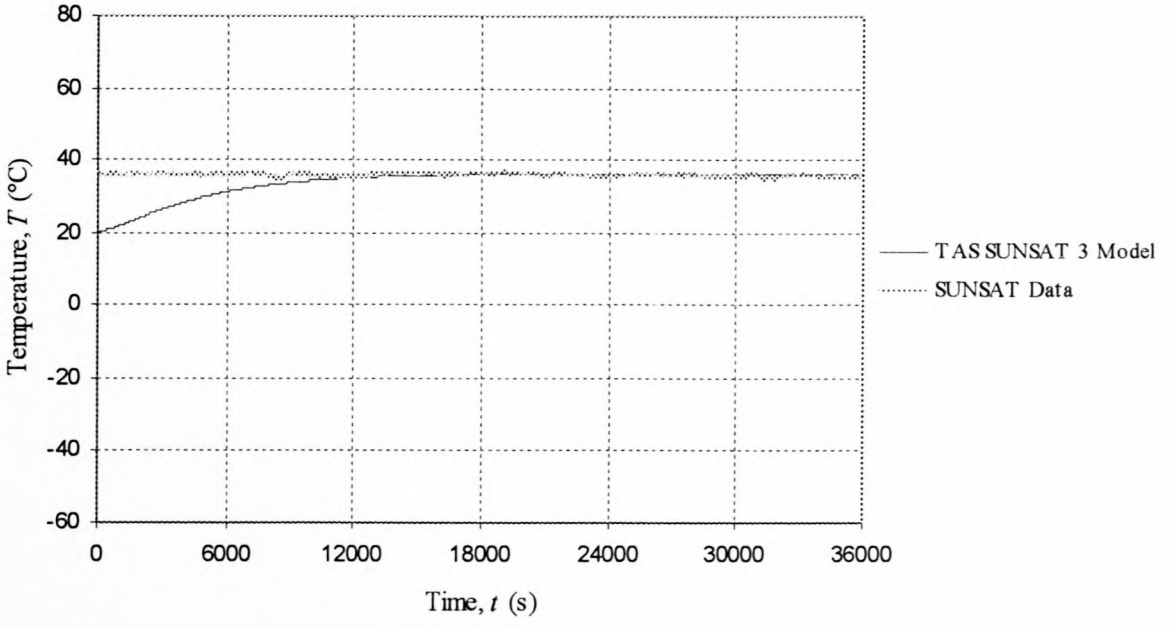

Figure G8 Comparison of SUNSAT battery temperature from 16 June 2000 with the TAS SUNSAT 3 model in a sun-synchronous polar orbit of β-angle = 90°

Appendix H: Results of the Case Study for Thermal Management and Control Techniques

The results presented in this appendix follow on from the thermal management and control techniques investigated in detail in chapter 7. The temperatures are given in tables that are subdivided into four tests. Each test has specific input variables, which are listed. The maximum, minimum and average temperatures are tabulated for each box plate and for the block, of the cubic-model.

Table H1 Data and temperature results of cubic-model, and for varying external surface solar absorptivity

Test H1a	**Test Details**					
	Input Variables			**Output Results**		
Model Components	Heating	$\alpha_{s,ext}$, $\alpha_{IR,int}$ (BOL)	ε_{ext}, ε_{int} (BOL)	Steady State Max. Temperature (°C)	Steady State Min. Temperature (°C)	Steady State Avg. Temperature (°C)
+Z box plate	-	0.5, 0.08	0.5, 0.15	-40.51	-62.11	-50.26
-Z box plate	-	0.5, 0.08	0.5, 0.15	-49.97	-69.38	-61.47
+Y box plate	1353 W/m^2	0.25, 0.08	0.5, 0.15	-41.30	-53.64	-47.25
-Y box plate	-	0.5, 0.08	0.5, 0.15	-59.13	-70.89	-67.01
+X box plate	-	0.5, 0.08	0.5, 0.15	-47.19	-70.07	-59.70
-X box plate	-	0.5, 0.08	0. 5, 0.15	-47.19	-70.07	-59.70
Internal block	30 W	0.08	0.15	-32.03	-43.84	-37.38
Test H1b	**Test Details**					
	Input Variables			**Output Results**		
Model Components	Heating	$\alpha_{s,ext}$, $\alpha_{IR,int}$ (BOL)	ε_{ext}, ε_{int} (BOL)	Steady State Max. Temperature (°C)	Steady State Min. Temperature (°C)	Steady State Avg. Temperature (°C)
+Z box plate	-	0.5, 0.08	0.5, 0.15	-3.47	-39.07	-21.35
-Z box plate	-	0.5, 0.08	0.5, 0.15	-10.95	-46.10	-31.89
+Y box plate	1353 W/m^2	0.5, 0.08	0.5, 0.15	1.28	-17.81	-8.95
-Y box plate	-	0.5, 0.08	0.5, 0.15	-35.74	-49.43	-44.50
+X box plate	-	0.5, 0.08	0.5, 0.15	-12.25	-48.00	-31.57
-X box plate	-	0.5, 0.08	0. 5, 0.15	-12.25	-47.99	-31.57
Internal block	30 W	0.08	0.15	-2.94	-16.39	-8.67
Test H1c	**Test Details**					
	Input Variables			**Output Results**		
Model Components	Heating	$\alpha_{s,ext}$, $\alpha_{IR,int}$ (BOL)	ε_{ext}, ε_{int} (BOL)	Steady State Max. Temperature (°C)	Steady State Min. Temperature (°C)	Steady State Avg. Temperature (°C)
+Z box plate	-	0.5, 0.08	0.5, 0.15	24.80	-23.52	-0.82
-Z box plate	-	0.5, 0.08	0.5, 0.15	18.23	-30.38	-10.86
+Y box plate	1353 W/m^2	0.75, 0.08	0.5, 0.15	33.45	8.49	19.53
-Y box plate	-	0.5, 0.08	0.5, 0.15	-19.85	-35.15	-29.38
+X box plate	-	0.5, 0.08	0.5, 0.15	13.99	-33.28	-11.81
-X box plate	-	0.5, 0.08	0. 5, 0.15	14.01	-33.27	-11.81
Internal block	30 W	0.08	0.15	17.78	2.93	11.73
Test H1d	**Test Details**					
	Input Variables			**Output Results**		
Model Components	Heating	$\alpha_{s,ext}$, $\alpha_{IR,int}$ (BOL)	ε_{ext}, ε_{int} (BOL)	Steady State Max. Temperature (°C)	Steady State Min. Temperature (°C)	Steady State Avg. Temperature (°C)
+Z box plate	-	0.5, 0.08	0.5, 0.15	47.82	-11.74	15.33
-Z box plate	-	0.5, 0.08	0.5, 0.15	41.99	-18.47	5.67
+Y box plate	1353 W/m^2	1, 0.08	0.5, 0.15	59.76	29.63	42.62
-Y box plate	-	0.5, 0.08	0.5, 0.15	-7.74	-24.44	-17.96
+X box plate	-	0.5, 0.08	0.5, 0.15	35.52	-22.23	3.58
-X box plate	-	0.5, 0.08	0. 5, 0.15	35.54	-22.21	3.58
Internal block	30 W	0.08	0.15	34.12	18.03	27.78

Table H2 Data and temperature results of cubic-model with a heat pipe, and for varying external surface solar absorptivity

Test H2a	**Test Details**					
	Input Variables			**Output Results**		
Model Components	Heating	$\alpha_{s,ext}$, $\alpha_{IR,int}$ (BOL)	ε_{ext}, ε_{int} (BOL)	Steady State Max. Temperature (°C)	Steady State Min. Temperature (°C)	Steady State Avg. Temperature (°C)
+Z box plate	-	0.5, 0.08	0.5, 0.15	-48.50	-64.02	-56.89
-Z box plate	-	0.5, 0.08	0.5, 0.15	-50.94	-66.40	-60.35
+Y box plate	1353 W/m^2	0.25, 0.08	0.5, 0.15	-45.38	-54.65	-50.56
-Y box plate	-	0.5, 0.08	0.5, 0.15	-60.81	-66.65	-63.93
+X box plate	-	0.5, 0.08	0.5, 0.15	-52.71	-66.65	-61.07
-X box plate	-	0.5, 0.08	0. 5, 0.15	-52.71	-66.65	-61.07
Internal block	30 W	0.08	0.15	-53.14	-58.82	-56.35
Test H2b	**Test Details**					
	Input Variables			**Output Results**		
Model Components	Heating	$\alpha_{s,ext}$, $\alpha_{IR,int}$ (BOL)	ε_{ext}, ε_{int} (BOL)	Steady State Max. Temperature (°C)	Steady State Min. Temperature (°C)	Steady State Avg. Temperature (°C)
+Z box plate	-	0.5, 0.08	0.5, 0.15	-11.35	-41.07	-28.81
-Z box plate	-	0.5, 0.08	0.5, 0.15	-11.81	-42.69	-30.52
+Y box plate	1353 W/m^2	0.5, 0.08	0.5, 0.15	-2.84	-18.73	-12.36
-Y box plate	-	0.5, 0.08	0.5, 0.15	-37.75	-44.03	-40.78
+X box plate	-	0.5, 0.08	0.5, 0.15	-16.36	-44.03	-32.93
-X box plate	-	0.5, 0.08	0. 5, 0.15	-16.36	-44.02	-32.93
Internal block	30 W	0.08	0.15	-25.09	-35.28	-31.09
Test H2c	**Test Details**					
	Input Variables			**Output Results**		
Model Components	Heating	$\alpha_{s,ext}$, $\alpha_{IR,int}$ (BOL)	ε_{ext}, ε_{int} (BOL)	Steady State Max. Temperature (°C)	Steady State Min. Temperature (°C)	Steady State Avg. Temperature (°C)
+Z box plate	-	0.5, 0.08	0.5, 0.15	16.45	-25.59	-8.93
-Z box plate	-	0.5, 0.08	0.5, 0.15	17.44	-26.66	-9.31
+Y box plate	1353 W/m^2	0.75, 0.08	0.5, 0.15	29.60	7.13	16.07
-Y box plate	-	0.5, 0.08	0.5, 0.15	-22.08	-28.87	-25.14
+X box plate	-	0.5, 0.08	0.5, 0.15	10.55	-28.87	-13.18
-X box plate	-	0.5, 0.08	0. 5, 0.15	10.56	-28.86	-13.18
Internal block	30 W	0.08	0.15	-5.19	-19.19	-13.55
Test H2d	**Test Details**					
	Input Variables			**Output Results**		
Model Components	Heating	$\alpha_{s,ext}$, $\alpha_{IR,int}$ (BOL)	ε_{ext}, ε_{int} (BOL)	Steady State Max. Temperature (°C)	Steady State Min. Temperature (°C)	Steady State Avg. Temperature (°C)
+Z box plate	-	0.5, 0.08	0.5, 0.15	39.14	-13.85	6.69
-Z box plate	-	0.5, 0.08	0.5, 0.15	41.25	-14.50	7.36
+Y box plate	1353 W/m^2	1, 0.08	0.5, 0.15	56.27	27.57	39.13
-Y box plate	-	0.5, 0.08	0.5, 0.15	-10.10	-17.45	-13.24
+X box plate	-	0.5, 0.08	0.5, 0.15	32.34	-17.45	2.22
-X box plate	-	0.5, 0.08	0. 5, 0.15	32.35	-17.43	2.22
Internal block	30 W	0.08	0.15	10.49	-6.84	0.05

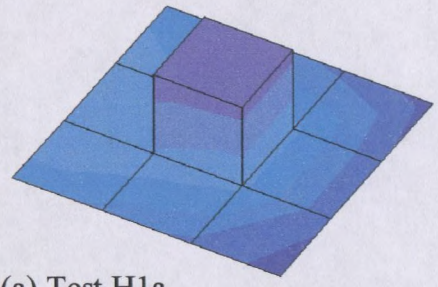

(a) Test H1a

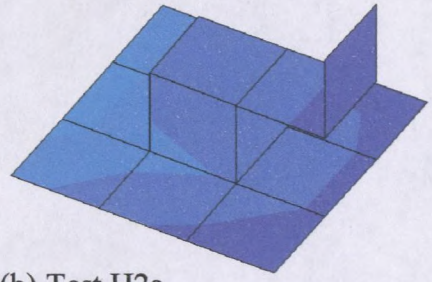

(b) Test H2a

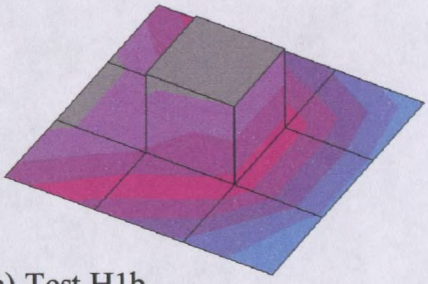

(c) Test H1b

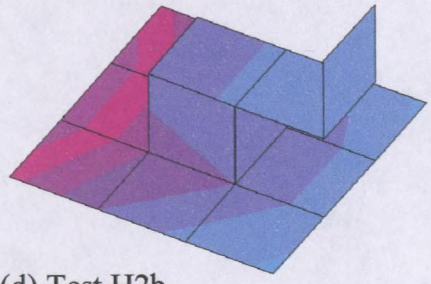

(d) Test H2b

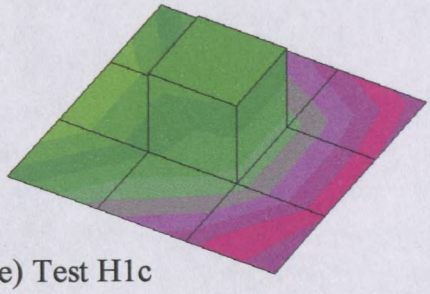

(e) Test H1c

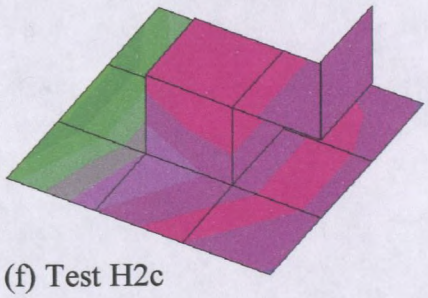

(f) Test H2c

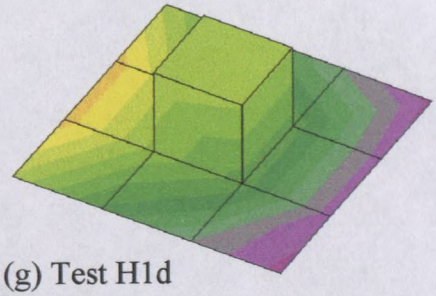

(g) Test H1d

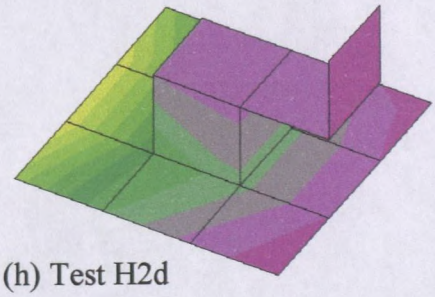

(h) Test H2d

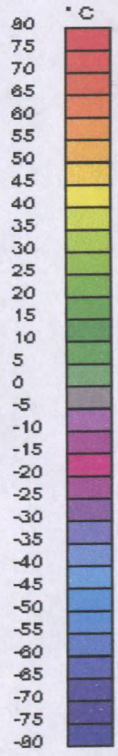

Figure H1 TAS temperature contour plot for cubic-model with and without a heat pipe, and for varying external surface absorptivity

Table H3 Data and temperature results of cubic-model, for varying internal heat generation

Test H3a	**Test Details**					
	Input Variables			**Output Results**		
Model Components	Heating	$\alpha_{s,ext}$, $\alpha_{IR,int}$ (BOL)	ε_{ext}, ε_{int} (BOL)	Steady State Max. Temperature (°C)	Steady State Min. Temperature (°C)	Steady State Avg. Temperature (°C)
+Z box plate	-	0.5, 0.08	0.25, 0.15	43.19	7.28	25.04
-Z box plate	-	0.5, 0.08	0.25, 0.15	36.00	0.51	14.90
+Y box plate	1353 W/m^2	0.5, 0.08	0.25, 0.15	48.35	29.12	37.97
-Y box plate	-	0.5, 0.08	0.25, 0.15	10.55	-2.96	1.95
+X box plate	-	0.5, 0.08	0.25, 0.15	34.48	-1.53	15.07
-X box plate	-	0.5, 0.08	0.25, 0.15	34.47	-1.51	15.07
Internal block	30 W	0.08	0.15	42.87	29.71	37.30
Test H3b	**Test Details**					
	Input Variables			**Output Results**		
Model Components	Heating	$\alpha_{s,ext}$, $\alpha_{IR,int}$ (BOL)	ε_{ext}, ε_{int} (BOL)	Steady State Max. Temperature (°C)	Steady State Min. Temperature (°C)	Steady State Avg. Temperature (°C)
+Z box plate	-	0.5, 0.08	0.5, 0.15	-3.47	-39.07	-21.35
-Z box plate	-	0.5, 0.08	0.5, 0.15	-10.95	-46.10	-31.89
+Y box plate	1353 W/m^2	0.5, 0.08	0.5, 0.15	1.28	-17.81	-8.95
-Y box plate	-	0.5, 0.08	0.5, 0.15	-35.74	-49.43	-44.50
+X box plate	-	0.5, 0.08	0.5, 0.15	-12.25	-48.00	-31.57
-X box plate	-	0.5, 0.08	0. 5, 0.15	-12.25	-47.99	-31.57
Internal block	30 W	0.08	0.15	-2.94	-16.39	-8.67
Test H3c	**Test Details**					
	Input Variables			**Output Results**		
Model Components	Heating	$\alpha_{s,ext}$, $\alpha_{IR,int}$ (BOL)	ε_{ext}, ε_{int} (BOL)	Steady State Max. Temperature (°C)	Steady State Min. Temperature (°C)	Steady State Avg. Temperature (°C)
+Z box plate	-	0.5, 0.08	0.75, 0.15	-27.49	-62.61	-45.06
-Z box plate	-	0.5, 0.08	0.75, 0.15	-35.03	-69.70	-55.71
+Y box plate	1353 W/m^2	0.5, 0.08	0.75, 0.15	-23.00	-41.84	-33.06
-Y box plate	-	0.5, 0.08	0.75, 0.15	-59.26	-72.90	-68.03
+X box plate	-	0.5, 0.08	0.75, 0.15	-36.24	-71.51	-55.33
-X box plate	-	0.5, 0.08	0.75, 0.15	-36.24	-71.50	-55.33
Internal block	30 W	0.08	0.15	-26.43	-39.95	-32.20
Test H3d	**Test Details**					
	Input Variables			**Output Results**		
Model Components	Heating	$\alpha_{s,ext}$, $\alpha_{IR,int}$ (BOL)	ε_{ext}, ε_{int} (BOL)	Steady State Max. Temperature (°C)	Steady State Min. Temperature (°C)	Steady State Avg. Temperature (°C)
+Z box plate	-	0.5, 0.08	1, 0.15	-43.20	-77.88	-60.51
-Z box plate	-	0.5, 0.08	1, 0.15	-50.76	-84.97	-71.20
+Y box plate	1353 W/m^2	0.5, 0.08	1, 0.15	-38.91	-57.52	-48.82
-Y box plate	-	0.5, 0.08	1, 0.15	-74.53	-88.09	-83.26
+X box plate	-	0.5, 0.08	1, 0.15	-51.92	-86.72	-70.79
-X box plate	-	0.5, 0.08	1, 0.15	-51.93	-86.72	-70.79
Internal block	30 W	0.08	0.15	-41.55	-55.29	-47.55

Table H4 Data and temperature results of cubic-model with a heat pipe, and for varying internal heat generation

Test H4a	**Test Details**					
	Input Variables			**Output Results**		
Model Components	Heating	$\alpha_{s,ext}$, $\alpha_{IR,int}$ (BOL)	ε_{ext}, ε_{int} (BOL)	Steady State Max. Temperature (°C)	Steady State Min. Temperature (°C)	Steady State Avg. Temperature (°C)
+Z box plate	-	0.5, 0.08	0.25, 0.15	35.17	5.19	17.55
-Z box plate	-	0.5, 0.08	0.25, 0.15	34.71	3.59	15.88
+Y box plate	1353 W/m^2	0.5, 0.08	0.25, 0.15	43.90	27.77	34.22
-Y box plate	-	0.5, 0.08	0.25, 0.15	8.59	2.20	5.50
+X box plate	-	0.5, 0.08	0.25, 0.15	30.21	2.20	13.43
-X box plate	-	0.5, 0.08	0.25, 0.15	30.23	2.21	13.44
Internal block	30 W	0.08	0.15	21.28	11.08	15.27
Test H4b	**Test Details**					
	Input Variables			**Output Results**		
Model Components	Heating	$\alpha_{s,ext}$, $\alpha_{IR,int}$ (BOL)	ε_{ext}, ε_{int} (BOL)	Steady State Max. Temperature (°C)	Steady State Min. Temperature (°C)	Steady State Avg. Temperature (°C)
+Z box plate	-	0.5, 0.08	0.5, 0.15	-11.35	-41.07	-28.81
-Z box plate	-	0.5, 0.08	0.5, 0.15	-11.81	-42.69	-30.52
+Y box plate	1353 W/m^2	0.5, 0.08	0.5, 0.15	-2.84	-18.73	-12.36
-Y box plate	-	0.5, 0.08	0.5, 0.15	-37.75	-44.03	-40.78
+X box plate	-	0.5, 0.08	0.5, 0.15	-16.36	-44.03	-32.93
-X box plate	-	0.5, 0.08	0. 5, 0.15	-16.36	-44.02	-32.93
Internal block	30 W	0.08	0.15	-25.09	-35.28	-31.09
Test H4c	**Test Details**					
	Input Variables			**Output Results**		
Model Components	Heating	$\alpha_{s,ext}$, $\alpha_{IR,int}$ (BOL)	ε_{ext}, ε_{int} (BOL)	Steady State Max. Temperature (°C)	Steady State Min. Temperature (°C)	Steady State Avg. Temperature (°C)
+Z box plate	-	0.5, 0.08	0.75, 0.15	-35.20	-64.56	-52.45
-Z box plate	-	0.5, 0.08	0.75, 0.15	-35.70	-66.20	-54.19
+Y box plate	1353 W/m^2	0.5, 0.08	0.75, 0.15	-26.90	-42.56	-36.27
-Y box plate	-	0.5, 0.08	0.75, 0.15	-61.28	-67.49	-64.29
+X box plate	-	0.5, 0.08	0.75, 0.15	-40.26	-67.49	-56.57
-X box plate	-	0.5, 0.08	0.75, 0.15	-40.25	-67.49	-56.57
Internal block	30 W	0.08	0.15	-48.73	-58.83	-54.67
Test H4d	**Test Details**					
	Input Variables			**Output Results**		
Model Components	Heating	$\alpha_{s,ext}$, $\alpha_{IR,int}$ (BOL)	ε_{ext}, ε_{int} (BOL)	Steady State Max. Temperature (°C)	Steady State Min. Temperature (°C)	Steady State Avg. Temperature (°C)
+Z box plate	-	0.5, 0.08	1, 0.15	-50.77	-79.80	-67.82
-Z box plate	-	0.5, 0.08	1, 0.15	-51.30	-81.44	-69.60
+Y box plate	1353 W/m^2	0.5, 0.08	1, 0.15	-42.65	-58.12	-51.89
-Y box plate	-	0.5, 0.08	1, 0.15	-76.54	-82.70	-79.53
+X box plate	-	0.5, 0.08	1, 0.15	-55.85	-82.70	-71.95
-X box plate	-	0.5, 0.08	1, 0.15	-55.85	-82.70	-71.94
Internal block	30 W	0.08	0.15	-64.10	-74.10	-70.00

Table H5 Data and temperature results of cubic-mode, for varying radiator emissivity

Test H5a	**Test Details**					
	Input Variables			**Output Results**		
Model Components	Heating	$\alpha_{s,ext}$, $\alpha_{IR,int}$ (BOL)	ε_{ext}, ε_{int} (BOL)	Steady State Max. Temperature (°C)	Steady State Min. Temperature (°C)	Steady State Avg. Temperature (°C)
+Z box plate	-	0.5, 0.08	0.5, 0.15	-3.47	-39.07	-21.35
-Z box plate	-	0.5, 0.08	0.5, 0.15	-10.95	-46.10	-31.89
+Y box plate	1353 W/m^2	0.5, 0.08	0.5, 0.15	1.28	-17.81	-8.95
-Y box plate	-	0.5, 0.08	0.5, 0.15	-35.74	-49.43	-44.50
+X box plate	-	0.5, 0.08	0.5, 0.15	-12.25	-48.00	-31.57
-X box plate	-	0.5, 0.08	0. 5, 0.15	-12.25	-47.99	-31.57
Internal block	30 W	0.08	0.15	-2.94	-16.39	-8.67
Test H5b	**Test Details**					
	Input Variables			**Output Results**		
Model Components	Heating	$\alpha_{s,ext}$, $\alpha_{IR,int}$ (BOL)	ε_{ext}, ε_{int} (BOL)	Steady State Max. Temperature (°C)	Steady State Min. Temperature (°C)	Steady State Avg. Temperature (°C)
+Z box plate	-	0.5, 0.08	0.5, 0.15	6.98	-29.33	-9.22
-Z box plate	-	0.5, 0.08	0.5, 0.15	-5.83	-40.28	-26.35
+Y box plate	1353 W/m^2	0.5, 0.08	0.5, 0.15	8.10	-12.65	-2.20
-Y box plate	-	0.5, 0.08	0.5, 0.15	-24.40	-42.99	-36.85
+X box plate	-	0.5, 0.08	0.5, 0.15	-3.29	-41.71	-24.31
-X box plate	-	0.5, 0.08	0. 5, 0.15	-3.29	-41.70	-24.31
Internal block	50 W	0.08	0.15	20.43	1.00	11.69
Test H5c	**Test Details**					
	Input Variables			**Output Results**		
Model Components	Heating	$\alpha_{s,ext}$, $\alpha_{IR,int}$ (BOL)	ε_{ext}, ε_{int} (BOL)	Steady State Max. Temperature (°C)	Steady State Min. Temperature (°C)	Steady State Avg. Temperature (°C)
+Z box plate	-	0.5, 0.08	0.5, 0.15	23.14	-20.33	2.13
-Z box plate	-	0.5, 0.08	0.5, 0.15	-1.15	-34.96	-21.29
+Y box plate	1353 W/m^2	0.5, 0.08	0.5, 0.15	16.70	-7.94	4.00
-Y box plate	-	0.5, 0.08	0.5, 0.15	-13.85	-37.12	-29.82
+X box plate	-	0.5, 0.08	0.5, 0.15	4.97	-35.97	-17.64
-X box plate	-	0.5, 0.08	0. 5, 0.15	4.97	-35.96	-17.64
Internal block	70 W	0.08	0.15	42.77	17.50	31.08
Test H5d	**Test Details**					
	Input Variables			**Output Results**		
Model Components	Heating	$\alpha_{s,ext}$, $\alpha_{IR,int}$ (BOL)	ε_{ext}, ε_{int} (BOL)	Steady State Max. Temperature (°C)	Steady State Min. Temperature (°C)	Steady State Avg. Temperature (°C)
+Z box plate	-	0.5, 0.08	0.5, 0.15	38.67	-11.99	12.78
-Z box plate	-	0.5, 0.08	0.5, 0.15	3.16	-30.08	-16.63
+Y box plate	1353 W/m^2	0.5, 0.08	0.5, 0.15	25.77	-3.62	9.72
-Y box plate	-	0.5, 0.08	0.5, 0.15	-4.00	-31.74	-23.33
+X box plate	-	0.5, 0.08	0.5, 0.15	12.63	-30.71	-11.49
-X box plate	-	0.5, 0.08	0. 5, 0.15	12.63	-30.70	-11.48
Internal block	90 W	0.08	0.15	64.15	33.18	49.58

Table H6 Data and temperature results of cubic-model with a heat pipe, and for varying radiator emissivity

Test H6a	**Test Details**					
	Input Variables			**Output Results**		
Model Components	Heating	$\alpha_{s,ext}$, $\alpha_{IR,int}$ (BOL)	ε_{ext}, ε_{int} (BOL)	Steady State Max. Temperature (°C)	Steady State Min. Temperature (°C)	Steady State Avg. Temperature (°C)
+Z box plate	-	0.5, 0.08	0.5, 0.15	-11.35	-41.07	-28.81
-Z box plate	-	0.5, 0.08	0.5, 0.15	-11.81	-42.69	-30.52
+Y box plate	1353 W/m^2	0.5, 0.08	0.5, 0.15	-2.84	-18.73	-12.36
-Y box plate	-	0.5, 0.08	0.5, 0.15	-37.75	-44.03	-40.78
+X box plate	-	0.5, 0.08	0.5, 0.15	-16.36	-44.03	-32.93
-X box plate	-	0.5, 0.08	0. 5, 0.15	-16.36	-44.02	-32.93
Internal block	30 W	0.08	0.15	-25.09	-35.28	-31.09
Test H6b	**Test Details**					
	Input Variables			**Output Results**		
Model Components	Heating	$\alpha_{s,ext}$, $\alpha_{IR,int}$ (BOL)	ε_{ext}, ε_{int} (BOL)	Steady State Max. Temperature (°C)	Steady State Min. Temperature (°C)	Steady State Avg. Temperature (°C)
+Z box plate	-	0.5, 0.08	0.5, 0.15	-3.47	-31.98	-19.23
-Z box plate	-	0.5, 0.08	0.5, 0.15	-6.85	-35.54	-24.36
+Y box plate	1353 W/m^2	0.5, 0.08	0.5, 0.15	2.73	-13.75	-6.63
-Y box plate	-	0.5, 0.08	0.5, 0.15	-26.67	-36.20	-31.71
+X box plate	-	0.5, 0.08	0.5, 0.15	-10.69	-36.20	-26.03
-X box plate	-	0.5, 0.08	0. 5, 0.15	-10.69	-36.20	-26.03
Internal block	50 W	0.08	0.15	-13.01	-23.26	-18.85
Test H6c	**Test Details**					
	Input Variables			**Output Results**		
Model Components	Heating	$\alpha_{s,ext}$, $\alpha_{IR,int}$ (BOL)	ε_{ext}, ε_{int} (BOL)	Steady State Max. Temperature (°C)	Steady State Min. Temperature (°C)	Steady State Avg. Temperature (°C)
+Z box plate	-	0.5, 0.08	0.5, 0.15	3.81	-23.61	-10.32
-Z box plate	-	0.5, 0.08	0.5, 0.15	-2.35	-29.03	-18.75
+Y box plate	1353 W/m^2	0.5, 0.08	0.5, 0.15	7.80	-9.25	-1.42
-Y box plate	-	0.5, 0.08	0.5, 0.15	-16.37	-29.36	-23.36
+X box plate	-	0.5, 0.08	0.5, 0.15	-4.72	-29.43	-19.72
-X box plate	-	0.5, 0.08	0. 5, 0.15	-4.73	-29.43	-19.72
Internal block	70 W	0.08	0.15	-1.63	-12.01	-7.35
Test H6d	**Test Details**					
	Input Variables			**Output Results**		
Model Components	Heating	$\alpha_{s,ext}$, $\alpha_{IR,int}$ (BOL)	ε_{ext}, ε_{int} (BOL)	Steady State Max. Temperature (°C)	Steady State Min. Temperature (°C)	Steady State Avg. Temperature (°C)
+Z box plate	-	0.5, 0.08	0.5, 0.15	10.59	-15.86	-1.98
-Z box plate	-	0.5, 0.08	0.5, 0.15	1.76	-23.04	-13.60
+Y box plate	1353 W/m^2	0.5, 0.08	0.5, 0.15	12.47	-5.14	3.39
-Y box plate	-	0.5, 0.08	0.5, 0.15	-6.73	-23.04	-15.60
+X box plate	-	0.5, 0.08	0.5, 0.15	1.27	-24.03	-13.91
-X box plate	-	0.5, 0.08	0. 5, 0.15	1.26	-24.03	-13.91
Internal block	30 W	0.08	0.15	9.16	-1.43	3.51

Table H7 Data and temperature results of cubic-model with a flat reflector internal surface coating, and for varying internal heat generation

Test H7a	**Test Details**					
	Input Variables			**Output Results**		
Model Components	Heating	$\alpha_{s,ext}$, $\alpha_{IR,int}$ (BOL)	ε_{ext}, ε_{int} (BOL)	Steady State Max. Temperature (°C)	Steady State Min. Temperature (°C)	Steady State Avg. Temperature (°C)
+Z box plate	-	0.5, 0.08	0.5, 0.15	-6.51	-37.47	-21.96
-Z box plate	-	0.5, 0.08	0.5, 0.15	-12.90	-42.98	-30.77
+Y box plate	1353 W/m^2	0.5, 0.08	0.5, 0.15	-2.49	-18.91	-11.33
-Y box plate	-	0.5, 0.08	0.5, 0.15	-34.44	-45.64	-41.73
+X box plate	-	0.5, 0.08	0.5, 0.15	-14.24	-44.84	-30.88
-X box plate	-	0.5, 0.08	0. 5, 0.15	-14.27	-44.79	-30.87
Internal block	30 W	0.08	0.15	-4.24	-17.30	-9.89
Test H7b	**Test Details**					
	Input Variables			**Output Results**		
Model Components	Heating	$\alpha_{s,ext}$, $\alpha_{IR,int}$ (BOL)	ε_{ext}, ε_{int} (BOL)	Steady State Max. Temperature (°C)	Steady State Min. Temperature (°C)	Steady State Avg. Temperature (°C)
+Z box plate	-	0.5, 0.08	0.5, 0.15	3.90	-28.14	-10.64
-Z box plate	-	0.5, 0.08	0.5, 0.15	-7.44	-36.73	-24.79
+Y box plate	1353 W/m^2	0.5, 0.08	0.5, 0.15	4.14	-13.43	-4.67
-Y box plate	-	0.5, 0.08	0.5, 0.15	-23.76	-38.92	-34.04
+X box plate	-	0.5, 0.08	0.5, 0.15	-5.78	-38.28	-23.62
-X box plate	-	0.5, 0.08	0. 5, 0.15	-5.83	-38.23	-23.61
Internal block	50 W	0.08	0.15	17.79	-1.27	9.11
Test H7c	**Test Details**					
	Input Variables			**Output Results**		
Model Components	Heating	$\alpha_{s,ext}$, $\alpha_{IR,int}$ (BOL)	ε_{ext}, ε_{int} (BOL)	Steady State Max. Temperature (°C)	Steady State Min. Temperature (°C)	Steady State Avg. Temperature (°C)
+Z box plate	-	0.5, 0.08	0.5, 0.15	18.71	-19.59	-0.17
-Z box plate	-	0.5, 0.08	0.5, 0.15	-2.39	-30.99	-19.26
+Y box plate	1353 W/m^2	0.5, 0.08	0.5, 0.15	12.05	-8.37	1.47
-Y box plate	-	0.5, 0.08	0.5, 0.15	-13.94	-32.76	-26.98
+X box plate	-	0.5, 0.08	0.5, 0.15	1.98	-32.27	-16.95
-X box plate	-	0.5, 0.08	0. 5, 0.15	1.92	-32.21	-16.93
Internal block	70 W	0.08	0.15	38.66	13.73	27.01
Test H7d	**Test Details**					
	Input Variables			**Output Results**		
Model Components	Heating	$\alpha_{s,ext}$, $\alpha_{IR,int}$ (BOL)	ε_{ext}, ε_{int} (BOL)	Steady State Max. Temperature (°C)	Steady State Min. Temperature (°C)	Steady State Avg. Temperature (°C)
+Z box plate	-	0.5, 0.08	0.5, 0.15	32.60	-11.70	9.56
-Z box plate	-	0.5, 0.08	0.5, 0.15	2.31	-25.67	-14.12
+Y box plate	1353 W/m^2	0.5, 0.08	0.5, 0.15	20.29	-3.67	7.14
-Y box plate	-	0.5, 0.08	0.5, 0.15	-4.85	-27.08	-20.46
+X box plate	-	0.5, 0.08	0.5, 0.15	9.14	-26.73	-10.78
-X box plate	-	0.5, 0.08	0. 5, 0.15	9.06	-26.66	-10.76
Internal block	90 W	0.08	0.15	58.49	27.80	49.58

Table H8 Data and temperature results of cubic-model with a flat absorber internal surface coating, and for varying internal heat generation

Test H8a	**Test Details**					
	Input Variables			**Output Results**		
Model Components	Heating	$\alpha_{s,ext}$, $\alpha_{IR,int}$ (BOL)	ε_{ext}, ε_{int} (BOL)	Steady State Max. Temperature (°C)	Steady State Min. Temperature (°C)	Steady State Avg. Temperature (°C)
+Z box plate	-	0.5, 0.9	0.5, 0.9	-7.20	-37.66	-22.75
-Z box plate	-	0.5, 0.9	0.5, 0.9	-12.69	-42.63	-30.46
+Y box plate	1353 W/m^2	0.5, 0.9	0.5, 0.9	-2.69	-18.71	-11.44
-Y box plate	-	0.5, 0.9	0.5, 0.9	-34.88	-45.35	-41.63
+X box plate	-	0.5, 0.9	0.5, 0.9	-14.65	-44.56	-30.87
-X box plate	-	0.5, 0.9	0.5, 0.9	-14.70	-44.52	-30.86
Internal block	30 W	0.9	0.9	-7.92	-19.07	-12.66
Test H8b	**Test Details**					
	Input Variables			**Output Results**		
Model Components	Heating	$\alpha_{s,ext}$, $\alpha_{IR,int}$ (BOL)	ε_{ext}, ε_{int} (BOL)	Steady State Max. Temperature (°C)	Steady State Min. Temperature (°C)	Steady State Avg. Temperature (°C)
+Z box plate	-	0.5, 0.9	0.5, 0.9	2.01	-28.60	-12.09
-Z box plate	-	0.5, 0.9	0.5, 0.9	-7.01	-36.18	-24.26
+Y box plate	1353 W/m^2	0.5, 0.9	0.5, 0.9	3.91	-13.03	-4.78
-Y box plate	-	0.5, 0.9	0.5, 0.9	-24.65	-38.49	-33.94
+X box plate	-	0.5, 0.9	0.5, 0.9	-6.45	-37.85	-23.62
-X box plate	-	0.5, 0.9	0.5, 0.9	-6.52	-37.81	-23.61
Internal block	50 W	0.9	0.9	10.84	-4.49	3.99
Test H8c	**Test Details**					
	Input Variables			**Output Results**		
Model Components	Heating	$\alpha_{s,ext}$, $\alpha_{IR,int}$ (BOL)	ε_{ext}, ε_{int} (BOL)	Steady State Max. Temperature (°C)	Steady State Min. Temperature (°C)	Steady State Avg. Temperature (°C)
+Z box plate	-	0.5, 0.9	0.5, 0.9	14.02	-20.31	-2.30
-Z box plate	-	0.5, 0.9	0.5, 0.9	-1.74	-30.21	-18.49
+Y box plate	1353 W/m^2	0.5, 0.9	0.5, 0.9	10.45	-7.75	1.36
-Y box plate	-	0.5, 0.9	0.5, 0.9	-15.29	-32.18	-26.87
+X box plate	-	0.5, 0.9	0.5, 0.9	1.06	-31.68	-16.94
-X box plate	-	0.5, 0.9	0.5, 0.9	0.96	-31.63	-16.93
Internal block	70 W	0.9	0.9	28.09	8.94	19.30
Test H8d	**Test Details**					
	Input Variables			**Output Results**		
Model Components	Heating	$\alpha_{s,ext}$, $\alpha_{IR,int}$ (BOL)	ε_{ext}, ε_{int} (BOL)	Steady State Max. Temperature (°C)	Steady State Min. Temperature (°C)	Steady State Avg. Temperature (°C)
+Z box plate	-	0.5, 0.9	0.5, 0.9	26.32	-12.67	6.73
-Z box plate	-	0.5, 0.9	0.5, 0.9	3.22	-24.63	-13.08
+Y box plate	1353 W/m^2	0.5, 0.9	0.5, 0.9	18.24	-2.82	7.05
-Y box plate	-	0.5, 0.9	0.5, 0.9	-6.66	-26.32	-20.32
+X box plate	-	0.5, 0.9	0.5, 0.9	7.99	-25.95	-10.75
-X box plate	-	0.5, 0.9	0.5, 0.9	7.86	-25.89	-10.74
Internal block	90 W	0.9	0.9	44.03	21.89	33.48

Table H9 Data and temperature results of cubic-model with a flat absorber internal surface coating, a flat reflector surface coating on the block, and for varying internal heat generation

Test H9a	**Test Details**					
	Input Variables			**Output Results**		
Model Components	Heating	$\alpha_{s,ext}$, $\alpha_{IR,int}$ (BOL)	ε_{ext}, ε_{int} (BOL)	Steady State Max. Temperature (°C)	Steady State Min. Temperature (°C)	Steady State Avg. Temperature (°C)
+Z box plate	-	0.5, 0.9	0.5, 0.9	-6.51	-37.47	-21.96
-Z box plate	-	0.5, 0.9	0.5, 0.9	-12.90	-42.98	-30.77
+Y box plate	1353 W/m^2	0.5, 0.9	0.5, 0.9	-2.49	-18.92	-11.33
-Y box plate	-	0.5, 0.9	0.5, 0.9	-34.44	-45.64	-41.73
+X box plate	-	0.5, 0.9	0.5, 0.9	-14.24	-44.84	-30.88
-X box plate	-	0.5, 0.9	0.5, 0.9	-14.27	-44.79	-30.87
Internal block	30 W	0.08	0.15	-4.24	-17.30	-9.89
Test H9b	**Test Details**					
	Input Variables			**Output Results**		
Model Components	Heating	$\alpha_{s,ext}$, $\alpha_{IR,int}$ (BOL)	ε_{ext}, ε_{int} (BOL)	Steady State Max. Temperature (°C)	Steady State Min. Temperature (°C)	Steady State Avg. Temperature (°C)
+Z box plate	-	0.5, 0.9	0.5, 0.9	3.90	-28.14	-10.64
-Z box plate	-	0.5, 0.9	0.5, 0.9	-7.44	-36.73	-24.79
+Y box plate	1353 W/m^2	0.5, 0.9	0.5, 0.9	4.13	-13.43	-4.67
-Y box plate	-	0.5, 0.9	0.5, 0.9	-23.76	-38.92	-34.04
+X box plate	-	0.5, 0.9	0.5, 0.9	-5.78	-38.28	-23.62
-X box plate	-	0.5, 0.9	0.5, 0.9	-5.83	-38.23	-23.61
Internal block	50 W	0.08	0.15	17.79	-1.27	9.11
Test H9c	**Test Details**					
	Input Variables			**Output Results**		
Model Components	Heating	$\alpha_{s,ext}$, $\alpha_{IR,int}$ (BOL)	ε_{ext}, ε_{int} (BOL)	Steady State Max. Temperature (°C)	Steady State Min. Temperature (°C)	Steady State Avg. Temperature (°C)
+Z box plate	-	0.5, 0.9	0.5, 0.9	18.71	-19.59	-0.17
-Z box plate	-	0.5, 0.9	0.5, 0.9	-2.39	-30.99	-19.26
+Y box plate	1353 W/m^2	0.5, 0.9	0.5, 0.9	12.05	-8.37	1.47
-Y box plate	-	0.5, 0.9	0.5, 0.9	-13.94	-32.76	-26.98
+X box plate	-	0.5, 0.9	0.5, 0.9	1.98	-32.27	-16.95
-X box plate	-	0.5, 0.9	0.5, 0.9	1.92	-32.21	-16.93
Internal block	70 W	0.08	0.15	38.66	13.73	27.01
Test H9d	**Test Details**					
	Input Variables			**Output Results**		
Model Components	Heating	$\alpha_{s,ext}$, $\alpha_{IR,int}$ (BOL)	ε_{ext}, ε_{int} (BOL)	Steady State Max. Temperature (°C)	Steady State Min. Temperature (°C)	Steady State Avg. Temperature (°C)
+Z box plate	-	0.5, 0.9	0.5, 0.9	32.60	-11.70	9.56
-Z box plate	-	0.5, 0.9	0.5, 0.9	2.31	-25.67	-14.12
+Y box plate	1353 W/m^2	0.5, 0.9	0.5, 0.9	20.29	-3.67	7.14
-Y box plate	-	0.5, 0.9	0.5, 0.9	-4.85	-27.08	-20.46
+X box plate	-	0.5, 0.9	0.5, 0.9	9.14	-26.73	-10.78
-X box plate	-	0.5, 0.9	0.5, 0.9	9.06	-26.66	-10.76
Internal block	90 W	0.08	0.15	58.49	27.80	43.93

Table H10 Data and temperature results of cubic-model with a flat reflector internal surface coating, a flat absorber surface coating on the block, and for varying internal heat generation

Test H10a	**Test Details**					
	Input Variables			**Output Results**		
Model Components	Heating	$\alpha_{s,ext}$, $\alpha_{IR,int}$ (BOL)	ε_{ext}, ε_{int} (BOL)	Steady State Max. Temperature (°C)	Steady State Min. Temperature (°C)	Steady State Avg. Temperature (°C)
+Z box plate	-	0.5, 0.08	0.5, 0.15	-4.04	-39.40	-22.10
-Z box plate	-	0.5, 0.08	0.5, 0.15	-10.64	-45.77	-31.54
+Y box plate	1353 W/m^2	0.5, 0.08	0.5, 0.15	1.19	-17.52	-8.96
-Y box plate	-	0.5, 0.08	0.5, 0.15	-36.29	-49.23	-44.49
+X box plate	-	0.5, 0.08	0.5, 0.15	-12.60	-47.79	-31.57
-X box plate	-	0.5, 0.08	0. 5, 0.15	-12.60	-47.79	-31.57
Internal block	30 W	0.9	0.9	-6.05	-17.91	-10.99
Test H10b	**Test Details**					
	Input Variables			**Output Results**		
Model Components	Heating	$\alpha_{s,ext}$, $\alpha_{IR,int}$ (BOL)	ε_{ext}, ε_{int} (BOL)	Steady State Max. Temperature (°C)	Steady State Min. Temperature (°C)	Steady State Avg. Temperature (°C)
+Z box plate	-	0.5, 0.08	0.5, 0.15	5.92	-29.95	-10.63
-Z box plate	-	0.5, 0.08	0.5, 0.15	-5.23	-39.66	-25.70
+Y box plate	1353 W/m^2	0.5, 0.08	0.5, 0.15	7.96	-12.09	-2.21
-Y box plate	-	0.5, 0.08	0.5, 0.15	-25.44	-42.62	-36.82
+X box plate	-	0.5, 0.08	0.5, 0.15	-3.93	-41.33	-24.31
-X box plate	-	0.5, 0.08	0. 5, 0.15	-3.93	-41.31	-24.30
Internal block	50 W	0.9	0.9	14.51	-1.88	7.27
Test H10c	**Test Details**					
	Input Variables			**Output Results**		
Model Components	Heating	$\alpha_{s,ext}$, $\alpha_{IR,int}$ (BOL)	ε_{ext}, ε_{int} (BOL)	Steady State Max. Temperature (°C)	Steady State Min. Temperature (°C)	Steady State Avg. Temperature (°C)
+Z box plate	-	0.5, 0.08	0.5, 0.15	18.70	-21.26	-0.02
-Z box plate	-	0.5, 0.08	0.5, 0.15	-0.23	-34.03	-20.30
+Y box plate	1353 W/m^2	0.5, 0.08	0.5, 0.15	15.11	-7.08	4.00
-Y box plate	-	0.5, 0.08	0.5, 0.15	-15.43	-36.56	-29.78
+X box plate	-	0.5, 0.08	0.5, 0.15	4.02	-35.39	-17.63
-X box plate	-	0.5, 0.08	0. 5, 0.15	4.02	-35.37	-17.62
Internal block	70 W	0.9	0.9	33.61	13.07	24.27
Test H10d	**Test Details**					
	Input Variables			**Output Results**		
Model Components	Heating	$\alpha_{s,ext}$, $\alpha_{IR,int}$ (BOL)	ε_{ext}, ε_{int} (BOL)	Steady State Max. Temperature (°C)	Steady State Min. Temperature (°C)	Steady State Avg. Temperature (°C)
+Z box plate	-	0.5, 0.08	0.5, 0.15	32.54	-13.25	9.84
-Z box plate	-	0.5, 0.08	0.5, 0.15	4.43	-28.79	-15.25
+Y box plate	1353 W/m^2	0.5, 0.08	0.5, 0.15	23.61	-2.42	9.74
-Y box plate	-	0.5, 0.08	0.5, 0.15	-6.15	-30.96	-23.26
+X box plate	-	0.5, 0.08	0.5, 0.15	11.36	-29.90	-11.45
-X box plate	-	0.5, 0.08	0. 5, 0.15	11.36	-29.88	-11.44
Internal block	90 W	0.9	0.9	51.41	27.06	40.13

Table H11 Data and temperature results of cubic-model with rubber insulation, and for varying internal heat generation

Test H11a	**Test Details**					
	Input Variables			**Output Results**		
Model Components	Heating	$\alpha_{s,ext}$, $\alpha_{IR,int}$ (BOL)	ε_{ext}, ε_{int} (BOL)	Steady State Max. Temperature (°C)	Steady State Min. Temperature (°C)	Steady State Avg. Temperature (°C)
+Z box plate	-	0.5, 0.9	0.5, 0.9	-6.97	-38.04	-22.65
-Z box plate	-	0.5, 0.9	0.5, 0.9	-13.21	-43.09	-30.97
+Y box plate	1353 W/m^2	0.5, 0.9	0.5, 0.9	-3.06	-19.22	-11.76
-Y box plate	-	0.5, 0.9	0.5, 0.9	-35.23	-45.73	-42.02
+X box plate	-	0.5, 0.9	0.5, 0.9	-14.75	-44.98	-31.25
-X box plate	-	0.5, 0.9	0. 5, 0.9	-14.78	-44.93	-31.24
Internal block	30 W	0.9	0.9	27.93	17.63	23.01
Test H11b	**Test Details**					
	Input Variables			**Output Results**		
Model Components	Heating	$\alpha_{s,ext}$, $\alpha_{IR,int}$ (BOL)	ε_{ext}, ε_{int} (BOL)	Steady State Max. Temperature (°C)	Steady State Min. Temperature (°C)	Steady State Avg. Temperature (°C)
+Z box plate	-	0.5, 0.9	0.5, 0.9	3.56	-28.99	-11.72
-Z box plate	-	0.5, 0.9	0.5, 0.9	-7.85	-36.95	-25.09
+Y box plate	1353 W/m^2	0.5, 0.9	0.5, 0.9	3.32	-13.83	-5.30
-Y box plate	-	0.5, 0.9	0.5, 0.9	-24.87	-39.14	-34.51
+X box plate	-	0.5, 0.9	0.5, 0.9	-6.63	-38.55	-24.18
-X box plate	-	0.5, 0.9	0. 5, 0.9	-6.66	-38.50	-24.17
Internal block	50 W	0.9	0.9	72.15	55.67	64.13
Test H11c	**Test Details**					
	Input Variables			**Output Results**		
Model Components	Heating	$\alpha_{s,ext}$, $\alpha_{IR,int}$ (BOL)	ε_{ext}, ε_{int} (BOL)	Steady State Max. Temperature (°C)	Steady State Min. Temperature (°C)	Steady State Avg. Temperature (°C)
+Z box plate	-	0.5, 0.9	0.5, 0.9	17.82	-20.70	-1.61
-Z box plate	-	0.5, 0.9	0.5, 0.9	-2.88	-31.29	-19.64
+Y box plate	1353 W/m^2	0.5, 0.9	0.5, 0.9	10.82	-8.86	0.64
-Y box plate	-	0.5, 0.9	0.5, 0.9	-15.33	-33.09	-27.62
+X box plate	-	0.5, 0.9	0.5, 0.9	0.83	-32.66	-17.69
-X box plate	-	0.5, 0.9	0. 5, 0.9	0.79	-32.60	-17.67
Internal block	70 W	0.9	0.9	115.39	92.71	104.26
Test H11d	**Test Details**					
	Input Variables			**Output Results**		
Model Components	Heating	$\alpha_{s,ext}$, $\alpha_{IR,int}$ (BOL)	ε_{ext}, ε_{int} (BOL)	Steady State Max. Temperature (°C)	Steady State Min. Temperature (°C)	Steady State Avg. Temperature (°C)
+Z box plate	-	0.5, 0.9	0.5, 0.9	31.28	-13.01	7.85
-Z box plate	-	0.5, 0.9	0.5, 0.9	1.78	-25.99	-14.53
+Y box plate	1353 W/m^2	0.5, 0.9	0.5, 0.9	18.76	-4.19	6.18
-Y box plate	-	0.5, 0.9	0.5, 0.9	-6.46	-27.48	-21.20
+X box plate	-	0.5, 0.9	0.5, 0.9	7.76	-27.18	-11.65
-X box plate	-	0.5, 0.9	0. 5, 0.9	7.71	-27.11	-11.62
Internal block	90 W	0.9	0.9	157.83	128.96	143.60

Table H12 Data and temperature results of cubic-model with plastic (Phenolic) insulation, and for varying internal heat generation

Test H12a	**Test Details**					
	Input Variables			**Output Results**		
Model Components	Heating	$\alpha_{s,ext}$, $\alpha_{IR,int}$ (BOL)	ε_{ext}, ε_{int} (BOL)	Steady State Max. Temperature (°C)	Steady State Min. Temperature (°C)	Steady State Avg. Temperature (°C)
+Z box plate	-	0.5, 0.9	0.5, 0.9	-7.15	-37.90	-22.63
-Z box plate	-	0.5, 0.9	0.5, 0.9	-13.23	-43.06	-30.96
+Y box plate	1353 W/m^2	0.5, 0.9	0.5, 0.9	-3.16	-19.23	-11.83
-Y box plate	-	0.5, 0.9	0.5, 0.9	-35.02	-45.67	-41.93
+X box plate	-	0.5, 0.9	0.5, 0.9	-14.86	-44.94	-31.23
-X box plate	-	0.5, 0.9	0. 5, 0.9	-14.86	-44.89	-31.22
Internal block	30 W	0.9	0.9	7.11	-3.95	1.99
Test H12b	**Test Details**					
	Input Variables			**Output Results**		
Model Components	Heating	$\alpha_{s,ext}$, $\alpha_{IR,int}$ (BOL)	ε_{ext}, ε_{int} (BOL)	Steady State Max. Temperature (°C)	Steady State Min. Temperature (°C)	Steady State Avg. Temperature (°C)
+Z box plate	-	0.5, 0.9	0.5, 0.9	3.16	-28.87	-11.71
-Z box plate	-	0.5, 0.9	0.5, 0.9	-7.86	-36.92	-25.08
+Y box plate	1353 W/m^2	0.5, 0.9	0.5, 0.9	3.25	-13.84	-5.36
-Y box plate	-	0.5, 0.9	0.5, 0.9	-24.67	-39.09	-34.43
+X box plate	-	0.5, 0.9	0.5, 0.9	-6.73	-38.51	-24.17
-X box plate	-	0.5, 0.9	0. 5, 0.9	-6.76	-38.46	-24.16
Internal block	50 W	0.9	0.9	37.30	20.08	29.09
Test H12c	**Test Details**					
	Input Variables			**Output Results**		
Model Components	Heating	$\alpha_{s,ext}$, $\alpha_{IR,int}$ (BOL)	ε_{ext}, ε_{int} (BOL)	Steady State Max. Temperature (°C)	Steady State Min. Temperature (°C)	Steady State Avg. Temperature (°C)
+Z box plate	-	0.5, 0.9	0.5, 0.9	17.43	-20.59	-1.60
-Z box plate	-	0.5, 0.9	0.5, 0.9	-2.90	-31.26	-19.64
+Y box plate	1353 W/m^2	0.5, 0.9	0.5, 0.9	10.65	-8.87	0.58
-Y box plate	-	0.5, 0.9	0.5, 0.9	-15.15	-33.05	-27.55
+X box plate	-	0.5, 0.9	0.5, 0.9	0.74	-32.63	-17.69
-X box plate	-	0.5, 0.9	0. 5, 0.9	0.69	-32.56	-17.67
Internal block	70 W	0.9	0.9	66.51	43.13	55.20
Test H12d	**Test Details**					
	Input Variables			**Output Results**		
Model Components	Heating	$\alpha_{s,ext}$, $\alpha_{IR,int}$ (BOL)	ε_{ext}, ε_{int} (BOL)	Steady State Max. Temperature (°C)	Steady State Min. Temperature (°C)	Steady State Avg. Temperature (°C)
+Z box plate	-	0.5, 0.9	0.5, 0.9	30.91	-12.91	7.86
-Z box plate	-	0.5, 0.9	0.5, 0.9	1.77	-25.97	-14.53
+Y box plate	1353 W/m^2	0.5, 0.9	0.5, 0.9	18.61	-4.21	6.13
-Y box plate	-	0.5, 0.9	0.5, 0.9	-6.29	-27.44	-21.14
+X box plate	-	0.5, 0.9	0.5, 0.9	7.67	-27.15	-11.64
-X box plate	-	0.5, 0.9	0. 5, 0.9	7.62	-27.08	-11.62
Internal block	90 W	0.9	0.9	94.92	65.38	80.52

Appendix I: SUNSAT Operating Data

This appendix presents temperature data from SUNSAT for specific sensors and for two specific periods in SUNSAT's lifetime.

Figures I1 to I6 give the temperature response of the solar panels, bottom plate and battery. All these previously mentioned figures are generated from data retrieved in July 1999 for SUNSAT still in an ideal orbit i.e., polar sun-synchronous orbit with a β-angle approximately equal to 0°. The result of which is an eclipse period of approximately 36 min duration that allows for the cooling of the SUNSAT subsystems. SUNSAT is also rotated about its Z-axis at an approximated rate of 6 "spins" per orbit.

On the 16 June 2000, SUNSAT was (according to the software Nova) in a path of zero eclipse (β-angle approximately equal to 90°). The rotation rate and the orientation of the satellite about its local axis at a point in time cannot be 100% established due to the changes that were being made by ground control to try alleviate the overheating problems. These changes were not accurately recorded. The few sensors that were functioning properly in July 1999, failed to record data at regular intervals in the year 2000, and a few of these sensors recorded almost no data. Only the temperature data from the +Y solar panel and the battery were consistent and useable. This data is plotted in figures I7 and I8.

What is most obvious from figure I7 is the dip in the SUNSAT +Y solar panel temperature data at a regular interval (± 6000 s) to below –20°C. It is quite obvious from figure I7 that SUNSAT was still passing through an eclipse, even though on the 10th of June 2000, according to the software that tracked SUNSAT, Nova, it was supposed to be in zero eclipse. The reason for this inconsistency is unknown. The eclipse is not as long as for the case of 3 July 1999, but still very evident.

(**Note**: The solar panels of the real SUNSAT are labeled according to the orientation system set-up by the designers, where as, the solar panels of the SUNSAT models generated in this thesis; SUNSAT 2 and SUNSAT 3, have orientation labeling that differs from the real SUNSAT. Therefore the actual +Y solar panel data from SUNSAT might not necessarily match the +Y solar panel for the SUNSAT 3 model.)

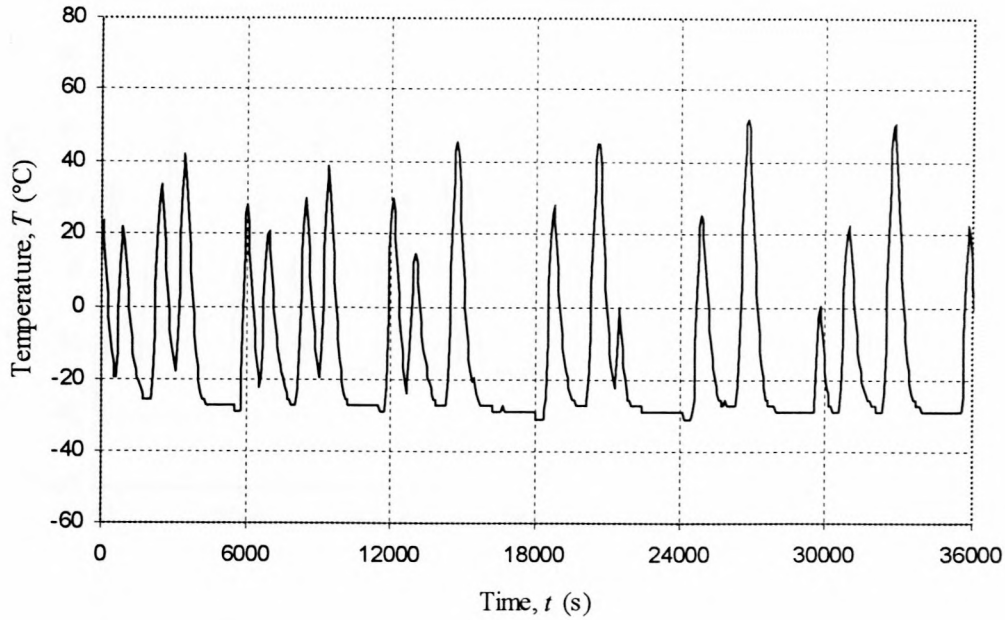

Figure I1 SUNSAT +Y solar panel temperature response on the 3 July 1999

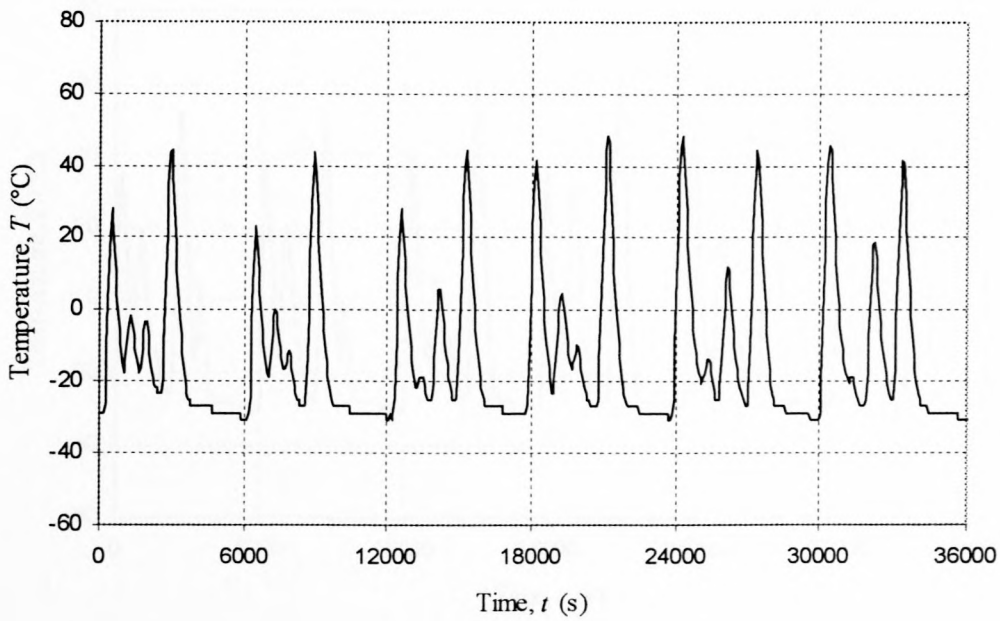

Figure I2 SUNSAT -Y solar panel temperature response on the 3 July 1999

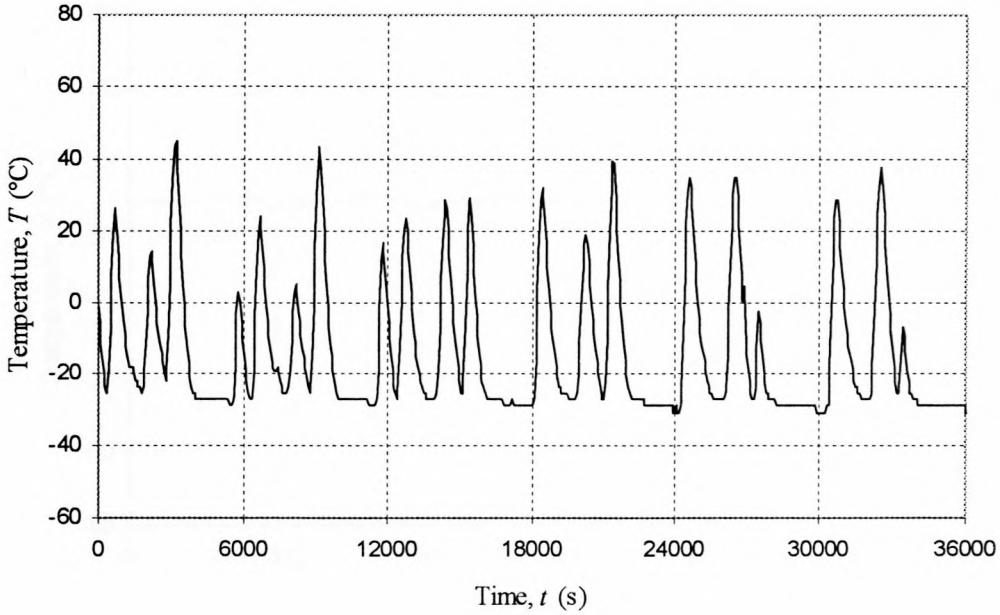

Figure I3 SUNSAT +X solar panel temperature response on the 3 July 1999

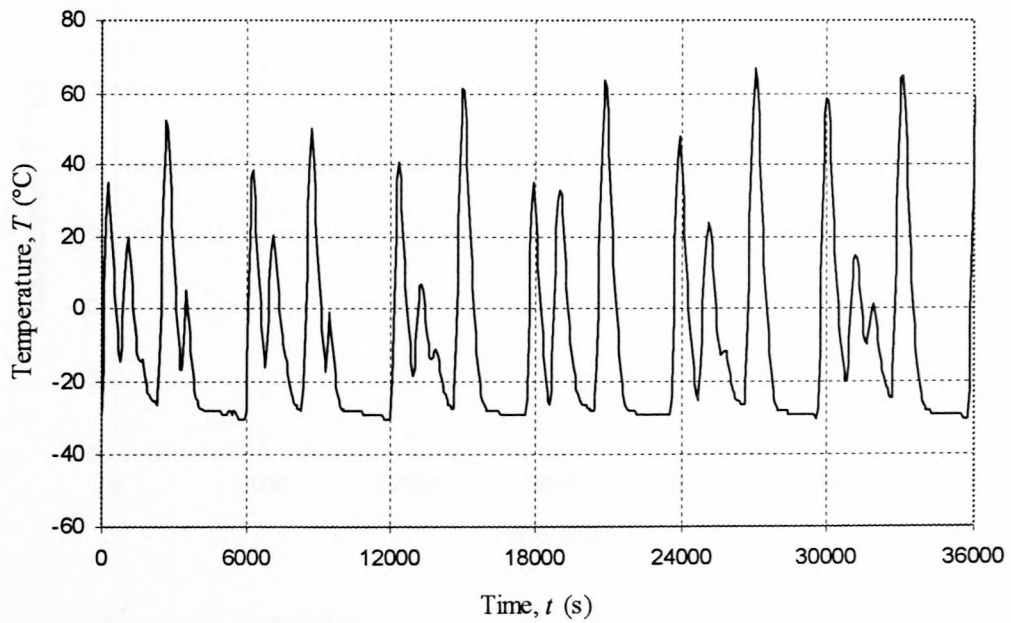

Figure I4 SUNSAT -X solar panel temperature response on the 3 July 1999

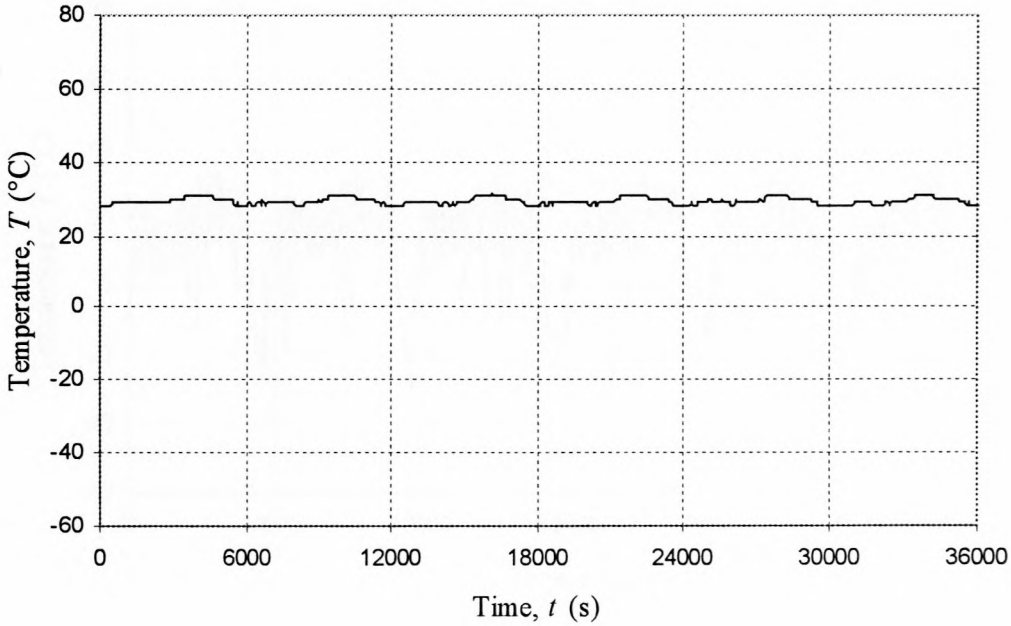

Figure I5 SUNSAT bottom-plate temperature response on the 3 July 1999

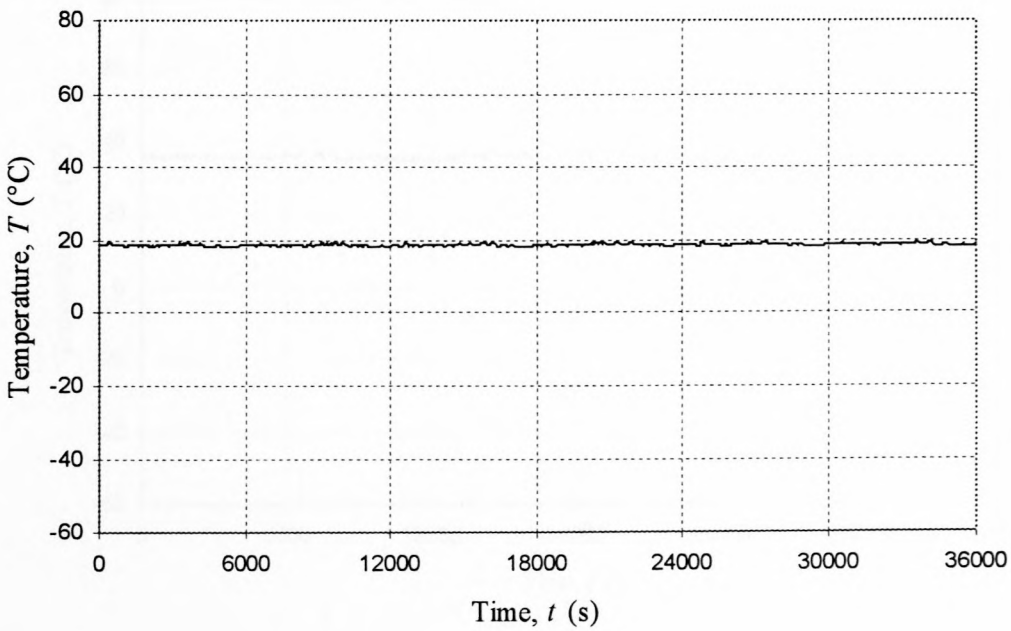

Figure I6 SUNSAT battery temperature response on the 3 July 1999

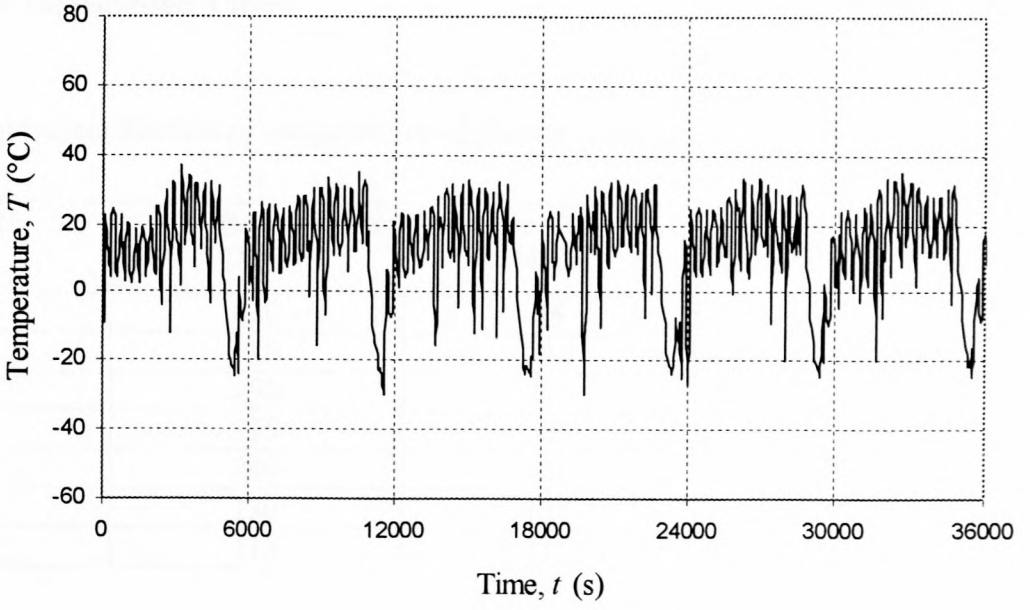

Figure I7 SUNSAT +Y solar panel temperature response on the 16 June 2000

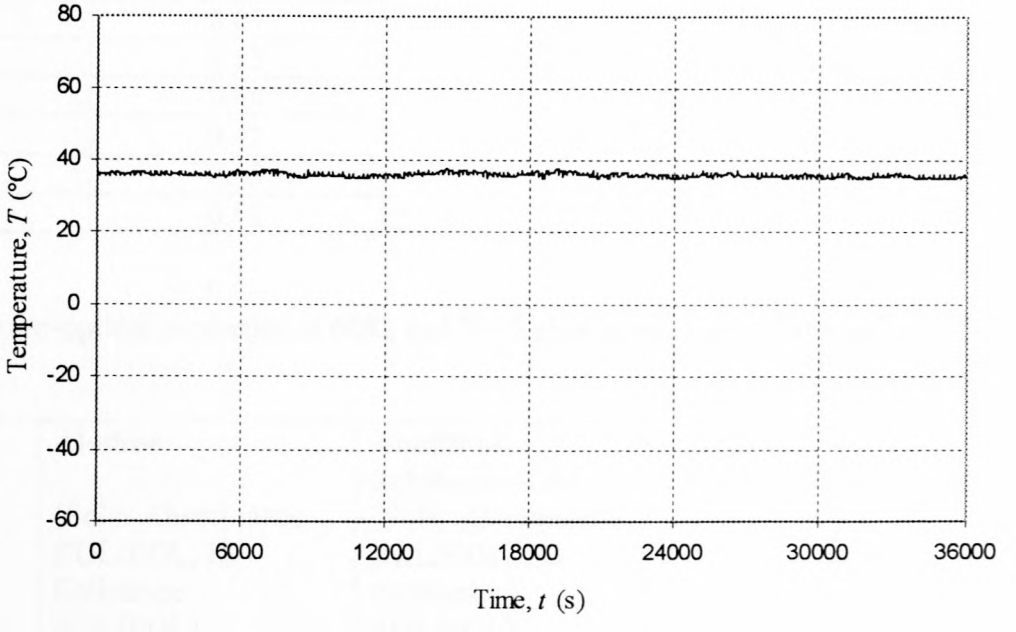

Figure I8 SUNSAT battery temperature response on the 16 June 2000

Appendix J: Information Tables

Table J1 Equivalent blackbody temperatures of planets (Langton, 1969)

Planets	**Radiation temperature (K)** Day	Night
Mercury	600	15
Venus	230	230
Earth	250	250
Moon	375	120
Mars	240	220
Jupiter	130	130
Saturn	115	115

Table J2 The average value of albedo for the planets and the moon (Langton, 1969)

Planet	**Average albedo, *a***
Mercury	0.07
Venus	0.76
Earth	0.36
Moon	0.07
Mars	0.15
Jupiter	0.44
Saturn	0.42
Uranus	0.45
Neptune	0.52

Table J3 Thermo-optical properties of 6082 and 7075 aluminum alloy (Strümpfer, 2002)

Thermo-optical properties	**Alodine** (Solar Absorptance BOL/EOL, IR Emittance BOL/EOL)	**Anodized Sulphuric Acid** (Solar Absorptance BOL/EOL, IR Emittance BOL/EOL)
Aluminum alloy 6082-T6	0.08/ No Data, 0.15/ No Data	
Aluminum alloy 7075-T6	0.08/ No Data, 0.15/ No Data	0.877/ 0.877, 0.424/ 0.477

Table J4 SUNSAT mass properties

Component	Mass	Location
Attachment Ring	1 kg	Bottom
Bottom Plate	2.5 kg	Bottom
Camera	4 kg	Tray 11
Solar Panels	4 x 0.775 kg	Side Panels
Slow Bus	1.5 kg	Tray 11
Fast Bus	1.5 kg	Tray 11
Batteries	2 x 3 kg	Tray 11
Reaction Wheels	1 kg	Tray 11
S-Band Sender	1.5 kg	Tray 11
Regulator	1 kg	Tray 11
RF	5.5 kg	Tray 1-10
Standard PCB	7 x 1.55 kg	Tray 1-10
Top Plate + Coils	2.4 kg	Top
Boom + Tip-Mass	4 kg	Top
Magnetometer	0.3 kg	Top
Horizon Sensor	2 x 0.2 kg	Top
Star Sensor	0.23 kg	Top
Sun Sensor	0.25 kg	Top
GPS Tray	3.5 kg	Tray 1-10
Bus Hardware	11 x 0.861 kg	Tray 1-11

Table J5 SUNSAT sub-sections totaled mass

Component/s	Total Mass
Tray 11 (lower-body)	17.361 kg
Tray 1-6 (top-body)	14.23 kg*
Tray 7-10 (middle-body)	14.23 kg*
Top	7.58 kg
Bottom	3.5 kg
Side Panels	3.1 kg
SUNSAT	**60 kg**

(* The total mass of trays 1-10 (28.46 kg) has been divided between trays 1-6 and trays 7-10.)

Table J6 SUNSAT temperature sensor locations and ground station (ESL) channels

Channel	Analog Sample	Unit	Location
TLM			
EXP			
37	SB_PA_TEMP	°C	S-Band Power Amplifier Temp. Located in bottom tray
50	T_STEPPER	°C	Stepper Motor Driver Temperature. Located in bottom tray
51	T_TUBE	°C	Camera Tube Temperature. Located in bottom tray
55	T_MIRROR_POT	°C	Camera Mirror Potentiometer Temperature. Located in bottom tray
58	T_CCD0	°C	CCD0 Temperature. Located on CCD, in tube, in bottom tray
59	T_CCD1	°C	CCD1 Temperature. Located on CCD, in tube, in bottom tray
60	T_CCD2	°C	CCD2 Temperature. Located on CCD, in tube, in bottom tray
ADCS			
64	TEMP_T800	°C	ADCS T800 Processor Temperature. Located on processor in first tray
65	TEMP_DRVR	°C	ADCS Horizon Sensor Driver Temperature. Located in horizon sensor box
69	SST1-Xas	°C	Sun sensor Temperature. Located outside satellite on -X axis sun sensor
70	SST2-Yas	°C	Sun sensor Temperature. Located outside satellite on -Y axis sun sensor
71	SST3-Zas	°C	Sun sensor Temperature. Located outside satellite on -Z axis sun sensor
75	HSSTEMP	°C	ADCS Horizon Sensor Temperature. Located in horizon sensor box
80	TEMP_ADCS	°C	Ambient Temperate in ADCS tray. Located in ADCS tray, just below top plate
85	SST4+Yas	°C	Sun sensor Temperature. Located outside satellite on +Y axis sun sensor
85	SST5+Xas	°C	Sun sensor Temperature. Located outside satellite on +X axis sun sensor
87	SST6+Zas	°C	Sun sensor Temperature. Located outside satellite on +Z axis sun sensor
RAM			
OBC1			
135	TEMP188	°C	OBC1 80188-processor temperature. Located on processor in 4th tray of satellite
OBC2			
166	TEMP386EX	°C	OBC2 80386-processor temperature. Located on processor in 3rd tray of satellite
167	TEMP387EX	°C	OBC2 80387-processor temperature. Located on processor in 3rd tray of satellite
RF			
199	PA2_TEMP	°C	Power Amplifier 2 temperature - location unknown
200	PA1_TEMP	°C	Power Amplifier 1 temperature - location unknown
203	VHF_TEMP	°C	Ambient temperature in VHF tray (about 1/3 from the bottom)
204	UHF_TEMP	°C	Ambient Temperature in UHF tray (about 1/3 from the bottom)
POWER			
225	T_BTMPL_INTCNT	°C	Temperature of bottom plate. Located in bottom tray
227	T_SP+Y_CNTR	°C	Temperature of center of solar panel in the +Y axis
229	T_SP+X_CNTR	°C	Temperature of center of solar panel in the +X axis
231	T_SP-Y_CNTR	°C	Temperature of center of solar panel in the -Y axis
232	T_BAT-X	°C	Temperature of battery pack 1. Located on battery pack in bottom tray
233	T_BAT+X	°C	Temperature of battery pack 2. Located on battery pack in bottom tray
238	T_IMAGERDRVRS	°C	Temperature of imager drivers. Located on driver chips in imager in tube
249	T_SP-X_CNTR	°C	Temperature of center of solar panel in the -X axis
250	T_SP-X_CRNR	°C	Temperature of corner of solar panel in the -X axis
251	T_SP-X_MIDEDG	°C	Temperature of middle of one of the edges of solar panel in the -X axis

Table J7 Properties of common surface finishes (Gilmore, 1994)

Surface Finish	**α (BOL)**	**ε (BOL)**
Optical Solar Reflectors		
8 mil Quartz Mirrors	0.05 to 0.08	0.80
2 mil Silvered Teflon	0.05 to 0.09	0.66
5 mil Silvered Teflon	0.05 to 0.09	0.78
2 mil Aluminized Teflon	0.10 to 0.16	0.66
5 mil Aluminized Teflon	0.10 to 0.16	0.78
White Paints		
S13G-LO	0.20 to 0.25	0.85
Z93	0.17 to 0.20	0.92
ZOT	0.18 to 0.20	0.91
Chemglaze A276	0.22 to 0.28	0.88
Black Paints		
Chemglaze Z306	0.92 to 0.98	0.89
3M Black Velvet	~0.97	0.84
Aluminized Kapton		
½ mil *	0.34	0.55
1 mil	0.38	0.67
2 mil	0.41	0.75
5 mil	0.46	0.86
Metallic		
Vapour Deposited Aluminum (VDA)	0.08 to 0.17	0.04
Bare Aluminum	0.09 to 0.17	0.03 to 0.10
Vapour Deposited Gold	0.19 to 0.30	0.03
Anodized Aluminum	0.25 to 0.86 (see note)	0.04 to 0.88 (see note)
Mylar		
Beta Cloth	0.32	0.86
Astro Quartz	~0.22	0.80
MAXORB	0.9	0.1

* 1 mil = 1 millionth of an inch

(**Note**: Anodizing and similar surface treatments generally produce highly variable optical properties that are difficult to control and are very irregular in any given surface.)

Table J8 Variation of albedo with latitude (Gilmore, 1994)

Latitude		**Probable Cold Case***	**Average**	**Probable Hot Case****
Max	Min	Albedo	Albedo	Albedo
90	80	0.69	0.69	0.75
80	70	0.83	0.68	0.50
70	60	0.56	0.53	0.39
60	50	0.56	0.44	0.38
50	40	0.46	0.37	0.33
40	30	0.37	0.31	0.26
30	20	0.29	0.26	0.25
20	10	0.27	0.24	0.20
10	0	0.26	0.25	0.24
0	-10	0.24	0.23	0.23
-20	-30	0.24	0.24	0.25
-30	-40	0.30	0.28	0.27
-40	-50	0.39	0.35	0.34
-50	-60	0.45	0.45	0.41
-60	-70	0.65	0.56	0.46
-70	-80	0.88	0.74	0.64
-80	-90	0.80	0.74	0.75

(*Determined using the lowest monthly average earth IR radiation with albedo value for same month.)

(**Determined using the highest monthly average earth IR radiation with albedo value for same month.)